Flowback Data Analysis for Evaluating Multi-fractured Horizontal Wells Completed in Unconventional Reservoirs

by

Yingkun Fu

A thesis submitted in partial fulfillment of the requirements for the degree of

Doctor of Philosophy

in

Petroleum Engineering

Department of Civil & Environmental Engineering
University of Alberta

Abstract

This work aims at characterizing fracture network and evaluating multi-fractured horizontal wells completed in unconventional reservoirs through flowback data analysis. A primary focus of this work is to estimate effective fracture pore-volume using flowback rate and pressure data. This work also studies well communication in multi-well pads through a combined analysis of flowback, tracer, and microseismic data. The key findings from this work are summarized in the following paragraphs.

Flowback data from tight oil and gas wells completed in the Woodford Formation show several days of single-phase water production. Diagnostic plots of rate-normalized pressure versus material balance time using single-phase flowback data show a unit slope, which represents pseudo-steady flow in fractures. This study applies an existing flowback tank model on flowback data during pseudo-steady flow to estimate effective fracture pore-volume. A procedure is proposed to estimate fracture compressibility, which is a key input of the tank model. This study further correlates the estimated fracture pore-volume with completion design parameters. The results show that total injected-water volume, gross perforated interval, and the number of clusters are among the key design parameters for an optimal fracturing treatment.

Flowback data from shale gas wells completed in the Horn River and Eagle Ford Formations show early multiphase production of gas and water. A similar rate-decline behavior in water production is observed on these wells during multiphase flowback period. This study shows that the water-rate decline can be described by a harmonic model, which can be used to evaluate

effective fracture pore-volume and predict water recovery. The results show a relatively good match between water recovery predicted by the harmonic model and the values measured during long-term production. Applying the harmonic-decline model on field data shows that water recovery remains very low after several years of production.

Microseismic, pressure interaction (frac-hit and interference), and tracer data are analyzed to investigate well communication among 52 wells completed in the Horn River Basin. The results show that lateral and vertical well communications occur at distances above 1 km and up to 130 m respectively. Tracer data analysis indicates that wells are connected through permeable pathways which allow the flow communication of water, gas, and proppants. These pathways are primarily hydraulic fractures and reactivated natural fractures. Also, this study demonstrates that well communication may last for over 2 years due to proppant flow which prevents fracture closure during flowback and post-flowback production.

Preface

Chapter 2 is published in *SPE Production and Operation* (Fu et al., 2017). Chapter 3 has been submitted for peer review. Chapter 4 is published in *SPE Production and Operation* (Fu et al., 2019). Chapter 5 is an extension of the AAPG/SPE conference paper (URTeC: 2697593), and has been submitted to *Marine and Petroleum Geology*.

I was responsible for model development, computer programming, writing and editing these papers. My co-authors were responsible for providing relevant data from their respective companies, providing useful comments and discussions on field practices, reviewing the manuscript drafts and securing company approvals for these publications. The necessary approvals to include the journal papers as chapters in this work are provided in sequential order in the Copyright Permissions section. The reference style from the Society of Petroleum Engineers was used in this study.

Dedication

This dissertation is dedicated to

my family for their inspiration, encouragements, and endless love.

Acknowledgements

I would like to thank my supervisor Dr. Hassan Dehghanpour for his guidance, support, and motivation throughout my PhD studies. He inspired my interests in scientific questions and engineering problems. His critical comments in my research work motivated my professional growth.

I thank my supervisor committee (Dr. Juliana Leung and Dr. Alireza Nouri), Dr. Thomas A. Blasingame, and Dr. Rick Chalaturnyk for their insights to improve this work. Also, I would like to thank Jones, R. Steven Jr., Doug Bearinger, Robert Hawks, and Claudio Virus for their technical support.

Special thanks to Alberta Innovates Technology Futures, Natural Sciences and Engineering Research Council of Canada, Nexen ULC, Trican Well Services, Newfield Exploration, and BP America for supporting this study.

I would like to appreciate my research group members (Dr. Obinna Ezulike, Dr. Ashkan Zolfaghari, Ali Habibi, Mingxiang Xu, Yanmin Xu, Sara Eghbali, Mahmood Yassin, Khan Athar, Lin Yuan, Son Tran, and Tamer Moussa) for their insightful discussions. I also appreciate the help from some staff members in the Civil and Environmental Engineering Department (Anne Jones and Arlene Figley).

My sincere thanks also go to Dr. Shihe Fan and Jinyu Xiao for their encouragements and advice through the journey.

I could not have come this far without the support of my parents (Chengshan Fu and Jingfen Li) and elder brothers (Yingzhen Fu and Dr. Yingqian Fu). I express my deepest gratitude to them for their endless love.

Table of Contents

List of Table

List of Figures

Chapter 1 Introduction

1.1 Overview

This part of the chapter briefly describes the key technologies and common field practices mentioned in Chapters 2-6.

1.1.1 Unconventional Reservoirs

Unconventional reservoirs are usually defined as sedimentary units that require stimulation for economical oil/gas production due to the low rock permeability or high fluid viscosity (Ma and Holditch 2016).

In this study, "*unconventional reservoirs*" refer to tight and shale oil/gas reservoirs. Tight reservoirs are low-permeability, hydrocarbon producing, non-source rocks such as sandstones and carbonates (Dong et al. 2016). Shale reservoirs are fine-grained and organic-rich rocks that produce oil and gas. Most shales are both source and reservoir rocks. In shale gas reservoirs, gas is stored in three ways: (1) adsorbed gas; (2) free gas; and (3) solution gas within oil (Aguilera 2016).

The primary feature of tight and shale reservoirs is their ultra-low permeability, which is generally lower than 0.1 mD (Grafton et al. 2016). Therefore, developing these unconventional reservoir requires a combination of horizontal drilling and multistage hydraulic fracturing for economic production of oil and gas.

Fig. 1.1 shows the geographical distribution of major tight and shale gas/oil reservoirs in North America. Most of them are located in the central and south part of the United States and Western Canada. This thesis mainly focuses on four unconventional reservoirs including Horn River, Montney, Woodford, and Eagle Ford.

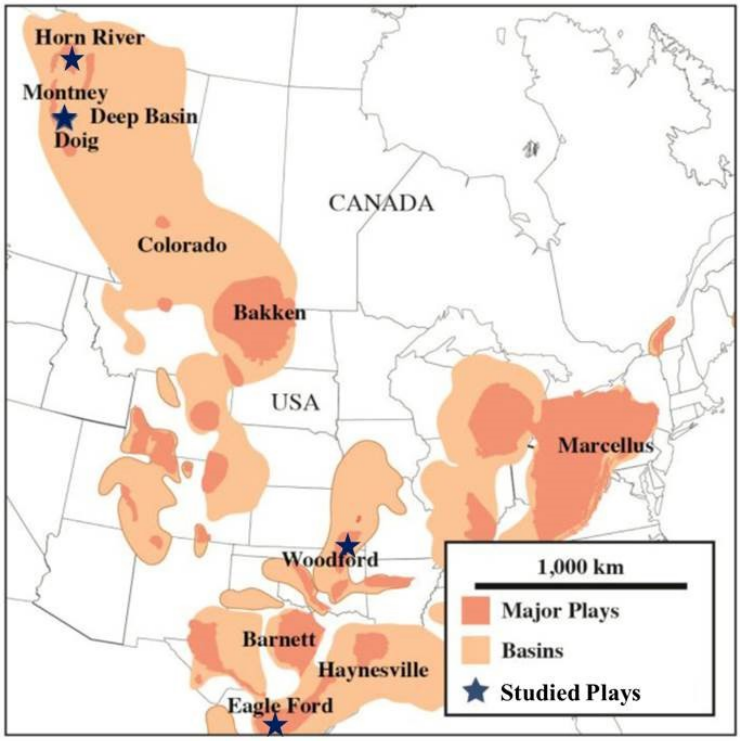

Fig. 1.1: Map of unconventional reservoirs in North America with four studied plays including Horn River, Montney, Eagle Ford, and Woodford (modified from Boyer et al. 2011 and McKean and Priest 2019).

1.1.2 Unconventional Reservoir Development

Fig. 1.2 describes the primary operational activities of developing unconventional resources. After the drilling process, a horizontal well mainly undergoes multi-stage hydraulic fracturing (Fig. 1.3) and flowback before putting it on production. Gas wells completed in the shale and tight formations may experience a period of extended shut-in (up to 3 months) for preparing flowback and production equipment at the surface. The following subsections describe horizontal drilling, multi-stage hydraulic fracturing, and flowback in unconventional reservoirs.

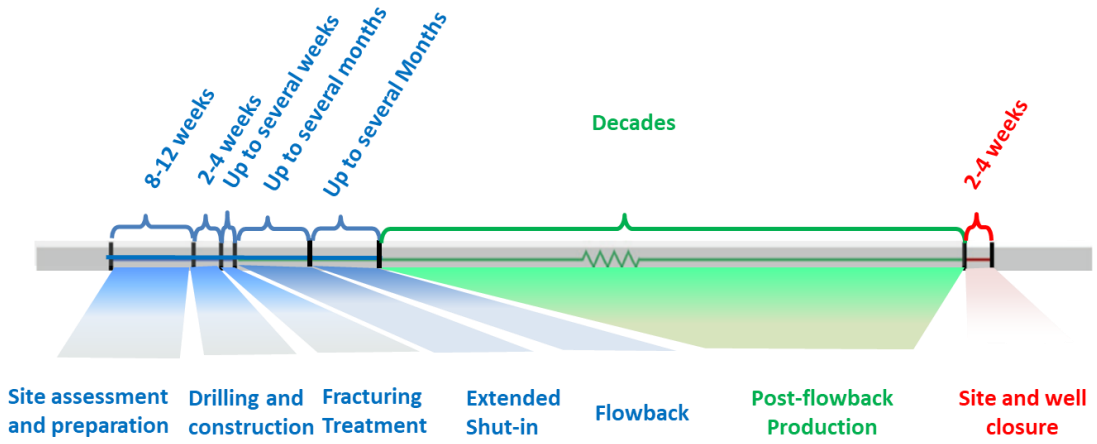

Fig. 1.2: General timeline and summary of activities for developing unconventional resources (modified from U.S. Environmental Protection Agency, 2016)

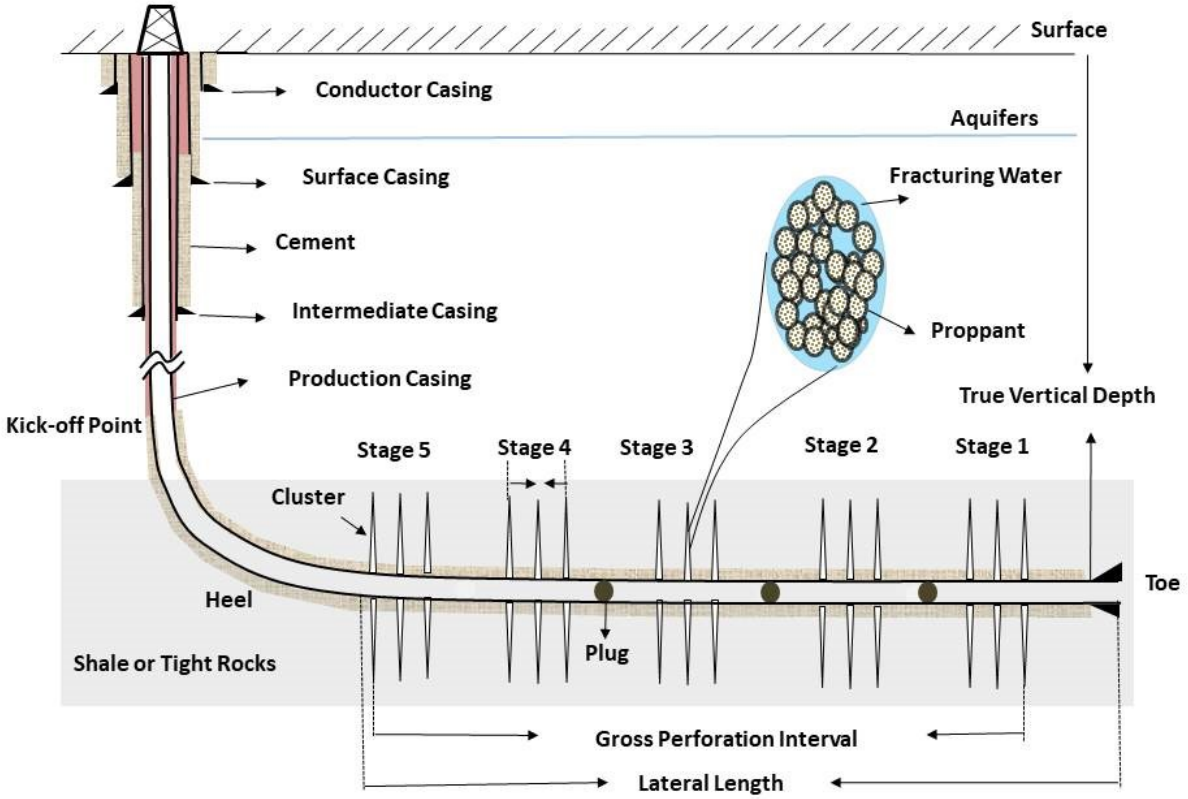

Fig. 1.3: Schematics showing the key concepts for multi-fractured horizontal wells completed in unconventional reservoirs (not to scale). The wellbore schematic is modified from the Ground Water Protection Council, ALL Consulting (2009).

1.1.2.1 Horizontal Drilling and Multiwell Pad

Horizontal well drilling. Horizontal wells play a key role in improving the gas/oil production from unconventional reservoirs. Compared with vertical drilling, horizontal drilling increases the contact area between wellbore and reservoir, and thus improves well productivity. Horizontal drilling is especially important to develop the unconventional reservoirs with thin pay zones and natural fractures (Lacy et al. 1992).

A horizontal well is initially drilled vertically until it reaches a designed depth, which is known as kickoff point (Fig. 1.3) . The well is then drilled at an increasing angle until it reaches to the target formation, followed by drilling horizontally to designed lateral length (Fig. 1.3). As shown in Fig. 1.4, conductor casing, surface casing, and intermediate casing are generally placed with cement to isolate the wellbore from aquifers and wellbore during the drilling process. Production casing is often placed into a drilled hole with cement to isolate the zone containing natural gas from other formations.

Multiwell pad. In recent years, operators tend to drill multiple wells from a single site (known as a pad) in unconventional reservoirs. Over 58% of wells drilled in unconventional reservoirs in the US are now drilled in multiwell pads (Ostadhassan et al. 2015). Multiwell pad drilling allows for maximizing reservoir penetrations with minimizing surface disturbance (U.S. EIA 2016). Also, multiwell pad reduces the costs in drilling, fracturing, and production operations.

1.1.2.2 Multi-stage Hydraulic Fracturing

Horizontal wells drilled in shale and tight reservoirs need to be fractured with multiple stages (Fig. 1.3) to achieve economical production rate. In a single stage, multiple clusters are generally used to create multiple fractures. The contact area between wellbore and reservoir can be significantly increased through these multiple fractures.

Hydraulic Fracturing Process. For a single horizontal well, the fracturing process starts from the stages at the toe and moves toward the stages at the heel. Fracturing each stage mainly involves

the following 2 key steps: 1) A section of wellbore is perforated to create holes connecting wellbore and formation. The perforation holes allow fracturing fluid and proppants entering formation, and subsequently allows hydrocarbon flowing into the wellbore; 2) Fracturing fluids carrying proppants and additives (generally less than 1%) are pumped down wellbore at high pressure to create fractures or reopen in-situ fractures. A cement plug is usually used to isolate the previous stages before fracturing the next stage. After fracturing treatment, the cement plugs are drilled out before flowback.

Multiple wells in a pad are often simultaneously or sequentially fractured to increase the access to natural fractures in shale and tight reservoirs. Fig. 1.4 illustrates the fracturing processes for multiple horizontal wells in unconventional reservoirs: Simultaneous fracturing describes the process of fracturing both wells at the same time, whereas sequential or modified sequential fracturing describes the process of fracturing two neighboring wells in a sequence. In this study, the horizontal wells completed in the Horn River Formation are fractured in a modified sequence.

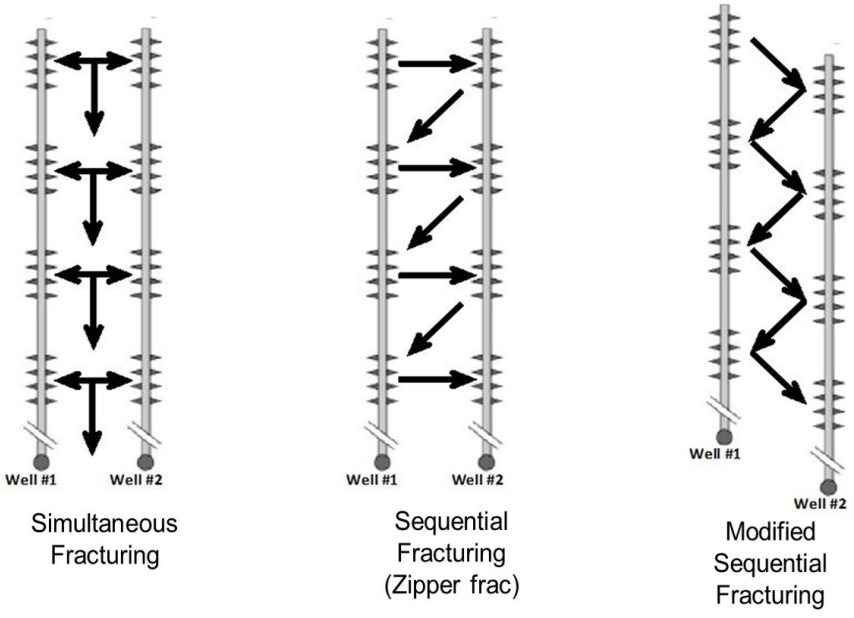

Fig. 1.4: Illustration of simultaneous, sequential, and modified sequential fracturing of two horizontal wells in unconventional reservoirs (modified from Nagel et al. 2013).

Hydraulic Fracturing Design. Table 1.1 summarizes the general design parameters the Horn River, Montney, Woodford, and Eagle Ford wells. The design of fracturing fluids, proppant, stage and clusters are described as follows:

(i) Fracturing fluids. The primary functions of fracturing fluid are to extend fractures and carry proppant into the formation. Fracturing fluid is typically a slurry of water and chemical additives. Additionally, gels, foams, and compressed gases, including nitrogen, carbon dioxide and air can be injected. The typical fracturing fluid for unconventional wells contains about 90% of water and up to 1% of chemical additives (Ezulike 2017).

(ii) Proppant. The purpose of proppant is to prevent the induced fractures from closing after the fracturing process. Typical proppant sizes are generally between 8 and 140 mesh (106 μm-2.36 mm). Silica sand is the most commonly used proppants. The other types of proppant materials include resin-coated sand and ceramic proppants. Resin materials are coated on sands to smooth the surface and make the shape more uniform. Resin-coated sand also has a higher strength to resist the fracture closure. Ceramic proppants are regarded as the most effective proppants because of uniform shape and relatively high strength.

(iii)Stage and cluster. Typically, horizontal wells in unconventional reservoirs are fractured with 8 to 22 stages. The average stage spacing varies from 100 to 120 m. Also, each stage is perforated with 1 to 6 clusters. Gross perforation interval (Fig. 1.3) varies from 1454 to 2200 m. Recent studies indicated that cluster spacing plays an important role in the effectiveness of hydraulic fracturing treatment (Cipolla et al. 2011; Cheng 2013). The cluster spacing depends on a number of variables including permeability, porosity, and the content of natural fractures (EPA 2011).

1.1.2.2 Flowback

After fracturing treatment, wells go through a period of flowback to clean them up for oil/gas production. The flowback period varies from several days to weeks. Most horizontal wells are

opened for flowback through production casing. In addition, choke at wellhead is used to control the rate and pressure during flowback.

In unconventional reservoirs, generally less than 30% of fracturing fluid (Zhou et al. 2016; Engelder 2012) is recovered to surface during flowback. However, the flowback water contains a relatively high concentration of salts after contacting with underhole shale and tight rocks. The salinity of flowback water can reach to 10 to 80 thousands ppm (Engelder et al. 2014). The flowback water is then disposed to avoid the contamination of freshwater resources at the surface.

Table 1.1: Summary of completion designs in the Horn River, Montney, Woodford, and Eagle Ford wells (*na* = not available)

Completion Design Parameters	Horn River	Montney (Sadeghi 2013)	Woodford (Grieser 2011)	Eagle Ford (Shelley et al. 2012)
Average total injected water volume, 10^3 m^3	64	28	39	25
Average gross perforation interval, m	2200	1519	1454	1376
Average number of fracture stages	22	8	14	16
Stage spacing, m	120	126	100	*na*
Cluster per stage	3-5	1-6	4-5	*na*
Proppant mass, tonnes	3700	900	1340	1800
Pump rate, m^3/min	12	*na*	14	11

1.1.3 Fracture Characterization

The production forecast for the multi-fractured horizontal wells is a key input for decision-making and investment in unconventional reservoirs. Hydrocarbon production from shale and tight reservoirs are significantly determined by fracture properties such as fracture permeability and surface area. Fracture characterization thus becomes crucial to forecast production in unconventional reservoirs. Also, fracture characterization is important to evaluate and optimize fracturing treatments in tight and shale reservoirs.

Outcrops, cores and image logs from tight and shale formations contain natural fractures (Gale et al. 2007). The apertures of natural fractures are typically less than 0.05 mm. The natural fractures are usually filled by calcite (Gale et al. 2007). During fracturing treatment, natural fractures

could be reactivated as the pore pressure increased by the injected fracturing water (Moradian et al. 2016). The interaction between hydraulic fractures and natural fractures further results in a complex fracture network. Fracture characterization is challenging due to the unknown fracture geometry and reactivation of natural fractures.

Table 1.2: Operational timeline for fracture characterization techniques in unconventional reservoirs.

Time	Techniques	Key Outputs
Pre-fracturing	DFIT Data Analysis	Closure Pressure Fracture Gradient Leak-off Coefficient Natural Fracture Detection
During Fracturing	Microseismic Data Analysis	Fracture Geometry (Fracture Height, Fracture Length, and Fracture Orientation) Fracture Complexity
Flowback	Flowback Data Analysis	Fracture Surface Area Fracture Complexity Effective Fracture half length Fracture Permeability Fracture Conductivity Effective Fracture Pore-volume
	Flowback Chemical Analysis	
Post-flowback	Rate-transient Analysis	Fracture Length Fracture-matrix Surface Area

Table 1.2 summarizes the primary techniques for fracture characterization in unconventional reservoirs mentioned or used in Chapter 2 to 6. These techniques include the analysis of diagnostic fracturing injection tests (DFIT) data, microseismic (MS) data, flowback data, and post-flowback production data. The following paragraphs briefly introduce these techniques.

1.1.3.1 DFIT Data Analysis

In unconventional reservoirs, DFIT data analysis is important for obtaining in-situ stress and reservoir properties before fracturing treatment. In DFIT, a small volume of water (<7 m^3) is injected through wellbore to create small hydraulic fractures. The well is then shut-in to record pressure-decline data. As shown in Fig. 1.5, the pressure profile for DFIT is often divided into two parts: 1) The early part is primarily related to fracture properties and in-situ stress; 2) The second part is dominated by reservoir properties.

The primary outputs from DFIT data analysis (see Table 1.2) provide key inputs for optimizing fracturing design, production data analysis, and reservoir simulation in unconventional reservoirs. Among these outputs, closure pressure is normally interpreted as minimum principal stress. Plots of pressure versus square root of time or *G*-function (a function of time) are commonly used to diagnose fracture closure pressure (Nolte 1979; Notle and Smith 1981).

Table 1.2 also lists the other outputs from DFIT data analysis including leak-off coefficient and fracture gradient. However, these outputs primarily represent the properties of unpropped fractures since proppants are not used in DFIT. Also, many factors associated with the data acquisition and interpretation of DFIT may yield unrealistic results for wells completed in the tight and shale reservoirs (Barree et al. 2015).

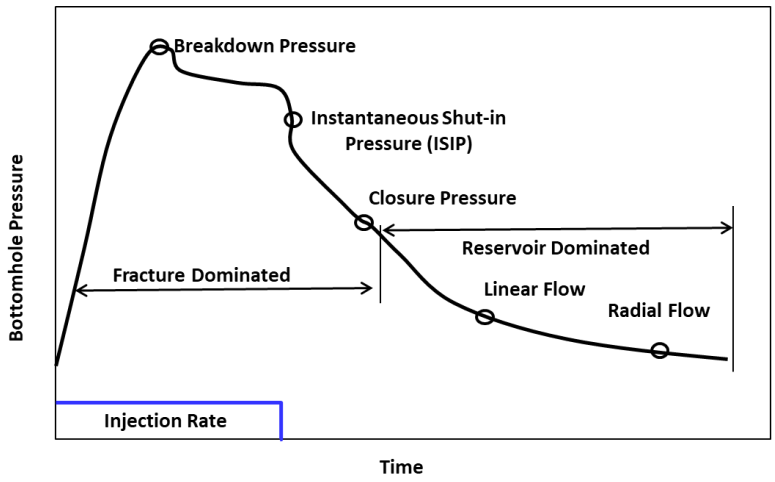

Fig. 1.5: Conceptual pressure profiles of DFIT (modified from Belyadi et al. 2016).

1.1.3.2 MS Data Analysis

MS monitoring provides a direct way of fracture characterization during fracturing treatment. MS data analysis is a technique of characterizing fracture network by recording and locating MS events (i.e. microseismicity). Each MS event represents a small burst of seismic wave energy recorded by geophones at downhole or wellhead during fracturing treatment (Calvez et al. 2016).

MS data analysis estimates the parameters of fracture geometry including fracture length, height, and orientations (Fisher et al. 2002, 2004; Warpinski et al. 2005; Maxwell and Cipolla 2011). Also, the complexity of fracture network can be inferred from MS data analysis (Xu and Calvez 2009). The outputs from MS data analysis have been used to calibrate and verify the other techniques of fracture characterization in unconventional reservoirs (Mayerhofer et al. 2011). However, MS data represent stress deformation but not necessarily the creation of conductive pathways for flow communication (Maxwell and Norton 2012). This may introduce a relatively high uncertainty in fracture characterization.

1.1.3.3 Flowback Data Analysis

After fracturing treatment, flowback data were generally ignored in the past. However, flowback data provide the earliest chance of fracture characterization for evaluating fracturing treatment and production forecast (Ezulike 2017; Williams-Kovacs 2017)

The salinity data of flowback water have been used to characterize the fracture complexity in shale reservoirs (Bearinger 2013; Zolfaghari et al. 2014). In addition, flowback tracer data have been used to evaluate the effectiveness of completion and fracturing, and to identify interwell connectivity of fracture network (Salman et al. 2014).

The frequency and quality of flowback data have been improved because of recent advances in probe technology (Ezulike 2017). The high-frequency rate and pressure data measured during flowback have been interpreted by analytical techniques to estimate fracture half-length, fracture permeability, fracture conductivity, and effective fracture pore-volume (Abbasi et al., 2012, 2014; Clarkson et al. 2013; Ezulike and Dehghanpour 2014; Alkouh et al. 2014; Kurtoglu et al. 2015; Xu et al. 2015, 2016, 2017). These analytical techniques are reviewed in the introduction of relevant chapters.

Numerical simulation has been applied on flowback rate and pressure data to qualitatively characterize fractures in unconventional reservoirs. Several studies simulated the flowback process of shale gas wells to investigate how fracture parameters impact flowback rate and

pressure (Cheng 2012; Li et al. 2013). However, it remains challenging to quantitatively characterize fractures by numerical simulation of flowback process. This is because numerical simulation requires a large number of uncertain inputs, which leads to considerable non-uniqueness of fracture parameter estimates. In addition, assigning the same average values of properties (e.g. compressibility) for fracture and matrix could lead to misleading results (Ezulike 2017).

1.1.3.4 Post-flowback Rate-transient Analysis

Rate-transient analysis (*RTA*) has proved to be a valuable tool of fracture characterization in unconventional reservoirs. The theory of *RTA* is analogous to that of pressure-transient analysis, which is commonly used to characterize conventional reservoirs. In *RTA*, fracture and reservoir properties are estimated by interpreting characteristic flow regimes on continuous post-flowback rate and pressure data (Clarkson 2011; Ilk et al. 2011a, 2011b; Bello 2009).

Transient linear flow is the dominant flow regime observed in fractured shale and tight gas wells (Wattenbarger et al. 1998; Ilk et al. 2011a, 2011b; Arevalo-Villagran and Wattenbarger 2011). Bello and Wattenbarger (2010) proposed a linear dual-porosity solution to account for the natural fracture network in shale gas reservoirs. Flow regime analysis from the model is used to estimate the product of the matrix-fracture surface area and matrix permeability using production data during the transient linear flow regime.

Most *RTA* models assume planar fracture geometry, which does not reflect the complex fracture networks in unconventional reservoirs (Warpinski et al. 2008). Also, post-flowback data from wells in unconventional reservoirs usually show multiphase production, which violates the assumption of single-phase in most *RTA* models (Clarkson 2013; Ezulike 2017). These assumptions contribute to non-uniqueness of fracture parameter estimates by *RTA*.

Numerical simulation can be a rigorous tool of fracture characterization for shale gas wells. Simulation has been applied to estimate hydraulic-fracture properties for shale gas wells through history-matching production rate and pressure data (Sun et al. 2015; Nejadi et al. 2015).

However, history-matching production data can be time-consuming for fracture characterization in unconventional reservoirs. To capture the dimensions of fractures, simulation models require very fine grids, which increase the computation time (Karimi-Fard et al. 2004; Hoffman and Chang 2009) Also, fracture parameters estimated from numerical simulation often have a high degree of uncertainty.

1.2 Research Motivation

Although the rate and pressure data were generally ignored during the flowback period, analyzing these flowback data provides the earliest chance to characterize fractures, evaluate fracturing treatment, and predict future well performance. In recent years, the flowback data were recorded with the improved probe technology. Several techniques have been developed to interpret flowback data for fracture characterization in shale and tight oil/gas wells. This section focuses on the key drawbacks of these techniques which motivate this work:

- A tank model has been developed and applied on single-phase flowback data to estimated effective fracture pore-volume (V_{ef}) for tight gas and oil wells. However, the input parameter of fracture compressibility is generallly unknown or hard to obtain. The unknown input leads to high uncertainties in the estimation of V_{ef}.
- Flowback data from most wells completed in tight reservoirs show a very short single-phase production of water. In fields such as Horn River Basin, flowback data from shale gas wells show immediate multiphase production. The single-phase flowback model is thus no longer applicable to estimate V_{ef} for the wells with early multiphase production.
- V_{ef} estimated by previous flowback models mainly represents the average volume of effective fractures. It remains unclear how V_{ef} changes during flowback, and how the fracture-volume change is related to flowback strategy.
- In general, only 10-30% of the injected fracturing water is recovered from tight and shale oil/gas wells during the flowback period. Studies have investigated the ultimate recovery of fracturing water through numerical simulation. However, there are high uncertainties in the inputs of numerical simulation. Also, the water recovery predicted by these studies

is not validated using field data. The fate of fracturing water thus remains unclear: Will all of it be eventually produced, or some of it will permanently remain in tight formations?

- Well interference is not considered in most of the flowback data analysis. However, pressure interference between wells (refer to *frac-hit* in Section 5.3.1) is commonly reported in multi-well pads during fracturing treatment. It is unclear if this pressure interference implies the creation of connected pathways for flow communication. The next question is whether the wells can still be connected during flowback? If connected, it is of great interests to investigate how well interference impacts flowback data analysis.

1.3 Research Hypotheses

The hypotheses of this thesis are summarized as follows:

- Single-phase flowback data can be interpreted to estimate fracture volume. Also, fracture volume can be related to completion design parameters.
- Fracture volume is lost during flowback. The volume loss is related to the choke size selected for flowback process.
- Water flowback follows a decline pattern that is primarily controlled by relative-permeability effects. Also, this decline pattern can be used to evaluate fracture volume and forecast water recovery.
- Wells in a pad could be connected during flowback. The connected pathways allow flow communication of water and gas between wells. Flowback data analyses could thus lead to misleading estimates of V_{ef} for wells with interference effects in the pad.

1.4 Research Objectives

The overall objective of this thesis is to evaluate multi-fractured horizontal wells through water flowback data analysis. The specific goals for this study are listed as follows:

- To estimate V_{ef} for multi-fractured wells completed in tight and shale reservoirs through flowback data analysis, and to investigate the relationship between V_{ef} and completion design parameters
- To evaluate the change in V_{ef} during flowback, and to investigate its relationship to choke size.

- To evaluate the recovery of fracturing water for wells completed in tight and shale reservoirs by conducting rate-decline analysis on water production data.
- To identify well interference in multi-well pads and evaluate how it impacts flowback data analysis.

1.5 Organization of Thesis

This work is divided into six chapters, all of which (except the last) have been published or submitted for peer-reviewed journal papers. Therefore, there might be some repetition of texts or figures in the chapters.

Chapter 1 presents a brief overview of the research background and introduces the research motivation and objectives of this study. Chapters 2 to 5 can be classified into 2 categories: (1) single-well flowback volumetric analysis, which is further divided into single-phase and multiphase cases, and (2) well interference in multi-well pads.

Chapter 2 interprets single-phase flowback data to estimate effective fracture pore-volume for seven tight oil/gas wells completed in the Woodford Formation. It also presents the correlation analysis of estimated effective fracture pore-volume and completion design parameters.

Chapter 3 shows the application of rate-decline analysis to estimate water recovery and effective fracture pore-volume for multi-fractured horizontal wells completed in the Horn River, Montney, Woodford, and Eagle Ford Formations.

Chapter 4 evaluates the fracture-volume loss for multi-fractured horizontal wells completed in the Eagle Ford Formation through flowback data analysis. This chapter also investigates the relationship between fracture-volume loss and choke-size managements during flowback.

Chapter 5 examines the lateral and vertical extents of initial effective fracture pore-volume by identifying well interference in the pads completed in Horn River shales. The frac-hit, MS, flowback tracer, and production data are analyzed to evaluate well interference during the

fracturing treatment, flowback, and post-flowback periods. This chapter also investigates the effect of well interference on fracture-volume estimation by flowback data analysis.

Chapter 6 summarizes the key conclusions from this work and recommendations for future studies.

The references from all chapters are combined and listed after Chapter 5. Similarly, the appendices from all chapters are combined and presented after the references.

Chapter 2 Estimating Effective Fracture Pore-Volume from Flowback Data and Evaluating Its Relationship to Design Parameters of Multistage Fracture Completion

2.1 Introduction

Fracture characterization is necessary to evaluate fracturing operations and forecast well performance. However, it is challenging to quantitatively characterize the complex fracture network in unconventional reservoirs because of unknown fracture geometry and reactivation of natural fractures. The high-frequency flowback rate and pressure data have proven to be useful to characterize fractures after stimulation operations. Several analytical models have been employed to calculate hydraulic fracture half-length and conductivity using early flowback data (Abbasi et al. 2012, 2014; Clarkson et al. 2013; Ezulike and Dehghanpour 2013, 2014a, 2014b). Most of these models assume planar fracture geometry, which does not reflect the fracture complexity in unconventional reservoirs. However, fracture volume is a geometry-independent parameter, which can be estimated by careful analysis of flowback data using the material balance and flow-regime analysis.

Adefidipe et al. (2014) and Xu et al. (2016) proposed a two-phase flowing material balance equation for estimating effective fracture pore-volume using early flowback data. They calculated effective fracture pore-volume using the linear relationship between rate-normalized pseudo-pressure and pseudo-time. They considered flowback drive mechanisms including gas expansion, water expansion, and fracture closure. Their results suggest that gas expansion is the primary drive mechanism at the onset of flowback. However, initial gas saturation in fractures is unknown in their model, which increases the uncertainty for estimating effective fracture pore-volume.

Xu et al. (2015) extended the conventional material balance equation to analyze two-phase flowback data and verified the proposed approach by numerical simulation. The results show

that estimated fracture volume strongly depends on initial gas saturation in fractures and fracture compressibility. Similarly, in this model initial gas saturation in fractures is an unknown parameter.

Alkouh et al. (2014) introduced a tank model for estimating effective fracture pore-volume for shale gas wells. Based on a simulation analysis, they concluded that at water saturation below 70%, the contribution of gas compressibility is at least 97% of total compressibility. The effects of water expansion and fracture closure were neglected in their model and thus cannot be applied to wells with single-phase water flowback.

Abbasi et al. (2012, 2014) and Abbasi (2013) developed a flowing material balance model to estimate fracture volume using early time single-phase water flowback data. They observed a linear relationship between rate-normalized pressure and material balance time. A flowing material balance model based on this linear relationship was proposed to estimate fracture parameters. However, fracture compressibility is an unknown input in their model, which increases the uncertainty of the results.

Flowback data from seven multi-fractured horizontal tight oil/gas wells in Anadarko Basin show two separate periods during the single-phase water production: Periods 1 and 2. The objectives of this chapter are to 1) understand the flowback drive mechanisms in Periods 1 and 2, 2) interpret the flowback data to estimate the effective fracture pore-volume, and 3) investigate its relationship to completion design parameters. This work hypothesizes that the fracture system is a tank during Periods 1 and 2, and the flowback data during Period 1 can be used to measure the fracture volume.

Diagnostic plots are constructed to understand the physics of Periods 1 and 2. Abbasi et al. (2012)'s tank model is applied on Period 1 to estimate effective fracture pore-volume of seven multi-fractured horizontal wells. A procedure is proposed to estimate fracture compressibility, which is a key input of the model. Finally, the estimated effective fracture pore-volume is

compared with completion design parameters such as total injected water volume, proppant mass, number of stages, and average cluster spacing.

2.2 Methodology

This study is done using the following six steps: (1) gathering and preparing flowback data; (2) understanding the flow behavior through diagnostic plots and flow regime analysis of early flowback data; (3) applying Abbasi et al. (2012)'s model of rate-normalized-pressure (*RNP*) versus material balance time (t_{MB}) on the flowback data; (4) estimating fracture compressibility using Diagnostic Fracturing Injection Test (*DFIT*) data; (5) quantifying and comparing drive mechanisms during early single-phase flowback data using the method proposed by Ezulike et al. (2016); (6) using the method of Pearson correlation coefficient to investigate the relationship between effective fracture-volume (V_{ef}) and completion design parameters, and to find the key parameters affecting V_{ef}.

2.2.1 Flow Regimes during Early Flowback

RNP and t_{MB} are usually used for flow regime identification (Song and Ehlig-Economides 2011). *RNP* is defined by dividing the difference between initial pressure in fractures (P_{fi}) and bottomhole pressure (P_{wf}) by water rate (q_w). *RNP* represents the pressure drawdown at a constant rate for a well producing at variable rate and variable pressure:

$$RNP = \frac{p_{fi} - p_{wf}}{q_w} \tag{2.1}$$

t_{MB} is defined by dividing the cumulative water production volume (W_p) by q_w. t_{MB} represents the equivalent time for a well producing the same amount of fluid at a constant flow rate (Palacio and Blasingame 1993):

$$t_{MB} = \frac{W_p}{q_w} \tag{2.2}$$

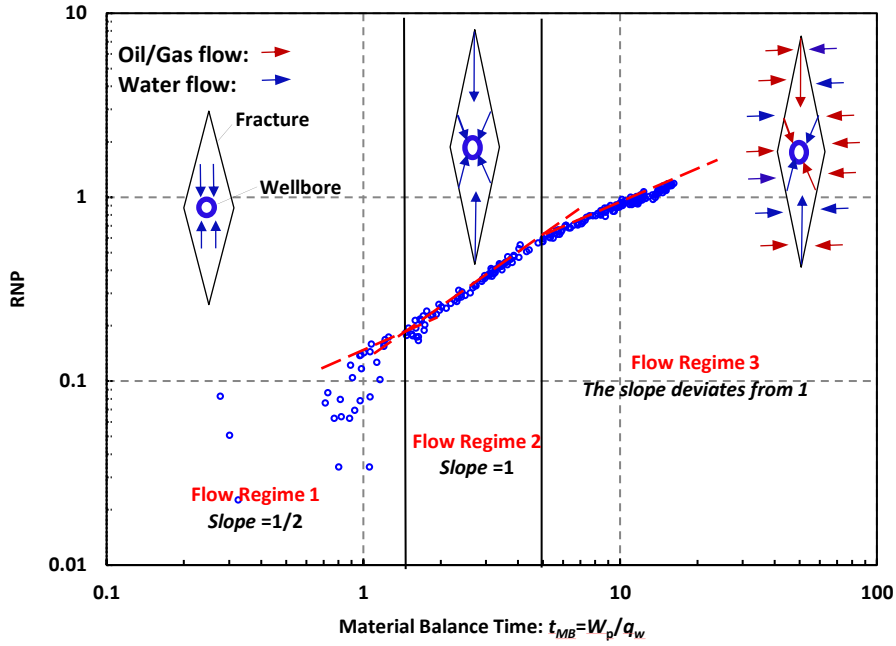

Fig. 2.1: Cross-sectional view of fracture and wellbore illustrating the three possible flow regimes during early flowback: (1) Flow regime 1 (transient linear flow within fractures) is represented by half-slope in log-log plot of *RNP* versus t_{MB}; (2) Flow regime 2 (fracture depletion) is represented by unit-slope in log-log plot of *RNP* versus t_{MB}; (2) Flow regime 3 (transition between fracture depletion and transient linear flow in matrix) is represented by a deviation from unit-slope in log-log plot of *RNP* versus t_{MB}. Blue and red arrows represent the flow of oil/gas and water.

Fig. 2.1 shows that three possible flow regimes may be identified using log-log plot of *RNP* versus t_{MB} during early flowback:

(1) Transient linear flow within fractures: It describes the flow of water along the primary fractures to the perforations (Crafton and Gunderson 2006; Bello 2009; Ezulike and Dehghanpour 2014b). This flow regime can be identified by half-slope in log-log plot of *RNP* and t_{MB}. However, the transient linear flow within fractures happens very soon. This flow regime may be masked by wellbore storage, which makes the early flowback data noisy.

(2) Fracture depletion: It describes water depleting from the fractures which behave as a closed-tank, and occurs when the pressure response reaches the boundary of the fractures (Ilk et al. 2010; Abbasi et al. 2012, 2014; Clarkson and Williams-Kovacs 2013). This flow regime can be represented by unit-slope in log-log plot of *RNP* versus t_{MB}.

(3) Transition between fracture depletion and transient linear flow in the matrix: It occurs when hydrocarbon breakthrough from matrix to fractures (Williams-Kovacs and Clarkson 2013). This flow regime can be identified by the deviation from unit-slope in log-log plot of *RNP* versus t_{MB}.

2.2.2 Flowback Tank Model for Estimating Effective Fracture Pore-volume

Abbasi et al. (2012, 2014) developed a linear relationship between *RNP* and t_{MB} for radial (Eq. 2.3) and linear (Eq. 2.4) flow in fractures, respectively:

$$RNP = \frac{B_w}{C_{st}} t_{MB} + \frac{\varphi_f C_t \mu B}{2 C_{st} K_f} r_e^2 [\frac{1}{2} \ln(\frac{4A}{C_A \gamma r_w^2})] \tag{2.3}$$

$$RNP = \frac{B_w}{C_{st}} t_{MB} + \frac{\varphi_f C_t \mu B}{3 C_{st} K_f} y_e^2 \tag{2.4}$$

where, A is the drainage area, m^2; B is the formation volume factor, m^3/m^3; C_A is the Dietz shape factor; C_t is the total compressibility, psi^{-1}; K_f is the fracture permeability, *md*; r_e is the drainage radius, *m*; r_w is the wellbore radius, *m*; y_e is the fracture half-length, *m*; μ is the viscosity of water, *cp*; γ is the Euler's constant; φ_f is fracture porosity, *fraction*; C_{st} is the total storage coefficient, which is defined as

$$C_{st} = V_{ef}(C_f + C_w) + V_{wb} C_{wb}$$

Wellbore storage is represented by $V_{wb}C_{wb}$. Wellbore volume is expected to be negligible compared with fracture volume. By ignoring wellbore storage, the total storage coefficient can then be simplified as

$$C_{st} = V_{ef}(C_f + C_w) \tag{2.5}$$

where, V_{ef} is the effective fracture pore-volume, m^3; C_f is the fracture compressibility, psi^{-1}; C_w is the water compressibility, psi^{-1}.

As shown in Fig. 2.2, effective fractures include the hydraulic and reactivated natural fractures communicating with wellbore and contributing to fluid recovery during flowback. V_{ef} represents the pore volume of effective fractures, and is independent of the assumed geometry. On the basis of Eqs. 2.3 and 2.4, V_{ef} could be estimated by

$$V_{ef} = \frac{B_w}{C_t m} \tag{2.6}$$

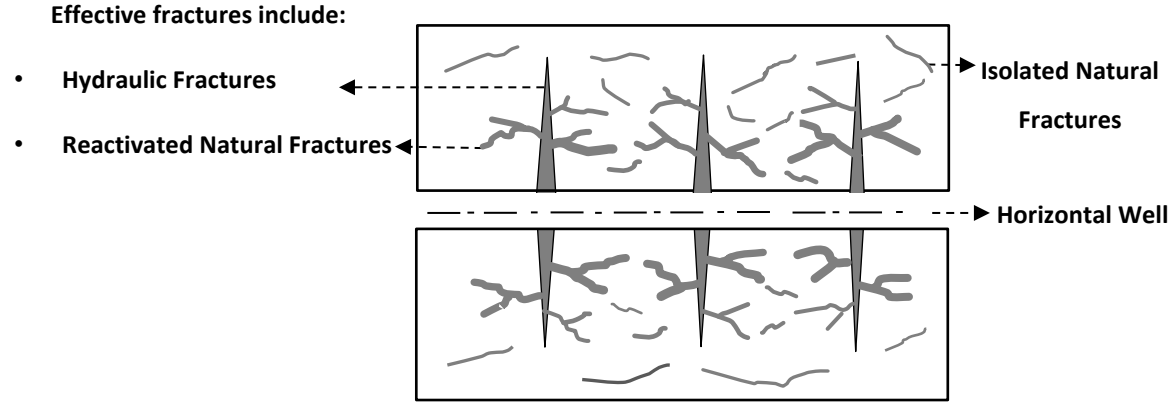

Fig. 2.2: Schematic of a multi-fractured horizontal well. Effective fractures include the hydraulic and reactivated natural fractures communicating with wellbore and contributing to the fluid recovery during flowback.

where m is the slope of RNP versus t_{MB} in the Cartesian plot and total compressibility (C_t) is defined as

$$C_t = C_f + C_w \tag{2.7}$$

Fig. 2.3 shows the procedure to estimate the maximum and minimum effective fracture pore-volume ($V_{ef\text{-}max}$ and $V_{ef\text{-}min}$) for the cases of minimum and maximum fracture compressibility ($C_{f\text{-}min}$ and $C_{f\text{-}max}$), respectively.

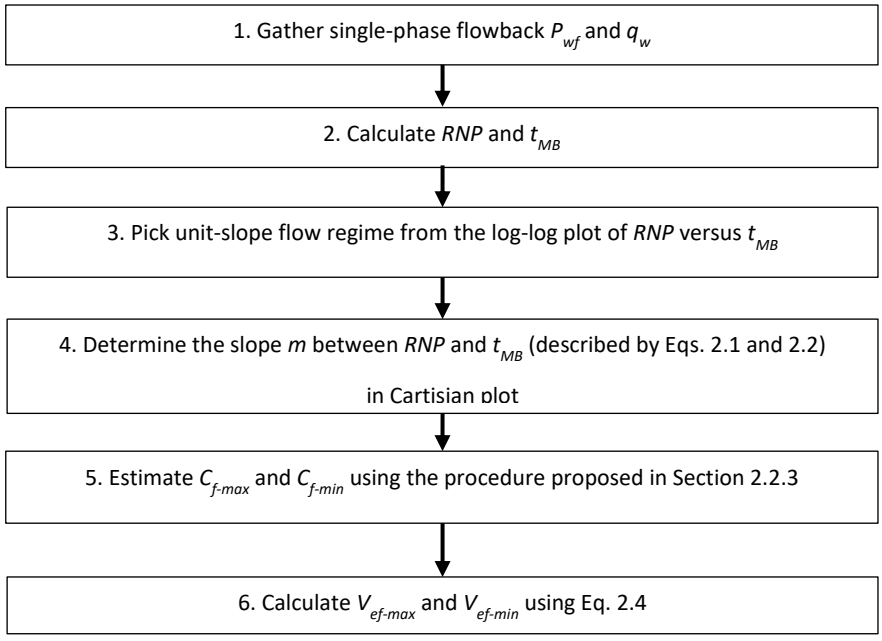

Fig. 2.3: Flow chart for estimating maximum and minimum effective fracture pore-volume.

2.2.3 Estimating Fracture Compressibility

In this study, Aguilera's (1999) graphical method is used to estimate fracture compressibility. Appendix A.1 shows the empirical correlation between C_f and two parameters: (1) net stress on fractures (P_n), which is defined as the difference between minimum principal in-situ stress (σ_{min}) and actual pressure in fractures, and (2) mineralization ratio, which is defined as the percentage of minerals in fractures. This subsection describes the method to estimate P_n and mineralization ratio, and the procedure to estimate fracture compressibility using *DFIT* data.

(i) Net stress on fractures

This study approximates the net stress on fracture (P_n) to be the effective pressure in the fractures:

$$P_n = \sigma_{min} - P_f \tag{2.8}$$

P_f represents the actual pressure in fractures. According to Darcy's law, the difference between P_f and bottomhole pressure (P_{wf}) is relatively low because of high fracture conductivity at early flowback (refer to Section 2.4.1 for more discussions). The difference between P_f and P_{wf} can thus be considered negligible compared with σ_{min}.

In Eq. 2.8, P_{wf} can be measured using bottomhole gauges or calculated using a proper well model and wellhead-pressure data. σ_{min} represents the minimum principal in-situ stress and is usually an unknown parameter. Closure pressure ($P_{closure}$) can be used to estimate σ_{min}. $P_{closure}$ is defined as the fluid pressure at which the fracture effectively closes (Economides and Nolte 2000). As described in Section 1.1.3.1, $P_{closure}$ can be obtained from DFIT data analysis. $P_{closure}$ is then used to estimate P_n by

$$P_n = P_{closure} - P_{wf} \tag{2.9}$$

Eq. 2.9 can be applied to calculate P_n directly for wells with *DFIT* data. However, *DFIT* is usually performed on a limited number of wells in field practice. As shown in Eq. 2.8, we infer $P_{closure}$ for wells without *DFIT* data using the correlation between closure pressure gradient ($G_{closure}$) and fracture gradient (G_f). $P_{closure}$ could be calculated by multiplying $G_{closure}$ with *TVD*. G_f could be calculated by dividing instantaneous shut-in Pressure (*ISIP*) by *TVD*. On the basis of a gross approximation, closure pressure can be linearly related to fracture gradient:

$$G_{closure} = \alpha \cdot G_f \tag{2.10}$$

However, closure pressure estimated from *DFIT* analysis is recommended wherever *DFIT* data are available. Closure pressure gradient, $G_{closure}$, is defined as closure pressure per *TVD*; fracture gradient, G_f, is obtained by dividing *ISIP* at the end of each stage by *TVD*, then averaging the gradient for all stages. The average value of G_f for all stages is used to account for the variation of fracture gradient along the wellbore. α is the coefficient relating $G_{closure}$ to G_f, and can be obtained from nearby wells with *DFIT* data. *ISIP* describes the pressure at the end of pumping, when the fracture is not closed yet, and thus, $ISIP > P_{closure}$. The estimated G_f at the end of pumping is then higher than $G_{closure}$. Therefore, α in Eq. 2.10 is less than 1.

After obtaining $P_{closure}$, Eq. 2.9 is used to estimate the minimum and maximum net stress on fractures ($P_{n\text{-}min}$ and $P_{n\text{-}max}$) together with the minimum and maximum bottomhole pressure ($P_{wf\text{-}min}$ and $P_{wf\text{-}max}$) during the flow regime of fracture depletion.

(ii) Mineralization ratio

Another input in Aguilera's (1999) graphical method is mineralization ratio, which represents the percentage of minerals in fractures. Williams-Kovacs and Clarkson (2013) proposed that minerals in fractures could be assumed as proppant. Mineralization ratio can be the percentage of proppant in fractures, and be related to fracture porosity (φ_f) by

$$mineralization\ ratio = 1 - \varphi_f \tag{2.11}$$

where φ_f is an unknown parameter in Eq. 2.11. This study considers the maximum fracture porosity of $\varphi_{f\text{-}max}$ =100% representing unpropped fractures and the minimum fracture porosity of $\varphi_{f\text{-}min}$ =47.5% representing fractures with cubic packing of proppants (Peters 2012). The arrangement of uncompacted grains is usually represented by cubic packing. The proppants in fractures are loosely packed during early flowback when the fractures are not completely closed, which may result in proppant production in some wells (Nguyen et al. 1996). This study assumes a uniform size and cubic packing for proppants in fractures. $C_{f\text{-}min}$ and $C_{f\text{-}max}$ correspond to the minimum and maximum porosity scenarios, respectively.

(iii) Procedure to estimate fracture compressibility

As illustrated by Fig. 2.4, the procedure to estimate fracture compressibility includes following steps:

- Obtain $P_{closure}$ for wells with *DFIT* data.
- Obtain the correlation between $G_{closure}$ and G_f, using Eq. 2.10, from wells with *DFIT* data.
- Calculate $P_{closure}$ for wells without *DFIT* data using the correlation in *Step 2*.
- Obtain $P_{wf\text{-}min}$ and $P_{wf\text{-}max}$ during the flow regime of fracture depletion.
- Calculate $P_{n\text{-}min}$ and $P_{n\text{-}max}$ for each well using Eq. 2.9.
- Read $C_{f\text{-}min}$ at the point of ($P_{n\text{-}max}$, 1-$\varphi_{f\text{-}max}$) and $C_{f\text{-}max}$ at the point of ($P_{n\text{-}min}$, 1- $\varphi_{f\text{-}min}$) from the graph shown in Appendix A.1.

2.2.4 Quantification of the Drive Mechanisms

According to Ezulike et al. (2016), the drive mechanisms of fracture closure and water expansion could be quantified by compaction-drive index (*CDI*) and water-drive index (*WDI*) separately. Fracture closure represents the reduction of V_{ef} caused by fluid withdrawal during flowback, proppant crushing/embedment, and compressibility of rock grains. During single-phase flowback, *CDI* and *WDI* are defined as

$$CDI = \frac{C_f}{C_t} \tag{2.12}$$

$$WDI = \frac{C_w}{C_t} \tag{2.13}$$

2.2.5 Pearson Correlation Coefficient

The Pearson correlation coefficient (*r*) by (Pearson 1895) provides a measure of linear correlation between two series of values, and ranges from -1 to 1. The positive and negative values of *r* mean positive and negative correlation, respectively. The larger value of absolute *r* means a better correlation between the two parameters. Eq. 2.14 shows how to calculate *r* for two series of data (x_i and y_i):

$$r = \frac{\sum_i (x_i - \bar{x})(y_i - \bar{y})}{\sqrt{\sum_i (x_i - \bar{x})^2} \sqrt{\sum_i (y_i - \bar{y})^2}} \tag{2.14}$$

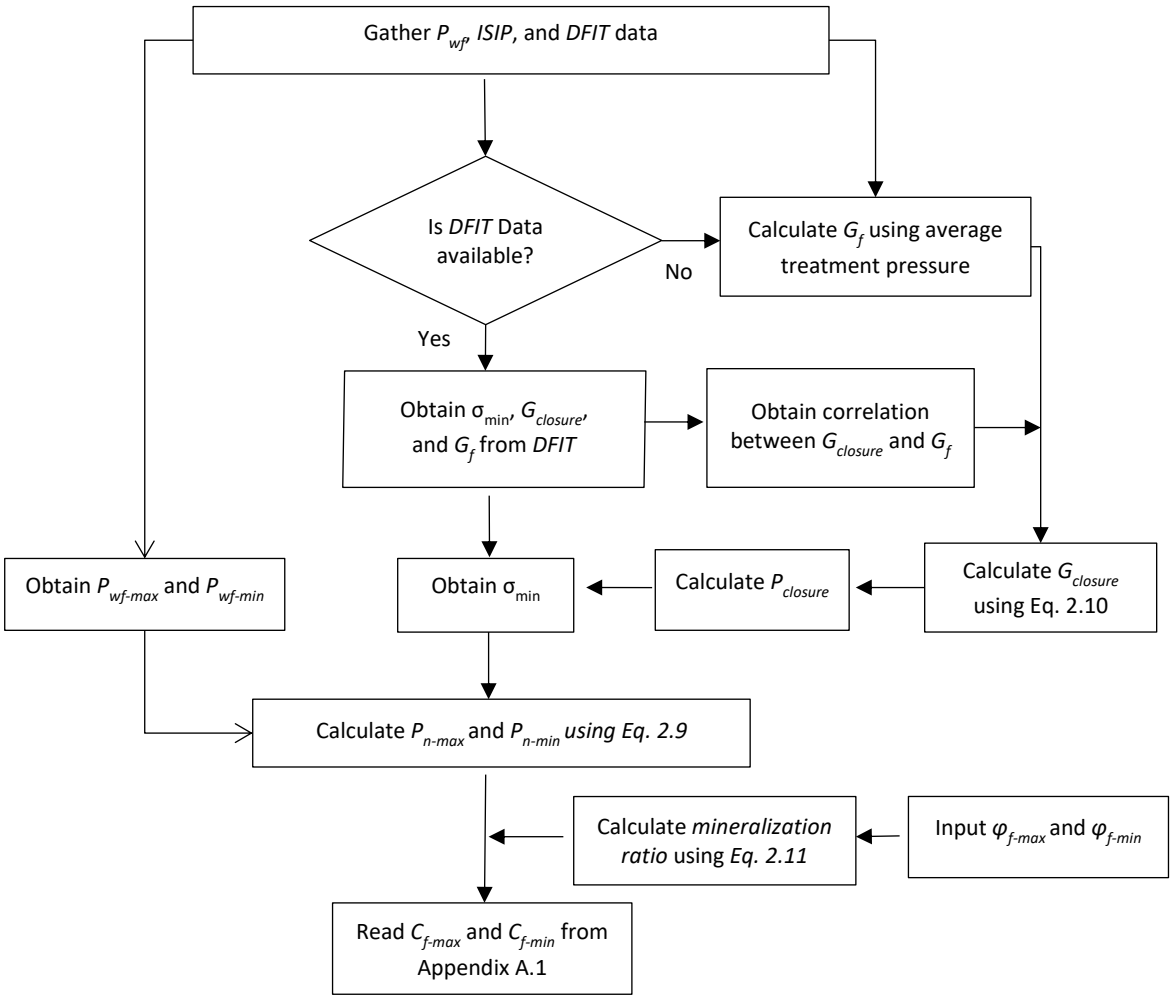

Fig. 2.4: Flow chart for estimating the maximum and minimum fracture compressibility with *DFIT* data

2.3 Flowback Rate and Pressure Behavior

This subsection first provides the basic information about reservoir, wells, and completion parameters. Also, this subsection qualitatively interprets the flowback rate and pressure data from the seven multi-fractured horizontal wells.

2.3.1 Well and Completion Information

The work studies seven single multi-fractured horizontal wells completed in Woodford Formation in Anadarko Basin (Fig. 2.5). Woodford is primarily a mudstone with a porosity range of 3-10 % and a permeability range of 10-100 nd.

Before hydraulic-fracturing treatment, a small-size fracturing is performed on the first stage at the toe to estimate the initial reservoir pressure (P_i). 50 to 200 barrels of water are pumped at the rate of 4 to 10 barrels/minute into 3 to 4 clusters in the first stage. The first stage in these wells shows breakdown during the pumping process. A gauge is then delivered to the first stage before the well is shut in. The gauge records the bottomhole pressure during shut-in for several days, until being pulled out for fracturing treatment of the remaining stages. P_i is obtained from a pressure build-up analysis done on the bottomhole pressure recorded by the gauge. After fracturing, the plugs used for isolating each stage are drilled out and the wells are shut in for 1-2 hours to set up the flowback equipment. Flowback for the seven wells is done through casing. The water/gas/oil rate and casing pressure are measured hourly during flowback.

Table 2.1 summarizes the completion information and reservoir properties including fluid type, *TVD*, the initial bottomhole pressure during flowback (P_{wfi}), initial reservoir pressure (P_i), and the bubblepoint pressure [P_b, which is obtained from the pressure/volume/temperature (PVT) analysis performed on the oil samples from these wells]. Wells A, B, D, and E are oil wells. P_i for these four oil wells varies from 4104 to 5815 psi. P_b for these four wells ranges from 3016 to 4133 psi. Wells C, F, and G are gas wells that have a larger *TVD* and P_i compared with the other four oil wells.

Table 2.1 lists the completion information including number of fracture stages, number of clusters, gross perforated interval (*GPI*), mass of proppant, and total injected water volume (*TIV*) for each well. Fig. 2.6 schematically illustrates fracture stages, perforation cluster, and *GPI*. Average stage spacing represents the average distance between stages, while the average cluster spacing represents the average distance between perforation clusters. *GPI* is defined as the distance between the first perforation cluster in the first stage and the last perforation cluster in

the last stage. As listed in Table 2.1, these wells have 9 to 12 fracture stages and 45 to 59 clusters. *GPI* varies from 1284 to 1490 m. *TIV* ranges from 13740 m^3 to 27620 m^3.

Table 2.1: Basic well and fracturing information

Well Name	Well Information					Fracturing Information				
	Fluid Type	*TVD*, m	P_{wfi}, psi	P_i, psi	P_b, psi	Number of Stages	Number of Clusters	*GPI*, m	Mass of Proppant, 10^6Kg	*TIV*, 10^3m^3
Well A	Oil	3113	5964	4147	4133	12	59	1350	1.62	27.62
Well B	Oil	2879	4983	4104	3016	9	45	1417	1.44	22.89
Well C	Gas	3734	8415	6438	-	9	45	1361	1.36	21.95
Well D	Oil	3928	8243	5815	3930	14	53	1490	1.12	16.60
Well E	Oil	3870	7865	5670	3857	16	51	1489	1.19	18.05
Well F	Gas	4497	9242	7859	-	12	47	1377	1.36	13.74
Well G	Gas	4542	9962	7772	-	11	55	1284	1.30	26.93

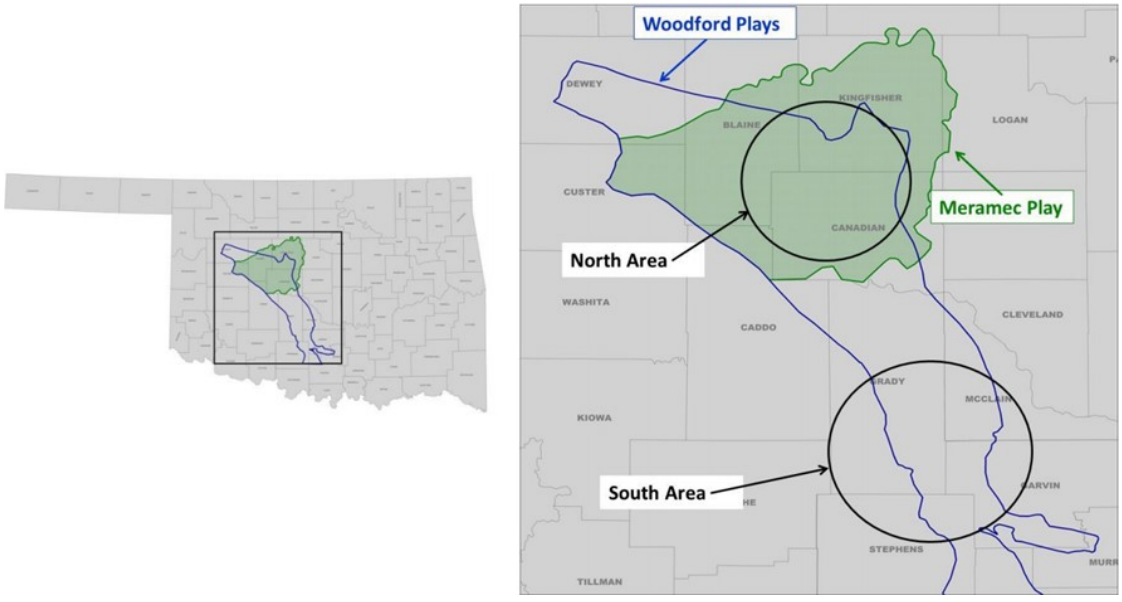

Fig. 2.5: Location of the Woodford Formation (from Jones et al., 2014).

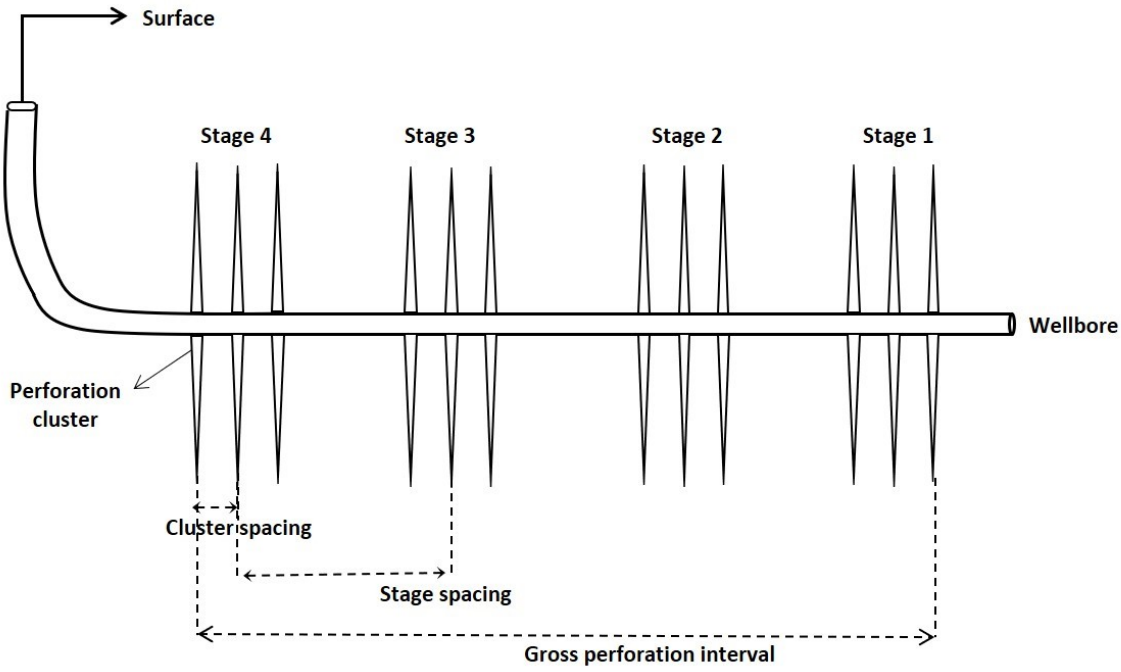

Fig. 2.6: Schematic of a multi-fractured horizontal well shows 4 stages with 12 perforation clusters. Gross perforation interval is defined as the distance between the first perforation cluster in the first stage and the last perforation cluster in the last stage.

2.3.2 Field Observations

Fig. 2.7 shows diagnostic plots of hourly-recorded flowback rate and pressure flowback data from Wells A and G which produce oil and gas, respectively. Appendix A.2 shows similar plots for Wells B, C, D, E, and F. These diagnostic plots show three distinct periods:

(1) Period 1 shows single-phase water production with declining pressure. It occurs at the early times and lasts approximately 3 to 7 days. In Period 1, both the casing pressure (P_{casing}) and the calculated bottomhole pressure (P_{wf}) are initially high and quickly drop with time. The water rate plots during Period 1 also show a peak which is followed by a decline behavior. Abbasi et al. (2012, 2014) also reported similar single-phase period in flowback data from several tight gas and oil wells.

(2) Period 2 happens at the end of Period 1, and shows single-phase water flowback with flattening pressure. P_{casing} and calculated P_{wf} generally flatten out before oil or gas production at the surface. This period happens at the end of Period 1. The pressure flattens about 3 to 7 days of flowback and lasts for about 1 to 6 days. This period disappears before the production of oil/gas at the surface.

Wells A and B show a delay between the end of flattening pressure and the appearance of oil/gas at the surface. This delay for these two wells is caused by shutting down the wells, for running gas lift. As shown in Table 2.4, the initial P_i for the two wells is relatively low. Gas lift is performed on Wells A and B shortly after Period 2.

(3) Period 3 shows multiphase flowback, occurring after the single-phase period. This period shows a short-term two-phase flow of water and gas production and a long-term three-phase of oil, gas, and water production. The two-phase flow lasts approximately 1 to 5 days. During Period 3, water is produced at a relatively low rate, and the casing pressure keeps dropping.

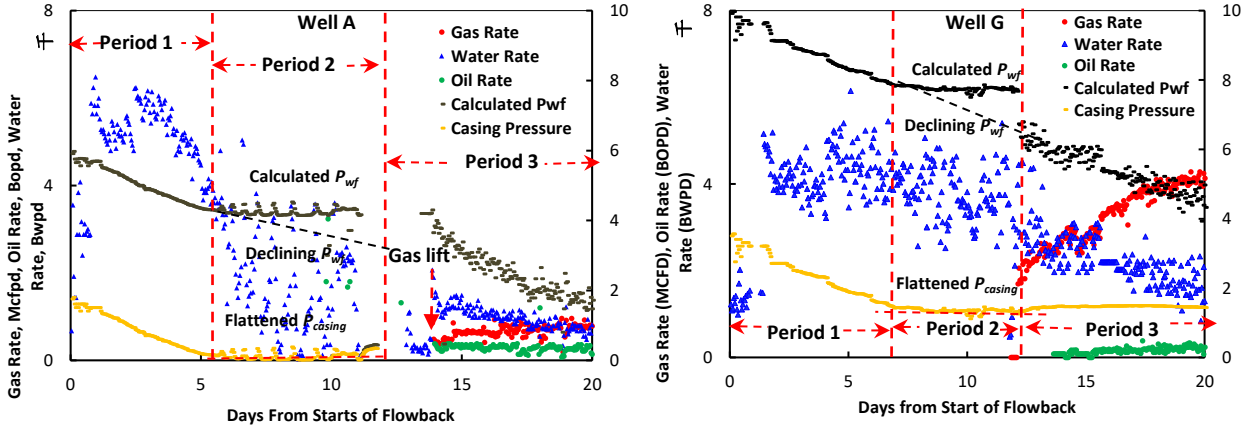

(a) (b)

Fig. 2.7: Hourly flowback data show three periods. Period 1 shows single-phase water production and declining pressure. Period 2 shows single-phase water production and flattening pressure. Period 3 shows multiphase production. (a) Well A is a tight oil well; (b) Well G is a tight gas well.

2.3.3 Comparative Analysis of Flowback Data

This section interprets the flattening of bottomhole and casing pressure during early flowback. Also, it investigates how initial reservoir pressure and hydrocarbon type affect the durations of Periods 1 and 2.

2.3.3.1 Flattening of Bottomhole and Casing Pressure

Fig. 2.7 shows a flattening in the recorded P_{casing} and calculated P_{wf} in Period 2. Jones et al. (2014) explains this phenomenon by the traces of oil/gas entering the wellbore and lightening the fluid column. However, this explanation appears inapplicable to the well data in Fig. 2.7, because no production of oil or gas is observed in Period 2. One possible reason is that the volume of produced oil or gas is insignificant compared with the large water volume during this period, which makes it challenging to record hydrocarbon production. Field experience indicates that the measurable oil rate begins at 1 to 2 bbl/hr, and the measurable gas rate begins at 200 to 2000 Mcf/D.

P_{casing} is measured at the surface and P_{wf} is calculated from wellhead data using Fanning single-phase correlation. Flowback water salinity is used to estimate water density. Pipe friction is calculated by using Fanning friction for single-phase water flow (IHS 2014). However, P_{wf} may be overestimated if the volume of oil or gas in wellbore is neglected for calculating it with casing pressure.

Jones et al. (2014) proposed that the flattening value of calculated P_{wf} could be approximated as reservoir pressure if the pressure drop along the fracture is assumed to be negligible. This approximation was validated by comparing the flattening P_{wf} with P_i estimated by DFITs data analysis. However, P_{wf} is calculated from casing pressure data by assuming single-phase water in wellbore. Flattening P_{wf} is due to flattening casing pressure, because the oil/gas volume in wellbore is not considered for calculating P_{wf} in Period 2. One may expect it does not show this falttening pressure at downhole condition. However, the flowback behaviors of bottomhole pressure needs further validation once measured P_{wf} are availanle.

This study further investigates the flattening pressure by constructing diagnostic plots of early flowback data. Fig. 2.8 shows the log-log plot of *RNP* versus t_{MB} and semi-log plot of the calculated P_{wf} versus t_{MB} for Wells A and G (see Appendix A.3 for the corresponding plots of the remaining five wells). Here, the semi-log plots of P_{wf} versus t_{MB} are compared with the log-log plots of *RNP* versus t_{MB}.

As shown in Fig. 2.8, the unit slope (fracture depletion) occurs during Period 1, and deviates as P_{wf} flattens out in Period 2. During Period 1, the pressure in fractures is expected to be higher than P_i. The fracture system during Period 1 can thus be treated as a closed-tank. The deviation from unit slope indicates the fluid influx from matrix into fracture network. Therefore, the flattened pressure in Period 2 can be interpreted as fracture-matrix flow communication. This study applies the tank model described in Section 2.2 to estimate V_{ef} using the flowback data during Period 1.

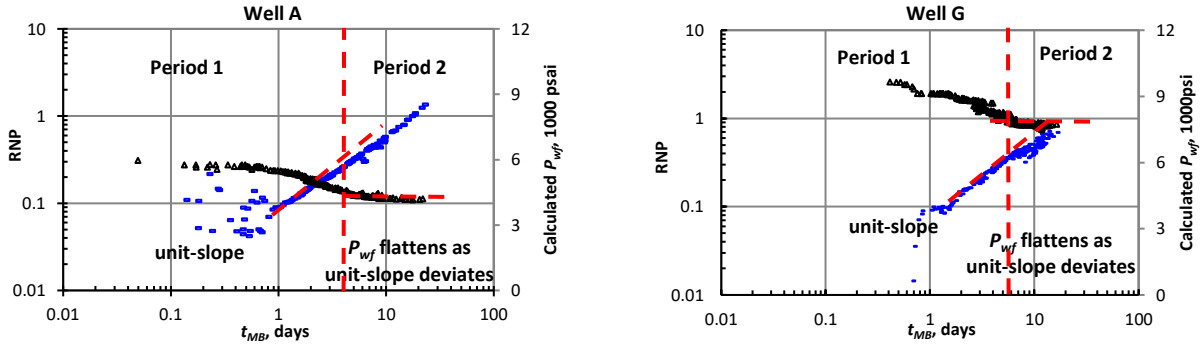

(a) (b)

Fig. 2.8: Log-log plot of *RNP* versus t_{MB} shows a clear unit slope before the calculated bottomhole pressure flattens out (*RNP* is in the unit of psi/stb/day). (a) Well A is a tight oil well; (b) Well G is a tight gas well.

2.3.3.2 The Duration of Period 1 and Period 2

The duration of Periods 1 and 2 is related to the water rate, which is influenced by choke size. A larger choke size leads to a higher flow rate, and leads further to shorter Periods 1 and 2. Therefore, the duration of Periods 1 and 2 is normalized with choke size to eliminate the effect of variable choke size during early flowback. The normalized time for Periods 1 and 2 is defined as the product of average choke size and the flowback duration for Periods 1 and 2, respectively.

Fig. 2.9 shows the effect of P_i on the normalized time of Periods 1 and 2. Fig. 2.9a shows a negative correlation between the normalized time for Period 1 and P_i. The negative correlation in Fig. 2.9 can be explained by the fact that wells with higher P_i show an earlier breakthrough. Fig. 2.9b shows a negative correlation between the normalized time of Period 2 versus P_i. The normalized time of Period 2 indicates the time of hydrocarbon transporting through fractures and wellbore to the surface. The negative correlation in Fig. 2.9b suggests that hydrocarbon front moves faster through fracture networks and wellbore for wells with higher P_i. This can be explained by Darcy's law: The flow rate of oil increases with the drawdown, which increases with P_i.

Also, from Fig. 2.9, gas wells generally show shorter Periods 1 and 2 compared with oil wells. Wells C and F are gas wells, and they have 5 days of Periods 1 and 2 in total, whereas the duration of the two periods for oil wells is more than 8 days. This can be explained by higher mobility of gas compared with oil when flowing through matrix pores, fractures, and wellbore.

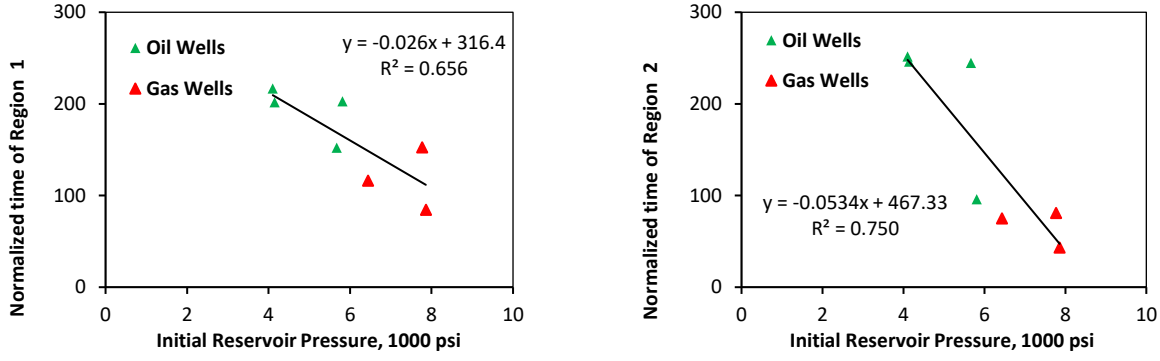

(a) (b)

Fig. 2.9: (a) Crossplot of normalized time of Period 1 versus P_i; (b) crossplot of normalized time of Period 2 versus P_i. The red and green points represent gas and oil wells, respectively.

2.4 Application and Discussions

This section is organized into the following five parts: (1) Estimating the fracture compressibility for each well; (2) comparing drive mechanisms before breakthrough of oil or gas; (3) estimating V_{ef} and comparing it with *TIV* and load recovery volume (*LRV*); (4) comparing the

propped and unpropped-fracture volume; and (5) investigating the correlations between the estimated V_{ef}, LRV, and completion-design parameters.

2.4.1 Fracture Compressibility

Here, fracture compressibility is estimated using the procedure proposed in Section 2.2.3. This subsection also evaluates the uncertainties in C_f caused by the assumption of negligible difference between P_f and P_{wf}.

Fig. 2.10 shows the correlation between closure pressure gradient and average fracture gradient as described by Eq. 2.10. There is no *DFIT* data available for the seven wells studied in this study. The correlation shown in Fig. 2.10 is obtained from the *DFIT* data of three offset wells. The closure pressure for the seven target wells are estimated using this correlation. Because this empirical correlation is based on limited data, it should be used with caution in other plays.

Fig. 2.11 compares the fracture gradient of each stage for the seven wells. Fig. 2.11 shows that the fracture gradient does not vary much with the sequence of stages except for Wells D and E. These two wells have abnormal high fracture gradient in the early stages caused by screenouts (a phenomenon that prevents proppant transport to deeper areas beyond the wellbore). The effect of screenouts indicates an incomplete fracturing treatment. Therefore, the fracture gradient data for the early two stages are neglected when estimating the average fracture gradient for Wells D and E.

Well D is used as an example to show how closure pressure is estimated using the correlation in Fig. 2.10. The average fracture gradient for Well D is 0.731 *psi/ft*. The closure pressure gradient is then calculated to be 0.5848 *psi/ft* using the correlation $y=0.8x$. The value of *TVD* for Well D is 12886 *ft*. The closure pressure for Well D is estimated to be 7536 *psi* after multiplying closure pressure gradient by *TVD*.

Table 2.2 lists the estimated range of fracture compressibility for the seven wells using the method described in Appendix A.1. The results of C_f are within the ranges reported in the

literature (Ezulike et al. 2016; Jones 1975; Aguilera 1999; Williams-Kovacs and Clarkson 2013).

As shown in Table 2.2, $C_{f\text{-}min}$ and $C_{f\text{-}max}$ are different for each well. Fracture compressibility for each well depends on P_n and φ_f (Jones 1975; Aguilera 1999). In this study, the same value of fracture porosity is used for each well. The difference in fracture compressibility between wells is caused by the difference in P_n. As shown in Eq. 2.8, P_n is a function of σ_{min} and P_{wf}, which are different for each well.

The estimated fracture compressibility varies from 10^{-5} psi^{-1} to 10^{-4} psi^{-1}, and is larger than the matrix compressibility (10^{-6} psi^{-1}). Tiab et al. (2001) reported that fracture compressibility is 10- to 100- fold higher than matrix compressibility. This can be explained by the difference in porosity of fracture and matrix.

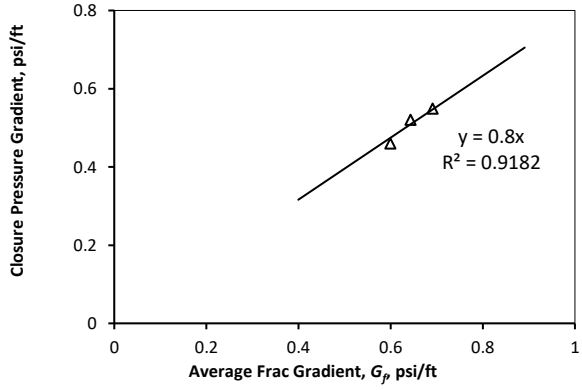

Fig. 2.10: Closure pressure gradient versus average fracture gradient obtained from *DFIT* data analysis

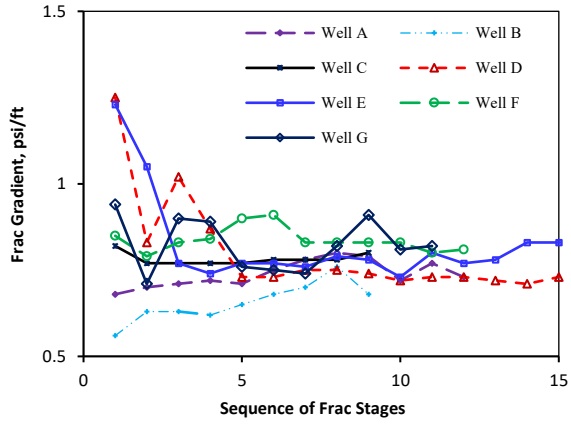

Fig. 2.11: Fracture gradient of each fracture stage for each well

Table 2.2: Computed fracture compressibility for each well. $C_{f\text{-}min}$ and $C_{f\text{-}max}$ correspond to ($P_{n\text{-}max}$, $1\text{-}\varphi_{f\text{-}max}$) and ($P_{n\text{-}min}$, $1\text{-}\varphi_{f\text{-}min}$), respectively. $\varphi_{f\text{-}min}$ and $\varphi_{f\text{-}max}$ are 47.5 and 100% for all wells.

Well Name	Average Fracture gradient, G_f, psi/ft	Minimum Principal In-situ Stress, σ_{min}, psi	Net Stress on Fractures, P_n, psi		Fracture Compressibility, C_f, 10^{-4} psi^{-1}	
			$P_{n\text{-}min}$	$P_{n\text{-}max}$	$C_{f\text{-}min}$	$C_{f\text{-}max}$
Well A	0.738	5291	371	935	1.21	5.95
Well B	0.657	4702	278	751	1.47	7.46
Well C	0.782	7490	554	1052	1.09	4.37
Well D	0.731	7536	551	1697	0.70	4.38
Well E	0.787	7995	379	2116	0.58	5.85
Well F	0.838	9886	761	1858	0.65	3.44
Well G	0.820	9602	1350	1782	0.67	2.28

Fig. 2.12 plots the relative error in $C_{f\text{-max}}$ versus fracture conductivity for Well E. The average fracture half-length for this well is assumed to vary from 160 to 650 ft. The values of fracture conductivity during flowback period are obtained from the literatures (Xu et al. 2017, Ezulike 2017, and Williams-Kovas 2017). The relative error in $C_{f\text{-}max}$ is estimated by the following steps: First, the pressure difference in fractures is calculated by Darcy's Law, where q_w is around 4000 *stbd,* and fracture height is about 260 *ft*; Second, the relative error in $C_{f\text{-}max}$ is calculated by comparing the estimated $C_{f\text{-}max}$ with and without considering spatial pressure difference in fractures.

In Fig. 2.12, the results show that the relative error in $C_{f\text{-}max}$ is generally less than 1% when fracture conductivity is larger than 256 *md·ft*. One may conclude that the assumption of

negligible pressure difference in fractures is reasonable for calculating fracture compressibility during Period 1.

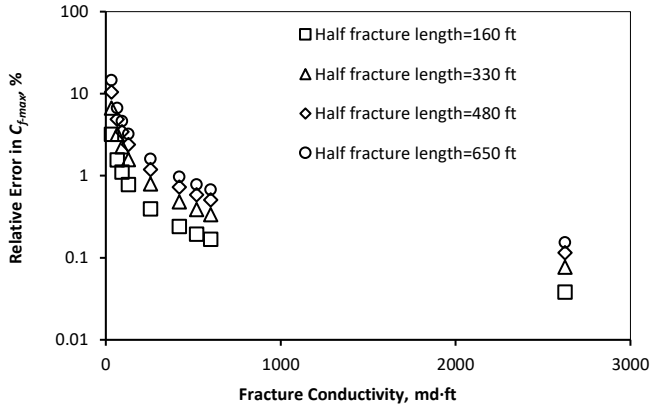

Fig. 2.12: Plot of relative error in $C_{f\text{-}max}$ versus fracture conductivity for Well E. The average fracture half-length of this well is assumed to vary from 160 to 650 *ft*.

2.4.2 Drive Mechanisms before Hydrocarbon Breakthrough

As mentioned in Section 2.3.2, Period 1 describes the period of flowback before hydrocarbon breakthrough, when the fractures are filled with single-phase water. Therefore, hydrocarbon breakthrough, hydrocarbon expansion, and water vaporization by flowing gas (Zhang and Ehlig-Economides, 2014) are not considered as drive mechanisms in this period. Here, the possible drive mechanisms for Period 1 include wellbore storage, water expansion, and fracture closure.

Fig. 2.13 shows the flowback pressure and rate related to Period 1 for Well G. Period 1 generally shows two stages: Stage 1 describes the early flowback when P_{wf} is higher than $P_{closure}$. As shown in Fig. 2.13, it occurs at the first few hours of flowback. In this stage, the calculated P_{wf} is generally high and noisy, and the water rate is relatively low. P_{wf} during this stage is higher than $P_{closure}$, indicating that fracture closure has not come into effect. This stage happens at the first few hours of flowback, and is influenced by the wellbore storage. It is expected that wellbore storage contributes to the early water production. Well G recovered about 130 m^3 of water during this stage, which is larger than its wellbore volume (approximately 65 m^3). A larger volume of recovered water compared with the wellbore volume suggests that the wellbore storage comes to an end in this stage.

Stage 2 describes the period after Stage 1 when P_{wf} drops below $P_{closure}$. As shown in Fig. 2.13, it lasts for approximately 6 days, and the bottomhole pressure drops quickly, whereas the water rate is relatively high. Also, the log-log plot of *RNP* and t_{MB} for Well G shows that fracture depletion (unit slope) starts from Day 2 and ends at Day 5 of flowback. The possible drive mechanisms during this stage include fracture closure and water expansion. *CDI* and *WDI* proposed by Ezulike et al. (2016) are used to quantify the drive mechanisms of fracture closure and water expansion. As shown in Table 2.3, the results indicate that *CDI* accounts for more than 90% of the early water production before hydrocarbon breakthrough. Therefore, the effect of fracture closure dominates Stage 2.

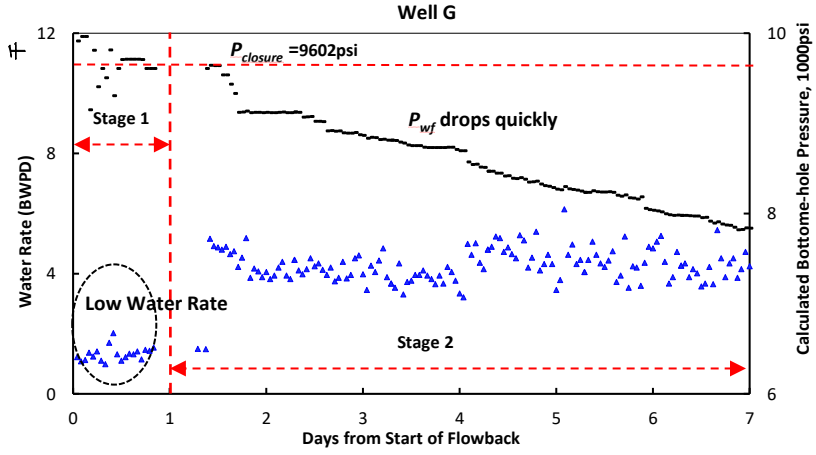

Fig. 2.13: The early flowback pressure and rate data in Period 1 for Well G generally show two stages: (1) Stage 1 shows high pressure and relatively low water rate; (2) Stage 2 shows quickly dropping pressure and relatively high water rate. The P_{wfi} for Well G is 9962 psi, which is higher than its $P_{closure}$ (9602 psi).

Table 2.3: Comparison of different drive mechanisms in Stage 2

Well Name	Water Drive Index (*WDI*, %)		Compaction Drive Index (*CDI*, %)	
	Minimum	Maximum	Minimum	Maximum
Well A	0.48	2.32	97.68	99.52
Well B	0.38	1.92	98.08	99.62
Well C	0.65	2.57	97.43	99.35
Well D	0.65	0.41	99.59	99.35
Well E	0.49	4.73	95.27	99.51
Well F	0.83	4.24	95.76	99.17
Well G	0.48	2.32	97.68	99.52

2.4.3 Effective Fracture Pore-Volume

On the basis of Eq. 2.6, C_f, B_w, C_w, and m are required for calculating V_{ef}. Table 2.4 lists the estimated values of C_f for the seven wells. It also lists the input values of B_w, C_w, and m. B_w and C_w under reservoir conditions are estimated using empirical methods proposed by McCain (1991). m is obtained through linear regression for RNP versus t_{MB} data, as described in Appendix A.4.

Table 2.4: Inputs for calculating V_{ef} using Eq. 2.6

Well name	*Water formation factors* (B_w)	Water compressibility (C_w, 10^{-6} psi^{-1})	Slope of RNP versus t_{MB} in the cartesian plot (m, psi/stb)
Well A	1.02	2.84	0.0579
Well B	1.02	2.92	0.0784
Well C	1.02	2.88	0.0752
Well D	1.02	2.73	0.1254
Well E	1.02	2.90	0.2031
Well F	1.02	2.88	0.1005
Well G	1.02	2.88	0.0760

Fluid efficiency (FE) is defined as the ratio of water volume stored in fractures to injected water volume (Economides and Nolte, 2000). If fracture system is assumed to be filled with water during fracture depletion, then V_{ef} can be taken as the water volume stored in fractures. Because V_{ef} is estimated using flowback data during Period 1 (see Section 2.3.3.1), FE from flowback analysis describes the fluid efficiency at the early flowback.

Table 2.5 lists the calculated values of the maximum and minimum effective fracture pore-volume ($V_{ef\text{-}max}$ and $V_{ef\text{-}min}$) for the seven wells, TIV, maximum and minimum fluid efficiency (FE_{max} and FE_{min}), and LRV. FE_{max} is defined as the ratio of $V_{ef\text{-}max}$ to TIV, and FE_{min} is defined as the ratio of $V_{ef\text{-}min}$ to TIV. V_{ef} is generally less than TIV, and the $V_{ef\text{-}max}$ is larger than LRV. A more detailed analysis of V_{ef}, TIV, and LRV is presented in Section 2.4.5.

$V_{ef\text{-}max}$ and $V_{ef\text{-}min}$ correspond to the $C_{f\text{-}min}$ and $C_{f\text{-}max}$, respectively. Fig. 2.14 shows that the estimated V_{ef} is very sensitive to C_f. V_{ef} decreases by more than 50% as C_f changes from $C_{f\text{-}min}$ to

$C_{f\text{-}max}$. As mentioned in Section 2. 2.3, estimating C_f using Appendix A.1 requires P_n and φ_f. P_n for each well is calculated using Eq. 2.10. However, φ_f is an uncertain value assumed to range from 47.5% to 100% for each well. Therefore, the uncertainty of estimating V_{ef} is mainly from the uncertainty in fracture porosity.

Table 2.5: Summary of estimated values for effective fracture pore-volume and fracturing parameters

Well Name	Effective Fracture Pore-Volume (V_{ef}, 1000 m^3)		Total Injected Volume (TIV, 1000 m^3)	Fluid Efficiency (FE,100%)		Load Recovery Volume (LRV, 1000 m^3, 3 years)	Load Recovery Ratio (3 years)
	$V_{ef\text{-}min}$	$V_{ef\text{-}max}$		FE_{min}	FE_{max}		
Well A	4.64	22.85	27.62	16.8	82.7	12.86	0.47
Well B	2.73	13.94	22.89	11.9	60.9	5.74	0.25
Well C	4.86	19.49	21.95	22.1	88.8	9.66	0.44
Well D	2.29	13.87	16.60	13.8	83.6	10.53	0.75
Well E	2.19	13.08	18.05	12.1	72.5	11.91	0.72
Well F	5.24	23.71	13.74	38.1	172.6	17.75	1.29
Well G	9.13	30.26	26.93	33.9	112.4	24.64	0.92

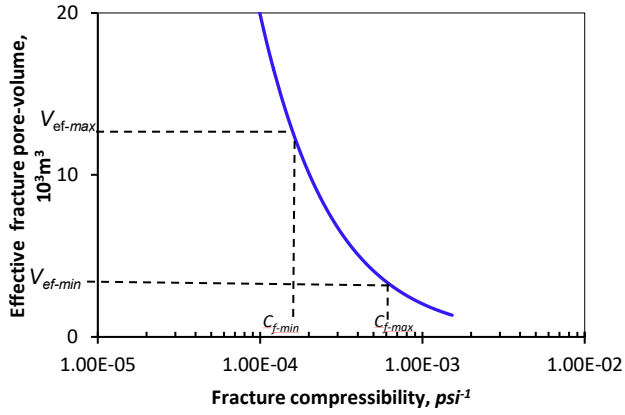

Fig. 2.14: Log-log plot of V_{ef} versus C_f using Eq. 2.6 shows that V_{ef} is sensitive to C_f

FE can be defined slightly different by use of *DFIT* data: the ratio of water volume stored in fractures at shut-in to *TIV*. This *FE* from *DFIT* describes the fluid efficiency during shut-in, and *FE* from flowback analysis describes the fluid efficiency during early-flowback period. The water in fractures may still leak into the matrix and natural fractures after shut-in. However, the seven wells studied in this chapter started their flowback up to 1 day after shut-in. Furthermore, *DFIT* analysis from one offset well shows an *FE* of approximately 87%. The high value of *FE*

reported from *DFIT* analysis implies low leakoff (Wallace et al. 2014). Therefore, *FE* from flowback analysis may approximate the value of *FE* from *DFIT*.

The values of $FE_{\max}$ in Table 2.5 for wells F and G are even higher than 100%. This may be a result of overestimating their $V_{ef\text{-}max}$ due to the relatively high uncertainty in fracture compressibility. The value of *FE* from DFIT analysis is close to the values of FE_{max} calculated from flowback analysis for the remaining five wells, suggesting that the estimated $V_{ef\text{-}max}$ is more representative than $V_{ef\text{-}min}$ for the fracture network. *FE* from DFIT is recommended for these wells with overestimated FE_{max}. However, $V_{ef\text{-}max}$ is used as effective fracture pore-volume in this chapter for the sake of consistency.

2.4.4 Propped and Unpropped Fracture Volume

Fig. 2.15 compares the volume of proppant, propped-fracture volume, unpropped-fracture volume, and $V_{ef\text{-}max}$ for each well. The volume of proppant is estimated by dividing the proppant mass by its density. The propped-fracture volume represents the effective fracture pore-volume with proppants, and the unpropped-fracture volume represents the effective fracture pore-volume without proppants. The propped-fracture volume is estimated by dividing the volume of proppant by the mineralization ratio. This study assumes negligible proppant crushing, embedment, and flowback for estimating propped-fracture volume. The mineralization ratio is approximately 52.5% when assuming cubic packings of proppant in fractures. The unpropped fracture volume is estimated by deducting the popped-fracture volume from $V_{ef\text{-}max}$.

For example, the type of proppant used for Well C is Santrol SDC, and the size of the proppant is 40/70 mesh. This type of proppant has a density of 2.57 g/cm^3. Well C pumps approximately 1360 tonnes of proppant. The calculated volume of proppant for Well C is about 529 m^3, and the propped-fracture volume is about 1008 m^3, and the unpropped-fracture volume is estimated at 18482 m^3.

Fig. 2.15 shows that the propped-fracture volume is relatively small compared with $V_{ef\text{-}max}$. The percentage of propped-fracture volume in $V_{ef\text{-}max}$ may be even smaller, because the proppants

may shrink, crush, and embed into the fracture walls under high-stress conditions (Warpinski 2010; Raysoni and Weaver 2013). This result suggests that most of the fracture volume is unpropped. McKenna (2014) modelled the proppant distribution using discrete-fracture-network (*DFN*) approach. Their results also indicate that the propped fracture volume accounts for a small portion of the total fracture volume. It is expected that the size of the proppant can not reach into the unpropped fractures.

Fig. 2.15 also compares the unpropped-fracture volume with *TIV*. It shows that the unpropped fracture volume accounts for more than 60% of the *TIV*. As mentioned in Section 2.3.3, V_{ef} is estimated using the flowback data in Period 1 when the fractures are filled with water. The unpropped-fracture volume can be approximated as the volume of fracturing water in unpropped fractures. The results indicate that the unpropped fractures host most of the fracturing water. Sharma and Manchanda (2015) also suggested that 90% of fracturing water is in unpropped fractures, by a simple calculation on the basis of the volumetric balance of the fracturing water.

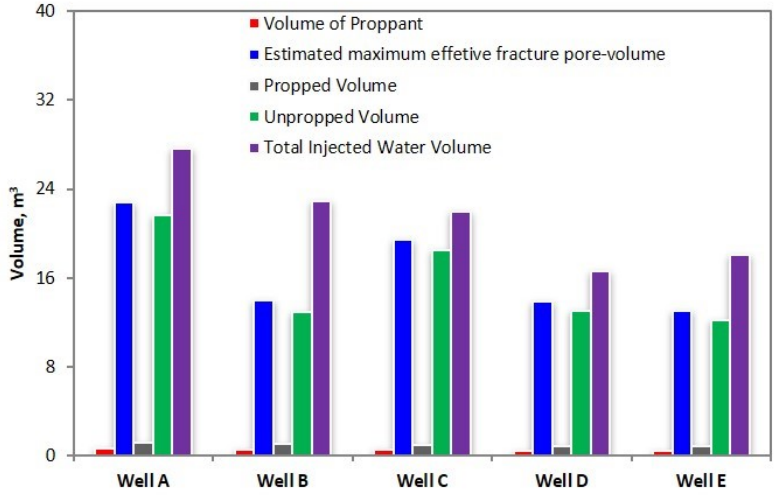

Fig. 2.15: Comparing the volume of proppant, $V_{ef\text{-}max}$, propped-fracture volume, unpropped-fracture volume, and *TIV* shows that the unpropped-fracture volume accounts for a large percentage of $V_{ef\text{-}max}$ and *TIV* (Wells F and G are not used for this comparison).

2.4.5 Correlation Analysis

This subsection investigates the correlations between $V_{ef\text{-}max}$ and *LRV*, and also the completion-design parameters including *TIV*, number of clusters, and *GPI*.

2.4.5.1 Load Recovery Volume and Effective Fracture Pore-Volume

As shown in Fig. 2.16 and Table 2.5, the estimated $V_{ef\text{-}max}$ for most wells is larger than *LRV* measured after three years. The load recovery ratio for Well F is more than unity, and this suggests that some water is produced from the formation, or fracturing water from offset wells due to communication. In general, *LRV* after 3 years can be considered as final *LRV*, because the water production rate is relatively low after three years.

V_{ef} decrease as fracture depletion progresses (see Flow Regime 2 in Fig. 2.1). $V_{ef\text{-}max}$ is assumed to be the upper limit of V_{ef} at the start of fracture depletion. As mentioned in Section 2.3.3, V_{ef} is taken as the water volume in the fractures when they are filled with water during fracture depletion. Therefore, $V_{ef\text{-}max}$ could be approximated as the initial water volume in the fractures.

Lower values of final *LRV* compared with $V_{ef\text{-}max}$ indicate that final *LRV* is still less than the initial water volume in fractures. This further indicates that there is still some non-recovered fracturing water left in fractures, even a long time after the starting production. Experimental studies of Parmar et al. (2014) suggest that a large volume of water can be trapped at the bottom of vertical fractures because of gravity effect. This phenomenon is also confirmed by the simulation studies of Sharma and Agrawal (2013). Furthermore, Sharma and Manchanda (2015) showed that the fracturing water can also be trapped in the unpropped fractures. As discussed in Section 2.4.4, most of the fracture volume is unpropped, which may host the non-recovered fracturing water.

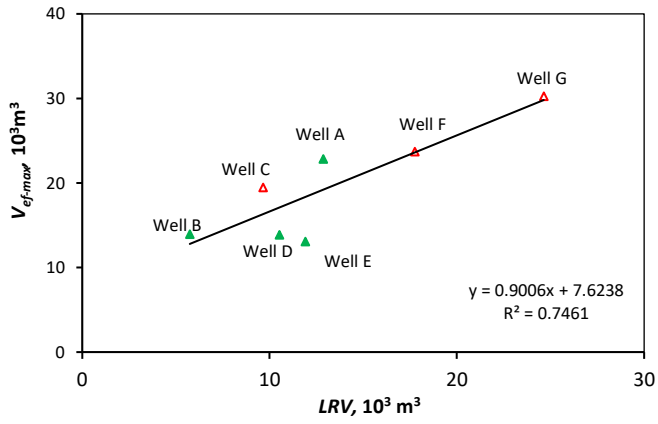

Fig. 2.16: Crossplot of $V_{ef\text{-}max}$ versus *LRV*. The red and green points represent gas and oil wells, respectively.

2.4.5.2 Effective Fracture Pore-Volume and Completion-design Parameters

Pearson correlation coefficient (r) is used to evaluate the possible correlations between $V_{ef\text{-}max}$ and completion design parameters and to explore the key factors controlling the fracture pore-volume. The Pearson correlation coefficients are obtained using Eq. 2.14 and the values of $V_{ef\text{-}max}$ and completion-design parameters.

Table 2.6: Pearson correlation coefficient between $V_{ef\text{-}max}$ and completion design parameters

Completion Design Parameters	Number of Stages	Number of Clusters	Stage Length	Gross Perforated Interval	Total Water Injected Volume	Proppant Mass	Average Treatment Rate
Pearson Correlation Coefficient (r) with $V_{ef\text{-}max}$	-0.395	0.557	0.007	-0.857	0.828	0.405	-0.204

Table 2.6 shows positive values of r between $V_{ef\text{-}max}$ and the number of clusters, stage length, *TIV*, and proppant mass, which suggests that these fracturing parameters have a positive effect on $V_{ef\text{-}max}$. It also shows negative values of r between $V_{ef\text{-}max}$ and number of stages, *GPI*, and average treatment rate, which suggests that these fracturing parameters have a negative effect on $V_{ef\text{-}max}$. Zhou et al. (2016) showed the similar effect of number of stages, proppant mass, and average treatment rate on the load recovery ratio within early three weeks. It is expected that the load recovery ratio within early three weeks is related to the $V_{ef\text{-}max}$.

In Table 2.6, the results show that *GPI, TIV*, and number of clusters have the highest coefficient values. This may suggest that *TIV*, *GPI* and the number of clusters are among the key design parameters for creating a larger effective fracture pore-volume. *GPI* and the number of clusters may be combined into one term: average cluster spacing, which is defined as *GPI* divided by the number of clusters. Detailed discussion on *TIV*, average cluster spacing are presented below.

(i) Total Injected Water Volume

As shown in Fig. 2.17 and Table 2.5, $V_{ef\text{-}max}$ for most wells is about 60% - 89% of *TIV*. Since $V_{ef\text{-}max}$ is the upper limit of V_{ef}, one may conclude that V_{ef} for most wells should be less than 60% - 89% of *TIV*. This means that more than 11% - 40% of the pumped water may be lost in matrix or ineffective fractures. However, $V_{ef\text{-}max}$ for the two gas wells (Wells F and G) is even larger than *TIV*. This suggests the possibility of estimating $V_{ef\text{-}max}$ as a result of underestimating the total compressibility.

Fig. 2.17 shows a positive correlation between $V_{ef\text{-}max}$ and *TIV*. This observation indicates that in general $V_{ef\text{-}max}$ increases with increasing *TIV*. For wells with larger *TIV*, fracturing water with more energy is pumped to crack the formation. Therefore, larger *TIV* generally contributes to a larger effective fracture pore-volume. However, there are some wells which have a relatively modest $V_{ef\text{-}max}$ even with a large *TIV* pumped. For example, well B has a larger *TIV* than Well C, but $V_{ef\text{-}max}$ for Well B is less than that for well C. One may expect that $V_{ef\text{-}max}$ for Well C is possibly overestimated. Well C is a gas well. As discussed above, $V_{ef\text{-}max}$ for a gas well is possibly overestimated due to underestimating the total compressibility.

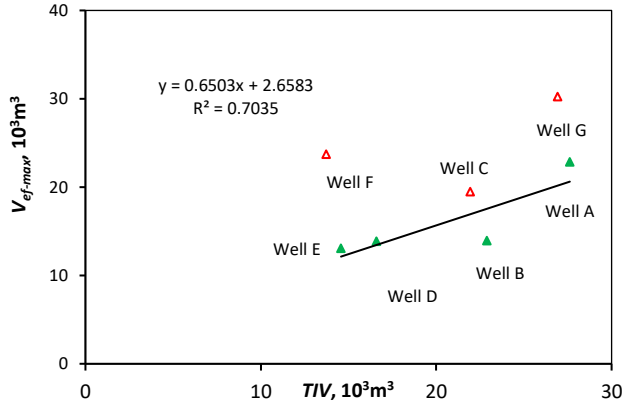

Fig. 2.17: Crossplot of $V_{ef\text{-}max}$ versus *TIV*. The red points represent gas wells, while the green points represent oil wells (Wells F and G are not used for calculating correlation).

(ii) Average Cluster Spacing

$V_{ef\text{-}max}$ is normalized by *TIV* ($V_{ef\text{-}max}$ /*TIV*) to eliminate the effect of *TIV on* $V_{ef\text{-}max}$. As discussed previously, $V_{ef\text{-}max}$ is possibly overestimated for the gas wells. Fig. 2.18 plots normalized $V_{ef\text{-}max}$ versus average cluster spacing only for the oil wells. The limited data in Fig. 2.18 shows that in general, the normalized $V_{ef\text{-}max}$ decreases by increasing average cluster spacing. In other words, closer cluster spacing generally leads to a larger effective fracture pore-volume. Ingram et al. (2014) stated that the cluster spacing has a significant effect on fracture initiation and propagation. A close cluster spacing may cause stress interference between clusters and influence the orientation of the fractures. However, a close cluster spacing also creates more inter-connected fractures, which enhances the connectivity and effectiveness of the fracture network.

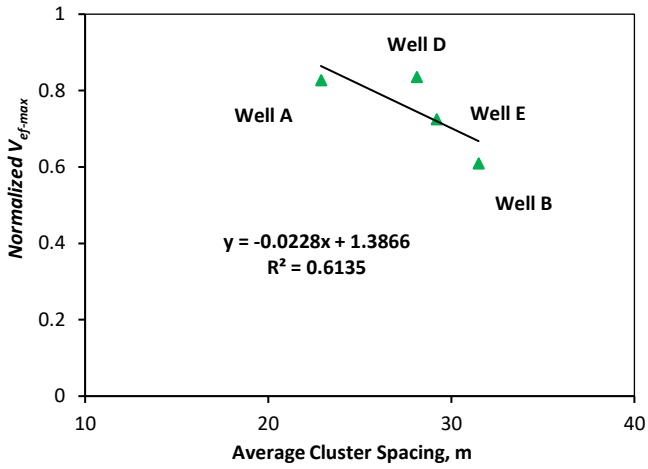

Fig. 2.18: Normalized $V_{ef\text{-}max}$ versus average cluster spacing for four oil wells shows a negative correlation.

2.5 Limitations and Recommendations

2.5.1 Estimating Effective Fracture Pore-volume

The estimated V_{ef} shows a relatively wide range from $V_{ef\text{-}min}$ to $V_{ef\text{-}max}$ corresponding to the choice of minimum and maximum fracture porosity, respectively. Therefore, the uncertainty in fracture porosity can be a major source of error. As discussed in Section 2.4.3, the results suggest that the fracture porosity of 47.5% is more representative than 100% for the target wells. However, the estimated $V_{ef\text{-}max}$ for two wells is even higher than their TIV. One may expect that the assumption of cubic packing underestimates fracture porosity for these wells. The product of TIV and fluid efficiency obtained from DFIT data analysis is recommended to estimate maximum V_{ef}.

The gross correlation in Eq. 2.10 can be the other source of error for estimating V_{ef}. As shown in Fig. 2.7, the gross correlation is obtained using limited *DFIT* data, and thus should be used with caution in other plays. The assumption of negligible difference between P_f and P_{wf} in Eq. 2.8 can be another source of error. Moreover, V_{ef} is estimated by interpreting the single-phase flowback data in Period 1, which represents the flowback period before hydrocarbon breakthrough from matrix into fractures. The calculated P_{wf} is expected to be accurate during Period 1. Thus, the errors in calculating P_{wf} may thus not affect the uniqueness of estimated V_{ef}.

2.5.2 Correlating Analysis

Correlating V_{ef} with completion-design parameters may be challenging because of limited number of wells. There might also be interdependency between the design parameters. Besides, formation parameters such as permeability may influence the process of leakoff, which may further affect the effective fracture pore-volume. Therefore, the correlations shown in this section may need further verification by use of data from more wells completed in this play.

2.6 Summary

Diagnostic plots are constructed to understand the rate and pressure behavior during early water flowback. A previous model is also applied on early-flowback data to estimate effective fracture pore-volume. A procedure is proposed to estimate fracture compressibility using diagnostic fracture injection test data. The correlation analysis of effective fracture pore-volume and various completion design parameters is the other contribution of this chapter. The conclusions can be summarized as follows:

(1) Diagnostic plots of flowback data show several days of single-phase water production. A phenomenon of flattening casing and bottomhole pressure is observed during single-phase flowback. Comparative analysis of the data indicates that the flattening pressure can be interpreted as this hydrocarbon breakthrough into the effective fracture system. The results suggest that the time of single-phase flowback depends on initial reservoir pressure and hydrocarbon type. Gas wells generally show shorter single-phase duration compared with the oil wells. Wells with higher initial reservoir pressure generally show longer single-phase flow period.

(2) The estimated effective fracture pore-volume is generally larger than final load recovery volume and less than total injected water volume. Comparative analysis of the unpropped fracture volume, estimated effective fracture pore-volume, load recovery volume, and total injected water volume indicates that most of the effective fractures are unpropped, and host the non-recovered fracturing water. The results also indicate that estimating effective fracture pore-volume requires reliable estimates of fracture compressibility.

(3) Total injected water volume and average cluster spacing are among the key completion design parameters for creating a larger effective fracture pore-volume. Increasing total injected water volume increases the effective fracture pore-volume. This is because pumping more water stimulates the formation with more energy. The limited data in this study shows that smaller average cluster spacing enhances the connectivity of the fracture network, and generally leads to a larger effective fracture pore-volume. However, the relationships between effective fracture pore-volume and completion design parameters presented in this study may need further validation in other plays where more wells with flowback data are available.

2.7 Nomenclature

Symbols

A	Drainage area, L^2, m^2, $[ft^2]$.
B	Formation volume factor.
C	Compressibility, Lt^2M^{-1}, atm^{-1}, $[Pa^{-1}, psi^{-1}]$.
G	Fracture gradient, $ML^{-2}t^{-2}$, $Pa.m^{-1}$, $[psi.ft^{-1}]$.
K	Permeability, L^2, m^2, $[D]$.
t	Time, t, s, $[hr, day]$.
P	Pressure of hydrocarbon phase, $ML^{-1}t^{-2}$, Pa, $[psi]$.
V	Volume, L^3, m^3, $[ft^3]$.
y	Fracture half length, L, m, $[ft]$.
μ	Viscosity, $ML^{-1}t^{-1}$, $Pa.s$, $[cP]$.
γ	Euler's constant.
φ	Porosity, dimensionless.

Subscripts

e	Equivalent or effective.
f	Fracture.
i	Initial.
max	Maximum.
min	Minimum.
t	Total.
w	Water.
wf	Bottomhole flowing.

Chapter 3 Fracturing Water Flowback Obeys a Simple Decline Model

3.1 Introduction

In recent years, unconventional tight resources have received great attention worldwide (Aguilera, 2014; Arora and Cai, 2014; Stamford and Azapagic, 2014; Weijermars, 2013). Hydraulic fracturing (HF) is now a common practice to recover oil and gas from unconventional tight resources in North America (Wang et al., 2017; Weijermars, 2014; Yuan, Luo, & Feng, 2015). During HF, millions of gallons of water (Clark et al., 2013; Gallegos et al., 2015; Jackson et al., 2015; Jiang et al., 2014; Kondash and Vengosh, 2015; Lutz et al., 2013; Middleton et al., 2015) are injected through a well into shale and tight formations to create fractures for hydrocarbon production. Together with the high-water demand, HF in unconventional reservoirs also associates with the increasing volume of produced water for disposal (Scanlon et al., 2014). The increasing water footprint of HF generates significant environmental concerns in recent years (Bowen et al., 2015; Gallegos et al., 2015; Kondash and Vengosh, 2015; Kondash et al., 2017; Reagan et al., 2015; Wilson et al., 2017).

The HF process is followed by a period of flowback (up to 3 months) to clean up the well before putting it on production. Studies have analyzed the chemical composition of flowback water (Haluszczak et al., 2013; Onishi et al., 2017; Vengosh et al., 2017; Zolfaghari et al., 2016; Henderson et al., 2012), and reported that the salinity of flowback water can reach over 280,000 ppm (Henderson et al., 2012; Onishi et al., 2017). The high salinity of flowback water is possibly due to interactions of injected water with shales under downhole conditions and mixing with in-situ brine (Birdsell et al., 2015; Kondash and Vengosh, 2015; Vengosh et al., 2014; Zolfaghari et al., 2016). In addition, flowback water may contain some chemical additives (such as friction reducers, scaling inhibitors, and acids) usually added to fracturing water (Birdsell et al., 2015). The produced water results in a significant burden of wastewater disposal (Kondash and Vengosh, 2015; Kondash et al., 2017). Projecting the water production after HF is thus of vital importance for water managements in developing unconventional tight reservoirs.

Studies have reported a large variation in water production for different unconventional reservoirs (Kondash and Vengosh, 2015). The water production volume after 1–2 years exceeds the total injected water volume (TIV) for the HF of wells completed in the Bakken, Eagle Ford (EF), Niobrara, Monterey-Temblor (Kondash and Vengosh, 2015), and Permian formations (Scanlon et al., 2014). In contrast, in Barnett, Haynesville, and Marcellus, the volume of produced water is typically low (10%–40%) even after several years of operation (Kondash and Vengosh, 2015; Nicot et al., 2014). Also, a significant variation in water production among wells is also reported in a shale play (Zhou et al., 2016). It remains uncertain about the factors controlling this large variation, making it challenging to accurately project water production. Flowback Model which can project water production thus becomes an essential for careful water management in unconventional reservoirs.

Numerical models have been employed to simulate the gas and water flow in tight and shale reservoirs (Cheng et al., 2015; Edwards et al., 2017; Ghanbari and Dehghanpour, 2016; Nicot et al., 2014). Ghanbari and Dehghanpour (2016) analyzed field flowback data of 18 Horn River (HR) wells, and showed that water imbibition into shale matrix plays an important role in flowback water production. Edwards et al. (2017) simulated the water and gas flow for 12 HR wells and showed that up to 17% of fracturing water could be ultimately recovered with the remainder imbibed into the shale formation, although long-term water rate data were not available to verify these simulation results.

Analytical models based on flow physics have been developed to describe water and gas/oil flow during the flowback process (Abbasi 2013; Alkouh et al. 2014; Abbasi et al. 2014; Ezulike et al. 2015, 2016, 2017; Xu et al. 2015, 2016, 2017). These models were applied on flowback data to characterize fractures and forecast long-term production in unconventional reservoirs. However, most of these models are limited to the conditions before hydrocarbon breakthrough from matrix into fractures during flowback. Flowback models (Clarkson & Williams-Kovacs, 2013; Ezulike and Dehghanpour, 2015; Xu et al., 2017) have been proposed to describe the flow of water and gas/oil after hydrocarbon breakthrough. However, the input parameters for these flowback models are generally unknown or hard to obtain.

Empirical decline models have been used to predict water production rate for unconventional wells by curve-fitting their historical production data (Bai et al. 2013, 2014, 2016; Kim et al. 2016; Kondash and Vengosh, 2015). Bai et al. (2013) and Bai and Carlson (2016) analyzed daily water rate data from multi-fractured horizontal wells in the Wattenberg field. Their results show a harmonic decline in water rate during the multiphase production period. However, the physical mechanism responsible for the observed harmonic decline in water production rate is poorly understood.

In this chapter, we hypothesize that (1) water-rate decline (WRD) after hydrocarbon breakthrough is primarily controlled by relative-permeability effects, and (2) WRD analysis can be used to predict post-flowback water recovery. To test these hypotheses, we (1) analyze water-rate data measured during flowback and post-flowback, and (2) apply rate-decline analysis to estimate water recovery for shale and tight gas wells completed in the EF, HR, Woodford (WF), and Montney (MT) formations.

3.2 Methodology

This study is conducted in the following 4 key steps:

(1) Analyzing rate and pressure data measured during flowback and post-flowback of 172 wells completed in the HR (Case-1), WF (Case-2), MT (Case-3), and EF (Case-4) Formations. Diagnostic plots are constructed to evaluate the drive mechanisms during the flowback process.

(2) Developing the water-rate decline (WRD) model by treating water flowback as a transient displacement process after oil/gas breakthrough from matrix into fractures.

(3) Validating the WRD model by comparing the predicted value of water recovery factor (RF_w) with field values measured during post-flowback period. RF_w is the ratio of cumulative water production volume (W_p) to total injected water volume (TIV).

(4) Applying the WRD model on water production data to estimate RF_w after 1 to 10 years of production for the 172 wells.

3.3 Water-rate Decline during Flowback and Post-flowback

This section briefly reviews the reservoir and completion data for the four field cases of HR, WF, MT, and EF. The drive mechanisms for water flowback are then evaluated by constructing diagnostic plots.

3.3.1 Reservoir and Well-completion Data

Fig. 3.1 describes the primary operational steps for developing the target wells after the drilling process. It generally takes 1 to 2 days for hydraulic fracturing operation. The wells undergo flowback for fracture cleanup before starting gas/oil production. EF and HR wells underwent a period of extended shut-in to prepare flowback equipment at surface. Finally, all wells were put on post-flowback production after flowback.

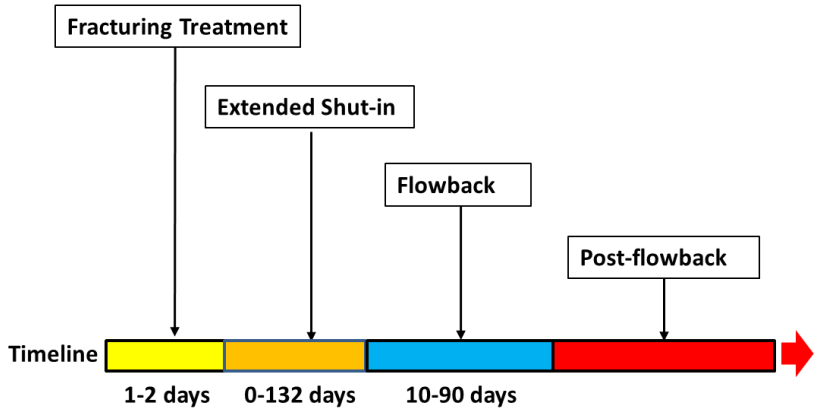

Fig. 3.1: General timeline for the operational steps for developing the target EF, HR, WF, and MT wells after the drilling process (modified from Alkouh et al. 2014).

Table 3.1 summarizes the reservoir and completion data for the target wells. Initial reservoir pressure for HR and MT wells are obtained from diagnostic fracturing injection tests (*DFITs*) of 40 HR and 39 MT wells. The initial reservoir pressure of WF wells is reported in Table 2.1, and that of EF wells is reported by Cander (2012).

Case-1 analyzed 24 multi-fractured horizontal wells completed in lower EF Formation (Pommer and Kitty 2012). The primary rock type is mudstone with low porosity (3-12 %) and permeability (100-700 nD) (Donovan et al. 2013; Dong et al. 2013). The fluid type for these wells is dry gas. Two of the wells were shut-in for 2-3 days before flowback. The rest were shut-in for 9 to 78 days before flowback. Rate and pressure data were recorded hourly during flowback.

Case-2 analyzed 26 multi-fractured horizontal wells, which are drilled in 3 pads (Pads B, C, and D) completed in Muskwa (MU), Otter Park (OP), and Evie (EV) shale members of the HR Formation. The fluid type for these 26 wells is dry gas. The wells were shut-in for 30 to 110 days before flowback. Rate and pressure data were recorded hourly during flowback and daily during post-flowback. More details about these wells are reported in previous publications (Abbasi 2013; Abbasi et al. 2014; Ezulike 2015, 2016, 2017; Xu et al. 2015, 2016, 2017).

Table 3.1: Summary of reservoir and well-completion data for the four field cases

Information	Case-1	Case-2	Case-3	Case-4
	Eagle Ford	Horn River	Woodford	Montney
Number of target wells	24	26	15	107
Fluid type	Dry gas	Dry gas	Black oil/gas-condensate	Dry-gas/gas-condensate
Rock type	Shale	Shale	Mudstone	Siltstone
Initial reservoir pressure, MPa	55-68	27-45	28-54	20-32
Average true vertical depth, m	2874-3349	2418-2714	3113-4542	1898-2256
Extended shut-in, days	2-78	30-132	0	0
Number of fracture stages	17-31	15-27	9-16	17-32
Range of total injected volume of water, 10^3 m^3	27.4-111.4	29.1-74.2	13.7-27.6	9.3-17.5

Case-3 analyzed 15 multi-fractured horizontal wells completed in the WF Formation (Foltz, 2015) in Anadarko Basin. These wells are located in south and north areas (see Fig. 2.5). Wells in the south area are at least 1000 m deeper than wells in the north area. The primary rock type is mudstone with low porosity (3-10%) and permeability (10-100 nD). The fluid type for these wells is black-oil or gas-condensate. The wells were put on flowback without extended shut-in after fracturing operations.

Case-4 analyzed 107 multi-fractured horizontal wells completed in Lower, Middle, and Upper zones of the MT Formation. The primary rock type is siltstone, which comprises shale and mudstone (Quintero et al., 2018). Rate and pressure data were recorded hourly during flowback. Well-completion and flowback data are obtained from BC Oil and Gas Commission website (BCOGC, 2016).

3.3.2 Field Observations

3.3.2.1 Case-1: Eagle Ford Wells

Fig. 3.2a shows casing pressure (P_{casing}), gas rate (q_g), and water rate (q_w) measured during the flowback period of a gas well completed in the EF Formation. The results show 3 regions: Region-1 shows single-phase water flowback which lasts several hours. Region-2 shows an increasing P_{casing} and a relatively sharp increase in q_g. Region 3 shows gradual stabilization of casing pressure.

Fig. 3.2b shows the semi-log plot of q_w versus W_p during the flowback and post-flowback periods. A straight-line behavior is observed during flowback. A similar behavior is observed for 9 other EF wells shown in Fig. B.1. The results show a relatively good match (R^2=0.94) between q_w measured during post-flowback period and the extrapolated straight-line fit to the flowback q_w data.

3.3.2.2 Case-2: Horn River Wells

Fig. 3.2c shows the rate and pressure data measured during flowback and post-flowback (during 2 years of production) for a well in Pad-B completed in the MU shale member. More details about Pad B are described by Abbasi (2013), Ezulike (2017), and Xu et al. (2015, 2016, 2017). The bottomhole pressure (P_{wf}) is calculated using the Gray correlation (1978) implemented in the IHS Harmony Software (IHS, 2018).

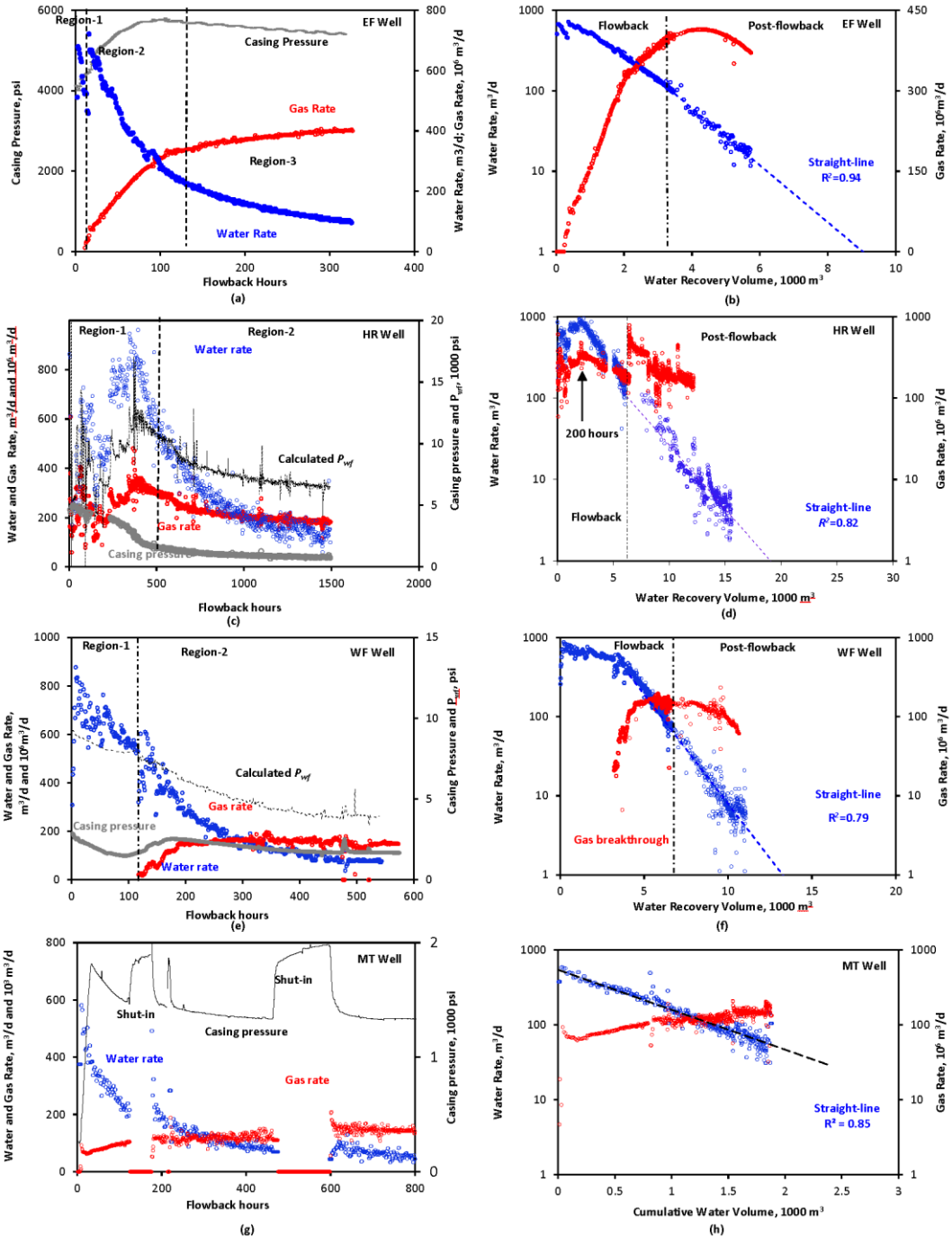

Fig. 3.2: Flowback rate and pressure data for typical wells completed in the (a) EF, (c) HR, (e) WF, and (g) MT formations generally show a gradual pressure stabilization during multiphase production period. The semi-log plots of water rate versus cumulative water production volume for the (b) EF, (d) HR, (f) WF, and (h) MT wells show a straight line during flowback period. There is a good match between the extrapolated straight line and measured water rate during post-flowback period for the EF, HR, and WF wells.

Fig. 3.2d plots the hourly flowback rate and pressure data for the target well. The flowback data are divided into two regions: Region-1 shows an immediate breakthrough of gas as flowback starts, a sharp decrease in pressure, and a general increasing trend of q_w and gas rate (q_g). Region-2 shows relatively stabilized pressure and a declining trend of q_g and q_w. This region occurs after 200 hours of flowback. The casing pressure (P_{casing}) is generally stabilized during Region-2.

Fig. 3.2d compares the semi-log plot of q_g and q_w versus W_p during flowback and post-flowback periods. After about 200 hours of flowback, a straight-line is observed in the semi-log plot of q_w versus W_P. The straight-line behavior is observed in similar plots for all target HR wells (see Fig. B.2). Fig. 3.2d shows a good match between q_w measured during post-flowback period and the extrapolated straight-line fit to the flowback data.

3.3.2.3 Case-3: Woodford Wells

Fig. 3.2e plots rate and pressure data measured during flowback and post-flowback (after 1 year of production) for a tight gas well completed in WF Formation. Fig. B.4a shows a similar plot of rate and pressure data for a tight-oil well completed in the same Formation. P_{wf} is calculated using the Gray correlation (1978) implemented in the IHS Harmony Software (IHS, 2014).

Fig. 3.2e shows rate and pressure data recorded during the first 530 hours of flowback for the target tight-gas well. The results show single-phase water flowback in the first 113 hours, followed by multiphase flow of gas and water. During single-phase period, q_w remains relatively high while P_{wf} drops significantly. The results show that P_{casing} increases, and then stabilizes after gas breakthrough. Fig. B.3a shows similar trends after oil breakthrough in the tight-oil well.

Fig. 3.2f compares the semi-log plot of q_g and q_w versus W_p during flowback and post-flowback periods. The results show a straight line in the semi-log plot of q_w and W_P after gas breakthrough. This straight line is also observed in the similar plot of q_w versus W_P for the other 6 WF wells (Fig. B.3a). The results show a relatively good match (R^2 =0.79) between q_w measured during

post-flowback period and the extrapolated straight-line fit to the flowback q_w data. Fig. B.3b shows a similar match for the tight-oil well.

3.3.2.4 Case-4: Montney Wells

Fig. 3.2g shows P_{casing}, q_g, and q_w recorded during the first 915 hours of flowback for a dry-gas well completed in the MT Formation. There are two shut-ins during the flowback period of this dry gas well. Fig. B.5 shows a similar plot of rate and pressure data for a gas-condensate well completed in the same formation.

Fig. 3.2g shows immediate gas production as flowback starts. Gas rate generally increases with time. P_{casing} generally flattens after about 200 hours of flowback (the pressure buildup is caused by shut-in). Fig. B.5 shows a period of single-phase water flowback in a gas-condensate MT well. q_w decreases after the gas and condensate production. Also, the results show that P_{casing} of the gas-condensate well generally flattens during the multiphase flowback period.

Fig. 3.2h compares the semi-log plot of q_g and q_w versus W_p during flowback period. A straight line can be fit to the water-rate data during flowback. Fig. B.6 and Fig. B.**7** show similar straight-line behavior for 10 dry-gas and 10 gas-condensate MT wells, respectively.

3.3.3 The Physics of Water Flowback

Here, diagnostic plots are constructed to investigate the drive mechanisms for water flowback. These diagnostic plots include log-log plot of rate-normalized pressure (*RNP*) and material balance time (t_{MB}) for wells with single-phase water flowback (*RNP* and t_{MB} are defined in Section 2.2.1). Log-log plot of gas-water ratio (*GWR*) and cumulative gas volume (G_p) is used for wells with early gas breakthrough.

3.3.3.1 Drive mechanisms before hydrocarbon breakthrough from matrix into fractures

Fig. 3.3a and b show log-log plots of *RNP* versus *MBT* during single-phase water flowback for one MT and one EF well, respectively. Similar plots for WF wells are shown in Appendix A.2. The unit-slope identified in the *RNP* plots which represent the "*supercharge"* effect, meaning

that the pressure in fractures is higher than that in matrix. Therefore, water is produced from the closed-tank fracture system without pressure support from the matrix system. Also, the unit-slope represents the pseudo-steady flow of water (Abbasi et al. 2014; Ezulike et al. 2016). As discussed in Section 2.2.4, fracture closure is the primary drive mechanism during the pseudo-steady flow for water production. The deviation from unit-slope indicates fluid influx from matrix into fractures.

Fig. 3.4 shows the diagnostic plots of *GWR* versus G_p for a shale gas well in HR Basin. *GWR* decreases in Region-1, and increases in Region-2. Ghanbari and Dehghanpour (2016) argued that gas produced in Region-1 is free gas already in the fractures before flowback starts. The primary drive mechanisms for water production in Region-1 are fracture closure and expansion of gas and water (Ezulike et al. 2016; Xu et al. 2017).

The early water flowback is due to fracture closure and gas expansion, which depends on pressure, controlled by choke size during flowback. However, flowback data can be quite noisy because of frequent choke-size changes during early flowback. The early declining trend in water production may thus be masked by the relatively noisy flowback data.

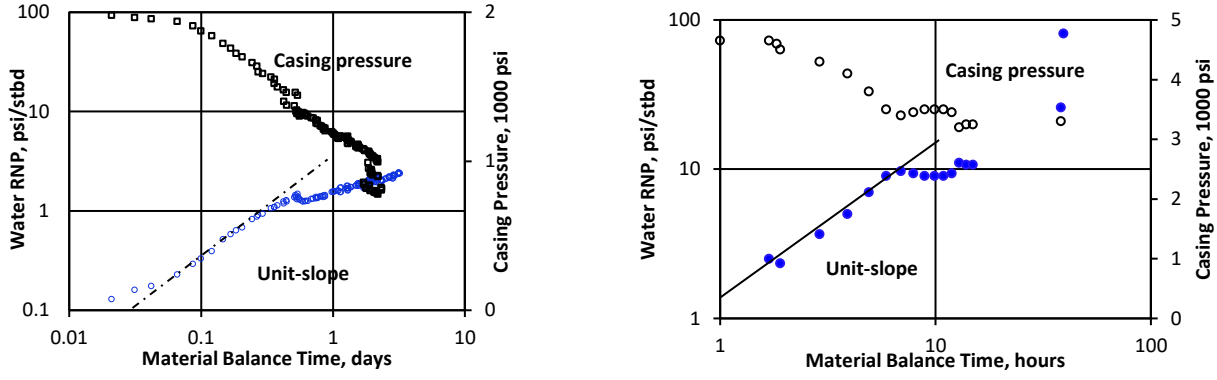

(a) (b)

Fig. 3.3: Log-log plot of rate-normalized pressure versus material balance time for (a) an MT well and (b) an EF well shows a unit-slope during single-phase water flowback. The unit-slope suggests that the fracture network behaves as a closed tank during single-phase flowback.

3.3.3.2 Drive mechanisms after hydrocarbon breakthrough from matrix into fractures.

Gas/oil expansion (Ezulike & Dehghanpour, 2014) and displacement of water by oil/gas (Abbasi 2013) are the primary drive mechanisms for water production after oil/gas breakthrough from matrix into fractures. Comparing pressure and rate profiles in Fig. 3.2 shows that pressure generally stabilizes during late flowback, suggesting pressure support due to gas/oil breakthrough from matrix to fractures (Jones et al., 2014). The pressure stabilization suggests that gas/oil expansion may not be the dominant drive mechanism for water production because of insignificant pressure change in fractures. The water-rate decline after pressure stabilization can then be explained by relative permeability effect (Abbasi 2013) where relative permeability of water in fractures decreases with increasing oil and/or gas saturation in fractures.

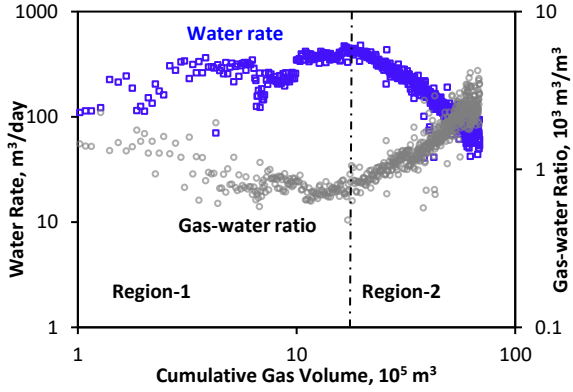

Fig. 3.4: Log-log plot of gas-water ratio versus cumulative gas volume for a Horn River well shows two regions: *GWR* decreases in Region-1, and it increases in Region-2.

3.4 Harmonic-decline Model

This section mathematically shows how water flowback can be described by the harmonic WRD model.

During multiphase flowback periods, the results show a trend of q_w linearly declining by increasing W_p in a semi-log plot, suggesting harmonic decline. This harmonic decline is a general trend for the target wells completed in the EF, HR, MT, and WF Formations. Bai and Carlson (2016) reported a similar trend in flowback data of 32 horizontal fractured wells completed in the Wattenberg field.

The harmonic-decline rate of oil is often observed in production during water flooding, where oil decline is mainly controlled by the relative-permeability effect (Baker 1998). Lijeck (1989) derived a harmonic-decline model for water flooding based on an exponential function of relative-permeability model. Here, a harmonic model is derived for the decline of q_w by considering the displacement of water by hydrocarbon in effective fractures during the flowback process.

The harmonic model is derived based on the following assumptions: (1) Two-phase flow of water and hydrocarbon is assumed for effective fractures. Water in effective fractures is displaced by hydrocarbon under a transient state. The average water saturation in effective fractures (S_w) is a function of time with negligible gradient along fracture network; (2) Water is primarily produced from effective fractures with negligible influx of water from matrix into fractures due to high capillary pressure and ultra-low permeability of shale and tight rocks (Babadagli et al., 2015; Chen and Horne, 2006; Engelder, 2012; Engelder et al., 2014); (3) The change in effective fracture pore-volume (V_{ef}) and fracture permeability (k_f) is negligible after the casing and bottomhole pressure stabilize during flowback.

According to Darcy's Law, water rate is proportional to k_f, the average relative permeability of water in effective fractures (k_{rw}), and the difference between average pressure in fractures ($P_{f\text{-}avg}$) and P_{wf}.

$$q_w \propto k_{rw} k_f (P_{f-avg} - P_{wf}) \tag{3.1}$$

Chen et al. (2013)'s relative-permeability model for coal reservoirs is used to describe the relationship between k_{rw} and S_w.

$$k_{rw} = k_{rw-\max} (S_w)^{\frac{2}{\lambda}+1+\eta} \tag{3.2}$$

Here, $k_{rw\text{-}max}$ represents the maximum relative-permeability of water in effective fractures; η is the fracture tortuosity coefficient which increases with increasing fracture complexity (Chen at al. 2013); λ is the cleat-size distribution index which can be as low as 0.22 for coal reservoirs (Chen at al. 2013). Porous media with secondary porosity (e.g. micro-fractures) have a relatively

small λ (Brooks and Corey 1966; Chen at al. 2013; Yang et al., 2016). The fracture system of tight and shale gas/oil wells consists of hydraulic fractures and micro fractures. The tight and shale gas/oil wells are thus expected to have a relatively smaller λ compared with wells completed in coal reservoirs.

Similar to Ezulike and Dehghanpour (2014), S_w is related to W_p and V_{ef} by

$$S_w = S_{wi} - \frac{W_p}{V_{ef}} \tag{3.3}$$

S_{wi} is the initial water saturation in fractures. S_{wi} is assumed to be 1 when flowback starts with single-phase water production. As described by Eq. 3.3, S_w changes with W_p, which further changes with time. k_{rw} is thus a function of time.

Combining Eq. 3.1, 3.2, and 3.3 results in

$$q_w \propto k_f k_{rw-\max} (S_{wi} - \frac{W_p}{V_{ef}})^{\frac{2}{\lambda}+1+\eta} (P_{f-avg} - P_{wf}) \tag{3.4}$$

By defining a and b as

$$a = \frac{C \cdot [k_f k_{rw-\max} (P_{f-avg} - P_{wf})]^b}{V_{ef}}$$

$$b = \frac{1}{\frac{2}{\lambda}+1+\eta}$$

where, C is the proportionality constant of Eq. 3.4.

Eq. 3.4 can be rearranged as

$$q_w{}^b = aV_{ef}(S_{wi} - \frac{W_p}{V_{ef}}) \tag{3.5}$$

During late flowback, the gas/oil influx from matrix into fractures provides pressure support for the fracture system, contributing to insignificant change in $P_{f\text{-}avg}$. Meanwhile, flowback data show that the flowing pressure is gradually stabilized during late flowback (see Fig. 3.2 and Fig.

B.8). It is thus reasonable to assume that $P_{f\text{-}avg}$ and P_{wf} drop with a similar rate with respect to time. aV_{ef} and k_f can also be assumed as constant by considering negligible fracture closure. These assumptions lead to the following relationship

$$(S_w - \frac{W_p}{V_{ef}}) \cdot \frac{d(aV_{ef})}{dt} \ll aV_{ef} \frac{d\left(S_w - \frac{W_p}{V_{ef}}\right)}{dt} \tag{3.6}$$

Taking the derivative of both sides of Eq. 3.5 gives

$$\frac{d(q_w{}^b)}{dt} = -a\frac{dW_p}{dt} \tag{3.7}$$

The water rate is also related to cumulative water volume by

$$\frac{dW_p}{dt} = q_w \tag{3.8}$$

By substituting Eq. 3.8 into 3.7, the general form of rate-decline model for water flowback is given by

$$\frac{1}{q_w}\frac{dq_w}{dt} = -D_i q_w{}^{1-b} \tag{3.9}$$

D_i is the rate-decline constant defined as a/b, day^{-1}.

b is a curve-fitting parameter which depends on fracture pore-size distribution and fracture tortuosity. b may approach 0 by decreasing λ and increasing η for complex fracture networks in shale and tight reservoirs. Harmonic decline is obtained when $b = 0$, and q_w and W_p are related to time by

$$q_w = \frac{q_i}{1 + D_i t} \tag{3.10}$$

$$W_p = \frac{q_i}{D_i}\ln(1 + D_i t) \tag{3.11}$$

where, q_i is the initial water rate during the flowback period showing the harmonic decline. The water recovery factor is then related to time by

$$RF_w = \frac{q_i}{TIV \cdot D_i} \ln(1 + D_i t) \tag{3.12}$$

After combining Eq. 3.10 and Eq. 3.11 to eliminate time, the linear relationship between ln (q_w) and W_p is given by

$$\ln(q_w) = -\frac{D_i}{q_i} W_p + \ln(q_i) \tag{3.13}$$

3.5 Application and Discussions

This section compares the RF_w values measured in the field with values predicted by the proposed model. Also, this section compares the estimated RF_w of the 172 wells completed in the four formations.

3.5.1 Validating Harmonic-decline Model

Fig. 3.5a compares the measured values of RF_w for a target EF well with the values predicted by the harmonic WRD model. D_i in Eq. 3.12 is obtained by fitting the model to the water flowback data. RF_w during post-flowback period is then predicted using D_i in Eq. 3.12. Here, we have post-flowback data of RF_w for 21 HR, 6 WF, 14 MT, and 8 EF wells up to 1000, 500, 30, and 80 days, respectively.

Fig. 3.5b compares RF_w measured during post-flowback period and that predicted by the WRD model for these 49 wells. The variation in RF_w (0.10-0.67) is mainly caused by the different lengths of production time for these wells. Fig. 3.5b shows a relatively good match between the measured and predicted RF_w values, suggesting that the WRD model can be used to estimate water recovery factor with a reasonable accuracy.

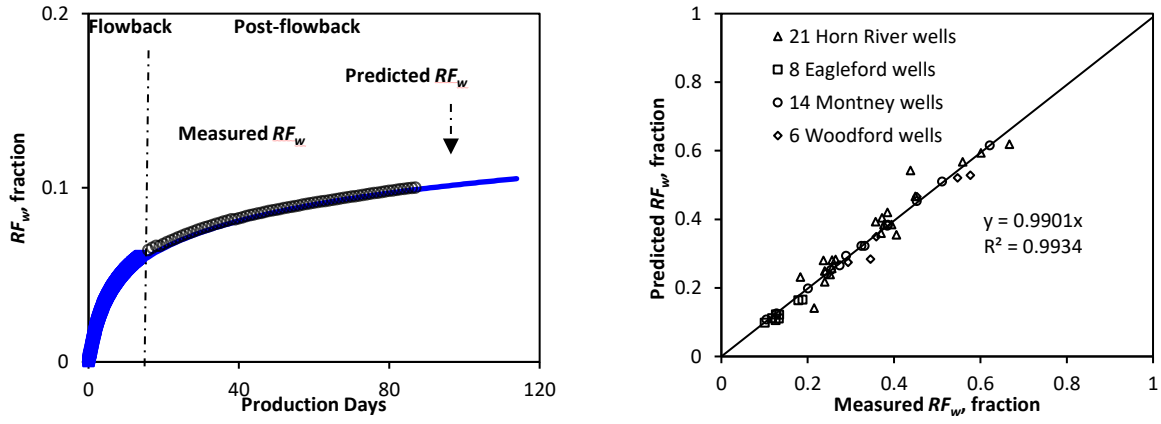

Fig. 3.5: (a) Comparison of water recovery factor measured during post-flowback period with that predicted by the harmonic-decline model for an EF well; (b) Crossplot of water recovery factor predicted by the harmonic-decline model with the measured values shows a good match for the wells completed in the Horn River, Eagle Ford, Montney, and Woodford Formations.

3.5.2 Fitting Results

Fig. 3.6 shows the statistical results of R^2 and D_i, which are obtained by fitting the harmonic-decline model to the water flowback data. Appendix B.6 lists the values of R^2 and D_i for each well. The relatively high R^2 (0.83 ± 0.09) suggests a good match between the measured and predicted water rate. Fig. 3.6a shows the boxplot of D_i for all wells. In general, D_i of these wells is less than 1 day^{-1}.

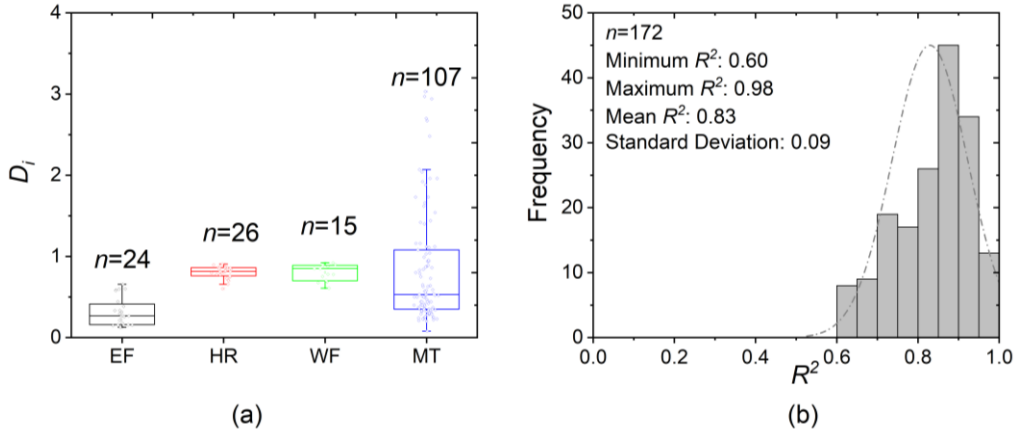

Fig. 3.6: (a) Boxplots of D_i and (b) distribution of R^2 for 172 target wells. D_i and R^2 are obtained by fitting the harmonic-decline model to water production data. The boxplot represents median (solid lines in boxes), 25th and 75th percentile (bottom and top borders of each box) values. n represents the total number of wells considered.

3.5.3 Water Recovery Factor

Fig. 3.7 plots RF_w predicted by the harmonic WRD model versus time for 172 target wells. RF_w is calculated by using D_i from Fig. 3.6 in Eq. 3.12. Fig. 3.7 shows that the estimated RF_w for all target wells are less than unity after 10 years of production. Recent studies suggest that fracturing water may account for a relatively small fraction of produced water after several years of flowback (Kondash et al., 2017; Osselin et al., 2018; Rowan et al., 2015; Soeder et al., 2014). We thus expect that most of fracturing water injected into these wells remains unrecovered even after 10 years of production. In addition, the water rate generally drops below 10 m^3/day after 1 year of production. Most of the recovered water is produced during the first year (see Fig. B.9).

Fig. 3.8 shows the distribution of RF_w predicted by WRD model after 1 year of production for all the target wells. Fig. B.10 shows a similar distribution of RF_w after 10 years of production for these wells. The mean values of RF_w for all the wells are lower than 0.4 after one year of production. The unrecovered water can remain in fractures (effective and ineffective) and matrix. The water remaining in effective fractures could be recovered during post-flowback period. However, the water leaked off into matrix may not be recoverable due to the high capillary pressure in shale and tight reservoirs (Ghanbari and Dehghanpour 2016; Edward et al. 2018). In addition, the water remaining in ineffective fractures (fractures disconnected from wellbore) will be hard to recover (Alkouh et al. 2014). Fracturing water can also be trapped in fractures because of gravity segregation (Parmar et al. 2014).

In Fig. 3.8, the results show a relatively-uniform distribution of RF_w for the EF wells. However, there is a relatively large variation in RF_w for the HR, WF, and MT wells, which can be explained as follows:

HR Wells. Fig. 3.9 compares the RF_w values of wells completed in MU, OP, and EV shale members of the HR Formation. The results show that RF_w of EV wells is generally lower than that of MU and OP wells. Ghanbari and Dehghanpour (2016) reported similar results of RF_w for the HR wells during flowback. Flowback chemical study (Zolfaghari et al. 2016) suggests a

relatively larger fracture surface area in EV wells than that in MU and OP wells. One may expect that a relatively high fraction of fracturing water is imbibed into shale formation because of large fracture surface area in EV wells during the extended shut-in period.

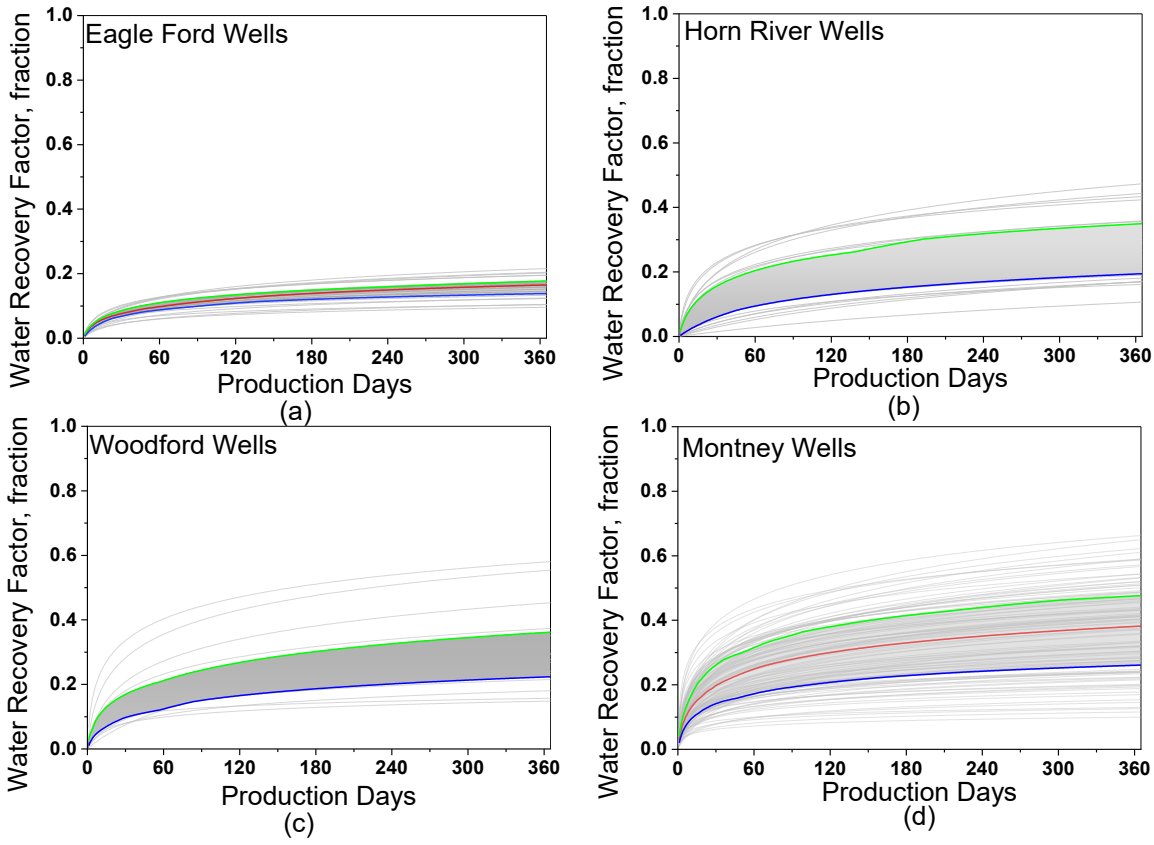

Fig. 3.7: Predicted water recovery factor versus production time for (a) EF, (b) HR, (c) WF, and (d) MT wells. The 25th and 75th percentiles and mean values are represented by the blue, green, and red lines, respectively.

Fig. 3.9 shows a relatively high variation in RF_w of MU and OP wells. Well communications are identified among these wells during flowback (see Section 5.4.3 in Chapter 5). In Chapter 5, tracer data analysis indicates that wells can still be connected during the flowback process. The wells opened for flowback earlier drain fracturing water from those opened later through connecting fractures. Therefore, the observed variations in RF_w of the MU and OP wells may be due to inter-well communication.

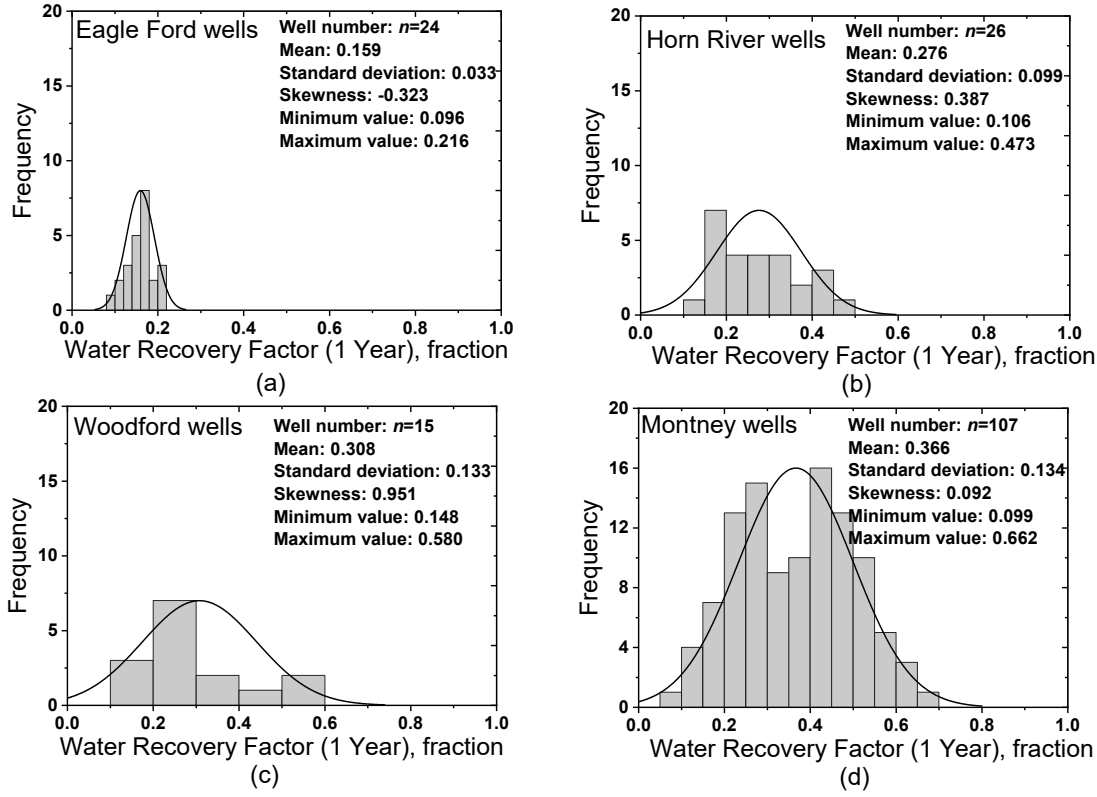

Fig. 3.8: Distribution of water recovery factor predicted by WRD model for (a) EF, (b) HR, (c) WF, and (d) MT wells after 1 year of production.

WF Wells. Fig. 3.10 shows that RF_w of WF wells in the south area is generally higher than that in the north area (Fu et al., 2017; Jones et al., 2014). WF Formation in the south area is at least 1000 m deeper than that in the north area. The higher initial reservoir pressure in the wells of south-area contributes to a relatively higher pressure drop and initial water rate, leading to a relatively higher RF_w.

MT Wells. Fig. 3.11 compares RF_w of wells completed in the Upper, Middle, and Lower MT Formations. The results show that RF_w of the Upper MT wells is higher than that of Middle and Lower MT wells. In 17 Upper MT wells, RF_w is higher than 0.9 after 10 years of production (Fig. B.10). Mobile formation water was reported from water-saturation measurements using core samples and well-log data from the Upper MT wells (Wood, 2013). The relatively higher RF_w of the Upper MT wells is possibly due to production of formation water in addition to fracturing water.

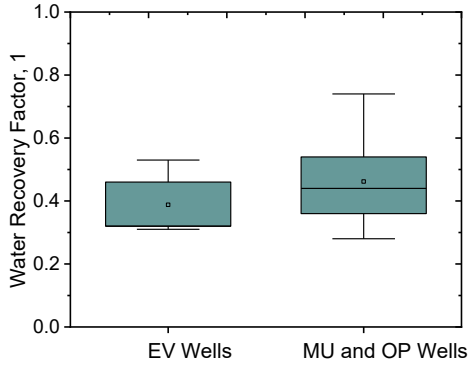

Fig. 3.9: The water recovery factor of EV wells is relatively lower than that of MU and OP wells after 1 year of production.

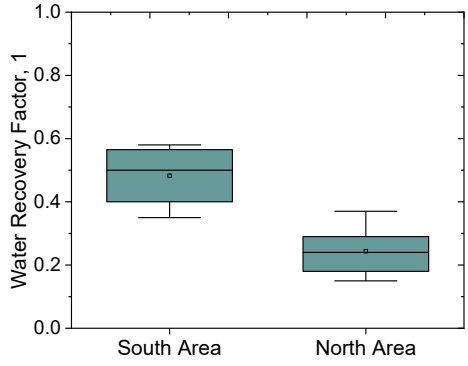

Fig. 3.10: The water recovery factor of WF wells in the south area is relatively higher than that of wells in the north area after 1 year of production.

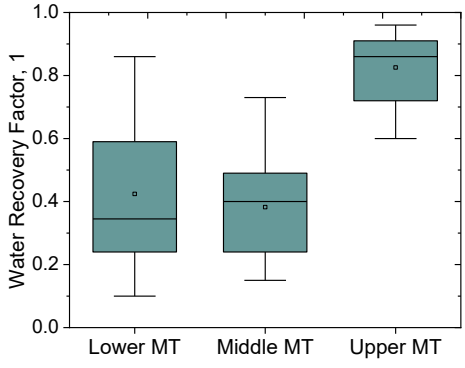

Fig. 3.11: The water recovery factor of Upper MT wells is relatively higher than that of Lower and Middle MT wells after 1 year of production.

3.5.4 Ultimate Recovery Volume versus Effective Fracture Pore-volume

Fig. 3.12a shows how ultimate W_p of an example MT well is estimated by extrapolating the harmonic-decline trend. Fig. 3.12b compares the values of ultimate W_p estimated by the WRD model with V_{ef} estimated by flowback tank models (Abbasi et al. 2014; Xu et al. 2017) for 32 wells completed in the HR, MT, and WF Formations. Appendix B.9 applies Abbasi et al. (2014)'s method on single-phase flowback data to estimate V_{ef} for the MT wells. However, the flowback tank models are not applicable to EF wells due to the early gas breakthrough from matrix into fractures as flowback starts. V_{ef} for EF wells are thus not reported in Fig. 3.12b.

Fig. 3.12b shows a reasonable match between the values of ultimate W_p and V_{ef}. Since the effective fractures are mainly filled with water at the beginning of flowback, the ultimate W_p estimated by the WRD model can be an approximation for V_{ef}. In Fig. 3.12b, however, we observe a relatively large scatter for the data points of the HR wells. Flowback data of the HR wells show immediate gas production, suggesting the existence of free gas in effective fractures. Thus, the observed scatter may be due to the uncertain input of initial gas saturation in the flowback tank model (Xu et al., 2015) for estimating V_{ef}.

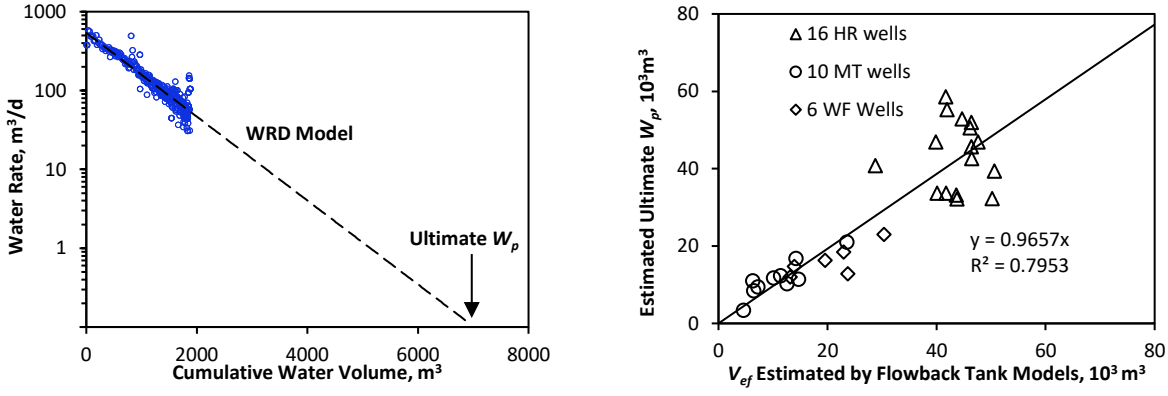

Fig. 3.12: (a) Estimating ultimate W_p by extrapolating the WRD model for an MT well; (b) Crossplot of V_{ef} estimated by flowback tank models and ultimate W_p estimated by WRD model for 32 wells completed in HR, MT, and WF Formations.

3.6 Limitations and Recommendations

The harmonic-decline model was derived by assuming negligible water flow from matrix into fractures. This assumption is challenging to be validated due to the uncertain mobile formation

water for target wells. It is possible that the produced water contains mobile formation water. For example, mobile formation water has been reported in the MT wells (Osselin et al., 2018; Wood, 2013). However, as suggested by Osselin et al. (2018), the produced formation water is more likely to come from nature fractures than matrix because of its ultra-low porosity, permeability, and residual water saturation (Balashov et al., 2015; Engelder et al., 2014). The hydraulic fractures intersect natural fractures filled with mobile water, which is possibly responsible for the formation water in produced water (Osselin et al., 2018). This may further explain why the water flowback of target MT wells still follows the harmonic-decline trend. Future studies should further differentiate the formation water from the produced water for the target wells, and determine the source of the formation water.

In this study, flowback water refers to the produced water after the fracturing treatments. Recent studies suggest that the produced water can be a mixture of fracturing water and formation brine (Barbot et al., 2013; Engle et al., 2016; Osselin et al., 2018; Rowan et al., 2015; Scanlon et al., 2014). However, this may not bias our key conclusion that a large fraction of fracturing water remains unrecovered for the target wells after long-time production. On average, the estimated RF_w is generally less than 0.5 after 10 years of production. The recovery of fracturing water is thus expected to be lower than the estimated RF_w for the target wells. In addition, applying the WRD model to project the recovery of fracturing water for wells in other shale/tight fields may need further validation. For example, wells in Permian Basin are reported to produce more water than injected after several months of production (Kondash and Vengosh, 2015; Scanlon et al., 2014). Analysis of geochemical isotope data have been proved to determine the fraction of fracturing water in the produced water (Capo et al., 2014; Engle et al., 2016; Osselin et al., 2018; Rowan et al., 2015; Scanlon et al., 2014). Combining the rate-decline analysis and geochemical isotopic analysis is recommended for projecting the recovery of fracturing water in future studies.

3.7 Summary and Conclusions

This chapter analyzed water-rate decline data of 172 multi-fractured wells completed in the Horn River, Woodford, Montney, and Eagle Ford Formations. By combining the Darcy's law

and relative permeability model, this chapter derived the harmonic relationship between water flowback rate and cumulative water production. The model was validated by comparing the predicted and measured values of water recovery. This study led to the following conclusions:

(1) Water flowback follows a harmonic decline trend after hydrocarbon breakthrough from matrix into fractures. The harmonic trend can be modeled by treating water flowback as a displacement process after hydrocarbon breakthrough from matrix into fractures.

(2) Comparative analysis of rate and pressure data suggests that the harmonic decline in water flowback is primarily due to the relative-permeability effects.

(3) The harmonic-decline model can be used to estimate water recovery with reasonable accuracy, under the assumption that water is primarily produced from effective fractures.

(4) The results show a positive correlation between estimated ultimate water production volume and effective fracture pore-volume for the Horn River, Montney, and Woodford wells.

(5) The results show that water recovery factor for the Eagle Ford, Horn River, Woodford, and Montney wells is generally less than 50% even after 10 years of production. A large fraction of fracturing water is expected to be trapped in the formation. The water recovery factor may depend on various parameters such as reservoir pressure, formation water saturation, and inter-well communication. This improves the understanding of the fate of fracturing water in unconventional fields.

3.8 Nomenclature

Symbols

A Drainage area, L^2, m^2, $[ft^2]$.
B Formation volume factor.
C Compressibility, Lt^2M^{-1}, atm^{-1}, $[Pa^{-1}, psi^{-1}]$.
K Permeability, L^2, m^2, $[D]$.

t	Time, t, s, $[hr, day]$.
P	Pressure of hydrocarbon phase, $ML^{-1}t^{-2}$, Pa, $[psi]$.
V	Volume, L^3, m^3, $[ft^3]$.
y	Fracture half length, L, m, $[ft]$.
μ	Viscosity, $ML^{-1}t^{-1}$, $Pa.s$, $[cP]$.

Subscripts

e	Equivalent or effective.
f	Fracture.
i	Initial.
t	Total.
w	Water.
wf	Bottom-hole flowing.

Chapter 4 Evaluating Fracture Volume Loss during Flowback and its Relationship to Choke Size: Fastback versus Slowback

4.1 Introduction

Flowback rate and pressure data have been analyzed to characterize the fracture network created by hydraulic fracturing operations (Crafton and Gunderson 2006; Abbasi et al. 2012, 2014; Clarkson and Williams-Kovacs 2013; Clarkson et al. 2014; Alkouh et al. 2014; Xu et al. 2015, 2016, 2017; Ezulike et al. 2016; Williams-Kovacs 2017). Several flowback models have been proposed and applied on early flowback data to estimate effective fracture pore-volume (V_{ef}) for shale and tight gas/oil wells (Abbasi et al. 2012, 2014; Xu et al. 2015, 2016, 2017; Ezulike et al. 2016). However, input parameters such as fracture compressibility are generally unknown or hard to estimate. This can lead to uncertainty in estimates of output parameters like V_{ef}.

Abbasi et al. (2012, 2014) and Abbasi (2013) developed a flowing material balance model (a linear relationship between rate-normalized pressure and material balance time) to estimate fracture volume using early time single-phase water flowback data. This model only works for wells with single-phase flowback. This limits its application on shale and tight gas/oil wells with early multiphase flowback.

Xu et al. (2015, 2016) proposed two-phase flowing material balance equations for estimating V_{ef} using early flowback data. They calculated V_{ef} using the linear relationship between rate-normalized pseudo-pressure and pseudo-time. However, since initial gas saturation in fractures and fracture compressibility are unknown in their models, there is uncertainty in the resulting output parameters.

In Chapter 2, Abbasi et al. (2012)'s flowing material balance model has been applied to estimate V_{ef} for tight oil and gas wells completed in the Woodford Formation. They reduced the uncertainty in V_{ef} by estimating in fracture compressibility using diagnostic fracturing injection

tests (*DFITs*) data. The results show a positive correlation between the estimated V_{ef} and cumulative water volume after 3 years of production.

Rate-decline analysis is widely used to forecast performance and estimate hydrocarbon reserves for oil and gas wells (Ahmed 2010; Duong 2011). Bai et al. (2013) applied rate-decline analysis on flowback data to forecast water production for Wattenberg wells. In this study, rate-decline analysis is applied to estimate the ultimate fracturing water recovery and evaluate its relationship to the created fracture volume.

The fracture volume estimated by the flowing material balance models (Adefidipe et al.; Xu et al. 2016; Abbasi et al. 2012, 2014) usually represents the initial volume of effective fractures at the onset of flowback. However, recent studies on flowback data of the Horn River (Xu et al. 2015; Ezulike et al. 2016) indicate that fracture closure is a key drive mechanism during flowback. This raises a key question about fracture volume change: How much fracture volume is lost with time?

Recent studies have demonstrated that choke size can impact long-term well performance. Fastback (flowback process with relatively large choke sizes) may damage fracture conductivity while slowback (flowback process with relatively small choke sizes) may delay the economic breakeven point (Deen et al. 2015; Tompkins et al. 2016). Another question is how choke size impacts loss in fracture volume during flowback.

Therefore, this chapter intends to: (1) apply decline analysis on water flowback rate to estimate initial effective fracture pore-volume for 14 wells completed in Eagle Ford Formation; (2) evaluate the loss in fracture volume; and (3) investigate the relationship between fracture volume loss and choke size.

4.2 Methodology

This study is conducted using these 4 key steps: (1) Quantifying and comparing drive mechanisms during early flowback using the method proposed by Ezulike et al. (2016); (2)

estimating initial effective fracture pore-volume (V_{fi}) by applying the rate-decline model described in Chapter 3 on water flowback data for the target wells; (3) evaluating fracture volume loss (dV_{ef}) using a fracture compressibility relationship; and (4) investigating the effect of choke-size variations on dV_{ef} for fastback and slowback wells.

4.2.1 Quantification and Comparison of Drive Mechanisms

The key drive mechanisms during early flowback include fracture closure, hydrocarbon expansion, and water expansion. As defined by Eq. 2.9, compaction-drive index (CDI) is used to quantify the drive mechanism of fracture closure. The mechanisms of gas and water expansion are quantified as hydrocarbon-drive index (HDI) and water-drive index (WDI) respectively. For gas wells, CDI, HDI, and WDI are defined by

$$HDI = \frac{S_g C_g}{C_t} \tag{4.1}$$

$$WDI = \frac{S_w C_w}{C_t} \tag{4.2}$$

where, C_t is the total compressibility, psi^{-1}; C_g is the gas compressibility, psi^{-1}; C_w is the water compressibility, psi^{-1}; C_f is the fracture compressibility, psi^{-1}. C_f is estimated by the method described in Section 2.2.3. S_g is the average gas saturation in effective fractures:

$$S_g = 1 - S_w \tag{4.3}$$

Average water saturation in effective fractures (S_w) is estimated by Eq. 4.4 under the following assumptions: (a) Water is mainly produced from effective fractures; (b) There is no influx of water from matrix into effective fractures. Also, the flow of water from effective fractures to matrix is negligible; And (c) the fracture-volume change is negligible compared with V_{fi} (see Section 4.3.2)

$$S_w = S_{wi} - \frac{W_p}{V_{fi}} \tag{4.4}$$

where, W_p is the cumulative water production volume, m^3. S_{wi} is the initial water saturation in effective fractures, dimensionless. Effective fractures are expected to be filled with water during single-phase flowback period. S_{wi} can thus be treated as 1 for the wells with single-phase flowback.

4.2.2 Evaluating Fracture-volume Loss using Fracture Compressibility

Fracture compressibility is related to effective fracture pore-volume by

$$C_f = \frac{1}{V_{fi}} \frac{dV_{ef}}{dP_f} \tag{4.5}$$

where, P_f is the average fracture pressure in *psi*. Similar to a previous study (Xu et al. 2017), P_f is approximated as the flowing bottomhole pressure.

The transient effective fracture pore-volume can then be estimated by

$$V_{ef} = V_{fi} - dV_{ef} = V_{fi} - V_{fi} C_f dP_f \tag{4.6}$$

The fracture volume-loss ratio (R_f) due to fracture closure during flowback is defined as

$$R_f = \frac{dV_{ef}}{V_{fi}} \tag{4.7}$$

4.3 Field Application

4.3.1 Quantification and Comparison of Drive Mechanisms

Fig. 4.1 compares CDI, HDI, and WDI for one of target Eagle Ford wells. Fracture closure is the dominant drive mechanism during the flowback of the target well. The difference between CDI and HDI decreases with time during flowback, mainly because HDI dominates over fracture closure when there is sufficient gas influx from matrix into fractures (Ezulike et al. 2016).

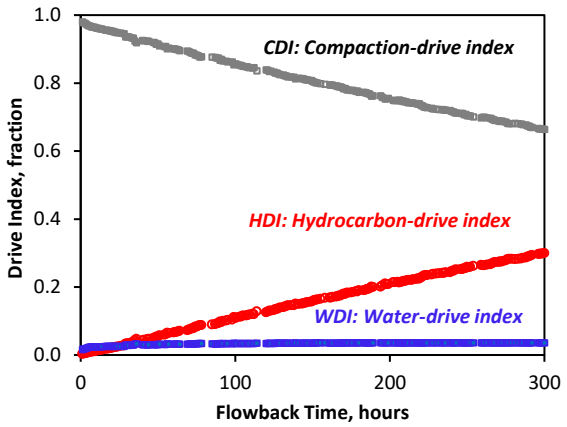

Fig. 4.1: CDI, HDI, and WDI profiles for a target Eagle Ford well during flowback period

4.3.2 Initial Effective Fracture Pore-volume

As shown in Fig. 4.2, water flowback of the target wells follows the harmonic-decline trend. V_{fi} for these wells is estimated by applying the water-rate decline method on flowback data (described in Section 3.5.4).

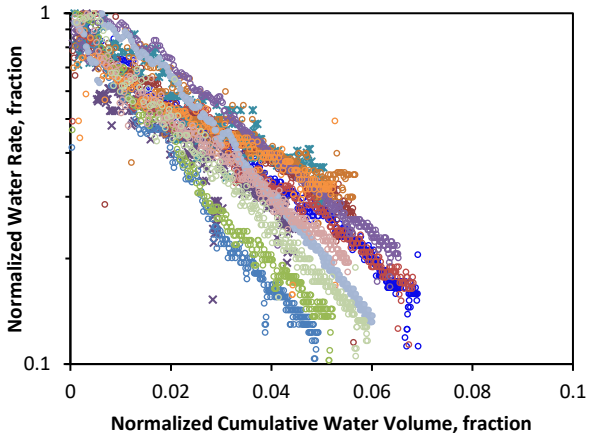

Fig. 4.2: Semi-log plot of normalized water rate and normalized cumulative water volume for 13 Eagle Ford wells. Water rate is normalized by the initial water rate at the onset of flowback. Cumulative water volume is normalized by total injected water volume. The water rate data for different wells are represented by different colors.

Fig. 4.3 compares the estimated V_{fi} with TIV for Eagle Ford wells. Fig. 4.3 shows a positive correlation between V_{fi} and TIV, indicating that injecting more water generally creates a larger effective fracture volume. However, several data points do not follow the general trend of V_{fi}

increasing with TIV. One may expect that completion design parameters other than TIV may also control V_{fi}. Fig. 4.4 shows a positive correlation between normalized effective fracture pore-volume (V_{fi}/TIV) with the number of fracture stages, suggesting that V_{fi} generally increases with the increasing number of stages.

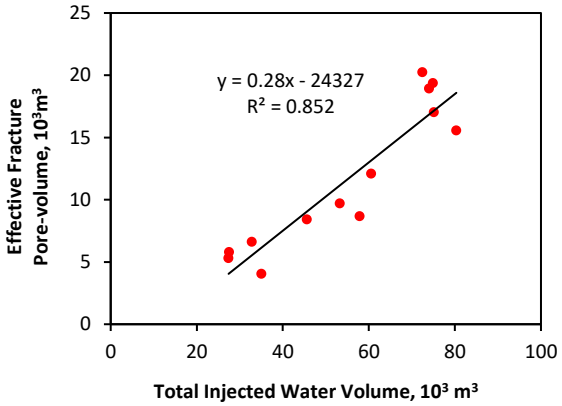

Fig. 4.3: A positive correlation between the estimated effective fracture pore-volume and total injected water volume for Eagle Ford wells.

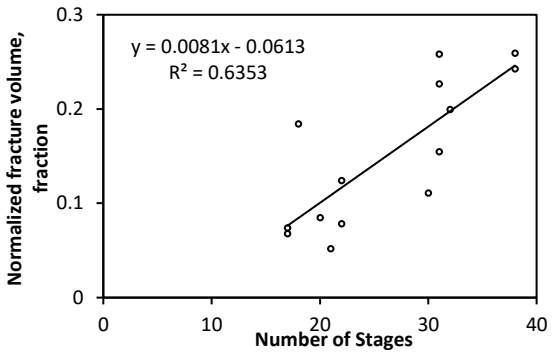

Fig. 4.4: Crossplot of normalized fracture volume versus number of stages shows a positive correlation for 14 Eagle Ford wells. Normalized fracture volume is defined as the initial effective fracture pore-volume divided by total injected water volume.

The slopes of the linear correlations in Fig. 4.3 suggest that on average 28% of TIV contributes to the creation of effective fractures in the Eagle Ford wells. One possible reason for the relatively low V_{fi}/TIV is that a significant amount of fracturing water is expected to be lost into dry-gas Eagle Ford Formation during fracturing and extended shut-in periods.

4.3.2 Evaluation of Fracture Volume Loss

This subsection shows how fracture volume decreases during the flowback of a target Eagle Ford well. The effect of choke size on dV_{ef} is then investigated for the Eagle Ford fastback and slowback wells.

4.3.2.1 Fracture Volume Loss during Flowback

Fig. 4.5 shows how V_{ef} decreases during the flowback of a target Eagle Ford well. The choke size for this well remains at 24/64 in. after 40 hours of flowback. About 10% of V_{fi} is lost during the first 300 hours of flowback, and fracture volume generally remains constant during late flowback. This indicates that the loss in fracture volume mainly happens during early flowback. The effect of fracture closure is expected to reduce during late flowback when there is sufficient gas influx from matrix into fractures.

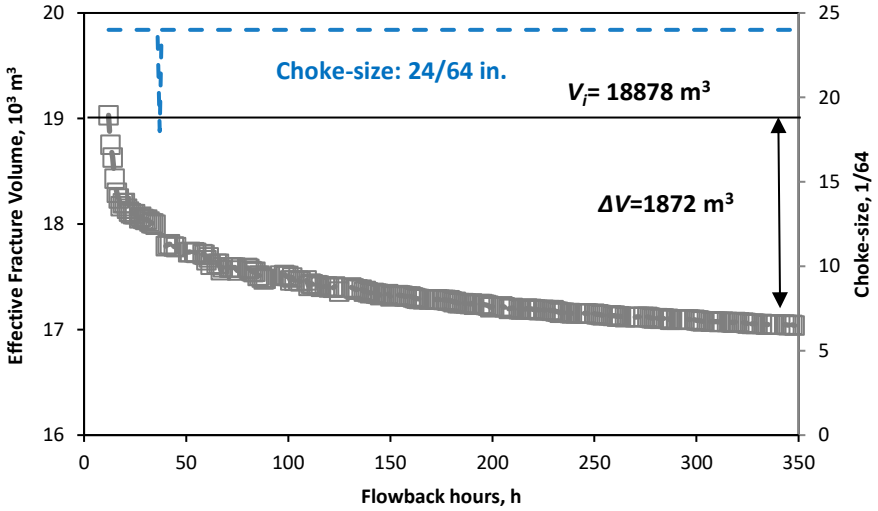

Fig. 4.5: Effective fracture pore-volume profile for an Eagle Ford well shows that fracture volume decreases during early flowback, and generally flattens during late flowback. Choke size remains at 18/64 initially, and then changes to 24/64 after 8 hours of flowback. The initial fracture volume is estimated by extrapolating the harmonic water-rate decline

4.3.2.2 Investigation of Choke Size on Fracture Volume Loss

Fig. 4.6 compares R_f for 3 fastback and 2 slowback wells completed in the Eagle Ford Formation. These 5 wells are located in the same area with similar reservoir pressure. Also, the completion design for these 5 wells is similar. Here, the choke size for the 3 fastback wells is 24/64 in. (large size), and that for the 2 slowback wells is 22/64 in. (small size). Only R_f of 5 Eagle Ford wells is compared with constant choke size, because the other 9 wells were flowed using variable choke sizes.

Fig. 4.6a shows a relatively higher R_f for fastback wells compared with that for slowback wells. About 8% and 5% of fracture volume are lost for fastback and slowback wells respectively after 200 hours of flowback. Fig. 4.6b plots R_f against load recovery of these wells (defined as W_p divided by TIV). R_f of fastback wells is higher than that of slowback wells, suggesting that fastback causes more fracture volume loss compared with slowback. Fig. 4.7 shows that fastback wells have more significant proppant production than slowback wells. One may expect that proppant production contributes to more severe fracture volume loss during flowback.

Fig. 4.6a shows that most of the loss in fracture volume of fastback wells happens in the early 100 hours of flowback and reaches to plateaus at late flowback periods after 300 hours. Similarly, R_f of slowback wells generally reaches to plateaus after 200 hours of flowback. The plateaus are expected to extend to long-term production periods when sufficient gas influx from matrix into fractures should limit fracture closure. Gas expansion will dominate over fracture closure when the product of gas compressibility and gas saturation in fractures is higher than fracture compressibility (Ezulike et al. 2016; Alkouh et al. 2014). Also, gas influx from matrix into fractures provides pressure support to the fracture system, reducing the fracture closure effect during post-flowback period.

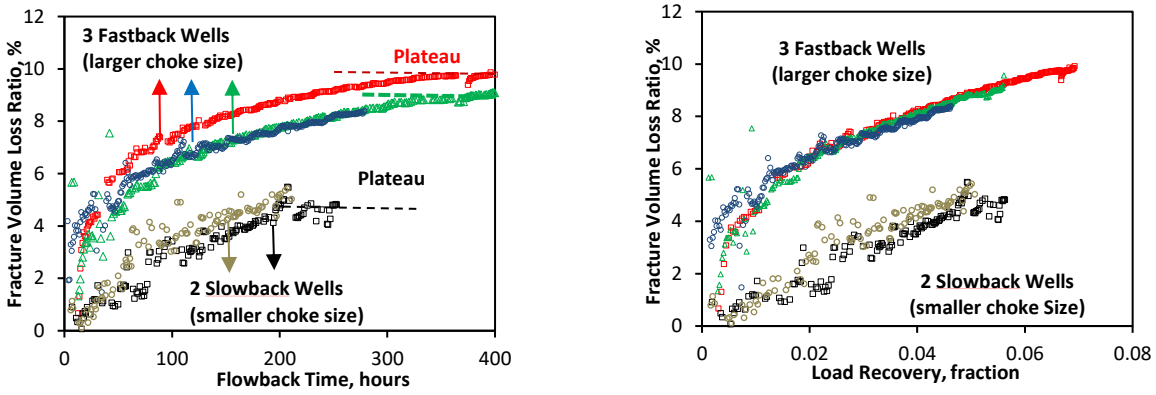

(a) (b)

Fig. 4.6: Fracture volume loss ratio versus (a) flowback time and (b) load recovery for fastback and slowback wells. Load recovery is defined as cumulative water volume divided by total injected water volume. There is more severe fracture volume loss for fastback wells compared with that for slowback wells.

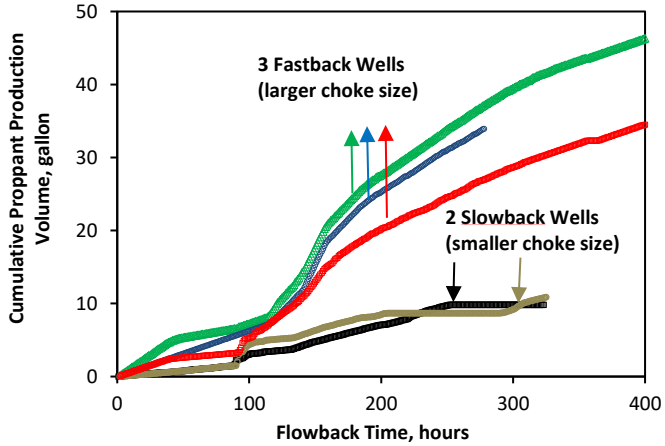

Fig. 4.7: Cumulative proppant production volume versus flowback time for fastback and slowback wells. There is more proppant production volume for fastback wells compared with that for slowback wells.

4.4 Limitations

4.4.1 Estimating Initial Effective Fracture Pore-volume

In the proposed method, the ultimate W_p is approximated as V_{fi} by assuming that V_{fi} is filled with water at the onset of flowback and that the water in effective fractures will be recovered during the flowback and post-flowback periods. In field cases such as Horn River Basin, flowback data show immediate two-phase production of gas and water (Xu et al. 2015, 2017; Ghanbari and

Dehghanpour 2016). Using rate-decline analysis may underestimate V_{fi} by neglecting initial hydrocarbon volume in effective fractures.

4.4.2 Evaluating Fracture-volume Loss

The results show a relatively higher R_f for wells with a choke size of 24/64 in. compared with wells with the choke size of 22/64 in. However, the choke sizes for fastback and slowback wells in this study are relatively very close. The results of fracture volume loss in fastback and slowback wells may thus need further validations by analyzing wells with a wider range of choke size during flowback. Also, it will be interesting to investigate how fracture volume loss during flowback affects gas production during the post-flowback period.

This chapter mainly studied the fracture volume loss for wells with constant choke size. However, wells may go through frequent choke-size changes during early flowback. The relationship between fracture-volume loss and flowback choke-size strategy is only for wells with constant choke size during flowback. Future studies should investigate how changing choke sizes impact fracture-volume loss during flowback.

4.5 Summary

This chapter investigated the effects of key drive mechanisms including fracture closure, gas expansion and water depletion on flowback of Eagle Ford wells. The results indicate that fracture closure is the dominant drive mechanism during early flowback period compared to fluid expansion. However, gas expansion is expected to overshadow fracture closure when there is sufficient gas influx from matrix into fractures.

This chapter also evaluated the change of effective fracture pore-volume during flowback for the Eagle Ford wells. The results show that the effective fracture pore-volume decreases during early flowback period, and generally remains constant during late flowback period. Comparative analysis shows a relatively higher fracture volume loss for fastback wells compared with that for slowback well, indicating that slowback may lead to less loss in fracture volume compared with fastback. With limitations on data available for wells operated at constant choke, the relationship

between fracture volume loss and choke size may need further validation in other plays where more wells with suitable flowback data are available.

4.6 Nomenclature

Symbols

B	Formation volume factor, L^3L^{-3}, ft^3scf^{-3}, $[bbl/stb]$.
b	Rate-decline constant, dimensionless.
C	Compressibility, Lt^2M^{-1}, atm^{-1}, $[Pa^{-1}, psi^{-1}]$.
D	Rate-decline constant, t^{-1}, $[hr^{-1}, day^{-1}]$.
P	Pressure of fluid, $ML^{-1}t^{-2}$, Pa, $[psi]$.
q	Rate, L^3t^{-1}, $m^3 \cdot s^{-1}$, $[RB/D]$.
R	Ratio, dimensionless.
RNP	Rate normalized pressure, $ML^{-4}t^{-1}$, $Pa \cdot m^{-3} \cdot s^1$, $[psi/RB \cdot D]$.
S	Fluid saturation, dimensionless.
t	Time, t, s, $[hr, day]$.
TIV	Total injected water volume, L^3, m^3, $[ft^3]$.
V	Volume, L^3, m^3, $[ft^3]$.
W	Cumulative production volume, L^3, m^3, $[ft^3]$.

Subscripts

cs	Casing.
$cond$	Condensate.
e	Equivalent or effective.
f	Fracture.
g	Gas.
i	Initial.
mb	Material balance.
$ulti$	Ultimate.
w	Water.
wf	Bottom flowing.
t	Total.

Chapter 5 How far can hydraulic fractures go? A comparative analysis of water flowback, tracer, and microseismic data from the Horn River Basin

5.1 Introduction

Hydraulic fracturing (HF) is a key technique for economic production of hydrocarbon from shales. During HF, a mixture of 10–100 thousand cubic meters of water and chemical additives is injected at high pressure to create pathways for hydrocarbon flow towards a wellbore (Davies et al., 2012; Kondash and Vengosh, 2015). A recent study (Jasechko and Perrone, 2017) shows that many active oil and gas wells are close to groundwater wells. The risk of contaminating groundwater wells during HF raises significant public concerns (Vidic et al., 2013). Geochemical studies in the Marcellus shales show elevated salinity and hydrocarbon concentrations in the surface water and groundwater wells (Warner et al., 2012; Olmstead et al., 2013; Llewellyn et al., 2015; Jackson et al., 2013; Darrah et al., 2014; Osborn et al., 2011). These studies suggest that the surface water and groundwater are possibly contaminated by formation brine and stray gas due to wellbore leakage (Warner et al., 2012; Darrah et al., 2014) or wastewater treatment at surface (Olmstead et al., 2013). However, it is challenging to demonstrate the potential risks of HF activities to water contamination (Vidic et al., 2013). The possibility of fracturing water and stray-gas contamination through conductive pathways connecting aquifer and shales remains uncertain. It is thus crucial to investigate how far fractures can go beyond the wellbore.

Several methods have been used to estimate fracture length (L) and height (H) for multi-fractured horizontal wells. Rate transient analysis and numerical modeling are common methods for estimating L and forecasting gas production. These methods usually assume uniform L and H for fracture stages (Patzek et al., 2013). The outputs thus mainly represent the average values of L and H, and not the upper limits. Also, H is generally assumed as formation thickness, neglecting the possibility of fracture growth beyond the target shale formations.

Microseismic (MS) data analysis has been used to estimate L and H in shale reservoirs. The pressure waves created by fracturing operations are monitored by geophones installed at

wellhead or in offset wells. These waves are then interpreted to estimate L and H. MS events detected away from the well have been used to infer maximum values of L and H. MS data analysis shows that the maximum L and H can be over 1 km in the Marcellus, Barnett, Woodford, Eagle Ford, and Niobrara shales (Davies et al., 2012; Warpinski et al., 2012; Fisher and Warpinski, 2012; Flewelling et al., 2013). However, the results from interpretation of MS data may have high uncertainties in L and H since MS data represent stress deformation, and may not necessarily represent the creation of conductive pathways for flow communication (Lacazette and Geiser, 2013; Maxwell and Norton, 2012; Maxwell et al., 2015; Fjar et al., 2008).

An increasing number of frac-hits have been reported in shale reservoirs in recent years (Appendix C.1 and Table C.1). Frac-hit is indicated by an observable pressure increase in a monitoring well while fracturing a nearby well (Brownlow et al., 2016). The lateral and vertical well spacing between frac-hit wells can be above 1 km and 150 m, respectively (see Fig. 5.1). However, it is unclear if the pressure increase monitored in frac-hit represents the creation of conductive pathways for fluid communication. Also, fractures tend to close during water and hydrocarbon production due to the drop in fracture pressure (Warpinski et al., 2012; Lacazette and Geiser, 2013). Therefore, the next question is: How long can the created conductive pathways sustain for fluid communication after the fracturing processes?

This chapter investigates fracture propagation in 4 well pads (Pads A to D) drilled in the Horn River shales in the Western Canadian Sedimentary Basin (Fig. 5.2a). As illustrated in Fig. 5.2b, the stages of all wells in a pad being fractured in a sequence. The well pads were completed in three shale members: Muskwa (MU), Otter Park (OP), and Evie (EV). These three shale members are overlain by Fort Simpson shale (Fig. 5.2b). First, frac-hits between wells in the lateral and vertical directions are analyzed to investigate the pressure interference during the fracturing process. MS data are analyzed to map the fracture propagation beyond the lateral and vertical well spacing of frac-hit wells. Tracer-injection results are then analyzed to identify the flow communications between frac-hit wells. Also, production interference data are analyzed to illustrate how long flow communications last after fracturing treatment.

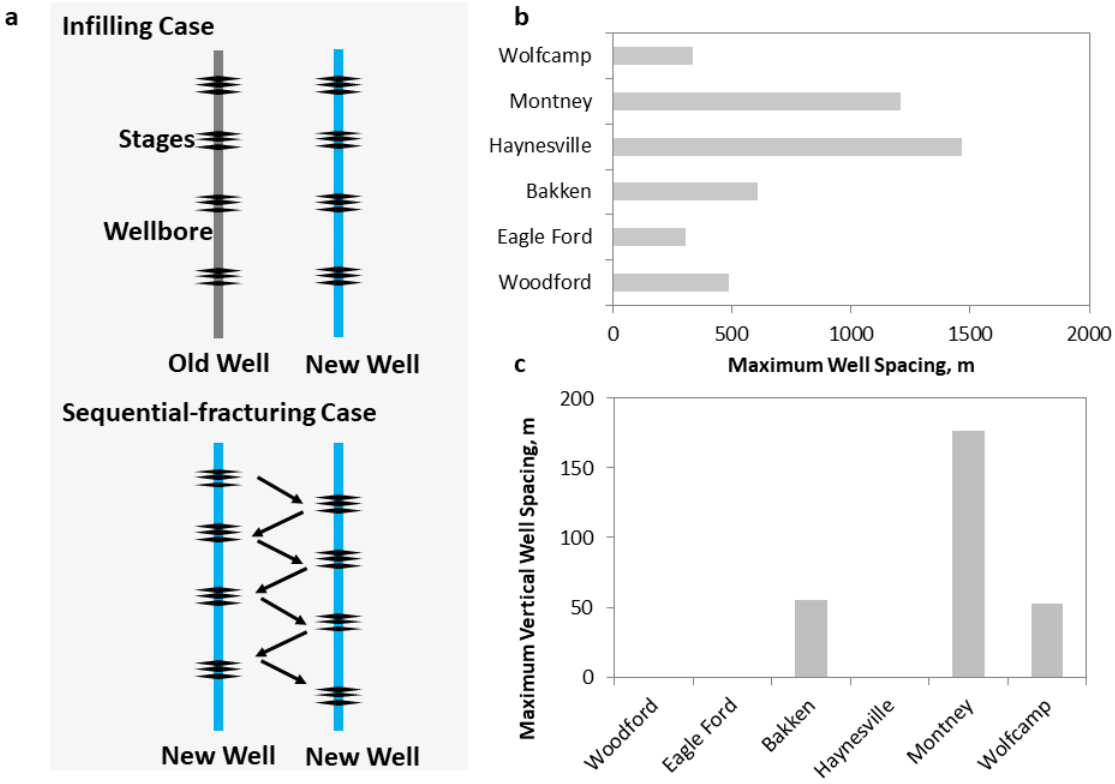

Fig. 5.1: (a) Schematics illustrate the concept of infill and sequential fracturing: Infill represents a new well is drilled adjacent to an existing well. Sequential fracturing represents that the first stages of wells are being fractured in a sequence before moving to their second stages. The arrow represents the fracturing sequence; (b) Distribution of maximum lateral well spacing between frac-hit wells reported in Woodford, Eagle Ford, Bakken, Haynesville, Montney, and Wolfcamp Formations; (c) Distribution of maximum vertical well spacing between frac-hit wells reported in Bakken, Montney, and Wolfcamp Formations (Table C.1 in the Appendix provides the data for each formation).

5.2 Methods and Materials

Fig. 5.2c describes the general operational timeline for 52 target wells in Pads A to D. Changes in well pressure during HF are recorded in fracturing and offset wells for frac-hit evaluation. Similarly, MS data are recorded by geophones installed in offset wells while fracturing these wells. Tracers (chemical ions and proppants coated with radioactive materials) are injected with water during HF. Gamma-ray logs are run during well shut-in to detect proppant transport between wells. Concentration of chemical tracers, rate and pressure are recorded during flowback.

Frac-hits. The results of 1009 frac-hits in Pads A to D are statistically analyzed to investigate pressure interference during the fracturing process. Frac-hit frequency and average pressure increase per frac-hit are then compared with lateral and vertical well spacing (S_L and S_H).

MS surveillance. This chapter statistically analyzed the fracture length (L_{MS}) and height (H_{MS}) estimated from MS data of 243 stages of 26 wells in Pads A, C and D (Appendix C.4 describes MS design).[1] P10, P50, and P90 values of L_{MS} and H_{MS} are calculated using MS event locations. L_{MS} and H_{MS} are then compared with average S_L and S_H from frac-hit analysis.

Tracer surveillance. A mixture of chemical tracers and water is injected into 27 wells in Pads A, C and D during HF. Similarly, proppants coated with radioactive materials are injected into 3 wells in Pad A and 4 wells in Pad D. Chemical tracer concentrations in Pads A and D are analyzed to investigate water flow between frac-hit wells. Gamma-ray logs are run in 8 wells to detect proppant transport between frac-hit wells during shut-in. Previous studies reported a relatively high content of H_2S (average *7 mol%*) in EV gas samples but negligible amounts in MU and OP gas samples (Drummond, 2018). In this study, H_2S is used as a natural tracer and its content in gas samples is recorded during flowback. The vertical gas flow between frac-hit wells is then investigated by comparing the H_2S content in MU, OP and EV wells.

Production interference. Flowback and post-flowback production data in Pads A to D are analyzed to identify well interference and evaluate how long the connecting pathways last after HF. This analysis compares pressure and rate changes in offset wells after creating a pressure pulse due to shut-in or re-opening of other wells.

---

1. The interpretations of MS data are obtained from the industry operator.

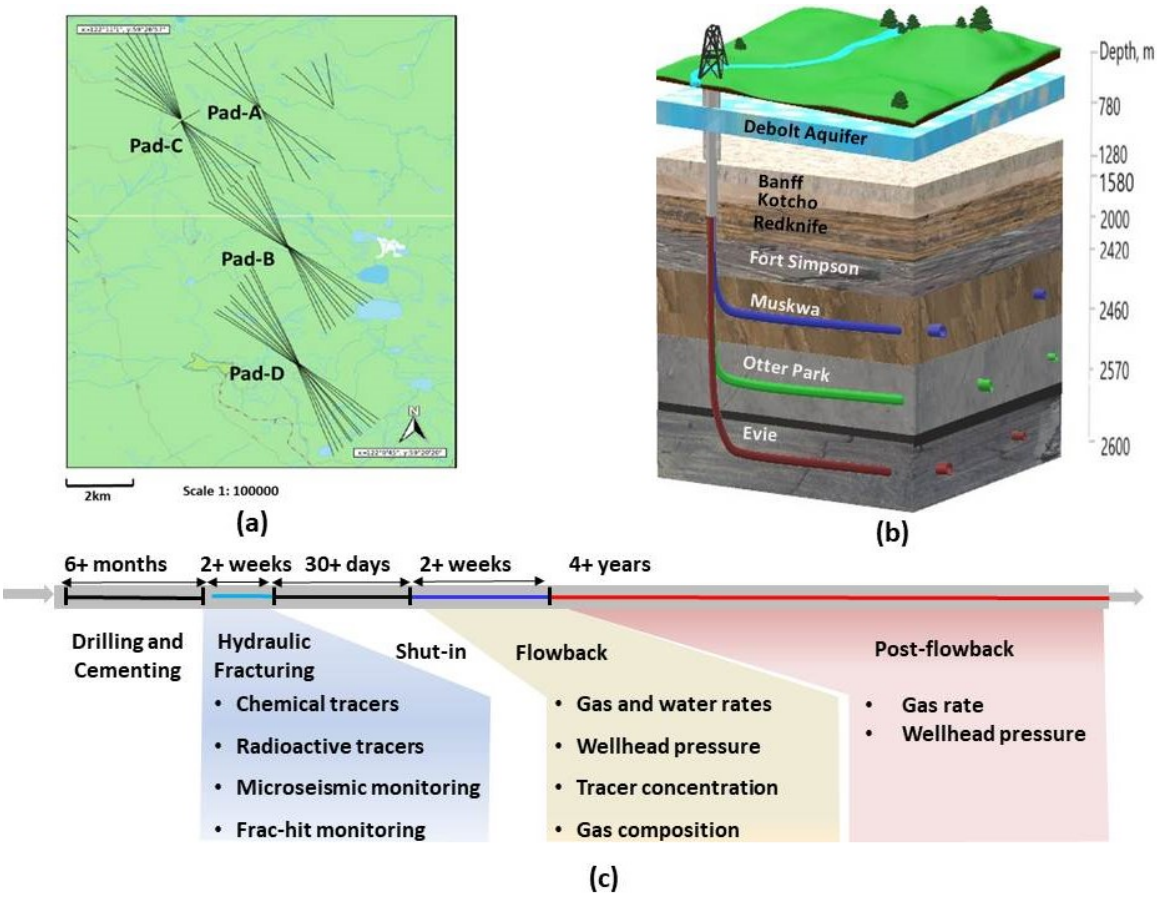

Fig. 5.2: (a) Location of Pads A, B, C and D drilled in Horn River shales, Western Canadian Sedimentary Basin (generated by MapPlace, 2018); (b) Sectional view of wellbore profiles with their relative positions in MU, OP and EV shale members. The average vertical spacing between wells in MU and OP members is 65 m and that between wells in MU and EV members is 130 m. Wells in MU, OP and EV members are in green, blue and red respectively; (c) General operational timeline for developing target shale gas wells (modified from U.S. Environmental Protection Agency, 2016). Chemical tracers are dissolved in fracturing water and sampled during flowback. Proppants are coated with radioactive tracers and detected by gamma-ray logs during well shut-in. Microseismic and frac-hit data are recorded during hydraulic fracturing. Pressure and rate data are measured during flowback and post-flowback processes.

5.3 Results

5.3.1 Frac-hits

Fig. 5.3a illustrates the concept of active and monitor wells during a frac-hit using vertical and lateral spacings (S_H and S_L). Overall, 1009 frac-hits are observed in monitor wells while

fracturing 631 stages of 28 active wells in Pads C and D (Table C.4 provides frac-hit data of Pads A and B).

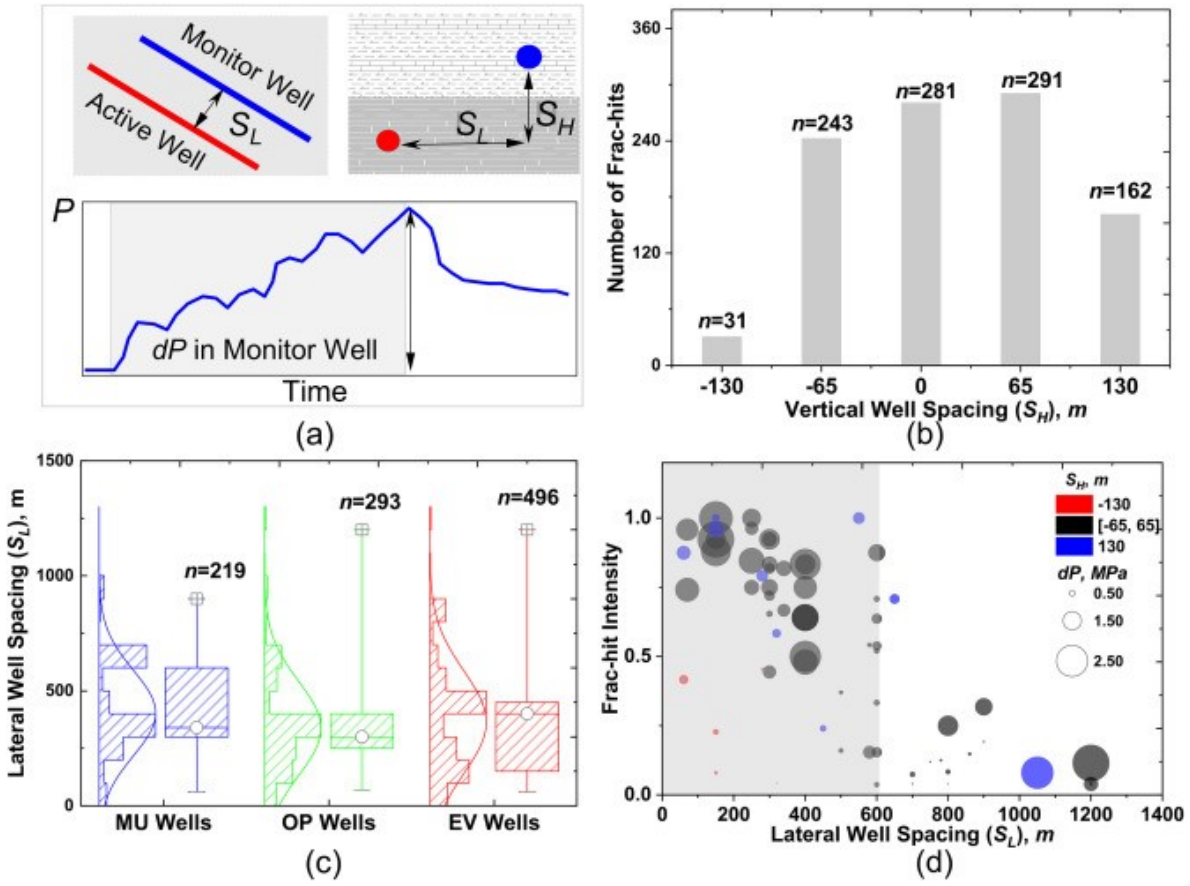

Fig. 5.3: (a) Schematic illustration of monitor and active wells for a frac-hit. S_L and S_H represent lateral and vertical well spacing between monitor and active wells. dP is pressure increase in monitor wellhead while fracturing an active well during frac-hit; (b) S_H distribution between active and monitor wells. S_H <0 means an active well is in another layer above a monitor well. S_H =0 means both monitor and active wells are in the same layer; (c) S_L boxplot while fracturing MU, OP, and EV wells. Each box shows median, 25th and 75th percentiles, whisker represents 90th percentile, and individual points show outliers; (d) Percentage of frac-hit per well versus S_L. The size of bubbles represents average dP per frac-hit. Red, black, and blue colors represent frac-hit with S_H =-130 m, 65 m≤ S_H ≤65 m, and S_H =130 m respectively.

Fig. 5.3b shows the distribution of 1009 vertical frac-hits. There are more vertical frac-hits (S_H ≠0) and intensive fracture propagation in the upward direction (S_H >0). Over 10% of upward, vertical frac-hits (n =162 of 1009) were detected on monitor wells while fracturing active wells 130 m below.

Fig. 5.3c shows the distribution of 1009 lateral frac-hits. Less than 1% of frac-hits (n = 9 of 1009) occur in well pairs over 1000 m apart laterally. The average and maximum S_L between frac-hit wells is about 360 m and 1200 m, respectively. In addition, the results show relatively more frac-hits while fracturing EV wells compared with OP and MU wells.

Fig. 5.3d shows frac-hit frequency per well (F) and average pressure increase per frac-hit (dP) versus S_L for 10 wells in Pad D. F is the normalized frequency of frac-hits on each monitor well when fracturing all stages of the active wells. The frequency of frac-hits on each monitor well is normalized by the total number of stages of active wells. F generally decreases with S_L. Well pairs with S_L < 600 m (shaded zone in Fig. 5.3d) have relatively high F values. Also, dP generally decreases with increasing S_L. In Pad D, dP varies from 0.12 to 3.56 MPa, and can go as high as 8.6 MPa during a frac-hit in Pad B (Table C.4).

5.3.2 Microseismic Data

Fig. 5.4a and b illustrate the concepts of P10, P50, and P90 values of MS-inferred fracture length (L_{MS}) and height (H_{MS}), which are determined by interpreting the location of the MS events (Section C.4 in Appendix C). The relative error in the location of MS events is 20 to 40 m and 10 m in the lateral and vertical directions, respectively.

Fig. 5.4c shows P10, P50, and P90 values of L_{MS} for 243 stages of wells in Pads A, C, and D. The minimum P90 value of L_{MS} is about -1 km. The maximum P10 value of L_{MS} is about 1.2 km. This means over 80% of MS events occur less than 1.2 km from the wellbore. In Fig. 5.5a, the statistical results of L_{MS} show that most MS events occur within -212±193 m < L_{MS} < 289±236 m. Also, Fig. 5.4c compares L_{MS} with average S_L between frac-hit wells. It shows that about 10% of fracture stages (n = 25 of 243) have higher P50 value of L_{MS} than average S_L. The maximum P10 value of L_{MS} approximates to the maximum S_L in Fig. 5.3c.

Fig. 5.4d shows P10, P50, and P90 values of H_{MS} for 243 stages of wells in Pads A, C and D. Maximum P10 value of H_{MS} is 164 m, indicating that less than 10% of MS events occur 164 m above wellbore. In Fig. 5.5b, the statistical results of H_{MS} show that most MS events occur within

-71±74 m < H_{MS} < 59±37 m. In Pad D, about 4.6% of MS events occur in Fort Simpson shale member during the hydraulic fracturing processes of MU, OP and EV wells (see Fig. 5.6). About 90% of fracture stages (n = 57 of 63) for EV wells have P10 value of H_{MS} above S_H = 65 m. Over 65% of fracture stages (n = 41 of 63) for OP wells have P90 value of H_{MS} below S_H = -65 m, and over 55% of them (n = 35 of 63) have P10 value of H_{MS} above S_H = 65m.

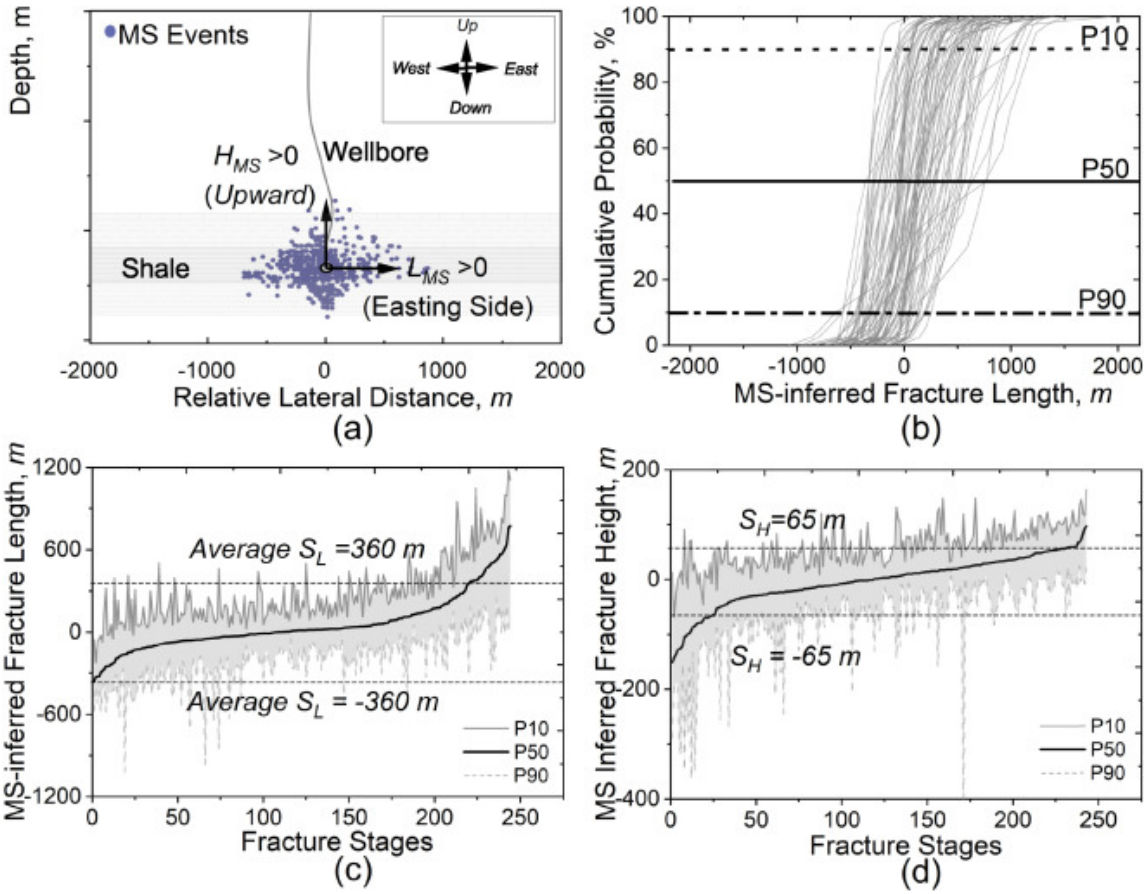

Fig. 5.4: (a) Schematic illustration of MS-inferred fracture length (L_{MS}) and fracture height (H_{MS}) from MS data analysis. Positive and negative L_{MS} values represent the relative distance of MS events from wellbore eastwards and westwards respectively. Similarly, positive and negative H_{MS} values represent the relative distance of MS events upwards and downwards respectively; (b) Lateral distribution of MS events for 75 fracture stages of wells in Pad C. P10, P50, P90 values of L_{MS} is the distance of 90%, 50%, and 10% of MS events away from wellbore; P10, P50, P90 values of (c) L_{MS} and (d) H_{MS} from MS data analysis of 243 stages in Pads A, C and D. L_{MS} and H_{MS} are sorted from minimum to maximum P50 values of fracture length and height. The dashed lines represent average lateral and vertical well spacing between frac-hit wells.

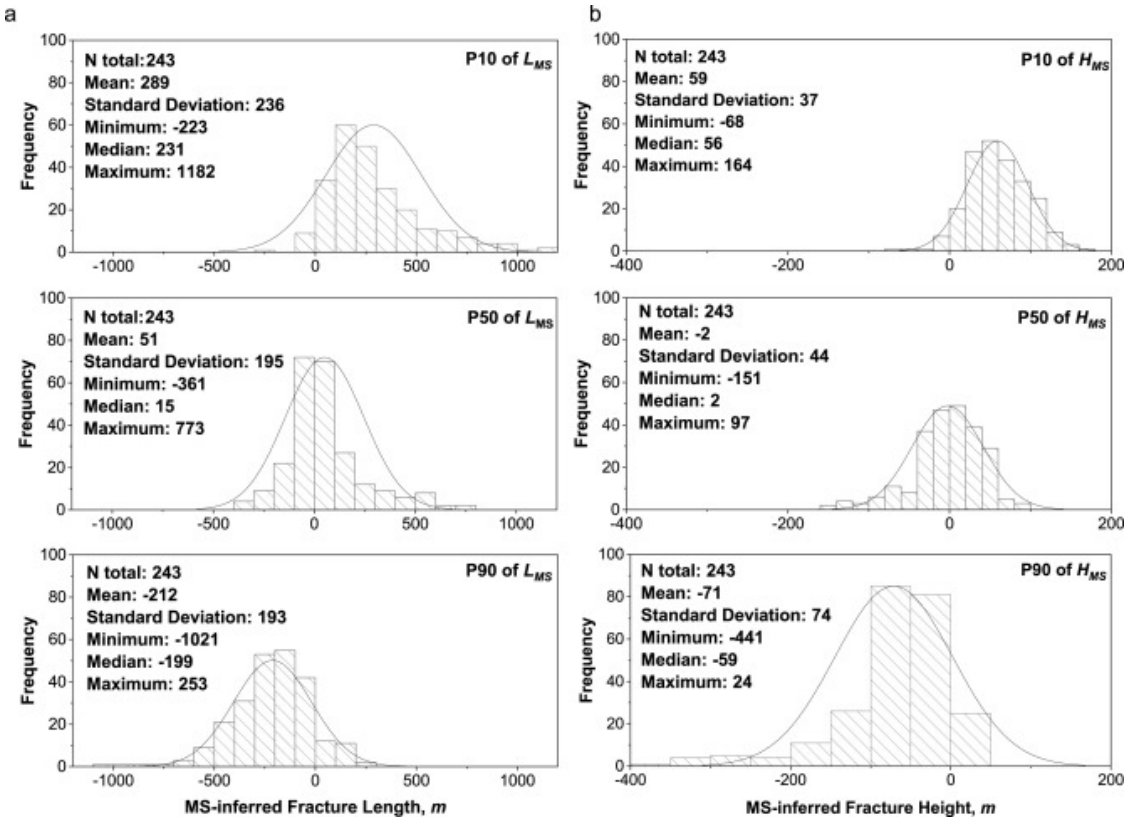

Fig. 5.5: Statistical results of P10, P50, P90 values of MS-inferred (a) fracture length and (b) fracture height for 243 stages of 26 wells in Pads A, C, and D.

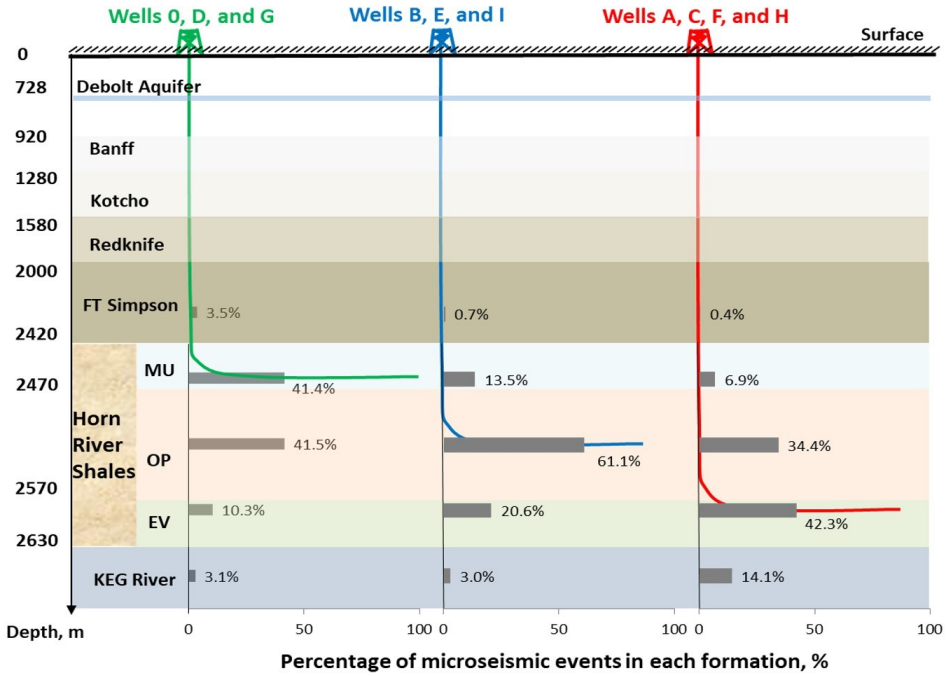

Fig. 5.6: Distribution of MS events in the vertical direction for 118 stages in 10 wells of Pad D.

5.3.3 Tracer Data

5.3.3.1 Chemical Tracers

Fig. 5.7a illustrates the injection design of chemical tracers for Pad D (Section C.5 in the Appendix provides detailed information about the tracer design for the target wells). Fig. 5.7b compares chemical tracer concentration in flowback water samples of Wells 0, E and A in Pad D. The results show a relatively high concentration of tracers from neighbouring wells in the lateral and vertical directions. For example, tracers injected into an OP well (Well E) are produced from an MU well (Well 0) 860 m away laterally (this could reach 1170 m in Pad A, see Fig. C.7). The tracers injected into an EV well (Well A) are produced from an overlying MU well (Well 0) in Pad D. In addition, analyzing the tracer data from Wells 0, A, and E in Pad D shows immediate tracer breakthrough from their neighbouring wells as flowback starts (Fig. C.5).

Fig. 5.7b shows a relatively high tracer concentration from neighbouring Wells F and G in Pad D occurring in Well E. The mass fraction of tracers injected into Wells F and G is higher than that injected into Well E (Fig. C.5). In Well E's flowback water sample, the tracer injected into Well E only accounts for 22% of total mass of 6 tracers. This suggests that most of Well E's produced water is from the fracturing water injected into other wells in Pad D. Also, the mass fraction of tracers injected into Well F increases during Well E's flowback (Fig. C.5). This indicates that fracturing water injected into Well F consistently flows into Well E during flowback.

5.3.3.2 Radioactive Tracers

Fig. 5.7a illustrates the flow direction of radioactive materials coated on proppants injected into Wells F, H and I in Pad D (Fig. C.7 shows similar results in Pad A). During well shut-in, tracer proppants from an EV well (Well F) are detected by gamma-ray logs in an MU well (Well G). Also, tracer proppants from EV well (Well F) are detected by gamma-ray logs of an offset EV well (Well H) 400 m away. In Pad A, tracer proppants from an OP well are detected by gamma-ray logs of an offset OP well 780 m away.

5.3.3.3 Natural Tracers

Fig. 5.7c compares H_2S concentration in 41 EV, MU, and OP wells to investigate the vertical gas flow between MU, OP and EV wells. During flowback, H_2S is identified in all 395 gas samples from 17 EV wells in Pads B, C and D. H_2S concentration in these wells varies from 17 to 550 ppm. Previous studies suggest negligible content in MU and OP shale gas samples (Drummond, 2018; Oil and Commission, 2014; BCOGC, 2019). Similarly, H_2S is not reported in gas samples from wells in Pad A (which has no EV wells). However, about 39% of gas samples (n =228 of 589) from MU and OP wells in Pads B, C and D contain H_2S, with concentrations varying from 1 to 100 ppm. H_2S produced from these MU and OP wells is expected to be sourced from underlying EV shale member.

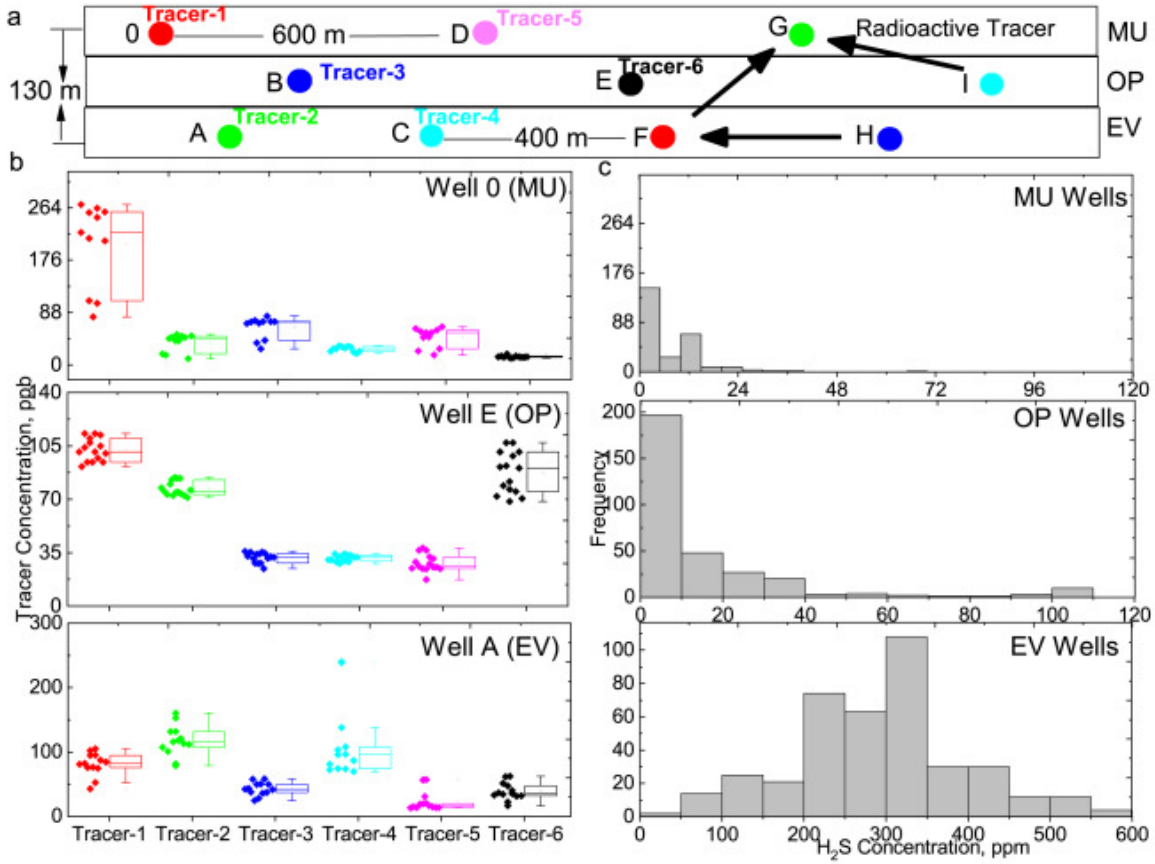

Fig. 5.7: A cross sectional view of wells and formations illustrating tracer-injection design for Pad D. Six types of chemical tracers (Tracer-1 to 6) are injected into 10 wells during hydraulic fracturing. All stages of each well are treated with a single type of chemical tracer. The arrows represent the flow direction of radioactive tracers between wells (see Fig. C7 in the Appendix for the response of radioactive tracers detected by gamma-ray logging). Tracer-1 to 6 are marked by 6 colors; (b) Boxplots of tracer concentration for three wells in Pad D: Well 0 (upper), Well E

(middle), and Well A (lower). Each color represents the type of tracers injected into Pad D; (c) Comparing H_2S concentration in 984 gas samples collected from 41 EV, MU, and OP wells in Pads B, C, and D.

5.3.4 Production Interference

Fig. 5.8a shows an example of well interference in Pad D after 1.7 years of post-flowback production. A pressure increases of 110 kPa is observed in an OP well (Well E) after shutting offset Well F (Fig. C.13). Similar interference occurs in Pads A and B during post-flowback (see Fig. 5.9 and Fig. C.12). The maximum *L* between wells with production interference is about 450 m.

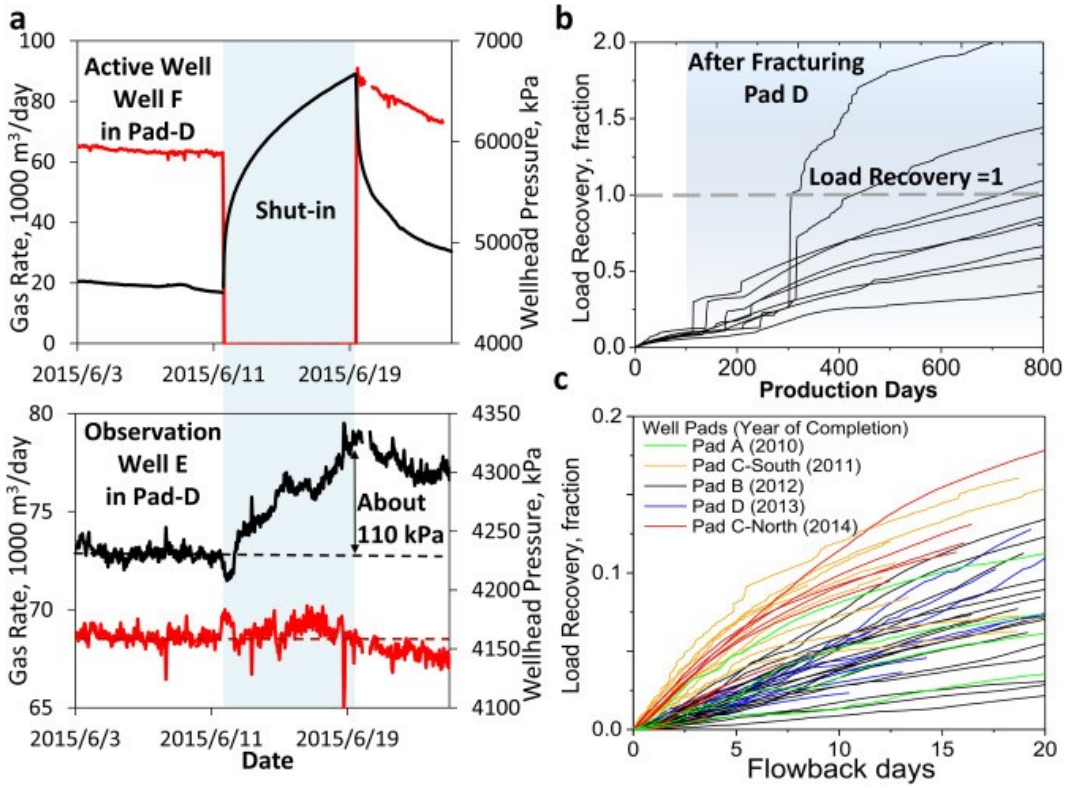

Fig. 5.8: (a) Pressure increase of about 110 kPa in Well E after shutting Well F, suggesting well interference after 624 days of production in Pad D; (b) Sudden increase in load recovery profiles of 9 wells in Pad B after hydraulic fracturing of wells in Pad D; c) Relatively largevariation in load recovery of 52 wells in Pads A, B, C, and D (Wells in the target 4 pads are marked by different colors).

Fig. 5.8c compares the load recovery of 9 wells in the south side of Pad B over a post-flowback period of 800 days. Load recovery is the ratio of produced water volume to the total injected

water volume. These wells experience a sudden increase in load recovery and water rate after hydraulic fracturing of wells in Pad D, about 1 km away (see Fig. C.14). Consistently, we observe that the load recovery of 4 wells in Pad B exceeds 1 after 800 days of production. However, formation water saturation in these shale members is at sub-irreducible conditions (see Section C.2 in the Appendix). The load recovery of wells in Pads A, C, and D are generally below 50% after 5 years of production (see Figs. C.15 and C.16). Load recovery values of higher than 1 in wells of Pad B suggest water production from other fracturing operations.

Production interference is also identified during flowback (see Fig. C.10). The lateral spacing of between wells undergoing interference can be up to 860 m. Also, the pressure response can be over 1000 kPa after opening an offset well for flowback. Fig. 5.8b shows a large variation (3-13%) in flowback load recovery of 52 wells completed in Horn River shales. After 20 days of flowback, the load recovery of 52 wells varies from 3% to 18%. Comparing the load recovery with flowback sequence in Pads B, C, and D shows a relatively higher load recovery of the wells which are opened earlier for flowback (see Fig. C.17).

5.4 Comparative analysis

In this section, we present a comparative analysis of well communication identified by frac-hit, chemical and radioactive tracer, and production interference.

Fig. 5.9 shows five cases (Case *I* to *V*) of well communication identified by different methods including frac-hit, radioactive and chemical tracer, and interference tests. In Case *I*, we identify flow communication of chemical tracers and production interference between two frac-hit wells in Pad D (see Fig. 5.7, Fig. 5.8a and Table C4 in the Appendix). In Cases *II* and *III*, two pairs of wells in Pads D and A are identified with flow communication of chemical and radioactive tracers and production interference. In Cases *IV* and *V*, flow communication of chemical tracers and production interference are identified for two pairs of frac-hit wells in Pad D.

Fig. 5.9 shows relatively close values of maximum L between wells with frac-hit and chemical tracer communication (1200 and 1170 m, respectively). The maximum L for frac-hit is observed

for a pair of EV wells in Pad D, and the maximum *L* for chemical tracer communication is observed for two wells from MU and OP members in Pad A. In Fig. 5.9, the maximum *L* between wells showing flow communication of radioactive tracers is 780 m, which is relatively close to the maximum L between wells showing production interference (860 m).

In Fig. 5.9, Case I shows the longest duration of well communication occurring to wells in Pad D after 624 days of production. In Case *I*, we also identify production interference between these wells after about 390 days of production, demonstrating the consistency of the interference results

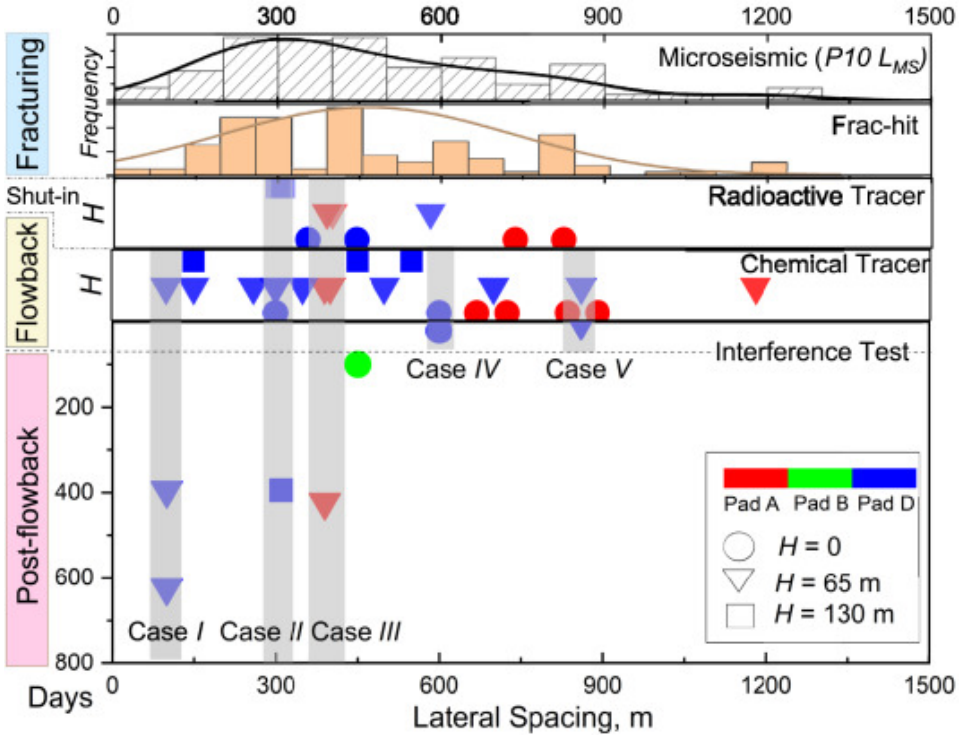

Fig. 5.9: Temporal and spatial distribution of well communication among wells in the target pads identified by different surveillance methods including frac-hit, chemical and radioactive tracers, and production interference. Histogram distribution of P10 values of MS-inferred fracture length is included here for comparison. The vertical gray bars represent five cases (Case *I* to *V*) which consistently show well communication identified by different methods. Circle, triangle, and square markers represent the wells with a vertical spacing of $H = 0$ (wells completed in the same layer), H =65, and H =135m, respectively. Red, green, and blue colors mark the wells in Pads A, B, and D, respectively.

5. 5 Discussions

5.5.1 Does Frac-hit Imply Flow Communication?

Breakthrough of chemical tracers from offset wells in active wells once flowback starts (see Fig. C.5) indicates the existence of pathways between frac-hit wells. Detection of radioactive tracers from offset wells in active wells suggests that the pathways are permeable enough for proppant flow. Detection of H_2S in gas samples of MU wells which usually have negligible H_2S suggests that these pathways allow vertical gas flow between frac-hit wells. We thus conclude that fracture-like pathways allowing flow communication of water, proppant, and gas exist between frac-hit wells.

In this study, frac-hit is identified by an observable pressure increase in a monitoring well while fracturing an offset well. It is possible that the pressure increase can be induced by poro-elastic effects (Couples et al., 2018; Couples, 2019; Lacazette and Geiser, 2013). Therefore, fluid flow may not necessarily occur between the frac-hit wells. However, this study has limited flowback tracer data to compare with frac-hit results. Future studies should further verify the relationship between frac-hit and flow communication where more chemical tracer data are available.

5.5.2 How Far Can Fractures Go?

The maximum L between wells with flow communication of chemical tracers is 1170 m, suggesting that fractures can connect wells over a lateral distance of 1 km. The results of radioactive tracers indicate that the length of conductive fractures connecting wells can reach 780 m. In the vertical direction, flow communication of chemical and radioactive tracers occurs to several MU and EV wells, suggesting that conductive fractures can connect wells with H=130 m completed in two layers. As wells in the target pads were fractured in a sequence (see Fig. 1), fractures of one stage in an active well may propagate into pre-existing hydraulic fractures, which are created by fracturing of an offset well. In addition, the intensive well communication over long distances is possibly due to the reactivation of faults or natural fractures, which is supported by the low b-values (close to 1) from MS data analysis (see Fig. C.4) (Yousefzadeh et al., 2019). Faults have been reported to intersect wells in the target pads (Hurd et al., 2012; Latimer et al., 2017; Ling and Barker, 2013; Reine and Dunphy, 2011), and thus may provide conduits for long-distance well communication.

MS data interpretation suggests low probability (10%) for lateral fracture extension beyond 1200 m, and upward fracture growth 164 m above wellbore. According to Lacazette and Geiser (2013), MS data interpretation may underestimate fracture height due to the pre-existing natural fractures. However, limited MS events (<5%) suggest a low chance of vertical fracture growth into overlying Fort Simpson shale, which is characterized as clay-rich shale with low brittleness index (Roche et al., 2015). There is also a relatively large stress contrast (Roche et al., 2015) and modulus contrast (Dunphy and Campagna, 2011) between Fort Simpson and Horn River shale members. In addition, fracture length and height might be overestimated by MS data interpretation due to indistinguishable sources of induced microseismicity, which can be caused by shear failure, fault slip/reactivation, and pore-pressure diffusion in addition to rock tensile failure (Fjar et al., 2008; Maxwell and Norton, 2012; Maxwell et al., 2015).

5.5.3 How Long Does Well Communication Last after Fracturing Operation?

High mass fraction of tracers from offset wells in active wells suggests well communication during flowback. Therefore, wells opened earlier in a flowback sequence will drain some water from shut-in wells in a pad. Well communication leads to large variations in load recovery of the target wells and is a factor controlling the fate of fracturing water.

In this study, production interference is generally identified within 1 h after the shut-in or re-opening of active wells. This is abnormal because the ultra-low permeability of shale rocks should delay this communication for several hours or even days (Awada et al., 2016). Hence, well communication here is most likely through induced fractures and not rock matrix. Also, pathways connecting communicating wells can remain open even after about 1.7 years of fluid production (see Fig. 5.9a). This is possibly due to proppant flow between the communicating wells, preventing complete fracture closure during flowback and post-flowback periods.

5.5.4 How Does Well Interference Impact Flowback Data Analysis?

The diagnostic plot of gas-water ratio (GWR) versus cumulative gas volume (G_p) has been used to identify fracture cleanup during flowback by previous studies (Ilk et al. 2010; Clarkson and

Williams-Kovacs 2013; Zhang and Ehlig-Economides 2014). As shown in Fig. 5.10, however, fracture cleanup is observed as half-slope only in late-opened wells. The drainage of fracturing water by early-opened wells decreases the water saturation in the fracture network of late-opened wells, leading to an earlier fracture cleanup of later-opened wells during flowback.

Xu et al. (2015) reported two regions in the diagnostic plot of *GWR*. The early and late regions are characterized by negative and positive *GWR* slopes, respectively. They developed a closed-tank material balance model to estimate effective fracture pore-volume using flowback data during the early region. However, the negative *GWR* slope is not observed in the wells with interference effects during their early flowback periods (see Fig. 5.10). One may further expect that the closed-tank material balance model is not applicable to estimate fracture volume for these wells with interference effects.

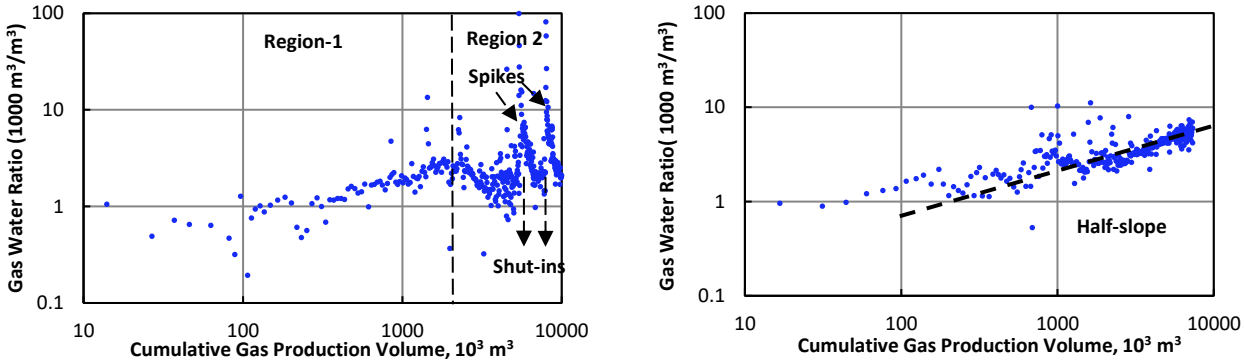

(a) (b)

Fig. 5.10: (a) Log-log plot of *GWR* versus G_p for an early-opened well in Pad D generally showing two regions: Region 1 is represented by an increasing trend of *GWR*; Region 2 is represented by a downward deviation from the increasing trend of *GWR*. The second region shows several spikes of high *GWR* due to shut-ins; (b) Log-log plot of *GWR* versus G_p for a late-opened well in Pad D shows an approximate half-slope.

In Fig. 5.11, rate-decline analysis of wells with interference effects shows a relatively higher estimated V_{ef} for early-opened wells compared with that for late-opened wells. V_{ef} of several wells estimated by rate-decline analysis can be even larger than the total injected water volume (see Fig. 3.12b). These results suggest that V_{ef} estimated by rate-decline analysis may not be

representative for the fracture volume created by the fracturing operation of an individual well. Flowback models considering the interference effect are recommended for future flowback data analysis.

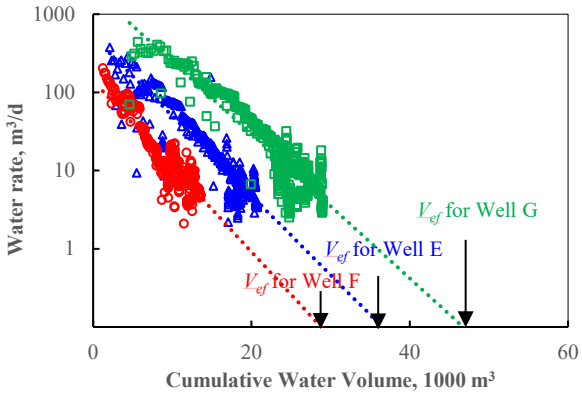

Fig. 5.11: Rate-decline analysis of water flowback data for three wells in Pad D showing a relatively higher estimated effective fracture volume for an early-opened well (Well G) than that for late-opened wells (Wells E and F).

5. 6 Limitations

5.6.1 Vertical Fracture Propagation

The analysis of tracer and production data confirmed that wells with a vertical spacing of 130 m can be inter-connected through fractures, which allow flow communication of gas and water between the wells. This study further reduced the uncertainties in vertical fracture propagation by analyzing MS data analysis, similar to a previous study by Davies et al. (2012), and indicated a relatively low probability of fracture height growing beyond 164 m. However, it remains uncertain whether fractures can propagate beyond this vertical distance in the target wells due to the uncertainties in MS data interpretation. Several new models have recently been developed to determine the fluid-injection-induced seismicity (Shapiro and Dinske, 2009; Rozhko, 2010). The accuracy in fracture-length/height estimation can then be improved through applying these new models to interpret MS data by considering the deformation effects, natural fractures, and interactions between fluids and formation rock.

5.6.2 Well Communication

Hourly wellhead pressure data were analyzed to identify well communication between the target wells. Well communication may be masked by wellbore effects such as fluid re-distribution or moving fluid interface, especially during early production period with multiphase flow of water and gas. The low frequency of pressure data may also limit identification of well communication. High-frequency bottomhole pressure data are thus recommended to identify well communications in multi-well pads completed in unconventional reservoirs. In addition, this study mainly presented a qualitative analysis of frac-hit, tracer, and production data to identify well communication in 4 Horn River Pads. It is of great interest to quantify well connectivity during the fracturing treatment, flowback, and post-flowback periods.

5. 7 Conclusions

This chapter presented a comparative study of frac-hit, microseismic, tracer and production data from 52 Horn River wells to investigate the extent of fracture propagation during hydraulic fracturing, evaluate well communication during frac-hit and estimate the duration of this well communication. The key conclusions are summarized as follows:

(1) Frac-hit wells can communicate through fracture-like pathways. The results of chemical, natural, and radioactive tracers indicate that these pathways allow the flow of water, gas, and proppant, respectively.

(2) Lateral and vertical well communications occur within distances above 1 km and up to 130 m, respectively. Analyzing microseismic data suggests a low probability for lateral fracture extension beyond 1200 m, and upward fracture extension 164 m above wellbore in the target pads.

(3) Well communication may last for over 1.7 years possibly due to proppant flow. The existence of proppants and fracture-surface roughness can prevent complete fracture closure during flowback and post-flowback processes.

Chapter 6 Conclusions and Recommendations

6.1 Conclusions

The thesis presented qualitative and quantitative analyses of flowback data to understand the fluid flow behaviors, characterize fracture volume, and predict water recovery for multi-fractured horizontal wells completed in tight and shale reservoirs. It also studied well interference in multi-well pads through a combined analysis of frac-hit, microseismic, tracer, and production data. The key findings from this thesis can be summarized in the following subsections:

6.1.1 Single-phase Flowback Data Analysis

- Jones et al. (2014) reported the behavior of flattening pressure in tight oil/gas wells completed in Woodford wells during the single-phase flowback period. In Chapter 2, this study constructed diagnostic plots to understand the physics of flattening pressure for these Woodford wells. The results indicate that the flattening pressure represents the hydrocarbon breakthrough from matrix into the effective fracture network, and that the fracture system can be treated as a tank before pressure flattening. Also, comparative analysis suggests that the duration of single-phase flowback period is related to initial reservoir pressure and hydrocarbon type.
- In Chapter 2, this study applied a previous model (Abbasi et al. 2012, 2014) on single-phase flowback data to estimate effective fracture volume for seven Woodford tight oil/gas wells. The estimated effective fracture pore-volume is generally larger than final load recovery volume and less than total injected water volume. Comparative analysis supports that most of the effective fractures are unpropped, and host the non-recovered fracturing water (Sharma and Manchanda 2015).
- In flowback data analysis, fracture compressibility is one key input which is generally unknown or hard to estimate. This study proposed a procedure to estimate fracture compressibility using diagnostic fracture injection test data. The estimated fracture compressibility varies from 10^{-5} psi^{-1} to 10^{-4} psi^{-1}, and is larger than the matrix compressibility (10^{-6} psi^{-1}). The fracture compressibility estimated by the proposed

procedure is within the ranges reported in the literature (Ezulike et al. 2016; Jones 1975; Aguilera 1999; Williams-Kovacs and Clarkson 2013).

- This study also investigated the relationship between effective fracture pore-volume and various completion design parameters using Pearson-correlation method. The results suggest that total injected-water volume, gross perforated interval, and the number of clusters are among the key design parameters for an optimal fracturing treatment.

6.1.2 Flowback Water-rate Decline Analysis

- Bai et al. (2013) reported that the daily water production data from multi-fractured horizontal wells in the Wattenberg field can be fitted by a harmonic decline trend. In Chapter 3, this study carefully examined the hourly water flowback data from 172 multi-fractured wells completed in the Montney, Horn River, Eagle Ford, and Woodford Formations. The results suggest that water production primarily follows harmonic decline during the multiphase flowback period. The harmonic-decline trend can be extended to post-flowback period of up to 1000 days of production.
- Chapter 3 investigated the mechanisms of harmonic-decline trend in water flowback. Comparative analysis of rate and pressure data suggests that the harmonic decline in water flowback is primarily caused by relative permeability effects. In addition, this study demonstrates that the harmonic trend can be modeled by treating water flowback as a displacement process after hydrocarbon breakthrough from matrix into fractures.
- In Chapter 3, the harmonic-decline model was validated for predicting water recovery by comparing the measured and predicted values of water recovery. The results indicate that the harmonic-decline model can be used to estimate water recovery with reasonable accuracy, under the assumption that water is primarily produced from effective fractures.
- Field studies have investigated the fate of fracturing water in shale and tight formations through numerical simulations (Edwards et al. 2017; Ghanbari and Dehghanpour 2016). However, long-term water rate data were not available to verify these simulation results. To extend these studies, Chapter 3 investigated the fate of fracturing water by rate-decline analysis of water production data from four unconventional reservoirs. The results show that water recovery factor for the Eagle Ford, Horn River, Woodford, and

Montney wells is generally less than 50% even after 10 years of production. A large fraction of fracturing water is expected to be trapped in the tight and shale formations.

- The results show a relatively large variation in the predicted water recovery factor among wells completed in the Horn River, Montney, and Woodford wells. Comparative analysis suggests that the variation in water recovery factor may depend on various parameters such as reservoir pressure, formation water saturation, and inter-well communication.
- This study proposed a method to estimate effective fracture pore-volume by rate-decline analysis of water flowback data. In Chapter 3, this method was validated by comparing the effective fracture volume estimated by rate-decline analysis with that estimated by flowback tank models (Abbasi et al. 2014; Xu et al. 2017). In Chapter 4, this study demonstrated that the initial effective fracture pore-volume can be estimated by applying rate-decline analysis on water flowback data from 21 Montney and Eagle Ford wells. The results show a general positive correlation between the estimated initial effective fracture pore-volume and the total injected water volume.

6.1.3 Fracture-volume Loss

- The fracture volume estimated by the flowing material balance models (Adefidipe et al.2014; Xu et al. 2016; Abbasi et al. 2012, 2014) usually represents the initial volume of effective fractures at the onset of flowback. In Chapter 4, this study evaluated the change in fracture volume during flowback using a fracture compressibility relationship. The results show that the effective fracture pore-volume decreases during early flowback period, and generally remains constant during late flowback period.
- In Chapter 4, this study also demonstrates that choke size can impact the loss in fracture volume during flowback. Comparative analysis shows a relatively higher fracture volume loss for fastback wells compared with that for slowback well, indicating that slowback may lead to less loss in fracture volume compared with fastback. Analyses of the field data lead to an improved understanding of the factors controlling water flowback and effective fracture volume.

6.1.4 Well Communication

- Chapter 5 examined the lateral extent and vertical extent of fracture network through a comparative analysis of frac-hit, microseismic, tracer, and production data from 52 Horn River wells. The results indicate that lateral and vertical well communications occur within distances above 1 km and up to 130 m, respectively. This study improves the understanding of lateral and vertical fracture propagation in shale reservoirs during hydraulic fracturing.
- In recent years, frac-hit is commonly reported in wells completed in tight and shale reservoirs. It was unclear if the pressure increase monitored in frac-hit represents the creation of conductive pathways for fluid communication. In Chapter 5, tracer-injection results were analyzed to identify the fluid communications between frac-hit wells. The results indicate that wells communicate through permeable pathways during frac-hits. These pathways allow the flow of water, gas, and proppant. These findings are key to optimize well placement for sustainable hydrocarbon development.
- In Chapter 5, production interference data were analyzed to investigate the duration of flow communications. This analysis compared pressure and rate changes in offset wells after creating a pressure pulse due to shut-in or re-opening of other wells. The results indicate that well communication may last for over 2 years due to proppant flow which prevents fracture closure during flowback and post-flowback periods.
- Most techniques of flowback data analysis were developed for single-well cases. Interference effects were not considered in their applications for multi-well pads. In Chapter 5, the results indicate that interference effects contribute to a large variation in the water recovery during flowback. Also, this study demonstrates that the techniques of flowback data analysis for single-well case may not be applicable to estimate effective fracture pore-volume for wells in a pad with interference effects.

6.2 Recommendations

Below are some recommendations for applying the results from this work and extending this work for future research:

- There is a relatively high uncertainty in effective fracture pore-volume and fracture-volume loss estimated by flowback volumetric analysis. This uncertainty mainly comes

from uncertainties in fracture porosity and closure pressure used to calculate fracture compressibility. Future works should consider reducing the uncertainties in fracture compressibility.

- The relationships between effective fracture pore-volume and completion design parameters need further validation on a significant number of wells to demonstrate their applicability.
- Negligible water flow between matrix and effective fractures is assumed for water flowback data analysis. Water influx from matrix to fractures needs to be accounted for in wells with mobile formation water.
- During flowback, choke size for most tight and shale gas/oil wells changes with time. The relationship between fracture-volume loss and flowback choke-size strategy from this work is for wells with constant choke size throughout flowback. Further studies should investigate how changing choke size impacts fracture-volume loss during flowback.
- The wellhead pressure response for detecting well interference may be affected in some wells by phase redistribution in wellbore. High-frequency bottomhole pressure data are recommended to quantify well connectivity during flowback and post-flowback periods. Also, well interference effects should be considered during flowback data analysis in future studies.

Bibliography

Abbasi M. A. 2013. A comparative study of flowback rate and pressure transient behavior in multi fractured horizontal wells. MSc Thesis. University of Alberta, Edmonton, Canada.

Abbasi, M., Dehghanpour, H., and Hawkes, R.V. 2012. Flowback Analysis for Fracture Characterization. Presented at the SPE Canadian Unconventional Resources Conference, Calgary, Alberta, Canada, 30 October - 1 November. SPE-162661-MS. http://dx.doi.org/10.2118/162661-MS.

Abbasi, M. A., Ezulike, D. O., Dehghanpour, H. et al. 2014. A Comparative Study of Flowback Rate and Pressure Transient Behavior in Multifractured Horizontal Wells Completed in Tight Gas and Oil Reservoirs. Journal of Natural Gas Science and Engineering, 17, 82-93. http://dx.doi.org/10.1016/j.jngse.2013.12.007.

Adefidipe, O. A., Dehghanpour, H. and Virues, C. J. 2014. Immediate Gas Production from Shale Gas Wells: A Two-Phase Flowback Model. Presented at the SPE Unconventional Resources Conference, The Woodlands, Texas, USA, 1-3 April. SPE-168982-MS. http://dx.doi.org/10.2118/168982-MS.

Agrawal, S., & Sharma, M.M. 2015. Practical insights into liquid loading within hydraulic fractures and potential unconventional gas reservoir optimization strategies. Journal of Unconventional Oil and Gas Resources, 11, 60–74.

Aguilera, R. 1999. Recovery Factors and Reserves in Naturally Fractured Reservoirs. Journal of Canadian Petroleum Technology 38 (07): 15-18. PETSOC-99-07-DA. http://dx.doi.org/10.2118/99-07-DA.

Aguilera, R. (2016). Shale gas reservoirs: Theoretical, practical and research issues. Petroleum Research, 1(1), 10-26.

Ahn, C. H., Chang, O. C., Dilmore, R., & Wang, J. Y. 2014. A Hydraulic Fracture Network Propagation Model in Shale Gas Reservoirs: Parametric Studies to Enhance the Effectiveness of Stimulation. Presented at SPE/AAPG/SEG

Unconventional Resources Technology Conference, Denver, Colorado, USA, 25-27 August. SPE-2014-1922580-MS. http://dx.doi:10.15530/urtec-2014-1922580.

Alkouh, A., McKetta, S. and Wattenbarger, R. A. 2014. Estimation of Effective-Fracture Volume Using Water-Flowback and Production Data for Shale-Gas Wells. Journal of Canadian Petroleum Technology 53 (05): 290-303. SPE-166279-PA. http://dx.doi.org/10.2118/166279-PA.

Anderson, D. M., Thompson, J. M., Cadwallader, S. D., Sebastian, H., Gil, I., & Lee, P. (2016). Maximizing Productive Stimulated Reservoir Volume in the Eagle Ford - An Infill Case Study. SPE/AAPG/SEG Unconventional Resources Technology Conference, i. https://doi.org/10.15530/URTEC-2016-2430961

Andrew Kondash and Avner Vengosh.Water Footprint of Hydraulic Fracturing. Environmental Science & Technology Letters 2015 2 (10), 276-280.

Arps, J.J. 1945. Analysis of Decline Curves. Trans., AIME 1945 160, 228-247.

Arevalo-Villagran, J. A., Wattenbarger, R. A., and Samaniego-Verduzco, F. 2006. Some History Cases of Long-Term Linear Flow in Tight Gas Wells. *J Can Pet Technol* 45 (3): 31–37. PETSOC-06-03-01. https://doi.org/10.2118/06-03-01.

Arora, V., & Cai, Y. 2014. Us natural gas exports and their global impacts. Applied Energy, 120, 95–103.

Awada, A., Santo, M., Lougheed, D., Xu, D., & Virues, C. 2016. Is That Interference? A Work Flow for Identifying and Analyzing Communication through Hydraulic Fractures in a Multiwell Pad. SPE Journal (05): 1554 - 1566. SPE-178509-PA. http://dx.doi: https://doi.org/10.2118/178509-PA

Bai, B., & Carlson, K. (2016). Spatial Analysis of Horizontal-Shale-Well Water Production in the Wattenberg Field, (December), 2–6.

Bai, B., Carlson, K., Prior, A., & Douglas, C. Sources of variability in flowback and produced water volumes from shale oil and gas wells. Journal of Unconventional Oil and Gas Resources, 2015,12, 1-5.

Baker, R. O. Reservoir Management for floods--Part II. J. Cdn.Pet. Tech. 1998, 37 (1), 12-17. https://doi.org/10.2118/98-01-DA.

Balashov, V.N., Engelder, T., Gu, X., Fantle, M.S. and Brantley, S.L.. A model describing flowback chemistry changes with time after Marcellus Shale hydraulic fracturing. AAPG Bulletin. 2015, 99(1), 143-154.

Barree, R. D., Miskimins, J., and Gilbert, J. 2015. Diagnostic Fracture Injection Tests: Common Mistakes, Misfires, and Misdiagnoses. *SPE Prod & Oper* 30 (2): 84–98. SPE-169539-PA. https://doi.org/10.2118/169539-PA.

BCOGC. 2016. Oil and Gas Commission Data Downloads. Retrieved from https://www.bcogc.ca

B.C. Oil, G. Commission Horn River Basin Unconventional Shale Gas Play Atlas. BC Oil & Gas Commission Publications (2014)

Bearinger, D. 2013. Message in a Bottle: SPE 168891/URTeC 1618676, Prepared for presentation at the 2013 Unconventional Resources Technology Conference, August 12- 14, 2013, Denver, Colorado, USA.

Beaudoin, W. P., Khalid, S., Allison, J., and Faurschou, K.: Horn River Basin: A Study of the Behaviour of Frac Barriers in a Thick Shale Package Using the Integration of Microseismic Geomechanics and Log Analysis. Paper presented in the Canadian Unconventional Resources Conference, Society of Petroleum Engineers, SPE147510-MS, 2011.

Bello, R.O. 2009. Rate Transient Analysis in Shale Gas Reservoirs with Transient Linear Behavior. Ph.D. thesis. Texas A & M University, College Station, Texas.

Belyadi, H., Yuyi, J., Ahmad, M., & Wyatt, J. (2016, September 13). Deep Dry Utica Well Spacing Analysis with Case Study. Society of Petroleum Engineers. doi:10.2118/184045-M

Belyadi, H., Fathi, E., Belyadi, F. (2016). Hydraulic Fracturing in Unconventional Reservoirs: Theories, Operations, and Economic Analysis. Professional Publishing, Gulf.

Bing Bai, Stephen Goodwin, Ken Carlson, Modeling of frac flowback and produced volume from Wattenberg oil and gas field, Journal of Petroleum Science and Engineering, 2013, 108, 383-392.

Birdsell, D. T.; Rajaram, H.; Dempsey, D.; Viswanathan, H. S. Hydraulic fracturing fluid migration in the subsurface: A review and expanded modeling results Resour. Res. 2015, 51 (9) 7159-7188

Bommer, P., Bayne, M., Mayerhofer, M., Machovoe, M., & Staron, M. (2017, January 24). Re-Designing from Scratch and Defending Offset Wells: Case Study of a Six-Well Bakken Zipper Project, McKenzie County, ND. Society of Petroleum Engineers.

Bommer, Peter A., and Marcus A. Bayne. "Active Well Defense in the Bakken: Case Study of a Ten-Well Frac Defense Project, McKenzie County, ND." SPE Hydraulic Fracturing Technology Conference and Exhibition. Society of Petroleum Engineers, 2018.

Bowen, Z.H., Oelsner, G.P., Cade, B.S., Gallegos, T.J., Farag, A.M., Mott, N., & Kappel, W.M. 2015. Assessment of surface water chloride and conductivity trends in areas of unconventional oil and gas development—Why existing national data sets cannot tell us what we would like to know. Water Resources Research, 51(1), 704–715

Boyer, C., Clark, B., Jochen, V., Lewis, R., & Miller, C. K. (2011). Shale Gas: A Global Resource. *Oilfield review* 23.3 (2011): 28-39.

Brooks, R.H., & Corey, A.T. (1966). Properties of porous media affecting fluid flow. Journal of the Irrigation and Drainage Division, 92(2), 61–90.

Brownlow, J. W., James, S. C., & Yelderman, J. C. (2016). Influence of hydraulic fracturing on overlying aquifers in the presence of leaky abandoned wells. Groundwater, 54(6), 781-792.

Butkovskyi, A.; Bruning, H.; Kools, S. A. E.; Rijnaarts, H. H. M.; Van Wezel, A. P. Organic Pollutants in Shale Gas Flowback and Produced s: Identification, Potential Ecological Impact, and Implications for Treatment Strategies. Environ. Sci. Technol. 2017, 51 (9), 4740-4754

Cander, H., 2012, Sweet spots in shale gas and liquids plays: Prediction of fluid composition and reservoir pressure: AAPG Search and Discovery article 40936, accessed June 1, 2015,

http://www.searchanddiscovery.com/documents/2012/40936cander/ndx_cander.pdf.

Cao, R., Li, R., Chen, C., & Girardi, A. (2017). Well Interference and Optimum Well Spacing for Wolfcamp Development at Permian Basin. Proceedings of the 5th Unconventional Resources Technology Conference, 1–11. https://doi.org/10.15530/urtec-2017-2691962

Capo R.C., Stewart B.W., E.L.Rowan, Kohl C.A.K., Wall A.J., Chapman E.C., Schroeder K.T., 2014. The strontium isotopic evolution of marcellus formation produced waters, southwestern pennsylvania. International Journal of Coal Geology. 126 2014, 57-63

Charry, L., Malpani, R., & Clark, B. 2016. A Step Change in the Learning Curve for Refracturing in the Eagle Ford. Unconventional Resources Technology Conference. https://doi.org/10.15530/URTEC-2016-2461344.

Chen, C.-Y., & Horne, R. (2006). Two-phase flow in rough-walled fractures: Experiments and a flow structure model. Water Resources Research, 42(3).

Chen, D., Pan, Z., Liu, J., Connell, L.D., 2013. An Improved Relative Permeability Model for Coal Reservoirs. *Int. J. Coal Geol*. 109–110, 45–57.

Cheng, Y. 2012. Impacts of the Number of Perforation Clusters and Cluster Spacing on Production Performance of Horizontal Shale-Gas Wells. SPE Res Eval & Eng 15 (01): 31-40. SPE-138843-PA. https://doi.org/10.2118/138843-PA.

Cipolla, C., Motiee, M., & Kechemir, A. (2018, August 9). Integrating Microseismic, Geomechanics, Hydraulic Fracture Modeling, and Reservoir Simulation to Characterize Parent Well Depletion and Infill Well Performance in the Bakken. Unconventional Resources Technology Conference.

Cipolla, C. L., Warpinski, N. R., Mayerhofer, M., Lolon, E. P., & Vincent, M. 2010. The Relationship Between Fracture Complexity, Reservoir Properties, and Fracture-Treatment Design. SPE Production & Operations 25 (04): 438-452, SPE-115769-PA. http://dx.doi:10.2118/115769-PA

Cipolla, C. L., Weng, X., Onda, H.. 2011. New Algorithms and Integrated Workflow for Tight Gas and Shale Completions. Presented at the SPE Annual Technical

Conference and Exhibition, Denver, Colorado, USA, 30 October-2 November. SPE-146872-MS. https://doi.org/10.2118/146872-MS.

Clark, C. E.; Horner, R. M.; Harto, C. B. Life Cycle Consumption for Shale Gas and Conventional Natural Gas Environ. Sci. Technol. 2013, 47, 11829-11836.

Clarkson, C. R. 2011. Integration of rate-transient and microseismic analysis for unconventional gas reservoirs: where reservoir engineering meets geophysics. CSEG Rec, 36, 44-61.

Clarkson, C.R. 2013. Production data analysis of unconventional gas wells: Review of theory and best practices. International Journal of Coal Geology, Volumes 109–110, April 2013, Pages 101–146. http://dx.doi.org/10.1016/j.coal.2013.01.002

Clarkson, C.R., Qanbari, F. and Williams-Kovacs, J.D. 2014. Innovative Use of Rate-Transient Analysis Methods to Obtain Hydraulic-Fracture Properties for Low-Permeability Reservoirs Exhibiting Multi-phase Flow. The Leading Edge 33 (10): 1108–1122.

Clarkson, C.R. and Williams-Kovacs, J. 2013. Modeling Two-Phase Flowback of Multifractured Horizontal Wells Completed in Shale. SPE Journal 18 (04): 795-812. SPE-162593-PA. http://dx.doi.org/10.2118/162593-PA.

Cohen, H.A.; Parratt, T.; Andrews, C. B. Potential Contaminant Pathways from Hydraulically Fractured Shale to Aquifers Ground 2013, 51 (3) 317-319

Corey, A.T. The interrelation between gas and oil relative permeabilities. Producers Monthly 19 (November) 1954, 38-41.

Couples G., Alruwaili K., Ma J.. 2018. Report on the experimental results of fluid fracturing–an energy-conserved framework. Deliverable 3.3 from the H2020 Project FracRisk, vol. 636811.

Couples G.. 2019. Phenomenological understanding of poro-elasticity via the micro-mechanics of a simple digital-rock model Geophysics, 84 (4) (2019), pp. 1-98.

Crafton, J. W. and Gunderson, D. W. 2006. Use of Extremely High Time-Resolution Production Data to Characterize Hydraulic Fracture Properties. Presented at the SPE Annual Technical Conference and Exhibition, New Orleans, Louisiana, USA. 24-27 September. SPE-49223-MS. http://dx.doi.org/10.2118/103591-MS.

Dake, L. P. (1983). Fundamentals of Reservoir Engineering. 1978. United States of America: Elesevier.

Daneshy, A., & Pomeroy, M. (2012). SPE 160480 In-situ Measurement of Fracturing Parameters from Communication Between Horizontal Wells. Spe. https://doi.org/10.2118/160480-MS

Darrah, Thomas H., Avner Vengosh, Robert B. Jackson, Nathaniel R. Warner, and Robert J. Poreda. Noble gases identify the mechanisms of fugitive gas contamination in drinking-water wells overlying the Marcellus and Barnett Shales. Proc. Natl. Acad. Sci. U.S.A. 2014, 111, (39), 14076-14081.

Davies, Richard J., Simon A. Mathias, Jennifer Moss, Steinar Hustoft, and Leo Newport. Hydraulic fractures: How far can they go? Marine and Petroleum Geology 37, no. 1 (2012): 1-6.

Deen, T., J. Daal, and J. Tucker. 2015. Maximizing Well Deliverability in the Eagle Ford Shale through Flowback Operations. Presented at the SPE Annual Technical Conference and Exhibition, Houston, Texas, USA, 28-30 September. SPE174831. https://doi.org/10.2118/174831-MS.

Dong, Tian, et al. "Porosity characteristics of the Devonian Horn River shale, Canada: Insights from lithofacies classification and shale composition." International Journal of Coal Geology 141 (2015): 74-90.

Dong, Tian, et al. "The impact of rock composition on geomechanical properties of a shale formation: Middle and Upper Devonian Horn River Group shale, Northeast British Columbia, Canada." AAPG Bulletin 101.2 (2017): 177-204.

Dong, Z., Holditch, S. A., & Lee, W. J. (2016). World Recoverable Unconventional Gas Resources Assessment. In Unconventional Oil and Gas Resources Handbook (pp. 53-70).

Donovan, A. D., Staerker, T. S., Pramudito, A., Gardner, R., Pope, M. C., Corbett, M., … Romero, A. M. (2013). A 3-D outcrop perspective of an unconventional carbonate mudstone reservoir. In Unconventional resources technology conference (pp. 613–619).

Drummond, Kenneth J.. 2014. Horn River Shale Gas: Summary of Wells Drilled and Production. http://www.drummondconsulting.com/

Dunphy, R., and Campagna. D.J. (2011). Fractures, Elastic Moduli & Stress: Geological Controls on Hydraulic Fracture Geometry in the Horn River Basin. Presented CSPG/CSEG/CWLS GeoConvention, Calgary, Alberta, Canada, 9 – 11 May.

Duong, Anh N. Rate-decline analysis for fracture-dominated shale reservoirs. SPE Reservoir Evaluation & Engineering 14, no. 03 (2011): 377-387.

Economides, M. J. and Nolte, K. G, Reservoir Stimulation, third edition. Wiley & Sons, Ltd.

Edwards, R. W. J., Doster, F., Celia, M. A., & Bandilla, K. W. Numerical modeling of gas and flow in shale gas formations with a focus on the fate of hydraulic fracturing fluid. Environ. Sci. Technol. 2017, 51(23), 13779-13787.

Ehlig-Economides, C. A. and Economides, M. J. 2011. Water As Proppant. Presented at SPE Annual Technical Conference and Exhibition, Denver, Colorado, USA, 30 October-2 November. SPE-147603-MS. http://dx.doi:10.2118/147603-MS.

Engelder, T. Capillary Tension and Imbibition Sequester Frack Fluid in Marcellus Gas Shale Proc. Natl. Acad. Sci. U. S. A. 2012, 109 (52) E3625-E3625.

Engelder, T.; Cathles, L. M.; Bryndzia, L. T. The Fate of Residual Treatment Water in Gas Shale Journal of Unconventional Oil and Gas Resources 2014, 7, 33-48.

Engle, M. A., Reyes, F. R., Varonka, M. S., Orem, W. H., Ma, L., Ianno, A. J., ... & Carroll, K. C. 2016. Geochemistry of formation waters from the Wolfcamp and "Cline" shales: Insights into brine origin, reservoir connectivity, and fluid flow in the Permian Basin, USA. Chemical Geology, 425, 76-92.

EPA (2011a) Proceedings of the technical workshops for the hydraulic fracturing study: well construction and operations. EPA 600/R-11/046. http://www.epa.gov/hfstudy/wellconstructworkshop.html. Accessed 12 Dec 2018

Esquivel, R., Blasingame, T. A., & Texas, A. (2017). Optimizing the Development of the Haynesville Shale — Lessons-Learned from Well-to-Well Hydraulic Fracture Interference. Urtec, (1), 1–22. https://doi.org/10.15530/urtec-2017-2670079

Ezulike D. O., Dehghanpour H. and Hawkes, R.V. 2013. Understanding Flowback as a Transient 2 Phase Displacement Process: An extension of the Linear Dual Porosity Model. Presented at the SPE Canadian Unconventional Resources Conference, Calgary, Alberta, Canada, 5-7 November. SPE-167164-MS. http://dx.doi.org/10.2118/167164-MS.

Ezulike, D. O. and Dehghanpour, H. 2014. Modelling flowback as a transient two-phase depletion process, Journal of Natural Gas Science and Engineering, 19, 258-278, https://doi.org/10.1016/j.jngse.2014.05.004.

Ezulike, D. O. and Dehghanpour, H. 2014a. A Workflow for Flowback Data Analysis – Creating Value out of Chaos. Paper resented at the Unconventional Resources Technology Conference held in Denver, Colorado, USA, 25-27 August. SPE-2014-1922047-MS. http://dx.doi.org/10.15530/urtec-2014-1922047.

Ezulike, D. O. and Dehghanpour, H. 2015. A Complementary Approach for Uncertainty Reduction in Post-flowback Production Data Analysis. Journal of Natural Gas Science and Engineering, 27, 1074-1091. http://dx.doi.org/10.1016/j.jngse.2015.09.059.

Ezulike, D. O., Dehghanpour, H., Virues, C. et al. 2016. Flowback Fracture Closure: A Key Factor for Estimating Effective Pore Volume. SPE Res Eval & Eng 19 (4): 567–582. SPE-175143-PA. https://doi.org/10.2118/175143-PA.

Ezulike, Obinna Daniel. Complementary Workflows for Analyzing Multiphase Flowback and Post-flowback Production Data in Unconventional Reservoirs. Diss. UNIVERSITY OF ALBERTA, 2017.

Fisher, M. Kevin, and Norman R. Warpinski. Hydraulic-fracture-height growth: Real data." SPE Production & Operations 27.01 (2012): 8-19.

Fisher, M.K., Wright, C.A., Davidson, B.M. et al. 2002. Integrating FractureMapping Technologies to Optimize Stimulations in the Barnett Shale. Paper SPE77441 presented at the SPE Annual Technical Conference and Exhibition, SanAntonio, Texas, 29 September-2 October. http://dx.doi.org/10.2118/77441-MS.

Fjar E., Holt R.M., Raaen A., Risnes R., Horsrud P.. 2008. Petroleum Related Rock Mechanics, Volume 53, Elsevier.

Flewelling, S.A.; Sharma, M. Constraints on Upward Migration of Hydraulic Fracturing Fluid and Brine Ground 2014, 52 (1) 9-19

Flewelling, S.A., Tymchak, M.P. and Warpinski, N.. Hydraulic fracture height limits and fault interactions in tight oil and gas formations. Geophysical Research Letters, 2013, 40(14), 3602-3606.

Frank O. Jones Jr. 1975. A laboratory study of the effects of confining pressure on fracture flow and storage capacity in carbonate rocks. Journal of Petroleum Technology 27 (01): 21-27. SPE-4569-PA. http://dx.doi.org/10.2118/4569-PA.

Foltz, K. E. 2015. Petrographic and petrophysical characterization of the woodford shale northern shelf, anadarko basin, oklahoma (Unpublished master's thesis). Oklahoma State University, Stillwater, OK.

Fu, Y., Ezulike, D. O., Dehghanpour, H., & Steven Jones, R. 2017. Estimating Effective Fracture Pore Volume from Flowback Data and Evaluating Its Relationship to Design Parameters of Multistage-Fracture Completion. *SPE Prod & Oper* 32(4): 423-439. SPE-175892-PA. http://dx.doi.org/10.2118/175892-PA.

G. J., Abolo, N., Lawal, H., Jackson, G., Weatherford, N. A., & Flores, C. (2013). A Novel Approach To Modeling and Forecasting Frac Hits in Shale Gas Wells - (SPE-164898). 75th EAGE Conference & Exhibition Incorporating SPE EUROPEC 2013 London, UK, 10-13 June 2013, (June 2013), 10–13.

Gale, J.F.W., Reed, R.M., and Holder, J. 2007. Natural fractures in the Barnett shale and their importance for hydraulic fracture treatments. AAPGBull. 91 (4): 603-622. http://dx.doi.org/10.1306/11010606061.

Gallegos, T. J.; Varela, B. A.; Haines, S. S.; Engle, M. A. Hydraulic fracturing use variability in the United States and potential environmental implications Resour. Res. 2015, 51 (7) 5839-5845.

Ghanbari, E.; Dehghanpour, H. The Fate of Fracturing Water: A Field and Simulation Study Fuel 2016, 163, 282-294.

Grafton, R. Q., Cronshaw, I. G., & Moore, M. C. (Eds.). 2016. Risks, Rewards and Regulation of Unconventional Gas: A Global Perspective. Cambridge University Press.

Gray, H. 1974. Subsurface controlled safety valve sizing computer program, Appendix B. Vertical flow correlation in gas wells, user manual for API 14BM.

Grieser, W.V. 2011. Oklahoma Woodford Shale: Completion Trends and Production Outcomes from Three Basins. Presented at the SPE Production and Operations Symposium, Oklahoma City, Oklahoma, USA 27–29 March. SPE-139813-MS. http://dx.doi.org/10.2118/139813-MS.

Ground Water Protection Council, ALL Consulting. Modern Shale Gas Development in the United States: A Primer; United States Department of Energy, Office of Fossil Energy: Washington, D.C., 2009; p 96.

Haluszczak, L.O., Rose, A.W., & Kump, L.R. (2013). Geochemical evaluation of flowback brine from marcellus gas wells in pennsylvania, usa. Applied Geochemistry, 28, 55–61.

Haustveit, K., Dahlgren, K., Greenwood, H., Peryam, T., Kennedy, B., Energy, D., & Dawson, M. (2017). New Age Fracture Mapping Diagnostic Tools-A STACK Case Study. SPE Hydraulic Fracturing Technology Conference and Exhibition, 24–26. https://doi.org/10.2118/184862-MS.

Henderson, C., Acharya, H. R., Matis, H., Kommepalli, H., Moore, B., & Wang, H. (2012). Cost effective recovery of low-TDS frac flowback water for re-use (DOE Report DE-FE0000784, 100).

Hoffman, B. T., Chang, W. M., Modeling Hydraulic Fractures in Finite Difference Simulators: Application to Tight Gas Sands in Montana, Journal of Petroleum Science and Engineering 69 (2009) 107–116.

Hurd O., Zoback M.D., et al. 2012. Stimulated shale volume characterization: multiwell case study from the horn river shale: I. geomechanics and microseismicity SPE Annual Technical Conference and Exhibition, Society of Petroleum Engineers.

IHS Harmony Software, 2014. “Pressure Loss Calculations”. http://www.fekete.com/SAN/WebHelp/Piper/WebHelp/c-te-pressure.htm (accessed 19/12/2016).

Ilk, D., Currie, S. M., Symmons, D. et al. 2010. A Comprehensive Workflow for Early Analysis and Interpretation of Flowback Data from Wells in Tight Gas/Shale

Reservoir Systems. Presented at SPE Annual Technical Conference and Exhibition, Florence, Italy, 19-22 September. SPE-135607-MS. http://dx.doi:10.2118/135607-MS.

Ilk, D., Okouma Mangha, V., and Blasingame, T.A. 2011a. Characterization of Well Performance in Unconventional Reservoirs Using Production Data Diagnostics. Presented at the SPE Annual Technical Conference and Exhibition, Denver, Colorado, 30 October–2 November. SPE-147604-MS. http://dx.doi.org/10.2118/147604-MS.

Ilk, D., Jenkins, C.D., Blasingame, T.A. 2011b. Production Analysis in Unconventional Reservoirs - Diagnostics, Challenges, and Methodologies. North American Unconventional Gas Conference and Exhibition, The Woodlands, Texas, 14–16 June. SPE-144376-MS. http://dx.doi.org/10.2118/144376-MS.

Ingram, S. R., Lahman, M. and Persac, S. 2014. Methods Improve Stimulation Efficiency of Perforation Clusters in Completions. Journal of Petroleum Technology 66 (04): 32-36. SPE-0414-0032-JPT. http://dx.doi.org/10.2118/0414-0032-JPT.

Jackson, R. B.; Lowry, E. R.; Pickle, A.; Kang, M.; DiGiulio, D.; Zhao, K. The Depths of Hydraulic Fracturing and Accompanying Water Use Across the United States Environ. Sci. Technol. 2015, 49 (15) 8969-8976.

Jackson, R. B.; Vengosh, A.; Darrah, T. H.; Warner, 675 N. R.; Down, A.; Poreda, R. J.; Osborn, S. G.; Zhao, K. G.; Karr, J. D., Increased stray gas abundance in a subset of drinking water wells near Marcellus shale gas extraction. Proc. Natl. Acad. Sci. U.S.A. 2013, 110, (28), 11250-11255.

Jasechko and Perrone D. Hydraulic fracturing near domestic groundwater wells. Proc. Natl. Acad. Sci. U.S.A. 2017, 114:13138–13143.

Jason Hendrick, Adam Baig, Eric von Lunen, and Ted Urbancic. Beyond the Microseismic Clouds: A Comprehensive Approach to Unconventional Gas Development. 2016. http://csegrecorder.com/articles/view/beyond-the-microseismic-clouds-a-comprehensive-approach

Jiang, M.; Hendrickson, C. T.; VanBriesen, J. M. Life Cycle Water Consumption and Waste Generation Impacts of a Marcellus Shale Gas Well Environ. Sci. Technol. 2014, 48, 1911-1920.

Jones, R. Steven Jr., R., Pownall, B. and Franke, J. 2014. Estimating Reservoir Pressure from Early Flowback Data. Presented at the Unconventional Resources Technology Conference held in Denver, Colorado, USA.

Jones, R. Steven Jr., R., Pownall, B. and Franke, J. 2014. Estimating Reservoir Pressure from Early Flowback Data. Presented at the Unconventional Resources Technology Conference held in Denver, Colorado, USA, 25-27 August. SPE-2014-1934785-MS. http://dx.doi.org/10.15530/urtec-2014-1934785.

Karimi-Fard, M., Durlofsky, L.J., Aziz, K., An Efficient Discrete-Fracture Model Applicable for General-Purpose Reservoir Simulators, Society of Petroleum Engineer Journal, 9 (2), 227–236, 2004.

Khodabakhshnejad, A., Aimene, Y., Mistry, N., Bachir, A., & Ouenes, A. (2017, October 4). A Fast Method to Forecast Shale Pressure Depletion and Well Performance Using Geomechanical Constraints - Application to Poro-Elasticity Modeling to Predict Mid and Far Field Frac Hits at an Eagle Ford and Wolfcamp Well. Society of Petroleum Engineers. doi:10.2118/187535-MS

Kim, S., Omur-Ozbek, P., Dhanasekar, A., Prior, A., & Carlson, K. Temporal analysis of flowback and produced water composition from shale oil and gas operations: Impact of frac fluid characteristics. Journal of Petroleum Science and Engineering, 2016, 147, 202-210.

King, G. E., Rainbolt, M. F., Swanson, C., & Corporation, A. (2017). SPE-187192-MS Frac Hit Induced Production Losses: Evaluating Root Causes , Damage Location , Possible Prevention Methods and Success of Remedial Treatments.

Kondash, A.; Vengosh, A. Footprint of Hydraulic Fracturing Environ. Sci. Technol. Lett. 2015, 2 (10) 276-280.

Kondash, A.J., Albright, E., & Vengosh, A. (2017). Quantity of flowback and produced waters from unconventional oil and gas exploration. Science of the Total Environment, 574, 314–321.

Kurtoglu, B., Salam, A. and Kazemi, H. 2015. Production Forecasting Using Flow Back Data. Paper SPE 172922, presented at the SPE Middle East Unconventional Resources Conference and Exhibition held in Muscat, Oman, 26-28 January.

Lacazette, Alfred, and Peter Geiser. "Comment on Davies et al., 2012—Hydraulic fractures: How far can they go?" Marine and Petroleum Geology 43 (2013): 516-518.

Lacy, S., Ding, W., and Joshi, S.D. 1992. Horizontal Well Applications and Parameters for Economic Success. Paper presented at the SPE Latin America Petroleum Engineering Conference, 8-11 March, Caracas, Venezuela. SPE-23676-MS. https://doi.org/10.2118/23676-MS.

Lascelles, P., Wan, J., Robinson, L., Allmon, R., Evans, G., Ursell, L., … Rao, V. (2017). Applying Subsurface DNA Sequencing in Wolfcamp Shales, Midland Basin. SPE Hydraulic Fracturing Technology Conference and Exhibition. https://doi.org/10.2118/184869-MS.

Latimer A., Hill M., Hendrick J., N.E. ULC. 2017. Pore Pressure Anomalies in the Horn River Basin, Northeastern BC.

Lawal, Hamed, et al. A novel approach to modeling and forecasting frac hits in shale gas wells. EAGE Annual Conference & Exhibition incorporating SPE Europec. Society of Petroleum Engineers, 2013.

Lester, Y.; Ferrer, I.; Thurman, E. M.; Sitterley, K. A.; Korak, J. A.; Aiken, G.; Linden, K. G. Characterization of Hydraulic Fracturing Flowback in Colorado: Implications for Treatment. Sci. Total Environ. 2015, 512–513, 637– 644

Li, C., Lafollette, R., Sookprasong, A., , et al., (26–28 March) 2013. Characterization of Hydraulic Fracture Geometry in Shale Gas Reservoirs Using Early Production Data. Paper IPTC-16896-MS presented at the SPE International Petroleum Technology Conference, Beijing, China. http://dx.doi.org/10.2118/16896-MS.

Lijek, S.J. Simple Performance Plots Used in Rate-Time Determination and flood Analysis. 1989. Paper SPE 19847 presented at the SPE Annual Technical Conference and Exhibition, San Antonio, Texas, USA.

Ling, K., & He, J. 2012. Theoretical Bases of Arps Empirical Decline Curves. Paper presented at Abu Dhabi International Petroleum Conference and Exhibition, 11-14 November, Abu Dhabi, UAE.

Ling J., Barker W.. 2013 Microseismic case study: investigating the natural fractures and faults of the muskwa and evie shale play in northeastern british columbia. SEG Technical Program Expanded Abstracts 2013, Society of Exploration Geophysicists, pp. 2135-2139

Llewellyn, Garth T., Frank Dorman, J. L. Westland, D. Yoxtheimer, Paul Grieve, Todd Sowers, E. Humston-Fulmer, and Susan L. Brantley. 2015. Evaluating a groundwater supply contamination incident attributed to Marcellus Shale gas development. Proc. Natl. Acad. Sci. U.S.A. 112, (20), 6325-6330.

Lutz, B.D., Lewis, A.N., & Doyle, M.W. (2013). Generation, transport, and disposal of wastewater associated with marcellus shale gas development. Water Resources Research, 49(2), 647–656.

Ma, Y.Z. and Holditch, S., 2015. *Unconventional oil and gas resources handbook: Evaluation and development*. Gulf professional publishing.

MapPlace. Acessed on May 20, 2018. http://www.mapplace.ca.

Maxwell, S. & Norton, M. Enhancing shale gas reservoir characterization using hydraulic fracture microseismic data. first break 30, 95–101 (2012).

Maxwell, S.C., Jones, M., Parker, R. et al. 2009. Fault Activation During Hydraulic Fracturing. In 79th Annual International Meeting, Society of Exploration Geophysicists, Expanded Abstracts, 1552–1556. https://doi.org/10.1190/1.3255145 Abbasi, M., Dehghanpour, H., and Hawkes, R.V. 2012. Flowback Analysis for Fracture Characterization. Presented at the SPE Canadian Unconventional Resources Conference, Calgary, Alberta, Canada, 30 October - 1 November. SPE-162661-MS. http://dx.doi.org/10.2118/162661-MS.

Maxwell, S.C. and Cipolla, C. 2011. What Does Microseismicity Tell Us AboutHydraulic Fracturing. Paper SPE 146932 presented at the SPE Annual TechnicalConference and Exhibition, Denver, Colorado, 30 October-2 November. http://dx.doi.org/10.2118/146932-MS.

Mayerhofer, M. J. and Meehan, D. N. 1998. Waterfracs - Results from 50 Cotton Valley Wells. Presented at the SPE Annual Technical Conference and Exhibition, New Orleans, Louisiana, USA, 27-30 September. SPE-49104-MS. http://dx.doi:10.2118/49104-MS

Mayerhofer, M. J., Stegent, N.A., Barth, J.O. et al. 2011. IntegratingFracture Diagnostics and Engineering Data in the Marcellus Shale. Paper SPE145463 presented at the SPE Annual Technical Conference and Exhibition, Denver,Colorado, 30 October-2 November. http://dx.doi.org/10.2118/145463-MS.

McCain, W. D. 1991. Reservoir-Fluid Property Correlations-State of the Art (includes associated papers 23583 and 23594). SPE Journal 6 (02): 266-272. SPE-18571-PA. http://dx.doi.org/10.2118/18571-PA.

McKean, Scott H., and Jeffrey A. Priest. "Multiple failure state triaxial testing of the Montney Formation." J*ournal of Petroleum Science and Engineering* 173 (2019): 122-135.

McKenna, J. P. 2014. Where Did The Proppant Go? Presented at the SPE/AAPG/SEG Unconventional Resources Technology Conference, Denver, Colorado, USA, 25-27 August. SPE-2014-1922843-MS. http://dx.doi.doi:10.15530/urtec-2014-1922843

McPhail, S., et al. "Shale units of the Horn River Formation, Horn River Basin and Cordova Embayment, northeastern British Columbia." Canadian Society of Petroleum Geologists and Canadian Well Logging Society Convention. 2008.

Middleton, R. S., Carey, J. W., Currier, R. P., Hyman, J. D., Kang, Q., Karra, S., ... & Viswanathan, H. S. 2015. Shale gas and non-aqueous fracturing fluids: Opportunities and challenges for supercritical CO2. Applied Energy, 147, 500-509.

Myers, T. Potential Contaminant Pathways from Hydraulically Fractured Shale to Aquifers Ground 2012, 50 (6) 872-882

Nagel, N., Zhang, F., Sanchez-Nagel, M., & Lee, B. 2013. Quantitative evaluation of completion techniques on influencing shale fracture ‘complexity’. In ISRM

International Conference for Effective and Sustainable Hydraulic Fracturing. OnePetro.

Nejadi, S., Leung, J.Y., Trivedi, J.J. 2015. Integrated Characterization of Hydraulically Fractured Shale-Gas Reservoirs—Production History Matching. SPE Reservoir Evaluation & Engineering, 18(4): 481-494. SPE-171664-PA. http://dx.doi.org/10.2118/171664-PA.

Ness, Shona, Roy Benteau, and Shelley Leggitt. "Horn River shales… boring and black?… or… beautifully complex." In GeoCanada Conference, Calgary, Alberta, vol. 9. 2010.

Nguyen, P. D., Weaver, J. D., Parker, M. A., King, D. G., Gillstrom, R. L., & van Batenburg, D. W. 1996. Proppant Flowback Control Additives. Presented at SPE Annual Technical Conference and Exhibition, Denver, Colorado, USA, 6-9 October, SPE-36689-MS. http://dx.doi:10.2118/36689-MS.

Nicot, J.-P.; Scanlon, B. R.; Reedy, R. C.; Costley, R. A. Source and Fate of Hydraulic Fracturing in the Barnett Shale: A Historical Perspective. Environ. Sci. Technol. 2014, 48(4), 2464-2471.

Nolte, K. G. 1979. Determination of Fracture Parameters from Fracturing Pressure Decline. Society of Petroleum Engineers. Presented at SPE Annual Technical Conference and Exhibition, Las Vegas, Nevada, USA, 23-26 September. SPE-8341-MS . http://dx.doi.org/10.2118/8341-MS.

Nolte, K. G. and Smith, M. B. 1981. Interpretation of Fracturing Pressures. J Pet Technol 33 (9): 1767–1775. SPE-8297-PA. http://dx.doi.org/10.2118/8297-PA.

Olmstead, Sheila M., Lucija A. Muehlenbachs, Jhih-Shyang Shih, Ziyan Chu, and Alan J. Krupnick. Shale gas development impacts on surface water quality in Pennsylvania. Proc. Natl. Acad. Sci. U.S.A. 2013, 110, (13), 4962-4967.

Onishi, V.C., Carrero-Parreño, A., Reyes-Labarta, J.A., Ruiz-Femenia, R., Salcedo-Díaz, R., Fraga, E.S., & Caballero, J.A. (2017). Shale gas flowback water desalination: Single vs multiple-effect evaporation with vapor recompression cycle and thermal integration. Desalination, 404, 230–248.

Osborn, S. G.; Vengosh, A.; Warner, N. R.; Jackson, R. B.2011. Methane contamination of drinking accompanying gas-well drilling and hydraulic fracturing Proc. Natl. Acad. Sci. U. S. A. 2011, 108 (20) 8172-8176

Osselin, F., Nightingale, M., Hearn, G., Kloppmann, W., Gaucher, E., Clarkson, C., & Mayer, B. 2018. Quantifying the extent of flowback of hydraulic fracturing fluids using chemical and isotopic tracer approaches. Applied Geochemistry, 93, 20–29.

Ostadhassan, M., Zamiran, S., Jabbari, H., Osouli, A., Bubach, B., & Oster, B. 2015. Stability Analysis of Multilateral High Density Pad Wells in the Three Forks Formation. SPE Western Regional Meeting, 27-30 April, Garden Grove, California, USA. SPE-174040-MS. http://dx.doi:10.2118/174040-MS

Palacio, J. C., & Blasingame, T. A. 1993. Decline-Curve Analysis With Type Curves - Analysis of Gas Well Production Data. Presented at SPE Rocky Mountain Regional/Low Permeability Reservoirs Symposium, Denver, Colorado, USA, 26-28 April. SPE-25909-MS. http://dx.doi.doi:10.2118/25909-MS

Parmar, J., Dehghanpour, H. and Kuru, E. 2014. Displacement of water by gas in propped fractures: Combined effects of gravity, surface tension, and wettability. Journal of Unconventional Oil and Gas Resources, 5, 10-21. http://dx.doi.org/10.1016/j.juogr.2013.11.005.

Patzek, Tad W., Frank Male, and Michael Marder. Gas production in the Barnett Shale obeys a simple scaling theory. Proc. Natl. Acad. Sci. U.S.A.2013, 110 (49): 19731-19736.

Pearson, K. 1895. Notes on regression and inheritance in the case of two parents. Proceedings of the Royal Society of London, 58: 240-242.

Peters E. J. 2012. Advanced petrophysics. Volume: Geology, Porosity, Absolute Permeability, Heterogeneity, and Geostatistics, Vol. 1, Greenlead Book Group (Reprint).

Peterson, N. (2018). SPE-189813-MS Case Study of Time-Based Stress Shadow Influences on New Well Fracture Propagation Patterns in the Montney, 3, 13–14. https://doi.org/10.2118/189813-MS.

Pommer, M., & Milliken, K. 2015. Pore types and pore-size distributions across thermal maturity, eagle ford formation, southern texaspores across thermal maturity, eagle ford. AAPG Bulletin, 99(9), 1713–1744.

Quintero, H., Mattucci, M., Hawkes, R., Zhang, K., & O'Neil, B. 2018. Nano-Particle Surfactant in Hydraulic Fracturing Fluids for Enhanced Post Frac Oil Recovery. Presented at the SPE Canada Unconventional Resources Conference, 13-14 March, Calgary, Alberta, Canada. SPE-189780-MS. http://dx.doi.org/doi:10.2118/189780-MS.

Rainbolt, M. F., & Esco, J. (2018). Paper Title: Frac Hit Induced Production Losses: Evaluating Root Causes, Damage Location, Possible Prevention Methods and Success of Remediation Treatments, Part II. SPE Hydraulic Fracturing Technology Conference and Exhibition, 187192(part I). https://doi.org/10.2118/189853-MS

Raysoni, N. and Weaver, J. 2013. Long-Term Hydrothermal Proppant Performance. SPE Production & Operations 28(04): 414-426, SPE-150669-PA. http://dx.doi:10.2118/150669-PA.

Reagan, M.T., Moridis, G.J., Keen, N.D., & Johnson, J.N. (2015). Numerical simulation of the environmental impact of hydraulic fracturing of tight/shale gas reservoirs on near-surface groundwater: Background, base cases, shallow reservoirs, short-term gas, and water transport. Water Resources Research, 51(4), 2543–2573.

Reine C.A., Dunphy R.B.. 2011. Weighing in on the seismic scale: the use of seismic fault measurements for constructing discrete fracture networks in the horn river basin. CSPG CSEG CWLS Convention.

Roche, Vincent, Melanie Grob, Thomas Eyre, and Mirko Van Der Baan. (2015). Statistical characteristics of microseismic events and in-situ stress in the Horn River Basin. *Proceedings of GeoConvention*.

Rowan, E.L., Engle, M.A., Kraemer, T.F., Schroeder, K.T., Hammack, R.W., & Doughten, M.W. 2015. Geochemical and isotopic evolution of water produced from Middle Devonian Marcellus shale gas wells, Appalachian Basin, Pennsylvania. AAPG Bulletin, 99(2), 181–206.

Rozhko A.Y.. 2010. Role of seepage forces on seismicity triggering. J. Geophys. Res.: Solid Earth, 115 (B11).

Sadeghi, S., 2013. An Evaluation of Completion Parameters and Well Performance in the Montney Formation in British Columbia, Canada (Doctoral dissertation).

Salman, A., Kurtoglu, B., and Kazemi, H. 2014. Analysis of Chemical Tracer Flowback in Unconventional Reservoirs. Presented at the SPE/CSUR Unconventional Resources Conference, Calgary, AB, Canada, 30 September – 2 October. SPE-171656-MS. http://dx.doi.org/10.2118/171656-MS.

Sani, Abu M., Seth B. Podhoretz, and Brent D. Chambers. "The Use of Completion Diagnostics in Haynesville Shale Horizontal Wells to Monitor Fracture Propagation, Well Communication, and Production Impact." SPE/CSUR Unconventional Resources Conference. Society of Petroleum Engineers, 2015.

Sardinha, C. M., Petr, C., Lehmann, J., et al. 2014. Determining Interwell Connectivity and Reservoir Complexity Through Frac Pressure Hits and Production Interference Analysis. Presented at SPE/CSUR Unconventional Resources Conference - Canada, Calgary, Alberta, Canada, 30 September - 2 October. http://dx.doi:10.2118/171628-MS.

Scanlon, B.R., Reedy, R.C., Nicot, J.-P. 2014. Comparison of water use for hydraulic fracturing for unconventional oil and gas vs conventional oil. Environmental Science & Technology, 48(20), 12386–12393.

Shapiro S.A., Dinske C.. 2009. Fluid-induced seismicity: pressure diffusion and hydraulic fracturing. Geophys. Prospect., 57 (2) (2009), pp. 301-310.

Sharma, M. and Agrawal, S. 2013. Impact of Liquid Loading in Hydraulic Fractures on Well Productivity. Presented in SPE Hydraulic Fracturing Technology Conference, Woodlands, Texas, USA, 4-6 February. SPE-163837-MS. http://dx.doi:10.2118/163837-MS.

Sharma, M. M. and Manchanda, R. 2015. The Role of Induced Un-propped (IU) Fractures in Unconventional Oil and Gas Wells. Presented at SPE Annual Technical Conference and Exhibition, Houston, Texas, USA, September 28-30. SPE-174946-MS. http://dx.doi:10.2118/174946-MS.

Shelley, R.F., Saugier, L.D., Al-Tailji, W.H., . 2012. Understanding Hydraulic Fracture Stimulated Horizontal Eagle Ford Completions. Presented at the SPE/EAGE European Unconventional Resources Conference, Vienna, Austria, 20&-22 March. SPE-152533-MS. http://dx.doi.org/10.2118/152533-MS

Shokri, A. R., Chalaturnyk, R. J., Bearinger, D., Virues, C., & Lehmann, J. 2017. Constraining the Complexity of Stimulated Reservoir Volume during Multi-Stage Hydraulic Fracturing of Horizontal Wells through Inter-Well Pressure Hit Modeling. Presented at the SPE Annual Technical Conference and Exhibition, 9-11 October, San Antonio, Texas, USA.

Silva, J., L. Ursell, and E. Percak-Dennett. "Applying Subsurface DNA Diagnostics and Data Science in the Delaware Basin." SPE Hydraulic Fracturing Technology Conference and Exhibition. Society of Petroleum Engineers, 2018.

Soeder, D. J., Sharma, S., Pekney, N., Hopkinson, L., Dilmore, R., Kutchko, B., ... & Capo, R. 2014. An approach for assessing engineering risk from shale gas wells in the United States. International Journal of Coal Geology, 126, 4-19.

Song, B., and Ehlig-Economides, C. A. 2011. Rate-Normalized Pressure Analysis for Determination of Shale Gas Well Performance. Presented at North American Unconventional Gas Conference and Exhibition, The Woodlands, Texas, USA, June 14-16. SPE-144031-MS. http://dx.doi:10.2118/144031-MS.

Sun, H., Zhou, D., Chawathé, A., & Liang, B. (2017). Understanding the Mechanism of Fracture Hits on Midland Basin Tight-Oil Production. Proceedings of the 5th Unconventional Resources Technology Conference, (Eia 2016), 1–12. https://doi.org/10.15530/urtec-2017-2662893

Sun, H., Chawathé, A., Hoteit, H. et al. 2015. Understanding Shale Gas Flow Behavior Using Numerical Simulation. *SPE J.* 20 (1): 142–150. SPE-167753-PA. http://dx.doi.org/10.2118/167753-PA.

Swami, Vivek, et al. "A Novel Approach to History Matching and Optimization of Shale Completions and EUR-a Case study of Eagle Ford Well." SPE Unconventional Resources conference. Society of Petroleum Engineers, 2017.

Swanson, C., Hill, W. A., Nilson, G., Griman, C., Hill, R., Sullivan, P., Pursley, J. (2018). Post-Frac-Hit Mitigation and Well Remediation of Woodford Horizontal Wells With Solvent/Surfactant Chemistry Blend. SPE/AAPG/SEG Unconventional Resources Technology Conference, 1–16. https://doi.org/10.15530/urtec-2018-2902400.

Stamford, L., & Azapagic, A. 2014. Life cycle environmental impacts of uk shale gas. Applied Energy, 134, 506–518.

Tiab, D., Restrepo, D. P. and Igbokoyi, A. O. 2006. Fracture porosity of naturally fractured reservoirs. Presented at International Oil Conference and Exhibition in Mexico, Cancun, Mexico, 31 August - 2 September. SPE-104056-MS. http://dx.doi.org/10.2118/104056-MS.

Tompkins, D., Sieker, R., Koseluk, D., & Cartaya, H. 2016. Managed Pressure Flowback in Unconventional Reservoirs: A Permian Basin Case Study. Presented at the SPE/AAPG/SEG Unconventional Resources Technology Conference, San Antonio, Texas, USA, 1-3 August. URTEC-2461207-MS. https://doi.org/10.15530/URTEC-2016-2461207.

Urban-Rascon, E., Virues, C., & Aguilera, R. (2018, March 13). 3D Geomechanical Modeling in the Complex Fracture Network of the Horn River Shale Using a Fully-Coupled Hybrid Hydraulic Fracture HHF Model: Permeability Evolution and Depletion. Society of Petroleum Engineers. https://doi.org /10.2118/189795-MS

U.S. EIA. 2016. Trends in U.S. Oil and Natural Gas Upstream Costs. U.S. Energy Information Administration. Retrieved December 11, 2018 from https://www.eia.gov/analysis/studies/drilling/pdf/upstream.pdf. Last Acessed 12 Dec 2018

U.S. Environmental Protection Agency. 2016. Hydraulic Fracturing for Oil and Gas: Impacts from the Hydraulic Fracturing Water Cycle on Drinking Water Resources in the United States (Final Report); Report EPA/600/R-16/236F; U.S. Environmental Protection Agency: Washington, DC.

Van Sickle, S., Galloway, J., Owen, T., Wearly, J., & Snyder, D. (2017). STACK Well Performance, a Multi-Pad Completion Comparison. SPE Europec Featured at 79th EAGE Conference and Exhibition. https://doi.org/10.2118/185819-MS

Vengosh, A.; Jackson, R. B.; Warner, N. R.; Darrah, T. H.; Kondash, A. J. 2014. A Critical Review of the Risks to Water Resources from Unconventional Shale Gas Development and Hydraulic Fracturing in the United States Environ. Sci. Technol. 2014, 48, 8334-8348.

Vengosh, A., Kondash, A., Harkness, J., Lauer, N., Warner, N., Darrah, T.H. 2017. The geochemistry of hydraulic fracturing fluids. Procedia Earth and Planetary Science, 17, 21–24.

Vidic, R. D.; Brantley, S. L.; Vandenbossche, J. M.; Yoxtheimer, D.; Abad, J. D., Impact of shale gas development on regional water quality. Science 2013, 340, (6134), 1235009.

Virues, C., Budge, J., & Lunen, E. von. (2015, September 28). Microseismic-Derived Expected Ultimate Fracture Half-Height Above/Below Wellbore in Unconventional Stimulated Reservoir Volume in a Multi-F ractured Horizontal 10 Well Pad - Canadian Horn River Basin Case Study. Society of Petroleum Engineers. https://doi:10.2118/174954-MS

Virues, C., Budge, J., & Von Lunen, E. (2015, July 20). Microseismic-Derived Ultimate Expected Fracture Half-Length in Unconventional Stimulated Reservoir Volume in a Multi-Fractured Horizontal 8 Well Full Pad - Canadian Horn River Basin Case Study. Unconventional Resources Technology Conference. https://doi.org/10.15530/URTEC-2015-2153989.

Wallace, J., Kabir, C. S., & Cipolla, C. Multiphysics Investigation of Diagnostic Fracture Injection Tests in Unconventional Reservoirs. Presented at SPE Hydraulic Fracturing Technology Conference, The Woodlands, Texas, USA, 4-6 February. SPE-168620-MS. http://dx.doi:10.2118/168620-MS.

Wang, K., Li, H., Wang, J., Jiang, B., Bu, C., Zhang, Q., & Luo, W. 2017. Predicting production and estimated ultimate recoveries for shale gas wells: A new methodology approach. Applied Energy, 206, 1416–1431.

Warner, N. R.; Christie, C. A.; Jackson, R. B.; Vengosh, A. Impacts of Shale Gas Waste Disposal on Quality in Western Pennsylvania Environ. Sci. Technol. 2013, 47, 11849-11857

Warner, Nathaniel R., Robert B. Jackson, Thomas H. Darrah, Stephen G. Osborn, Adrian Down, Kaiguang Zhao, Alissa White, and Avner Vengosh. Geochemical evidence for possible natural migration of Marcellus Formation brine to shallow aquifers in Pennsylvania. Proc. Natl. Acad. Sci. U.S.A. 2012, 109, (30), 11961-11966.

Warpinski, N. R., Mayerhofer, M.J., Vincent, M.C., Cipolla, C.L., and Lolon, E.P. 2008. Stimulating Unconventional Reservoirs: Maximizing Network Growth While Optimizing Fracture Conductivity. Paper SPE 114173 presented at the SPE Unconventional Reservoirs Conference, Keystone, Colorado, 10–12 February

Warpinski, N. R. 2010. Stress Amplification and Arch Dimensions in Proppant Beds Deposited by Waterfracs. SPE Production & Operations 25 (04): 461-471, SPE-119350-PA. http://dx.doi:10.2118/119350-PA.

Warpinski, Norman R., Jing Du, and Ulrich Zimmer. Measurements of hydraulic-fracture-induced seismicity in gas shales. SPE Production & Operations 27.03 (2012): 240-252.

Wattenbarger, R.A., El-Banbi, A.H., Villegas, M.E. et al. 1998. Production Analysis of Linear Flow Into Fractured Tight Gas Wells. Presented at the SPE Rocky Mountain Regional/Low-Permeability Reservoirs Symposium, Denver, 5–8 April 1998. SPE-39931-MS. http://dx.doi.org/10.2118/39931-MS.

Weijermars, R. 2013. Economic appraisal of shale gas plays in continental europe. Applied Energy, 106, 100–115.

Weijermars, R. 2014. Us shale gas production outlook based on well roll-out rate scenarios. Applied Energy, 124, 283–297.

Williams-Kovacs, J. D. and Clarkson, C. R. 2013. Stochastic Modeling of Multi-Phase Flowback From Multi-Fractured Horizontal Tight Oil Wells. Presented at SPE Unconventional Resources Conference Canada, Calgary, Alberta, Canada, 5-7 November. SPE-167232-MS. http://dx.doi org/10.2118/167232-MS.

Williams-Kovacs, J.D. 2017. Quantitative Analysis of Multi-Phase Flowback From Multi-Fractured Horizontal Wells. PhD Thesis Dissertation. University of Calgary, Calgary, Alberta.

Wilson, M., Worrall, F., Davies, R., & Hart, A. 2017. Shallow aquifer vulnerability from subsurface fluid injection at a proposed shale gas hydraulic fracturing site. Water Resources Research, 53(11), 9922–9940.

Wood, James. Water distribution in the Montney tight gas play of the western Canadian sedimentary basin: significance for resource evaluation. SPE Reservoir Evaluation & Engineering 16, no. 03 (2013): 290-302.

Xu, Y., Adefidipe, O. A. and Dehghanpour, H. 2015. Estimating Fracture Volume Using Flowback Data from the Horn River Basin: A Material Balance Approach. Journal of Natural Gas Science and Engineering, 25, 253-270. http://dx.doi.org/10.1016/j.jngse.2015.04.036.

Xu, Y., Adefidipe, O. A. and Dehghanpour, H. 2016. A flowing material balance equation for two-phase flowback analysis. Journal of Petroleum Science and Engineering, 142, 170-185. http://dx.doi.org/10.1016/j.petrol.2016.01.018.

Xu, Y., Ezulike, O. D., Zolfaghari, A., Dehghanpour, H., & Virues, C. 2016, September 26). Complementary Surveillance Microseismic and Flowback Data Analysis: An Approach to Evaluate Complex Fracture Networks. Society of Petroleum Engineers.

Xu Y., Dehghanpour H., Ezulike O. D., Virues C.. 2017. Effectiveness and time variation of induced fracture volume: Lessons from water flowback analysis, Fuel, 210, 844-858. https://doi.org/10.1016/j.fuel.2017.08.027.

Yang, Z., Neuweiler, I., Méheust, Y., Fagerlund, F., Niemi, A. 2016. Fluid trapping during capillary displacement in fractures. Advances in Water Resources, 95, 264–275.

Yousefzadeh, Abdolnaser, Qi Li, Claudio Virués, and Roberto Aguilera. 2019. An Interpretation of Microseismic Spatial Anomalies, b-values, and Magnitude Analyses to Identify Activated Fracture Networks in Horn River Basin. SPE Production & Operations.

Yuan, J., Luo, D., & Feng, L. et al. 2015. A review of the technical and economic evaluation techniques for shale gas development. Applied Energy, 148, 49–65.

Zhang, J., Kamenov, A., Hill, A. D. et al. 2014. Laboratory Measurement of Hydraulic-Fracture Conductivities in the Barnett Shale. SPE Production & Operations 29 (03): 216-227, SPE-163839-PA. http://dx.doi:10.2118/163839-PA

Zhang, Y. and Ehlig-Economides, C. 2014. Accounting for Remaining Injected Fracturing Fluid in Shale Gas Wells. Presented at SPE/AAPG/SEG Unconventional Resources Technology Conference, Denver, Colorado, USA, 25-27 August. SPE-2014-1892994-MS. http://dx.org/10.15530/urtec-2014-1892994.

Zhou, Q.; Dilmore, R.; Kleit, A. N.; Wang, J. Y. Evaluating Fracture-Fluid Flowback in Marcellus Using Data-Mining Technologies SPE Production & Operations 2016, 31 (2) 133-146.

Zolfaghari, A., Dehghanpour, H., Ghanbari, E., & Bearinger, D. 2016. Fracture characterization using flowback salt-concentration transient. SPE Journal, 21(01), 233–244.

Zorn, E. V., Hammack, R., & Harbert, W. (2014, February 4). Time Dependent b and D-values, Scalar Hydraulic Diffusivity, and Seismic Energy From Microseismic Analysis in the Marcellus Shale: Connection to Pumping Behavior During Hydraulic Fracturing. Society of Petroleum Engineers. https:// doi.org /10.2118/168647-MS.

Appendices

Appendix A Single-phase Flowback Data Analysis

A.1 Estimates of Fracture Compressibility

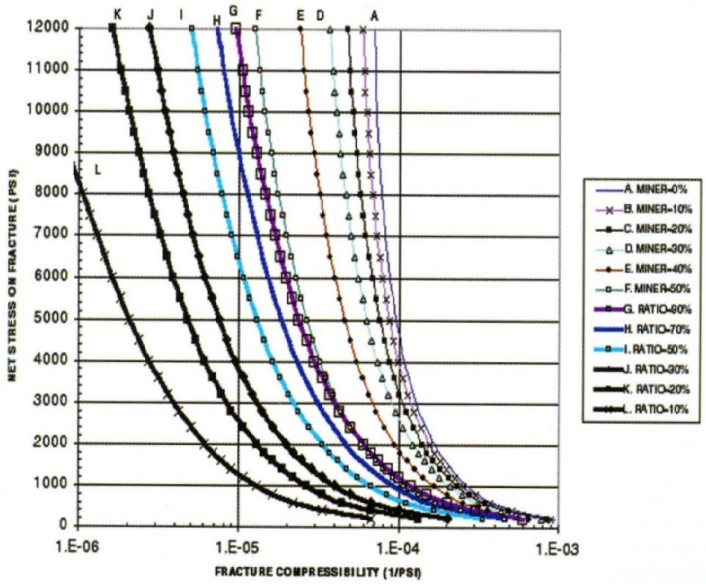

Fig. A.1: Charts for estimating fracture compressibility. Miner is the estimated percentage of secondary mineralization in the natural fractures. Ratio is fracture porosity divided by the summation of fracture porosity and vug porosity. Reproduced from "Recovery Factors And Reserves In Naturally Fractured Reservoirs", by R. Aguilera, 1999, *Journal of Canadian Petroleum Technology*, 38, Page 16. Copyright 1999 by PETROLEUM SOCIETY OF C.I.M. [ETC.]

A.2 Diagnostic Plots of Flowback Rate and Pressure Data

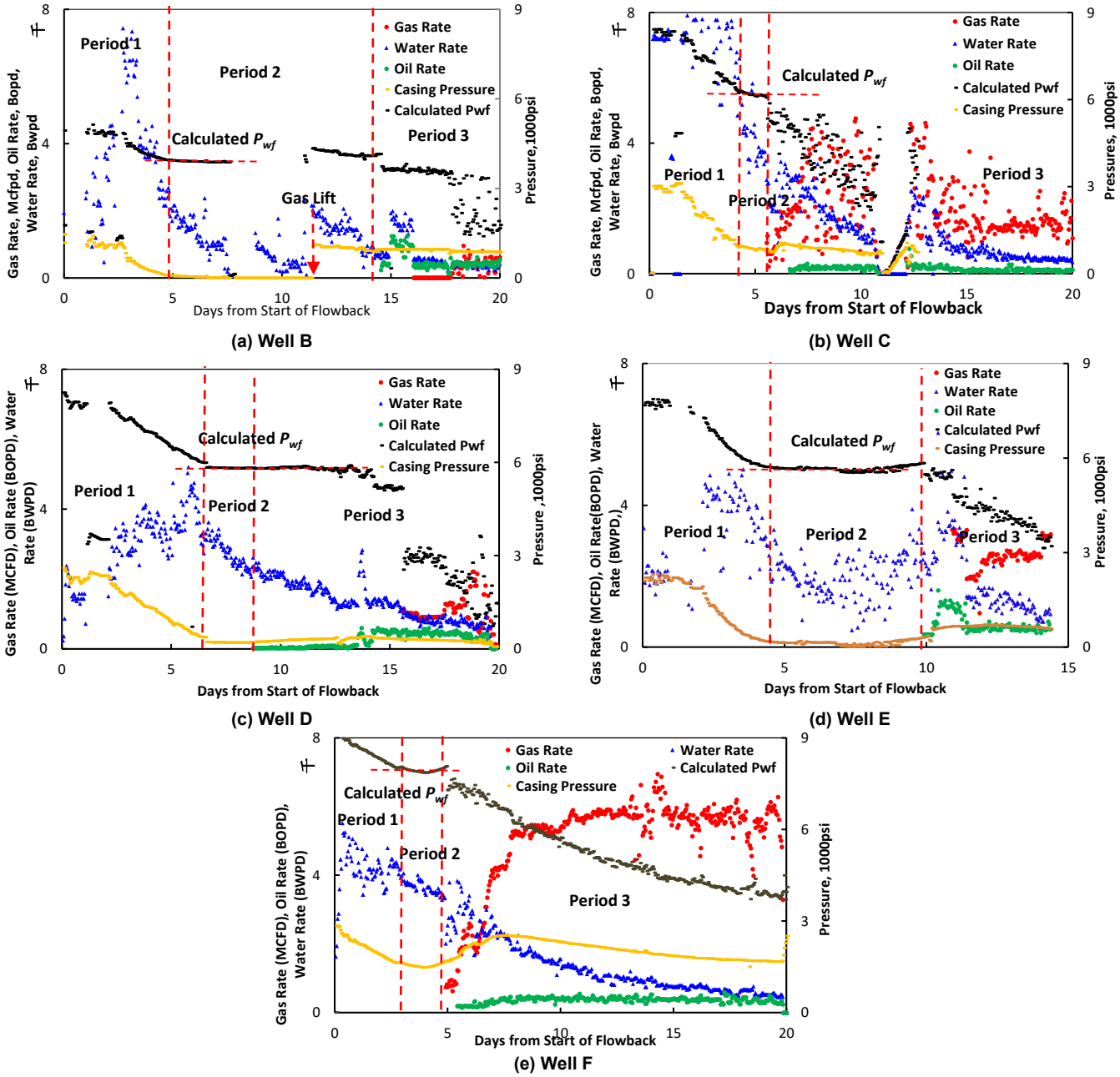

Fig. A.2: Hourly flowback data show three periods. Period 1 shows single-phase of water production and declining pressure. Period 2 shows single-phase of water production and flattening pressure. Period 3 shows multiphase production.

A.3 Analysis for Early Single-Phase Flowback Data

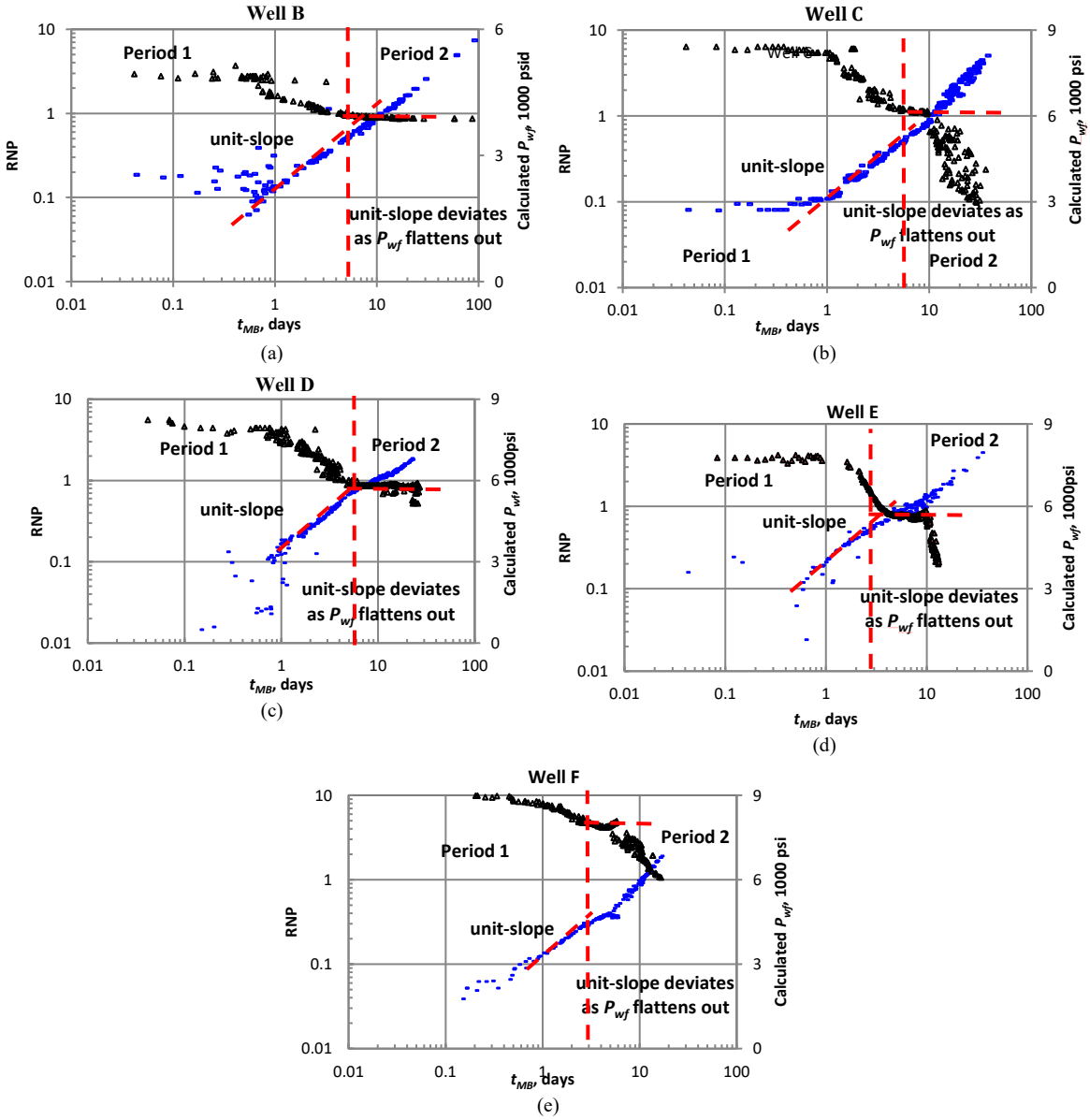

Fig. A.3: Log-log plot of *RNP* versus t_{MB} shows a clear unit slope before the calculated bottomhole pressure flattens out.

A.4 Cartesian Plot of *RNP* and t_{MB}

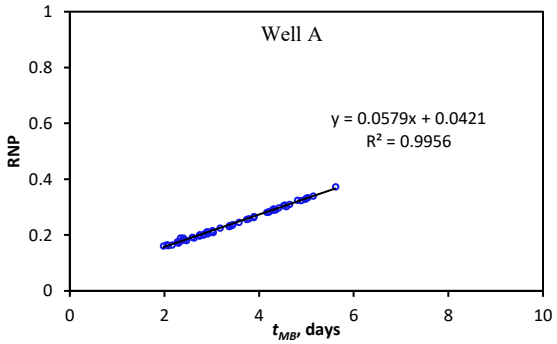

(a)

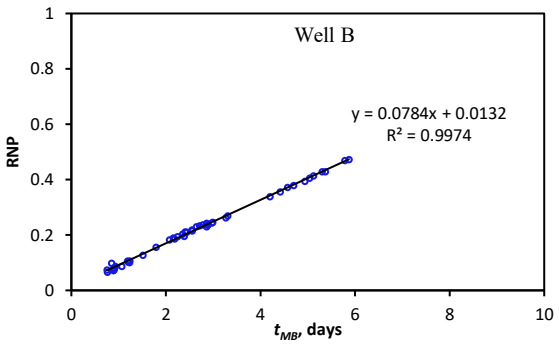

(b)

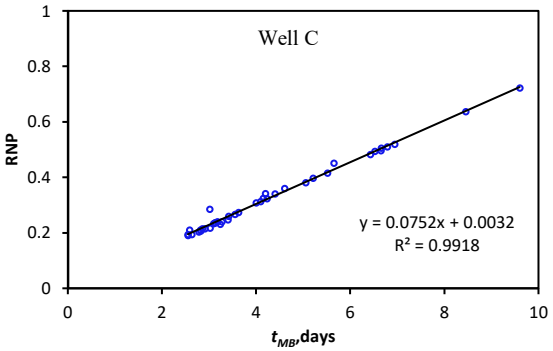

(c)

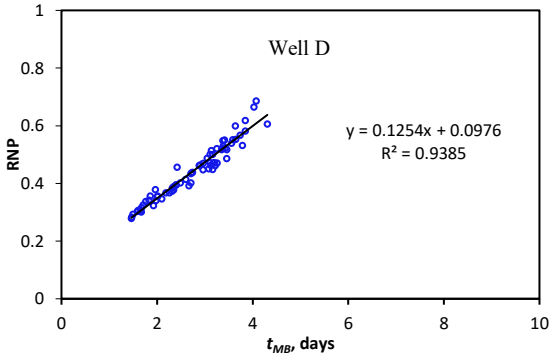

(d)

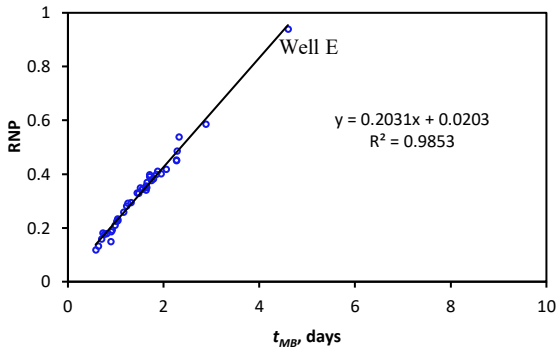

(e)

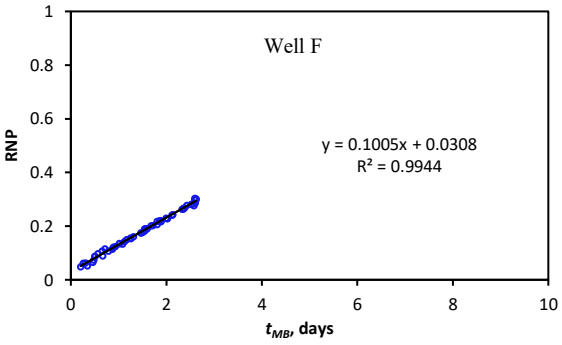

(f)

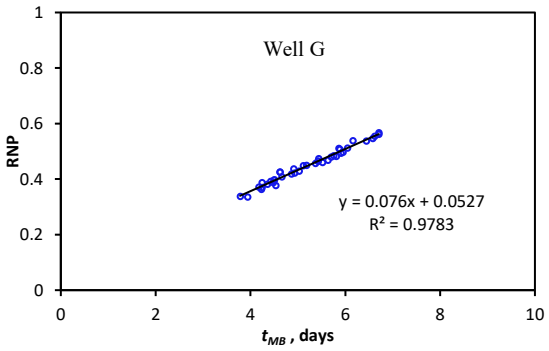

(g)

Fig. A.4: *RNP* versus t_{MB} in cartesian plot and linear fit for each well

Appendix B Water-rate Decline Analysis

B.1 Water-rate Decline Analysis of Eagle Ford Wells

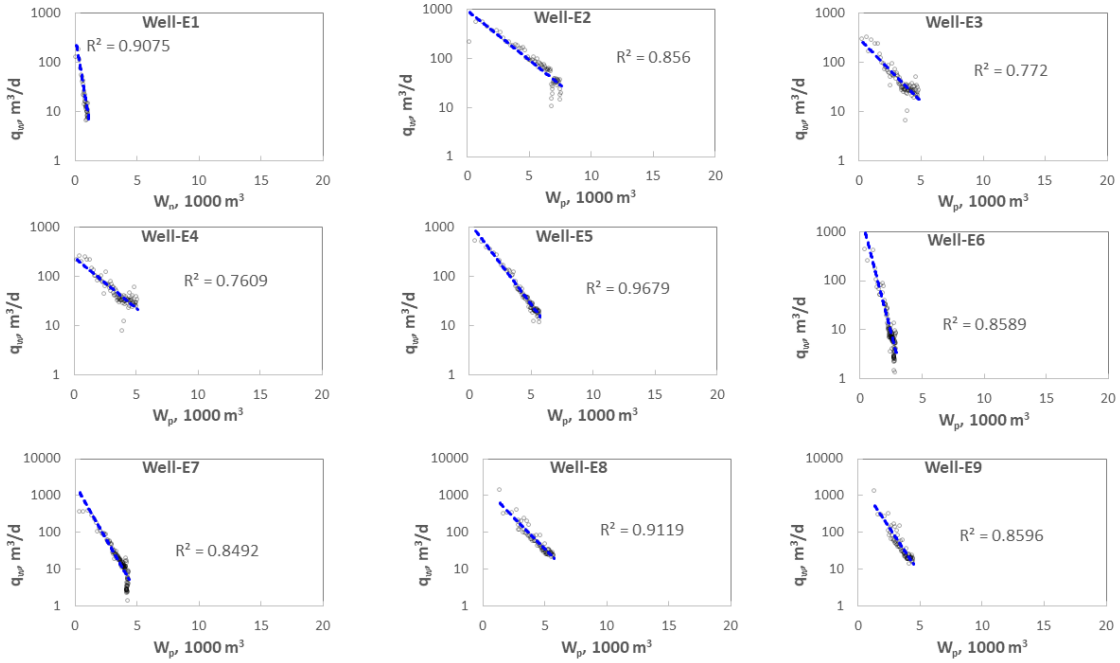

Fig. B.1: Semi-log plots of water rate versus cumulative water volume for 9 Eagle Ford wells with early two-phase flowback. The water rate data are fitted by a straight line with a relatively good match.

B.2 Water-rate Decline Analysis of Horn River Wells

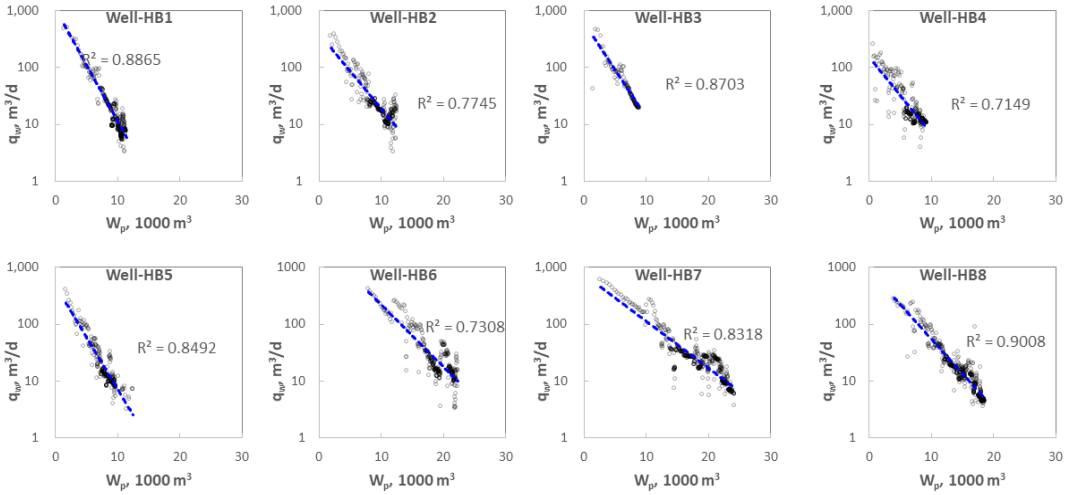

(a)

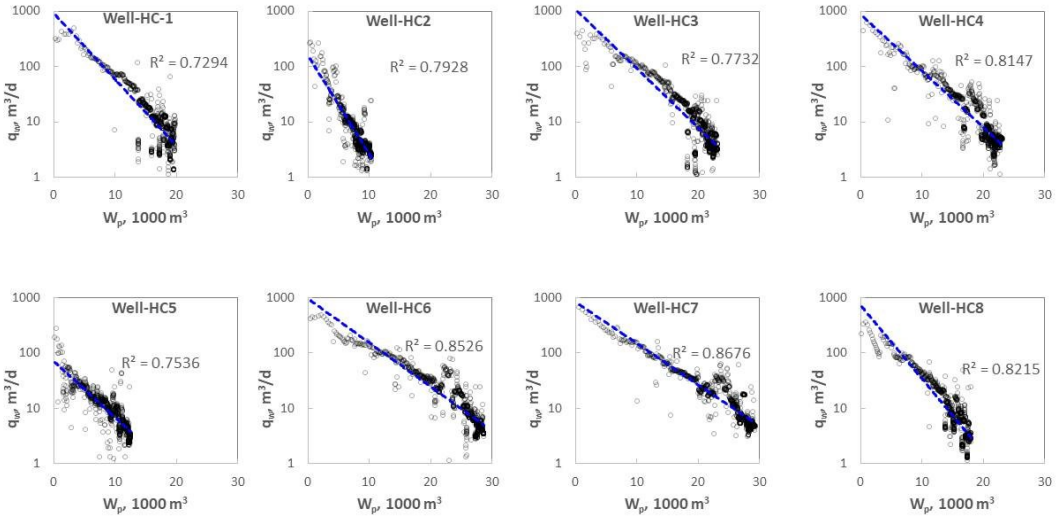

(b)

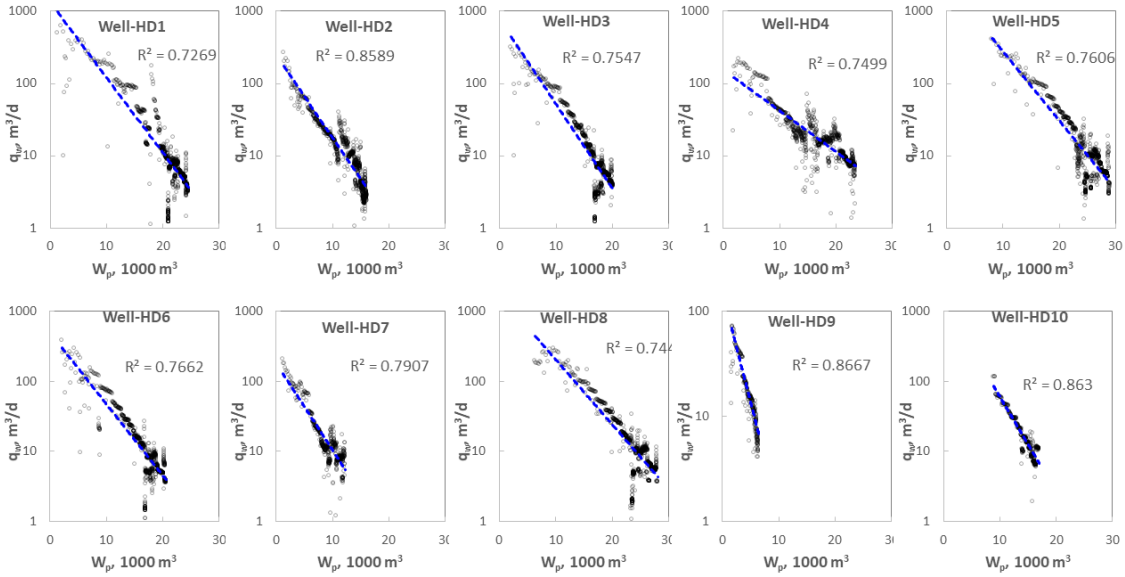

(c)

Fig. B.2: Semi-log plots of water rate versus cumulative water volume show a straight line in Horn River wells in (a) Pad B, (b) Pad C, and (c) Pad D.

B.3 Water-rate Decline Analysis of Woodford Wells

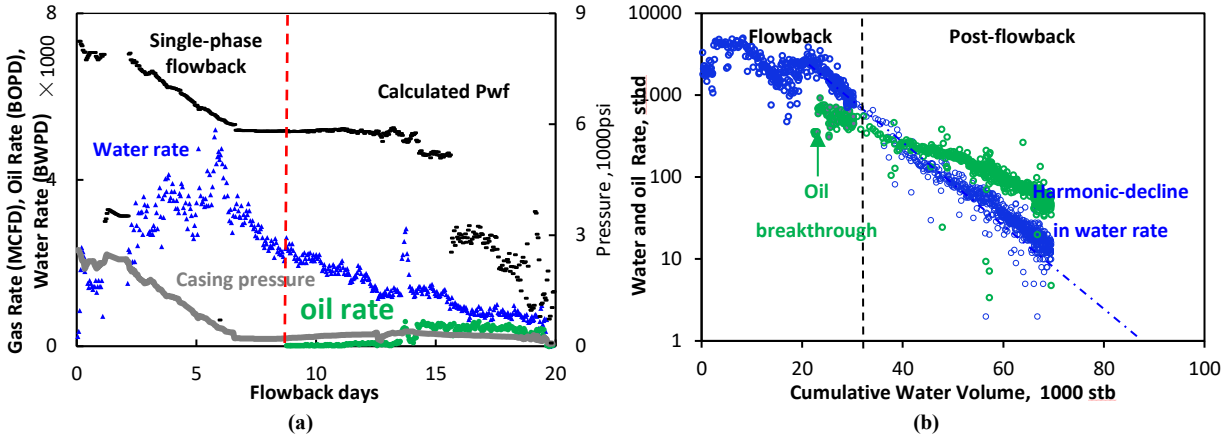

Fig. B.3: Plots of rates and pressure for a tight-oil well completed in the Woodford: (a) Flowback data of this well generally shows two regions: Region-1 is represented by a single-phase period with significant pressure drops and relatively high water rate; Region-2 shows a generally stabilized pressure while relatively sharp decrease in water rate; (b) The semi-log plot of water rate versus cumulative water volume shows a straight line during flowback.

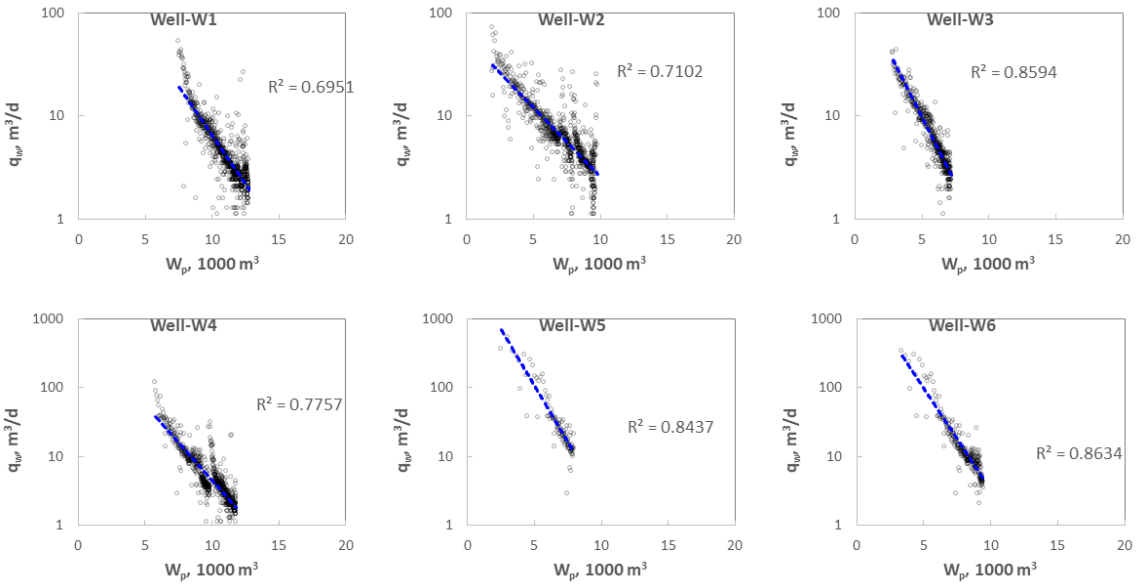

Fig. B.4: Semi-log plots of water rate versus cumulative water volume show a straight line in 6 Woodford Wells.

B.4 Water-rate Decline Analysis of Montney Wells

In Fig. B.6a, we observe 3 regions: Region-1 shows single-phase water flowback with a significant decrease in P_{casing}, which lasts for about 66 hours. Region-2 shows two-phase gas and water production, with an increasing trend of P_{casing} which lasts for 20 hours. Region-3 shows three-phase flow of water, gas, and condensate, with decreasing q_w after the condensate production.

Fig. B.6b compares the semi-log plot of q_g and q_w versus W_p during flowback period. We can fit two straight-lines to the data of Regions 2 and 3. The straight line in Region-3 is relatively steeper compared with that in Region-2. During multiphase flowback, we observe the similar straight-lines in the semi-log plots of q_w versus W_p for 10 gas-condensate MT wells (see Fig. B.8). Also, the water flowback data for 10 dry-gas MT wells can be fitted by a straight line (see Fig. B.7).

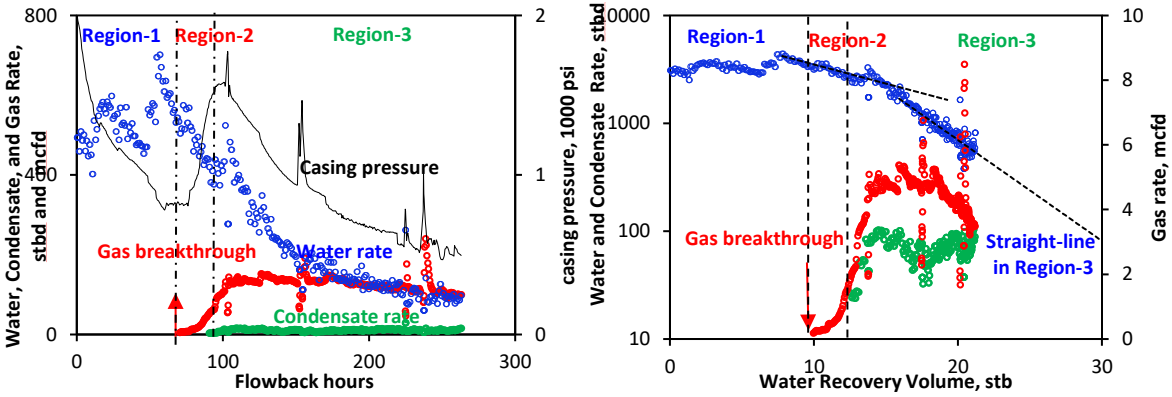

Fig. B.5: Plots of rate and pressure data for a gas-condensate well completed in the MT Formation: (a) Flowback data generally show 3 regions: Region-1 showing single-phase water production with significant pressure drop; Region-2 showing two-phase gas and water flowback with increasing casing pressure; Region-3 showing three-phase flow of gas, water, and condensate; (b) Semi-log plot of water rate versus water recovery volume shows straight-lines in Regions 2 and 3.

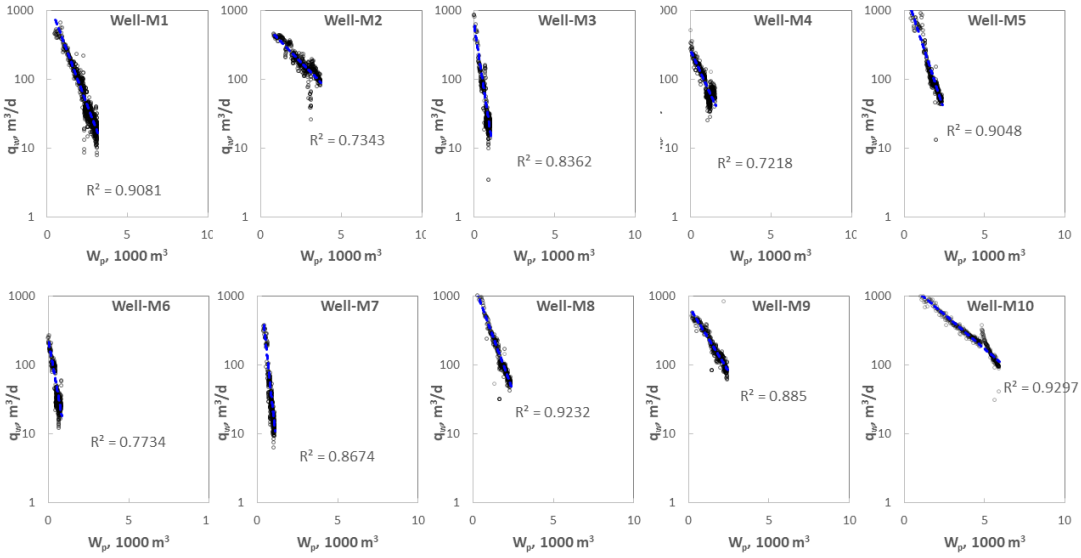

Fig. B.6: Semi-log plots of water rate versus cumulative water volume for 10 dry-gas Montney wells show a straight-line behavior during two-phase flowback. The water rate data are fitted by the straight-line with a relatively good match during flowback.

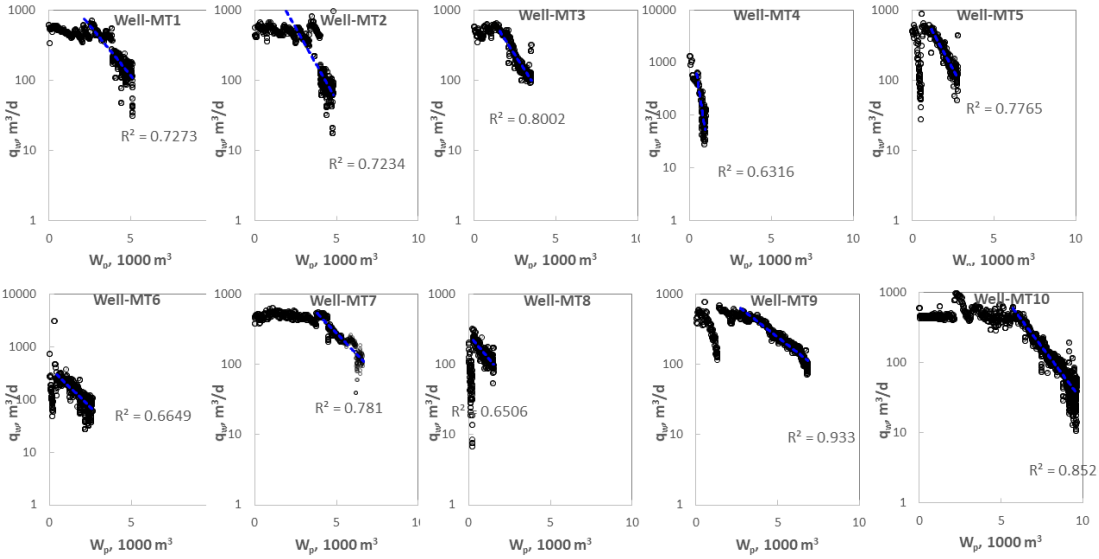

Fig. B.7: Semi-log plots of water rate versus cumulative water volume for 10 gas-condensate Montney Wells with single-phase flowback. The water rate data are fitted by a straight-line during multiphase flowback.

B.5 Stabilizing Pressure Profiles

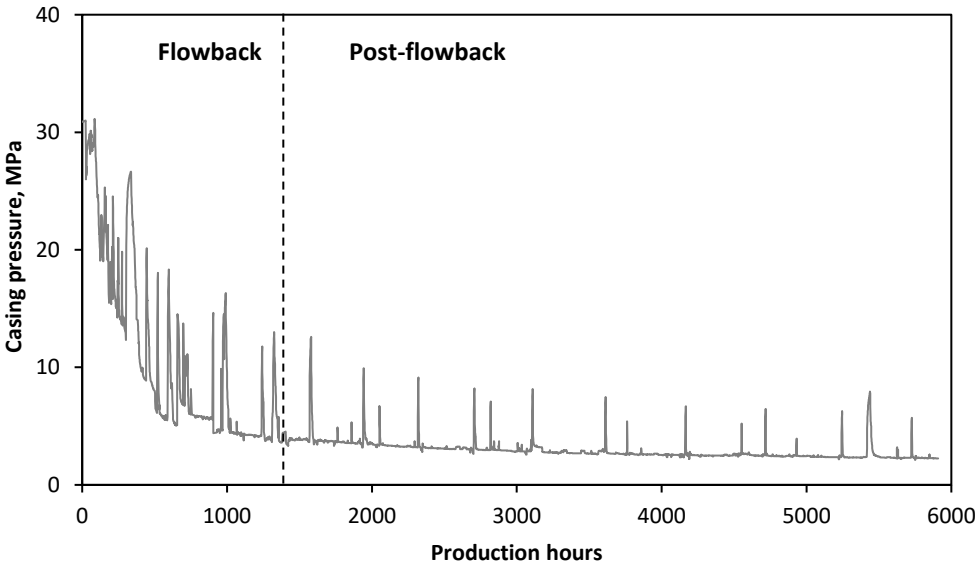

Fig. B.8: Field data from a multi-fractured horizontal well completed in Horn River Formation show a gradually stabilized pressure at the late period of flowback.

B.6 Results of Estimated Water Recovery Factor

Table B.1: Summary of TIV, water production days, measured water recovery factor, D_i, q_i, relative error, and estimated water recovery factor after 1 to 10 years of production for 26 Horn River wells

Well Name	TIV, 10^3 m^3	Water Production Days	Measured RF_w	D_i	q_i, m^3/d	R^2	Estimated Water Recovery Factor, fraction		
							1 year	*5 years*	*10 years*
Well-HB1	56	1000	0.257	0.10	314	0.72	0.20	0.28	0.32
Well-HB2	42	1000	0.405	0.03	160	0.62	0.29	0.46	0.53
Well-HB3	47	1000	0.370	0.11	389	0.72	0.28	0.40	0.46
Well-HB4	53	1000	0.239	0.02	80	0.65	0.16	0.27	0.32
Well-HB5	56	1000	0.239	0.06	192	0.80	0.18	0.27	0.31
Well-HB6	70	1000	0.376	0.45	1917	0.77	0.31	0.41	0.45
Well-HB7	65	1000	0.394	0.18	883	0.79	0.31	0.43	0.49
Well-HB8	74	1000	0.265	0.19	716	0.82	0.21	0.29	0.33
Well-HC1	57	1000	0.374	0.26	943	0.72	0.29	0.40	0.44
Well-HC2	48	1000	0.216	0.06	149	0.81	0.16	0.24	0.28
Well-HC3	53	1000	0.440	0.29	1187	0.83	0.36	0.48	0.53
Well-HC4	52	1000	0.450	0.20	859	0.82	0.36	0.49	0.55
Well-HC5	49	1000	0.257	0.02	69	0.77	0.17	0.30	0.36
Well-HC6	51	1000	0.559	0.18	974	0.86	0.44	0.61	0.69
Well-HC7	49	1000	0.601	0.14	830	0.86	0.47	0.66	0.74
Well-HC8	51	1000	0.360	0.19	647	0.85	0.29	0.39	0.44
Well-HD1	59	1000	0.415	0.34	1430	0.86	0.34	0.46	0.51
Well-HD2	64	1000	0.252	0.06	247	0.86	0.19	0.28	0.32
Well-HD3	68	1000	0.300	0.21	772	0.81	0.24	0.33	0.37
Well-HD4	61	1000	0.384	0.02	154	0.76	0.27	0.46	0.54
Well-HD5	57	1000	0.512	0.57	2575	0.78	0.42	0.55	0.61
Well-HD6	67	1000	0.310	0.15	599	0.85	0.25	0.34	0.39
Well-HD7	61	1000	0.237	0.03	122	0.83	0.17	0.28	0.32
Well-HD8	54	1000	0.526	0.42	1931	0.86	0.43	0.57	0.63
Well-HD9	64	1000	0.185	0.01	34	0.60	0.11	0.23	0.30
Well-HD10	67	1000	0.315	0.04	213	0.70	0.23	0.35	0.41

Table B.2: Summary of TIV, water production days, measured water recovery factor, D_i, q_i, relative error, and estimated water recovery factor after 1 to 10 years of production for 15 Woodford wells

Well Name	TIV, 10^3 m^3	Water Production Days	Measured RF_w	D_i	q_i, m^3/d	R^2	Estimated Water Recovery Factor, fraction		
							1 year	*5 years*	*10 years*
Well-W1	28	1000	0.469	0.28	617	0.78	0.37	0.50	0.56
Well-W2	22	331	0.294	0.03	74	0.69	0.30	0.49	0.57
Well-W3	18	690	0.413	0.11	191	0.92	0.35	0.50	0.56
Well-W4	17	308	0.572	0.95	1563	0.75	0.58	0.74	0.81
Well-W5	27	191	0.391	0.21	595	0.78	0.45	0.62	0.69
Well-W6	14	327	0.547	0.37	578	0.85	0.55	0.73	0.81
Well-W7	46	81	0.173	0.19	534	0.85	0.27	0.37	0.41
Well-W8	44	170	0.180	0.28	572	0.89	0.21	0.29	0.32
Well-W9	55	231	0.147	3.99	4700	0.89	0.16	0.19	0.21
Well-W10	53	231	0.210	0.11	370	0.70	0.23	0.33	0.37
Well-W11	43	191	0.243	0.27	735	0.68	0.29	0.39	0.44
Well-W12	44	161	0.238	0.87	1815	0.87	0.28	0.35	0.39
Well-W13	46	60	0.105	0.17	343	0.61	0.18	0.25	0.28
Well-W14	35	161	0.207	0.76	1146	0.90	0.24	0.31	0.34
Well-W15	45	550	0.160	0.54	680	0.89	0.15	0.19	0.21

Table B.3: Summary of TIV, water production days, measured water recovery factor, D_i, q_i, relative error, and estimated water recovery factor after 1 to 10 years of production for 107 Montney wells

Well Identifer	TIV, 10 m^3	Flowback Days	Measured RF_w	D_i	q_i, m^3/d	R^2	Estimated Water Recovery Factor, fraction		
							1 year	*5 years*	*10 years*
34092	20	20	0.209	0.80	669	0.96	0.24	0.31	0.33
32938	23	12	0.140	0.64	770	0.96	0.28	0.37	0.40
28442	8	5	0.119	0.57	378	0.96	0.44	0.57	0.62
34241	11	27	0.246	0.51	610	0.96	0.57	0.75	0.82
28443	9	3	0.050	2.04	357	0.96	0.13	0.16	0.17
28128	8	14	0.169	3.03	651	0.95	0.20	0.24	0.26
32940	15	14	0.240	0.50	645	0.95	0.45	0.59	0.65
34091	21	25	0.283	0.86	593	0.94	0.19	0.25	0.27
32934	17	4	0.064	0.44	457	0.94	0.30	0.40	0.44
29929	8	4	0.218	1.08	608	0.94	0.44	0.56	0.61
32574	19	28	0.267	0.29	316	0.94	0.28	0.37	0.41
32638	14	51	0.435	0.75	792	0.93	0.41	0.53	0.58
28312	16	8	0.136	0.53	655	0.93	0.42	0.54	0.60
28346	8	7	0.166	0.32	247	0.93	0.49	0.65	0.72
28440	10	4	0.138	0.40	299	0.93	0.38	0.51	0.56
34242	20	27	0.241	0.34	371	0.92	0.27	0.36	0.40
32799	9	28	0.253	1.73	1184	0.92	0.47	0.58	0.63
28350	8	6	0.173	0.79	575	0.92	0.50	0.64	0.70
34094	21	26	0.343	0.94	1356	0.92	0.40	0.51	0.56
32627	9	22	0.292	1.66	1329	0.92	0.59	0.74	0.80
33294	11	42	0.367	0.20	259	0.92	0.53	0.73	0.81
32637	14	49	0.413	0.53	535	0.91	0.38	0.50	0.55
32625	12	51	0.473	0.83	797	0.91	0.47	0.61	0.66
29967	12	17	0.133	1.54	892	0.91	0.32	0.40	0.43
32629	9	21	0.298	2.94	2160	0.91	0.59	0.72	0.78
32796	10	29	0.258	2.48	1806	0.91	0.48	0.59	0.64
28110	16	88	0.198	1.04	725	0.91	0.26	0.33	0.36
32793	10	29	0.249	1.62	980	0.90	0.40	0.51	0.55
29954	13	22	0.146	0.73	448	0.90	0.26	0.34	0.37
34090	17	21	0.279	0.40	272	0.90	0.20	0.26	0.29
32630	9	21	0.199	1.16	812	0.90	0.46	0.58	0.64
34152	13	16	0.170	1.96	1039	0.90	0.27	0.34	0.37
32582	17	46	0.392	0.24	550	0.90	0.59	0.80	0.89
29999	14	21	0.219	1.11	1252	0.90	0.49	0.62	0.67
33142	20	18	0.293	0.52	788	0.90	0.39	0.51	0.57
28438	9	4	0.082	0.89	376	0.89	0.26	0.34	0.37
32635	12	37	0.477	0.40	582	0.89	0.62	0.82	0.91
32634	13	36	0.305	0.29	376	0.89	0.47	0.63	0.70
32923	16	25	0.154	0.52	586	0.89	0.37	0.49	0.53
33169	21	19	0.120	0.39	362	0.88	0.22	0.29	0.32
32616	10	86	0.724	0.37	307	0.88	0.40	0.53	0.59
34149	16	16	0.219	0.36	379	0.88	0.32	0.43	0.47
34240	7	20	0.233	0.63	373	0.88	0.43	0.56	0.62
30927	19	6	0.111	0.50	552	0.87	0.30	0.39	0.43
32939	13	8	0.139	0.84	463	0.87	0.24	0.30	0.33
34093	25	26	0.294	0.56	683	0.87	0.26	0.34	0.37
28439	9	4	0.083	1.42	520	0.87	0.26	0.33	0.36
32798	6	36	0.173	1.96	384	0.87	0.20	0.25	0.27
32632	9	11	0.155	0.87	693	0.87	0.49	0.63	0.69
32771	24	44	0.162	0.40	413	0.87	0.21	0.28	0.31
33176	23	18	0.087	0.41	447	0.86	0.24	0.32	0.35
32639	14	51	0.533	0.35	506	0.86	0.52	0.69	0.77
28485	10	7	0.066	0.95	289	0.86	0.18	0.23	0.25
32907	19	70	0.254	2.67	2042	0.86	0.28	0.35	0.38
28347	8	6	0.147	0.58	389	0.86	0.43	0.56	0.61
32765	24	60	0.430	0.44	873	0.85	0.42	0.55	0.61
33512	15	8	0.188	1.44	773	0.85	0.22	0.28	0.30
33513	18	8	0.167	1.16	637	0.85	0.19	0.24	0.26

33976	16	57	0.308	0.36	630	0.85	0.54	0.72	0.80
32794	8	36	0.133	2.07	585	0.85	0.24	0.30	0.32
32795	6	34	0.255	2.70	529	0.85	0.24	0.30	0.32
32910	15	17	0.350	0.94	1190	0.84	0.49	0.62	0.68
29962	21	9	0.247	0.25	431	0.84	0.37	0.50	0.56
32922	18	47	0.461	0.22	375	0.83	0.42	0.57	0.63
29924	10	26	0.333	0.53	523	0.83	0.52	0.68	0.75
32636	12	35	0.437	0.32	435	0.83	0.53	0.71	0.79
32628	11	17	0.290	1.73	1598	0.82	0.54	0.68	0.74
28133	8	9	0.252	1.92	1003	0.82	0.43	0.54	0.58
34150	16	18	0.284	0.35	177	0.82	0.15	0.20	0.23
32792	8	31	0.174	1.12	161	0.82	0.12	0.15	0.16
32908	15	4	0.091	2.97	1453	0.82	0.22	0.27	0.30
32700	27	22	0.101	0.37	591	0.82	0.29	0.38	0.42
28108	13	28	0.178	0.63	600	0.82	0.41	0.54	0.59
33162	15	19	0.052	0.59	243	0.81	0.15	0.19	0.21
29937	15	22	0.113	0.33	358	0.80	0.36	0.47	0.53
33139	20	24	0.121	1.88	572	0.80	0.10	0.12	0.13
30998	18	23	0.113	0.34	411	0.80	0.33	0.44	0.49
34586	21	13	0.269	0.26	783	0.79	0.65	0.88	0.98
28017	16	99	0.621	0.29	396	0.79	0.41	0.55	0.61
31267	12	47	0.523	0.54	621	0.78	0.51	0.66	0.73
32797	7	33	0.114	0.65	214	0.77	0.24	0.31	0.34
32631	12	21	0.324	1.12	1434	0.77	0.66	0.84	0.92
32002	17	83	0.386	0.28	506	0.77	0.48	0.65	0.72
33172	27	20	0.123	0.29	463	0.77	0.28	0.37	0.41
28588	7	4	0.185	6.47	792	0.77	0.13	0.16	0.17
28132	8	9	0.204	1.40	759	0.75	0.43	0.54	0.59
29990	14	97	0.277	0.23	166	0.74	0.23	0.32	0.35
32581	16	29	0.106	0.23	264	0.74	0.32	0.43	0.48
28070	13	38	0.286	0.24	439	0.73	0.61	0.83	0.92
32708	19	26	0.581	0.25	386	0.73	0.38	0.51	0.57
30961	16	37	0.302	0.99	846	0.73	0.32	0.40	0.44
33541	14	26	0.126	0.33	298	0.73	0.30	0.41	0.45
30389	17	35	0.303	0.50	642	0.72	0.39	0.51	0.56
33295	18	32	0.154	0.23	336	0.72	0.36	0.49	0.54
32706	18	26	0.500	0.44	863	0.72	0.57	0.75	0.82
28109	11	11	0.130	0.44	332	0.72	0.33	0.44	0.49
28107	15	28	0.104	0.44	317	0.71	0.25	0.33	0.36
32696	9	34	0.182	0.30	251	0.69	0.46	0.61	0.68
29992	14	16	0.059	0.21	187	0.67	0.27	0.37	0.41
30989	8	8	0.091	0.42	263	0.67	0.40	0.53	0.59
29919	9	8	0.158	0.47	420	0.65	0.51	0.67	0.74
32800	8	14	0.068	1.03	231	0.65	0.17	0.21	0.23
32697	25	28	0.376	0.39	1024	0.65	0.51	0.68	0.75
33114	26	21	0.092	0.30	487	0.64	0.30	0.40	0.44
32951	18	6	0.035	0.08	142	0.62	0.33	0.49	0.55
32814	8	13	0.142	0.50	358	0.61	0.47	0.61	0.67
29926	10	8	0.148	0.35	300	0.60	0.41	0.55	0.61

Table B.4: Summary of TIV, water production days, measured water recovery factor, D_i, q_i, relative error, and estimated water recovery factor after 1 to 10 years of production for 22 Eagle Ford wells

Well Name	TIV, 10^3 m^3	Water Production Days	Measured R_w	D_i	q_i, m^3/d	R^2	Estimated Water Recovery Factor, fraction		
							1 year	*5 years*	*10 years*
Well-E1	37	11	0.049	0.66	537	0.97	0.12	0.16	0.17
Well-E2	34	11	0.068	0.38	518	0.94	0.19	0.26	0.29
Well-E3	35	11	0.052	0.60	515	0.96	0.13	0.17	0.19
Well-E4	63	14	0.065	0.34	764	0.98	0.17	0.23	0.26
Well-E5	29	9	0.063	0.44	486	0.72	0.20	0.26	0.28
Well-E6	60	14	0.060	0.58	921	0.98	0.14	0.18	0.20
Well-E7	56	12	0.055	0.29	570	0.83	0.16	0.22	0.24
Well-E8	44	12	0.059	0.58	683	0.86	0.15	0.19	0.21
Well-E9	62	5	0.030	0.27	578	0.98	0.16	0.21	0.24
Well-E10	85	14	0.062	0.27	883	0.89	0.18	0.24	0.27
Well-E11	83	13	0.044	0.60	956	0.96	0.10	0.13	0.15
Well-E12	113	25	0.039	0.27	636	0.71	0.10	0.13	0.14
Well-E13	100	25	0.038	0.16	406	0.60	0.10	0.15	0.16
Well-E14	81	20	0.061	0.15	511	0.91	0.17	0.24	0.27
Well-E15	72	20	0.061	0.15	451	0.90	0.17	0.23	0.26
Well-E16	71	20	0.058	0.16	436	0.92	0.16	0.22	0.25
Well-E17	48	17	0.069	0.33	559	0.86	0.17	0.23	0.25
Well-E18	78	17	0.056	0.14	492	0.84	0.18	0.25	0.28
Well-E19	81	21	0.073	0.26	785	0.85	0.17	0.23	0.26
Well-E20	84	16	0.044	0.13	417	0.83	0.15	0.22	0.24
Well-E21	77	9	0.051	0.21	762	0.88	0.20	0.28	0.31
Well-E22	76	11	0.057	0.18	689	0.89	0.22	0.30	0.33

B.7 Water-rate Forecast

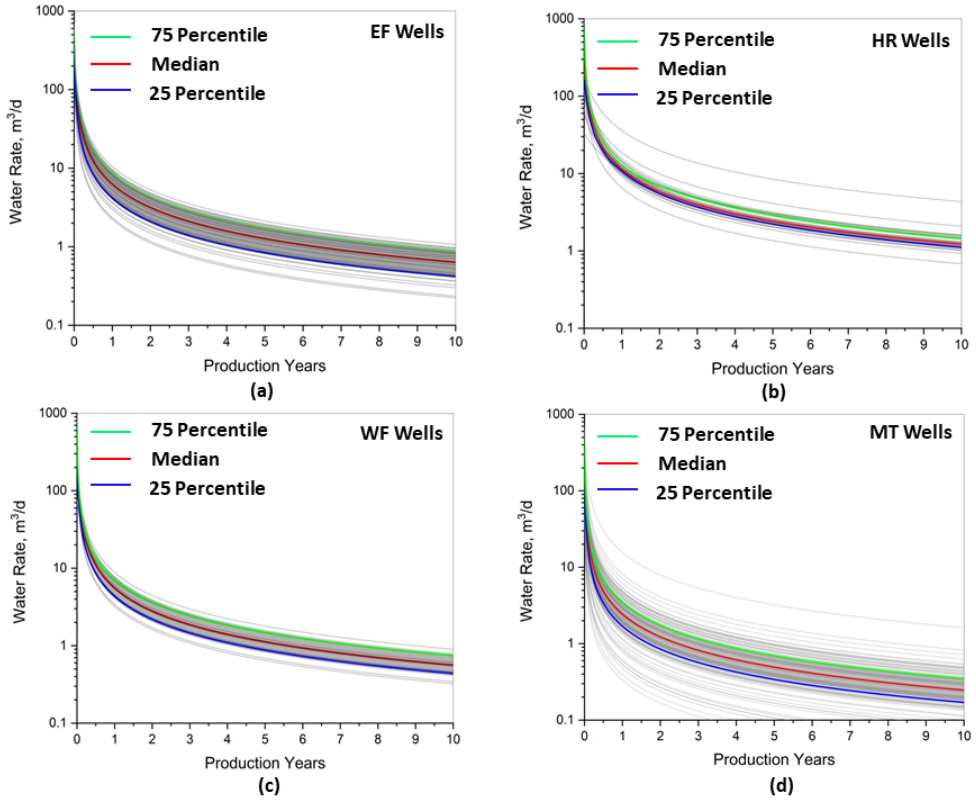

Fig. B.9: Predicted water rate versus production time for (a) EF, (b) HR, (c) WF, and (d) MT wells. The 25th and 75th percentiles and mean values are represented by the blue, green, and red lines, respectively.

B.8 Water Recovery Forecast

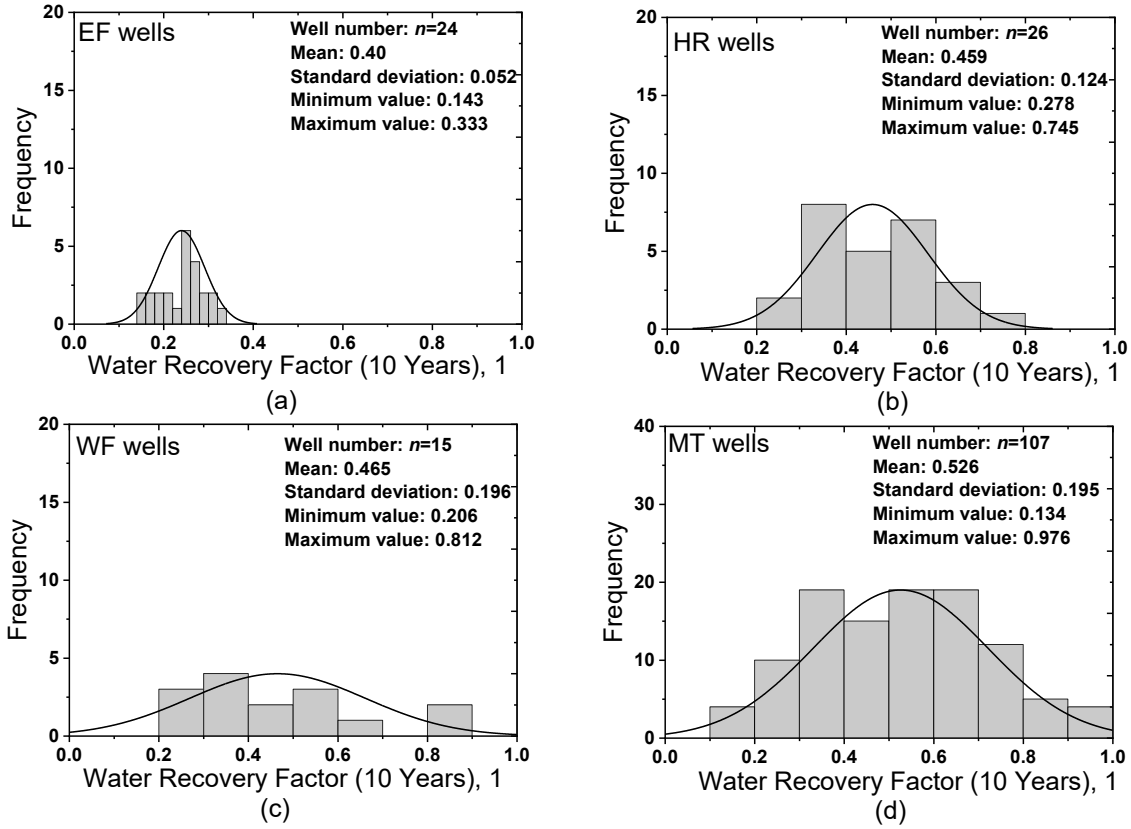

Fig. B.10: Distiribution of estimated water recovery factor for (a) EF, (b) HR, (c) WF, and (d) MT wells after 10 years of production.

B.9 Results of Effective Fracture Pore-volume of Montney Wells

Table B.5 lists the estimated fracture compressibility (C_f), the slope (m) between RNP and t_{MB}, and V_{ef} for these 8 wells estimated by applying Abbasi et al. (2012)'s tank model on the single-phase flowback data. The closure pressure for these target wells is around 44.93 MPa from the DFIT analysis. Fracture porosity is 47.5% by assuming cubic packing of proppants in fractures.

Table B.5: Summary of fracture compressibility, the slope between RNP and t_{MB}, and V_{ef} estimated by flowback tank model for 8 Montney wells

Well Name	C_f, 10^{-5} psi^{-1}	m	V_{ef} using Abbasi et al. (2012)'s model, $10^3 m^3$
Well M-1	12.03	0.72	11.36
Well M-2	10.86	0.72	12.55
Well M-3	6.93	2.18	6.43
Well M-4	6.27	3.37	4.57
Well M-5	7.62	0.54	23.54
Well M-6	3.93	1.64	14.64
Well M-7	4.82	1.96	10.08
Well M-8	12.68	0.55	14.16

Appendix C Well Communication

This appendix includes 6 sections: Section C.1 provides a brief literature review of frac-hits in 6 unconventional North American reservoirs. Section C.2 describes the reservoir, drilling, and completion information associated with target 52 wells. Section C.3 to C.6 provide additional results and discussions that support conclusions in the main body of this paper. These include 4 sections show the detailed descriptions of field design for frac-hits, microseismic (MS), tracer, and production interference tests among target wells.

C.1 Literature Review of Frac-hits in Unconventional Reservoirs

Table C.1 summarizes the dates, spacing, and types of frac-hits reported in 6 North American unconventional reservoirs including: Woodford, Eagle Ford, Bakken, Haynesville, Marcellus, Montney, and Wolfcamp. Frac-hits commonly happen in 2 fracturing scenarios. They are infill and sequential fracturing. a illurstrates these fracturing scenarios. Frac-hits in infill fracturing are observed as pressure increase in an existing well during the fracturing treatment of an adjacent new well. Frac-hits in sequential fracturing are observed as pressure increase during the fracturing treatment of an adjacent well, which is sequentially fractured.

As listed in Table C.1, frac-hits laterally happen between wells that are up to 1200 m from each other within the Wolfcamp Formation. However, frac-hits are also reported between wells completed in different formations. Vertically, frac-hits occur between wells that are up to 170 m apart in different formations.

C.2 Reservoir, Drilling, and Completion Information

This section provides details about the formations, drilling, and fracturing design of 55 wells in the Horn River Basin. This section describes the data source and basic properties of target shale formations. It also shows the well structure and drilling parameters for well pads. Finally, this section lists the key completion design information including the stages, clusters, injected water volume, and sand mass.

C.2.1 Data Source

The reservoir information is mainly obtained from Sardinha et al. (2014), Virues et al. (2015b), and the B.C. Oil and Gas Commission (BCOGC) website. The drilling and fracturing information for each well is obtained using a unique well identifier (UWI) from BCOGC online data on September 2018.

C.2.2 Formation

The target wells are completed in 3 shale members of Horn River Formation: Evie (EV), Otter Park (OP), and Muskwa (MU). The total thickness of Horn River shales varies from 140 to 210 m, at the depth between 2200 and 2700 m. The Horn River shales are overlain by Ft. Simpson shale, which is clay rich and has relatively low porosity and permeability (Dong et al. 2015; 3017). There is a thin barrier of Middle Devonian Carbonate (*MDC*) between OP and EV shales. Here, we mainly describe the EV, MDC, OP, and MU Formations.

EV: EV shale is located in the lower part of the Horn River Formation, and consists of organic-rich siliceous shale. Its total thickness varies from 40 to 70 m. Total organic content (TOC) for EV shale is around 0.049. EV shale has ultra-low porosity (4.5%) and permeability (205 nD). Its mineralogy is mainly quartz (48%) and calcite (31%), with a small fraction of clay (8%) and dolomite (<2%).

MDC: MDC is a barrier between EV and OP shales. Its total thickness is generally less than 40 m. TOC (1.4%), porosity (3%), and permeability (100 nD) are relatively lower than those of EV and OP shales. MDC is mudstone. The mineralogy of MDC shale is 40 to 80% calcite, up to 30% dolomite, 5 to 20% quartz, with minor clay and pyrite.

OP: OP shale is in the middle part of the Horn River Formation. It mainly consists of calcareous shale. The average formation thickness of OP shale is about 120 m. TOC for OP shale is around 0.034. OP shale has ultra-low porosity (3.8%) and permeability (174

nD). Its mineralogy is mainly quartz (69.1%), clay (23.2%), calcite (6.3%) and dolomite (<4%).

MU: MU shale is located in the upper part of the Horn River Formation. It mainly consists of organic-rich shale. In the study area, its total thickness varies from 20 to 60 m. TOC for MU shale is around 0.031. MU shale has ultra-low porosity (4.3%) and permeability (194 nD). Its mineralogy is mainly quartz (69.1%) and clay (17.3%), with a small fraction of calcite and dolomite (<1%).

C.2.3 Drilling

As illustrated in Fig. C.1, this study investigates 4 pads including Pads A, B, C, and D, which have 8, 18, 19, and 10 wells, respectively. These horizontal wells were drilled from a single surface pad location. The general orientation of these wells is NW-SE, which is in the direction of minimum principal stress.

Fig. C.2a describes the location of conductor, casings and cements in the vertical section of wellbore. The conductor has a diameter of 406 mm, and is around 36 m below the wellhead. The surface casing and surface cements extend from ground surface to around 782 m, isolating wellbore from Debolt aquifer which is at the depth of around 700 m. The production casing and cement extend from ground surface to the toe section of wellbore.

Table C.2 lists UWI, spud date, total depth (TD), true vertical depth (TVD) for these 55 horizontal wells in 4 pads. In this study, we use a short well name to represent UWI. For example, Well BA represents well A in Pad B. Spud date represents the onset of drilling a well. These target 55 wells were drilled from 2009 to 2012. Drilling each pad generally takes 1 to 2 months. As illustrated in Fig. C.2b, TVD describes the vertical distance from ground surface to the lateral section of wellbore. TD describes the total length of the wellbore. Below describes the detail drilling information for each pad:

(1) Pad A comprises 8 horizontal wells drilled in 2010. 4 wells are drilled on the south side, and the other 4 are on the north side. These 8 wells are completed in the MU and OP Formations. The average lateral spacing between neighboring wells within MU and OP Formations is around 780 m, respectively. The vertical spacing between MU and OP wells varies from 31 to 46 m. The average TVD for these 8 wells varies from 2429 to 2508 m.

(2) Pad B comprises 18 wells drilled in 2011. 9 wells are drilled on the north side and the other 9 are on the south side. 6 wells are each completed in MU, OP, and EV Formations. The average lateral spacing between neighbouring wells in each formation is about 300 m. The vertical spacing between MU and OP wells is up to 60m, and that between OP and EV wells is up to 153 m. The average TVD for 18 wells varies from 2433 to 2594 m.

(3) Pad C comprises 19 wells. 9 wells are drilled on the south side in 2011, and the other 10 wells are drilled on the north side in 2014. On the south side of Pad C, 3 wells are each completed in MU, OP, and EV Formation respectively. The average lateral spacing between neighboring wells completed within MU and OP is about 300 m. The lateral spacing between neighboring EV wells is 600 m. The average vertical spacing between OP and MU wells and between EV and OP wells is around 60 m, respectively. In the north side of Pad C, 2, 3, and 5 wells are completed in the MU, OP, and EV Formations, respectively. The average lateral spacing between neighboring wells completed within MU, OP, and EV Formation is around 400 m, respectively. The average vertical spacing between OP and MU wells and between OP and EV wells is around 60 m, respectively.

(4) Pad D comprises 10 wells drilled in 2012. These 10 wells are located in the same side of Pad D. 3, 3, 4 wells are completed in the MU, OP, and EV Formation, respectively. The average lateral spacing between neighboring wells completed within MU and OP Formation is about 600 m, respectively. The average lateral spacing between neighboring wells completed in the EV shale is 300 m. The average vertical spacing between OP and MU wells and between OP and EV wells is around 65 m, respectively.

D.2.4 Completion

After 6 to 12 months of drilling, target wells move to the completion period. The wells were perforated before fracturing treatment. Wells in a pad are then fractured in a sequence. It generally takes less than 1 month to complete a pad. After fracturing treatment, wells are shut-in for 1 to 2 months for preparing the flowback equipment at wellhead.

Table C.2 summaries the completion information including the stages, clusters, injected water volume, and sand mass of target wells in 4 pads. Fig. C.2b illustrates the concepts of stage and clusters. The target wells were multi-fractured with 17 to 27 stages. The stage spacing generally varies from 100 to 120 m. In general, there are about 3 to 5 clusters for each stage of wells in Pads B, C, and D. The cluster spacing in a stage generally varies from 25 to 40 m. In Pad A, 4 wells are fractured with a single cluster for each stage.

The total completed length of target wells varies from 1400 to 2500 m. Each stage is fractured with a large volume of slick water and sand. On average, 200 tons of sand and 2800 m^3 of water are injected into each stage at pressures between 50 and 70 MPa. The sand size varies from 100 to 40/70 mesh.

C.3 Frac-hit Data

In this section, we provide the source of frac-hit data. Also, we describe the design of pressure monitoring and key results for frac-hit data analysis in target wells.

C.3.1 Data Source

The main sources of frac-hit information for Pads A, B, C, and D include industry, BCOGC, and existing literature. The average pressure increase caused by frac-hits in Pads C and D is obtained from existing literature (Sardinha et al. 2014; Shokri et al. 2017).

The frac-hits in Pads A and B from BCOGC are incomplete. In this study, we mainly show the results of frac-hits in Pads C and D.

C.3.2 Frac-hit Surveillance Design

During fracturing treatment of each stage in a target well, wellhead pressures of offset wells in a pad are continuously recorded in a frequency of seconds. The pressure increase caused by each frac-hit between 2 wells is then averaged for all stages. Table C.4 lists the average pressure increase caused by frac-hit in 4 pads reported online and existing literature.

C.4 Microseismic Data

In this section, we provide the source of MS data. Also, we describe the design and results of MS surveillance in target wells.

C.4.1 Data Source

The results of MS surveillance on 243 stages of wells in Pads A, C, and D are mainly obtained from industry. The MS design for Pads A, C, and D are obtained from existing literature (Sardinha et al. 2014; Shokri et al. 2017; Virues et al. 2015a, 2015b; Urban-Rascon). MS surveillance is not applied in Pad B.

C.4.2 Microsesimsic Surveillance Design

During fracturing treatment, acoustic waves are generated and propagated in the Formation. The velocities of these waves are monitored at downhole geophones (see Fig. C.3). MS data were monitored during the fracturing treatments of 49 stages of 7 wells in Pad A, 145 stages of 9 wells in Pad C, and 119 stages of 10 wells in Pad D.

The signals monitored at downhole geophones are processed to locate the MS event, each of which represents a small earthquake. The location of MS events is then interpreted to estimate fracture length, fracture height, and fracture width. The relative error in the estimated fracture height and fracture length is 10 m and 20 to 40 m, respectively.

The frequency and magnitude of MS events are also reported in the MS data. The after linear-regression of magnitude and the logrithm of frequency provide two key properties, namely D-value and B-value. D-value is usually used to describe the distribution of MS events. D-values of 0, 1, 2 and 3 indicate a point clustering, a linear clustering, a planar distribution and a uniform distribution of MS events in space respectively (Yousefzadeh et al. 2018; Zorn et al. 2014). B-value is an indicator of stress regime and failure mode of MS events (Yousefzadeh et al. 2018; Zorn et al. 2014). B-values <1, ~1 and >1 indicate reverse faulting or fracture closing, reactivation of fault or natural fractures (Maxwell et al. 2009), and extension of hydraulic fractures (Zorn et al. 2014), respectively.

C.4.3 Results of MS Data

Table C.3 summarizes the key MS results including the number of stages monitored MS data, the total number of MS events, and the number of MS events located within 500 m away from wellbore, D-value, B-value, fracture length, fracture height, and fracture width.

In total, 265156 MS events are monitored during the fracturing treatments of 243 stages in Pads A, C, and D. About 89% (n =235569) of MS events occur within 500 m from the wellbore. In other words, about 11% of MS events occur more than 500 m away from wellbore. In Pad D, the results show that most of the MS events are recorded less than 200m above the wellbores (see Fig. 5.6). There are 3.5%, 0.7%, and 0.4% of MS events recorded in the FT Simpson while fracturing these 118 stages of wells in Pad D. During the fracturing treatment of OP wells in Pad D, about 13.5 % of MS events are recorded in the MU Formation. EV wells have 34% and 6.9% percent of events are recorded in the OP and MU Formations, respectively.

Fig. C.4a shows the stastistical results of B-value for 239 stages in Pads A, C, and D. B-values for 5 stages are not available in Pad D. 7 out of 239 stages have a B-value close to 1 This indicates the reactivation of natural fractures or fault reactivation during the fracturing treatment. Fig. C.4b shows the statistical results of D-value for 243 stages in

Pads A, C, and D. D-value for 1 stage is not available in Pad C. D-values vary from 0.14 to 3.14. 90% of D-values range from 2 to 3, suggesting a planar to uniform distribution of MS events.

C.5 Tracer Surveillance Data

This section provides the source of tracer data, and describes the design and results of tracer surveillance in target wells.

C.5.1 Data Source

We mainly obtained the tracer-surveillance information in Pads A and D from industry, BCOGC, and existing literature. We obtained the design of artificial tracers in Pad D from industry. The tracer concentration profiles for 3 wells are available in Pad D. We obtained the design of artificial tracers in Pad A from BCOGC website. The results of artificial tracers in Pad A were modified from Virues et al. (2015a).

C.5.2 Tracer Design

Fig. C.7 describes the design of chemical and radioactive tracers in Pad A. A specific chemical tracer is injected to each well in Pad A. The tracer concentration is measured during flowback period. Proppants coated with Iridium and Scandium were injected into Wells B and E in Pad A. Proppants coated with Antimony were injected into Wells A and G in Pad A. Gamma-ray logs were run on all wells in Pad A to measure the radioactive materials in Pad A.

Fig. C.8a illustrates the design of radioactive tracer in Pad D. Proppants coated with Iridium, Scandium, and Antimony were injected into Wells I, H, and F, respectively. Gamma-ray logs were run on Wells F, G, H, and I to measure the radioactive materials in Pad A.

C.5.3 Results of Tracer

Artificial Tracer. In Pads A, C, and D, chemical tracers and radioactive tracers are injected with water and proppants during their fracturing treatments. The surveillance of artificial tracers is used to investigate flow communications of proppants between wells in these target pads. The results of artificial tracers in Pad C are not available. Here, we mainly describe the design and results of artificial tracers in Pads A and D.

Chemical Tracer. During fracturing treatment, chemical tracers are mixed with fracturing water before pumping them underground. The concentration of these conservative tracers is measured together with rate and pressure data during flowback process. A conservative tracer has negligible adsorption or decay in the presence of formation rock and fluids (Shook et al. 2017). In Pad D, 6 unique conservative tracers are injected with water during fracturing treatment. In Pad B, 8 chemical tracers are injected into each well during fracturing treatment.

As illustrated in Fig. C.5, chemical tracers injected into OP wells are reported in the flowback water of MU wells in Pad D. This suggests that fracturing water from EV wells can travel upward at least 65 m above OP Formation. Also, Fig. C.6 shows that tracers injected to a MU well (Well D0) are reported in an EV well (Well DA)'s flowback water, suggesting that fracturing water from MU wells can travel downward to EV Formation.

Fig. C.7 shows that the chemical tracers injected into Well AG are reported in the flowback water of Well AB in Pad A. The lateral spacing between these two wells is about 1180 m. The results suggest the fracturing water can travel more than 1000 m away from wellbore in the lateral direction.

Radioactive Tracers. Radioactive tracers are embedded in proppants. These proppants with isotopes are pumped with fracturing water. Gamma-ray logs were run to detect these radioactive tracers after fracturing treatment. In Pad D, proppants embedded with Scandium 146, Iridium 192, and Antimony 124 are pumped into Well DF37, DH37 and

DI37, respectively. Fig. C.7a illustrates the tracer design in Pad A. Proppants embedded with Scandium 146 and Iridium 192 are pumped into Wells AB and AE, respectively.

As illustrated in Fig. C.8, the radioactive tracers injected into Well DF are detected by the Gamma-ray logs of Well DG in Pad D. This suggests that proppants from Well DF can travel upward at least 130 m. Fig. C.7a also shows that proppants injected into Well BA were detected in the Gamma-ray logs of Well BC in Pad A. The results suggest the proppants can travel 780 m away in the lateral direction.

Natural Tracers. Gas samples were collected from wells in Pads A, B, C, and D. The composition of H_2S and CO_2 were weekly reported during flowback period. The gas composition of H_2S and CO_2 from MU and OP wells is different from those from EV wells because of the MDC barrier separating them.

Fig. C.9 compares the CO_2 content in the gas samples of MU, OP, and EV wells. In general, EV wells have relatively higher CO_2 content than MU and OP wells. In several MU wells, the gas content can reach to 16%, which is very close to that in EV wells.

C.6 Production Interference

In this section, we provide the data source and methods of production interference in target wells. We list 6 cases of well interference in addition to the main body of this paper.

C.6.1 Data Source

We mainly obtained the production data of rates and pressure in Pads A, B, C, and D from industry. The flowback data include wellhead pressure, water rate and gas rate. They are hourly reported for all pads. The available production data after flowback include the hourly gas rate and wellhead pressure.

C.6.2 Methods

We analyze the change in casing pressure of shut-in wells when other wells in the pad are shut-in and re-opened to evaluate well interference during flowback and post-flowback.

C.6.3 Results of Interference

Short-term Well Interference. Fig. C.10 illustrates two cases of well interference in Pad D during flowback period. Fig. C.15 shows the distribution of load recovery for target 52 wells during 20 days of flowback. The results show that there is relatively large variation (from 0.03% to 12.03%) in load recovery of the Horn River wells.

Long-term Well Interference. Fig. C.10 to Fig. C.14 illustrate four cases of well interference in Pads A, B, and D after up to 2 years of production.

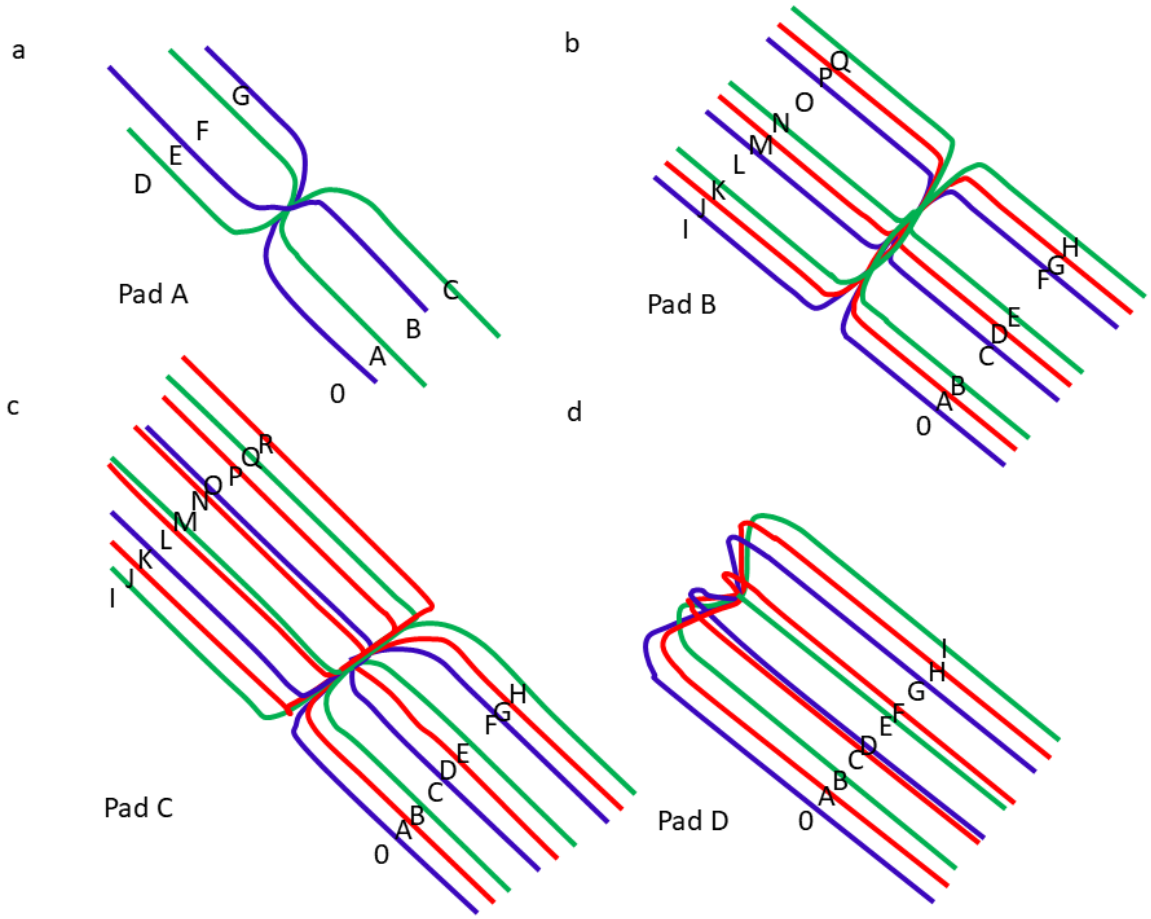

Fig. C.1: Layout of (a) Pad A, (b) Pad B, (c) Pad C, and (d) Pad D. The green, blue, red lines represent that the wells completed in Muskwa, Otter Park, and Evie shale, respectively.

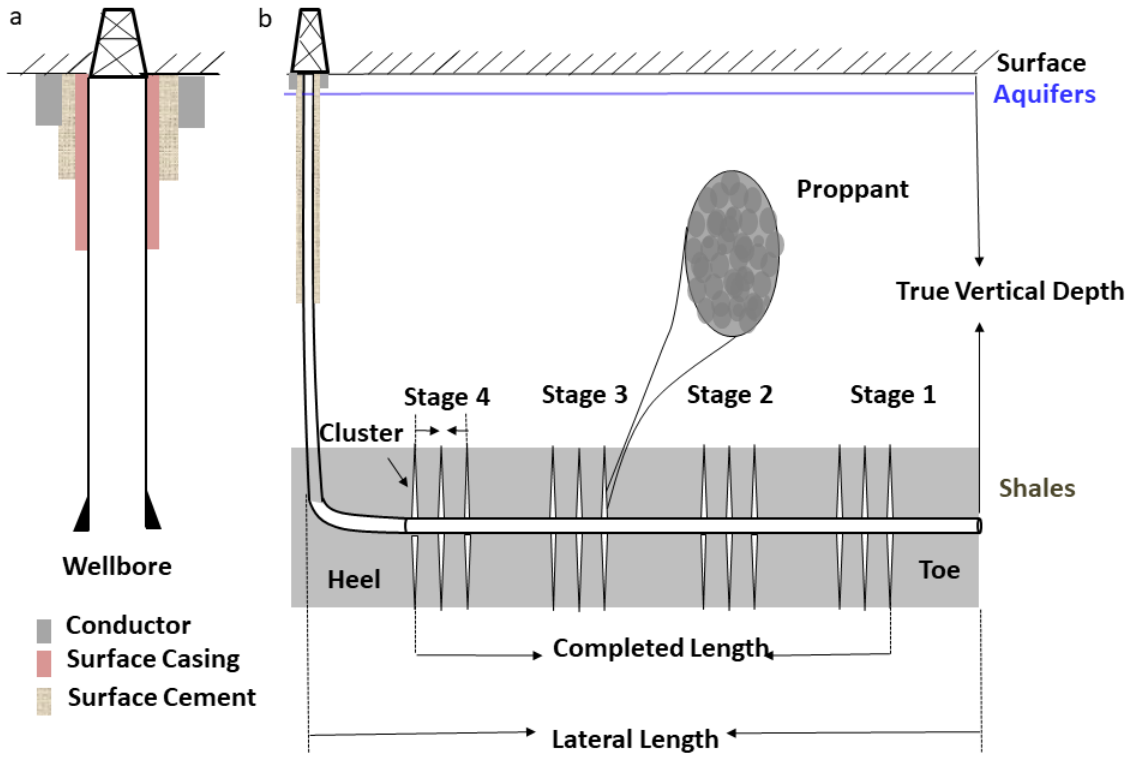

Fig. C.2: Schematics showing a) well structure of vertical section and (b) drilling and fracturing design parameters including true vertical depth, lateral length, toe, heel, stages, clusters, and completed length.

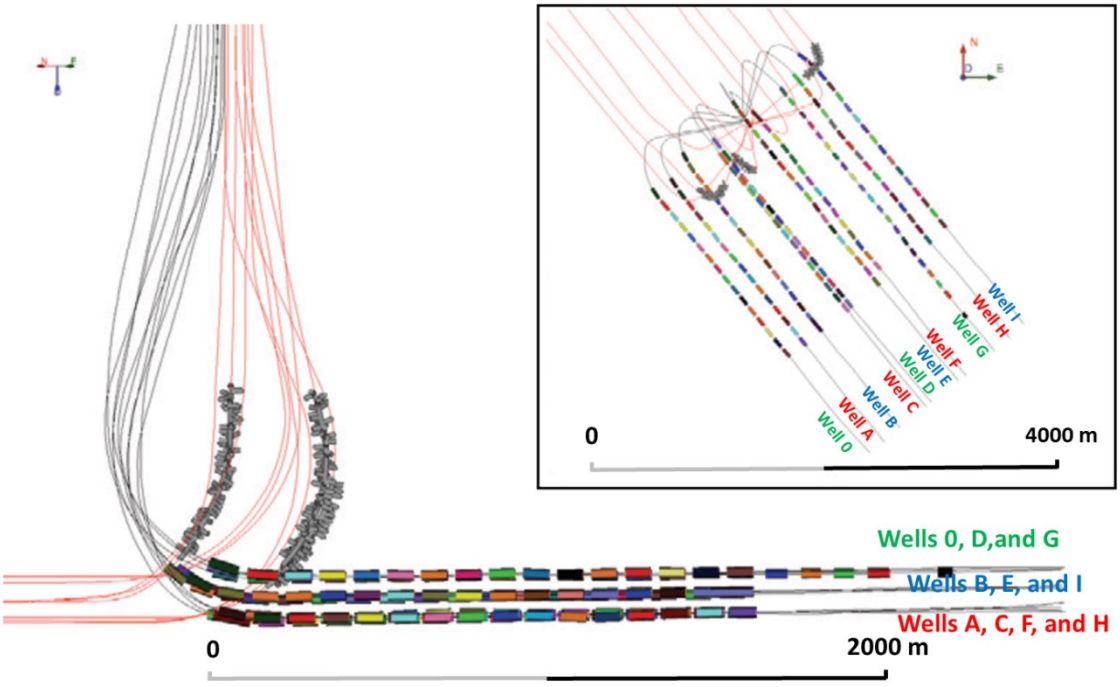

Fig. C.3: A cross section view (left) and map view (right) of the monitoring arrays (gray) used to monitor the completion stages (colored) (modified from Hendrick et al. 2016).

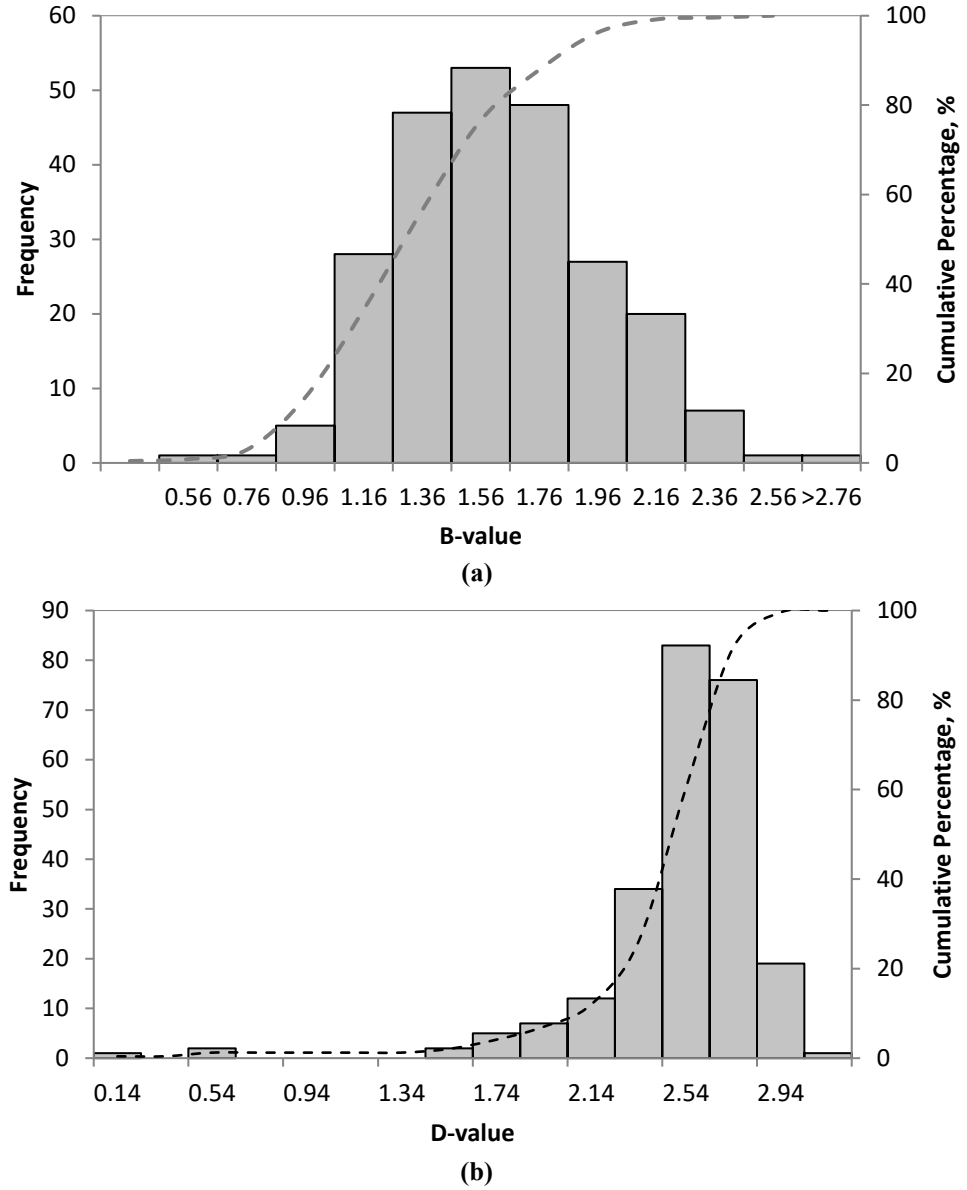

Fig. C.4: Distribution of (a) B-value and (b) D-value of wells in Pads A, C, and D.

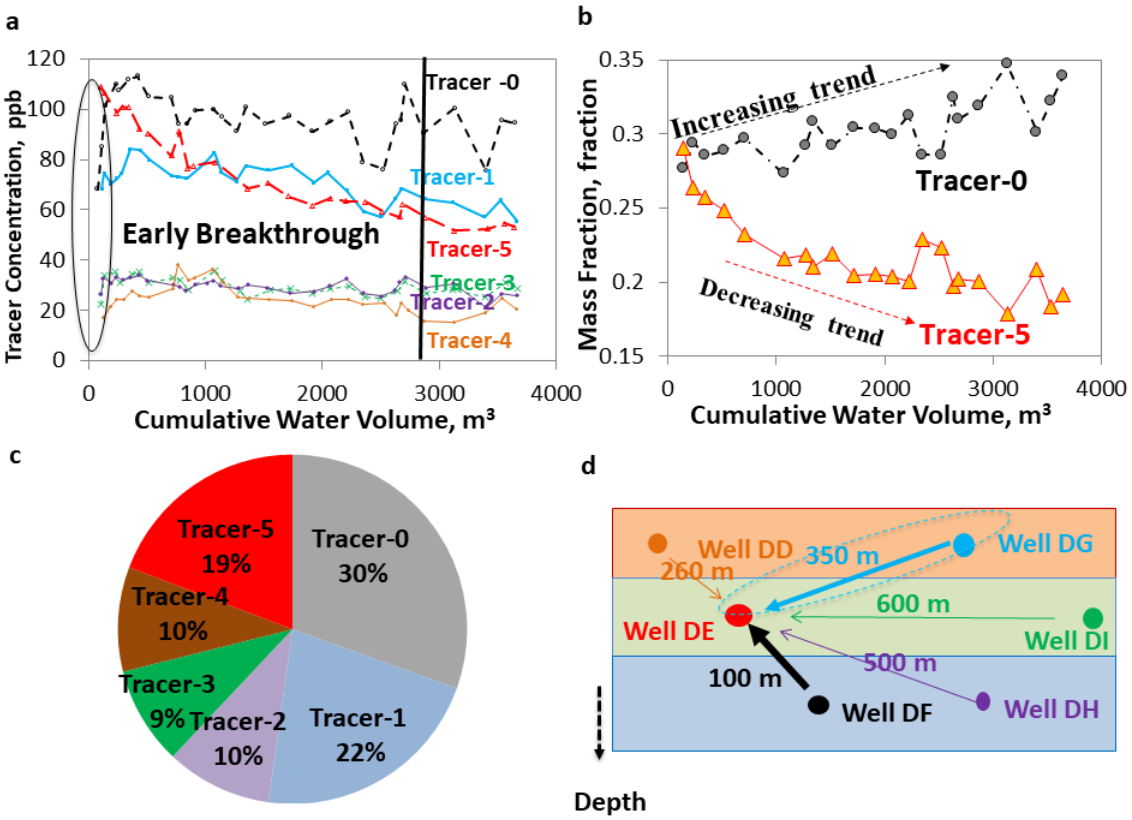

Fig. C.5: (a) Concentration profiles of chemical tracers injected into Pad D in the water samples of Well DE; (b) Mass fraction of tracer injected into Well DF (Tracer-0) increases, and that of tracer injected into Well DE (Tracer-5) decreases during Well DE's flowback process; (c) Mass fraction of Tracers 0 and 1 are higher than that of Tracer-5 after 2880 m^3 of water volume recovered in Well DE; (d) Schematics illustrate the possible pathway of tracer flow in Pad D.

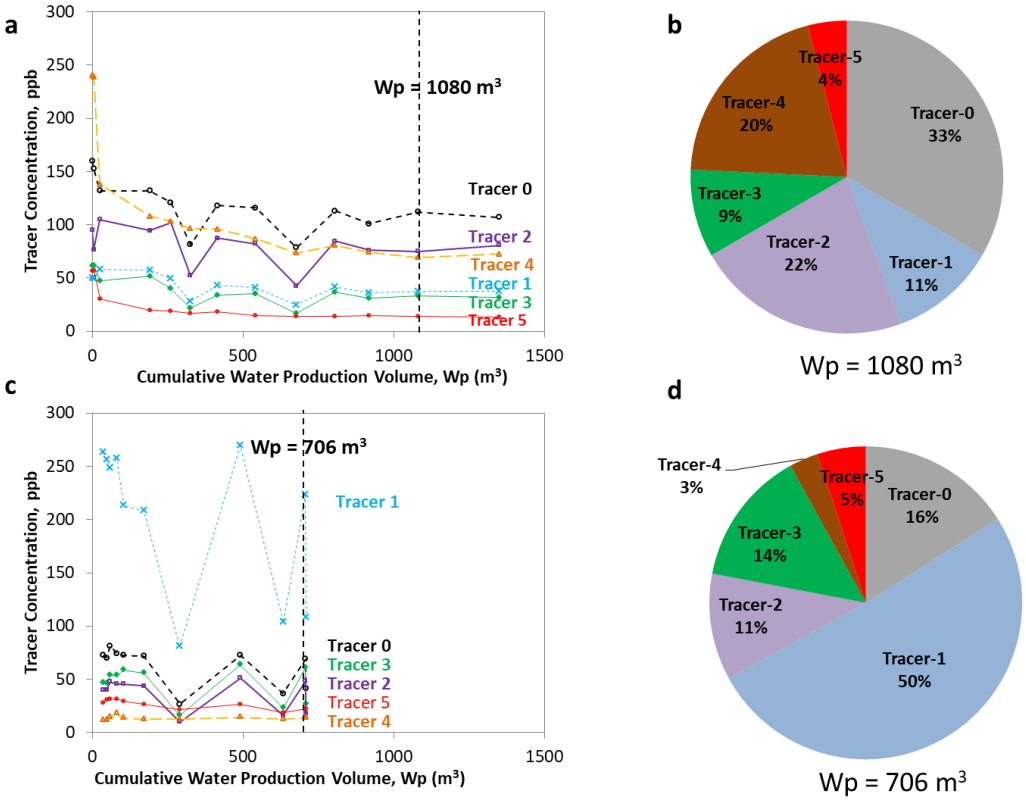

Fig. C.6: Tracer concentration profiles for (a) Well D0 and (c) Well DA during flowback. Comparing the concentration of Tracers-0, 1, 2, 3, 4, and 5 for (b) Well 0 and (d) Well A shows a relatively high tracer concentration from other wells in the pad. Tracers-0, 1, 2, 3, 4, and 5 are colored by gray, blue, green, yellow, red, and pink, respectively. The vertical dashlines in (a) and (c) represent the time when flowback water sampled for (b) and (d).

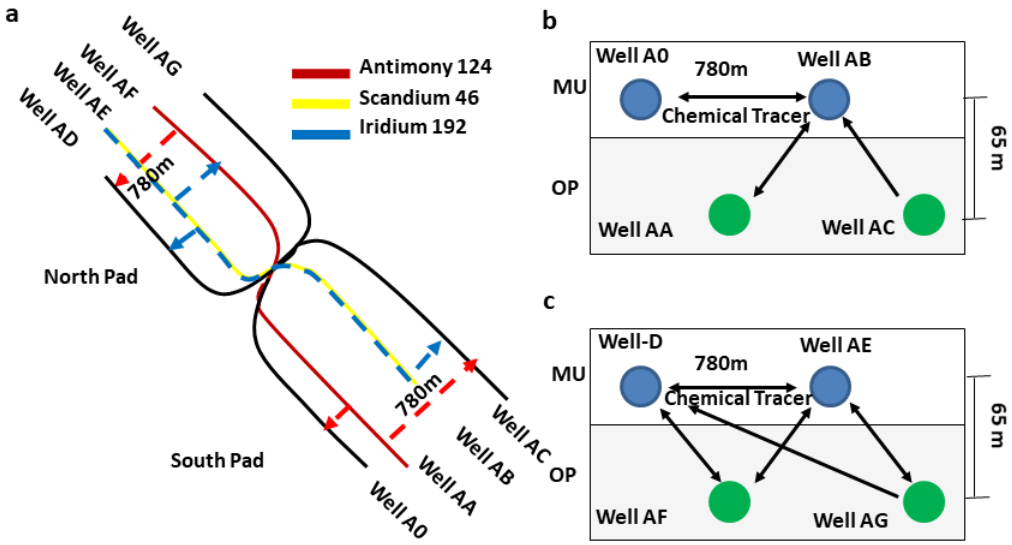

Fig. C.7: Results of artificial tracer surveillance results in Pad A: (a) Proppants traced with radioactive materials are detected by the Gamma-ray loggings in wells 780 m away. The stages injecting Antimony, Scandium, and Iridium are colored by red, yellow, and blue, respectively; (b) and (c) Illustrations of chemical tracer migration in south and north side of Pad A, respectively.

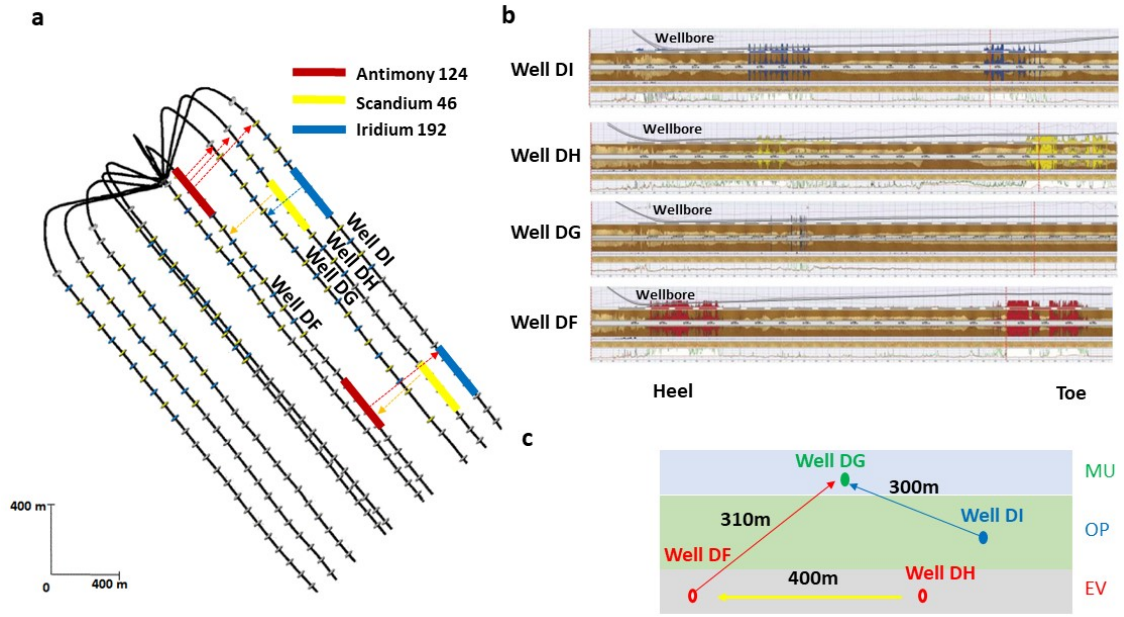

Fig. C.8: Illustration of radioactive tracers migrating across wells in Pad D: (a) Proppants traced with radioactive materials of Antimony, Scandium, and Iridium are injected into different stages of Wells DF, DH, and DI, respectively; (b) Response of Iridium is observed on the Gamma-ray loggings at the downhole of Well G; (c) Illustration of proppant migrating among Wells DF, DG, DH, and DI.

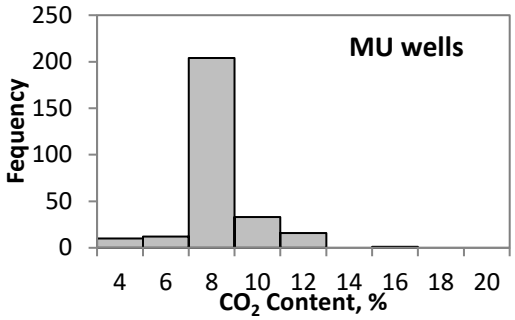

(a)

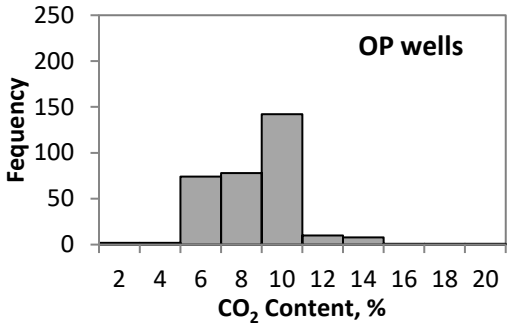

(b)

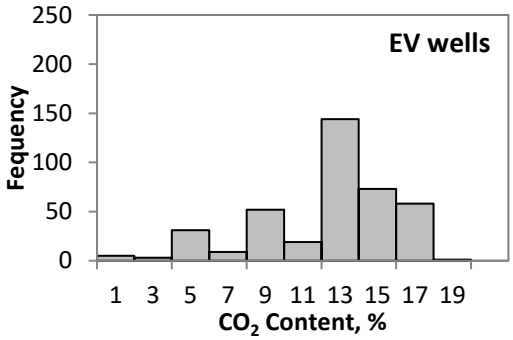

(c)

Fig. C.9: The distribution of CO_2 content of gas samples from (a) MU, (b) OP, and (c) EV wells.

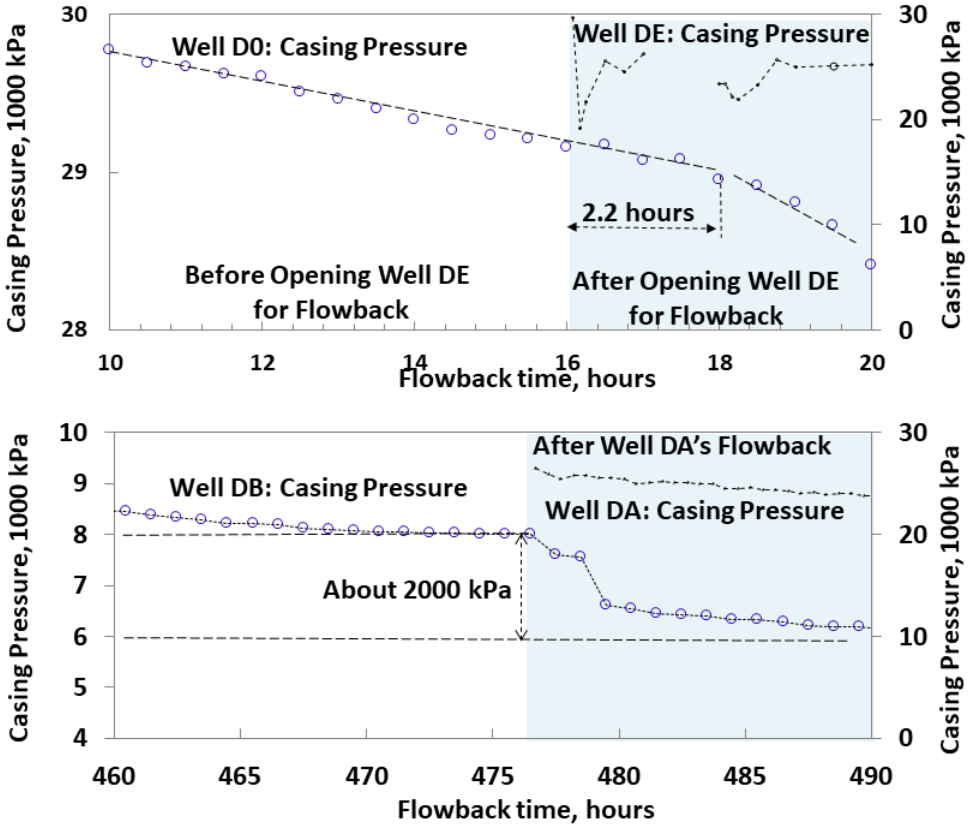

Fig. C.10: Two Cases of well interference in Pad D during flowback period: Well D0's response to Well DE's opening for flowback: (a). Well D0 shows a much steeper decline in casing pressure 2.2 hours after opening Well DE: (b). Well DB37's casing pressure drops around 2000 kPa after opening Well E; The choke size for Well DB37 remains constant after opening Well DA.

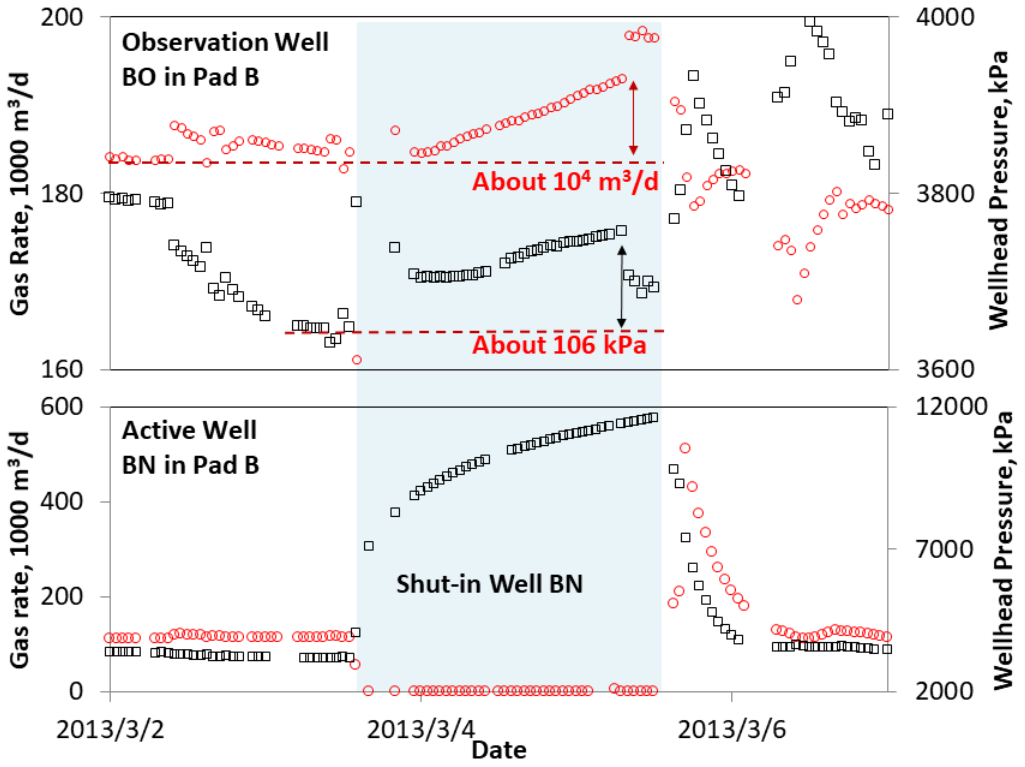

Fig. C.11: Well interference between Wells BO and BN in Pad B after 1 year of production. The well spacing between these 2 wells is about 450 m. After shut-in of Well BN, a pressure increase of 106 kPa and an increase of gas rate are observed on Well BO.

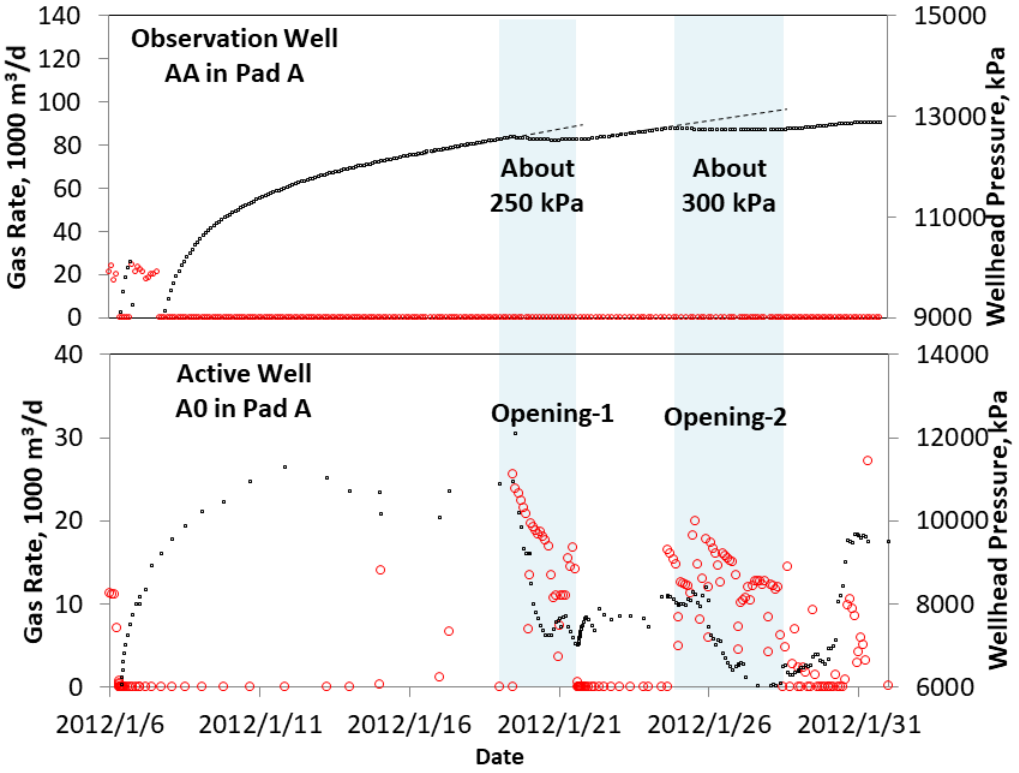

Fig. C.12: Well interference between Wells A0 and AA in Pad A after 1 year of production. The vertical well spacing between these 2 wells is about 65 m. After the re-openings of Well A0, pressure disturbances are observed on Well AA.

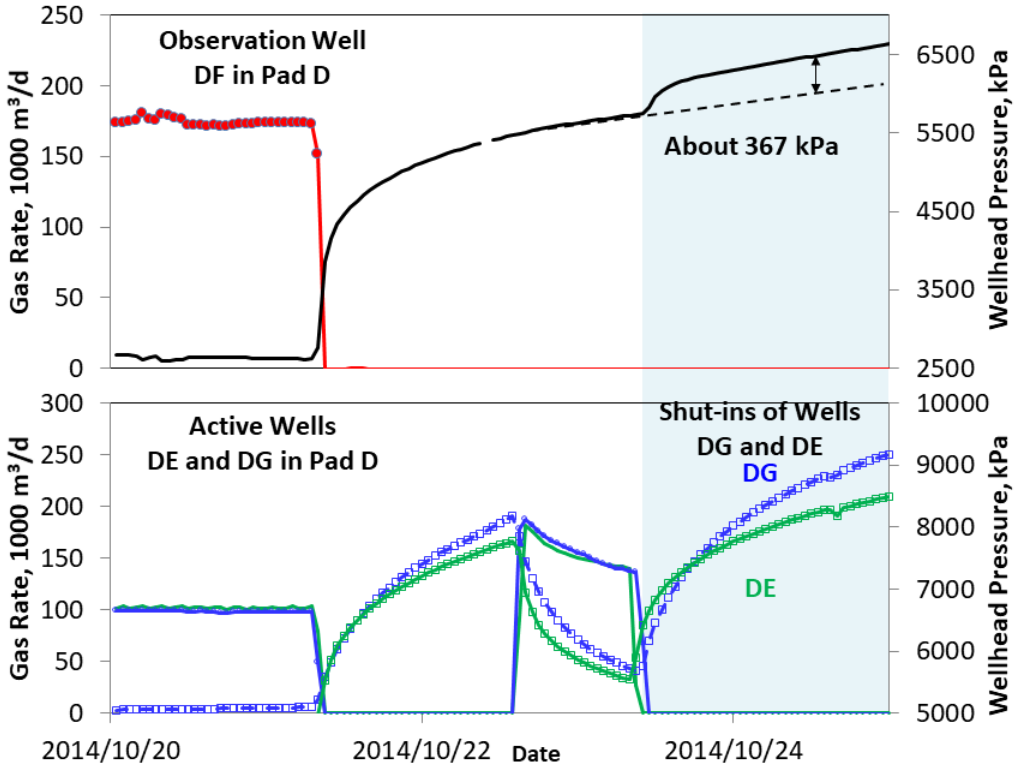

Fig. C.13: Well interference between Wells DF, DG, and DG in Pad D after 1 year of production: After the shut-in of Wells DE and DG, a pressure increase of 367 kPa is observed in Well DF.

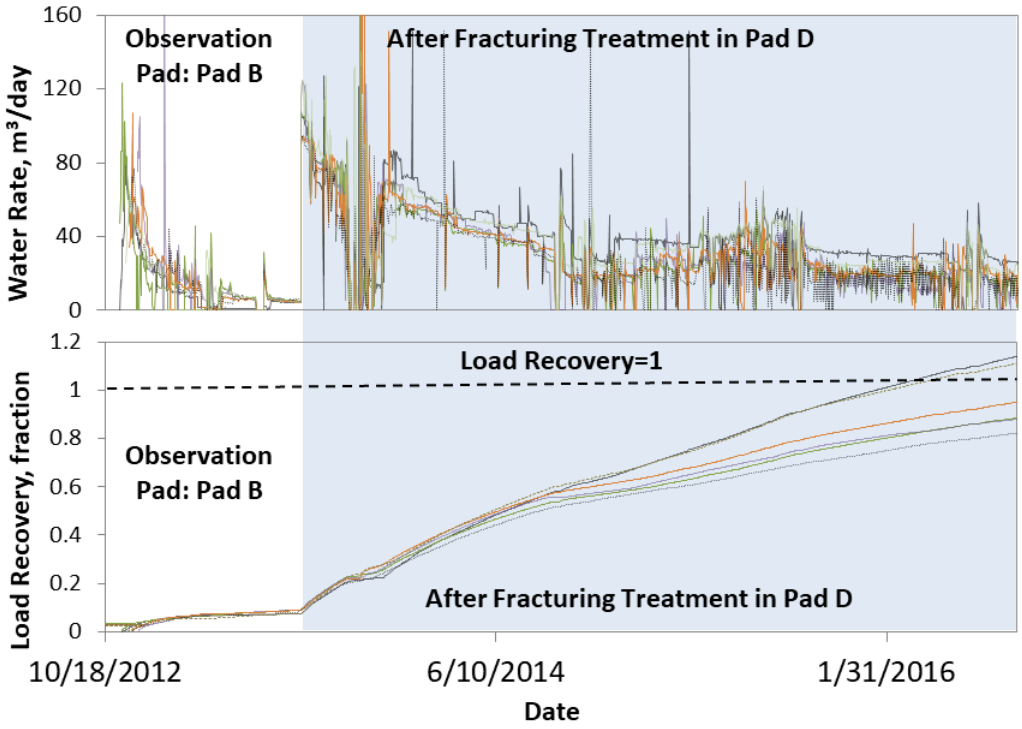

Fig. C.14: Well interference between wells in Pads B and D: (a) Daily production data from Pad B show a significant increase in water rate after the fracturing Pad D. Tracers from Pad D are reported in the produced water from Pad B. (b) The load recovery of 2 wells in Pad B is larger than 1 after about 2 years of production.

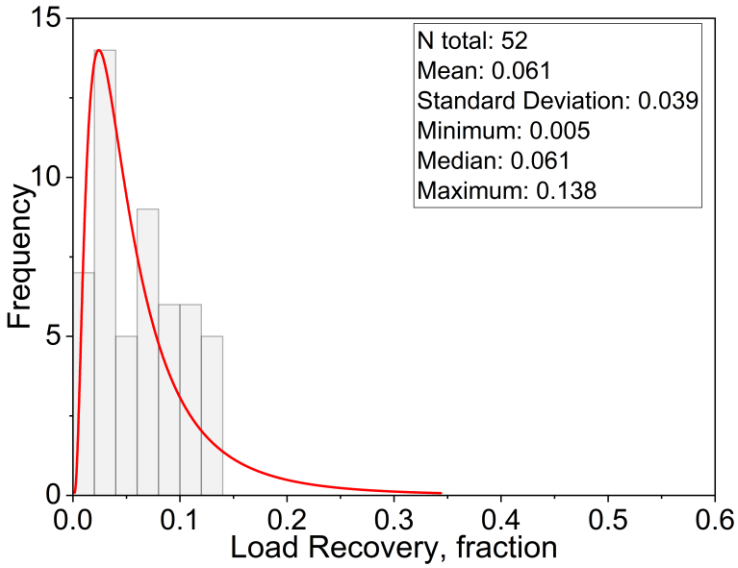

Fig. C.15: Statistical results of load recovery for 52 wells in 4 pads after 20 days of flowback.

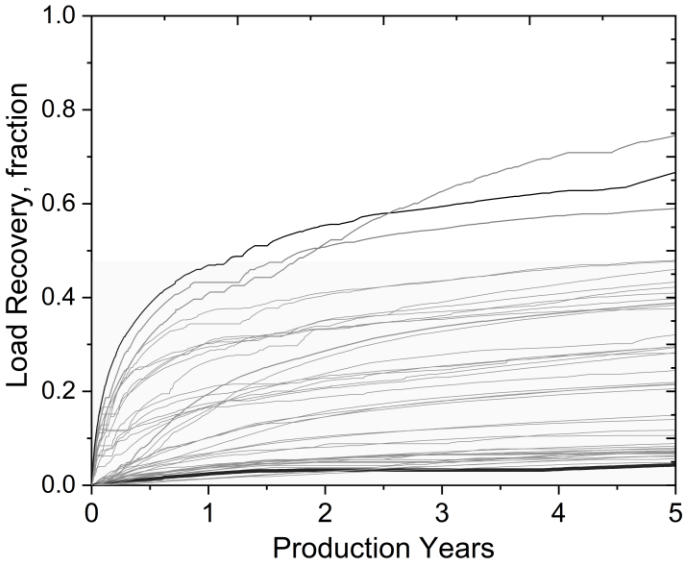

Fig. C.16: Load recovery profiles of 34 wells in Pads A, C, and D show higher values than 0.5 after 5 years of production, except for 3 wells in Pad C.

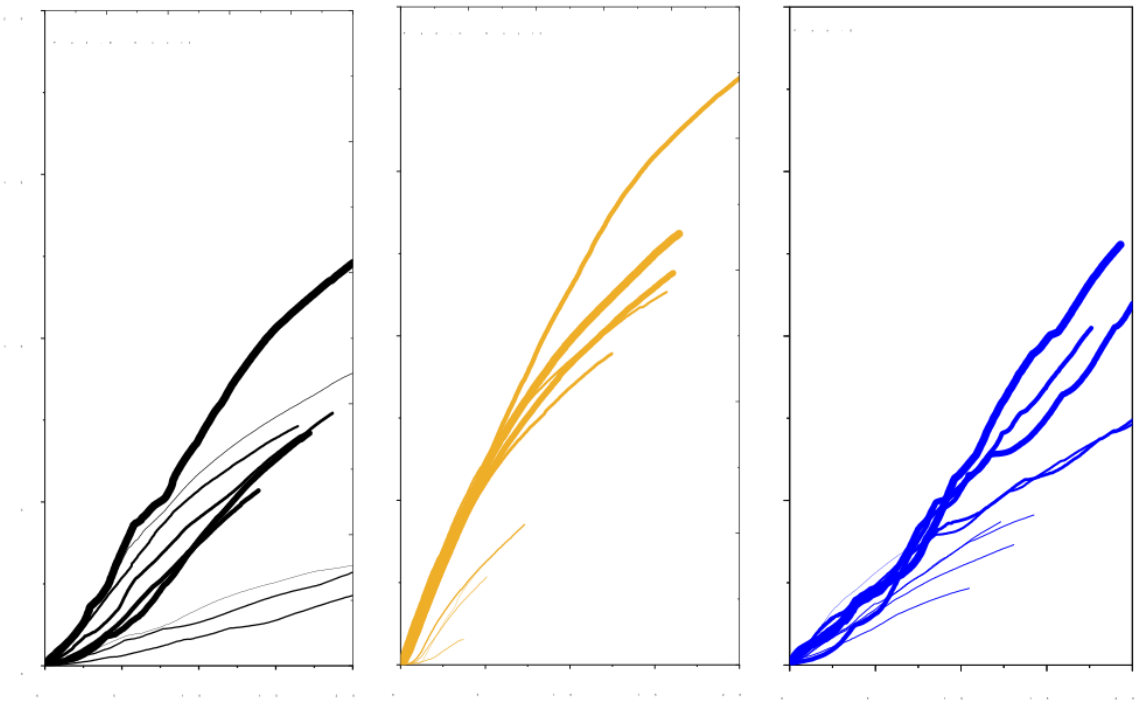

Fig. C.17: Load recovery profiles of Pads B, C, and D showing a general higher load recovery in early-open wells (thick lines) than that in late-open wells (thin lines).

Table C.1: Summary of the frac-hit information of location, time, types, and well spacing for the North American shale and tight oil/gas wells reported in recent literature. na = no available data.

Shale Formation	Location	Year	Type of Frac-hit	Maximum Well Spacing, m		Data Source
				In lateral direction	In vertical direction	
Woodford	Kingfisher County, Oklahoma, US	na	Infill	na	na	Haustveit et al. 2017; Sickle et al. 2017
	Grady County, Oklahoma, US	na	Infill	na	na	Swanson et al. 2018
		2015	Infill	488	na	King et al. 2017
Eagle Ford	na	2014	Infill	229	na	King et al. 2017
	na	2015	Sequential	296	na	King et al. 2017
	na	na	Infill	305	na	Kurtoglu et al. 2015
	na	na	Infill	107	na	Kurtoglu et al. 2016
	na	2015	Infill	213	na	Anderson et al. 2016
	Dimmit County, Texas, US	na	Sequential	152	na	Swami et al. 2017
Bakken	North Dakota, US	2011	Infill	265	25	Daneshy and Pomeroy, 2012
	McKenzie County, North Dakota, US	2015	Sequential	427	>55	Bommer et al. 2017
		2016	Infill	610	na	Bommer et al. 2018
Haynesville	North Louisiana, US	2013	Infill	1463	na	Esquivel and Blasingame, 2017
	na	2014	Sequential	na	na	Esquivel and Blasingame, 2017
	Texas and Louisiana, US	na	Infill	1233	na	Sani et al. 2015
	na	na	Infill	na	na	Lawal et al. 2013
Marcellus	na	na	Infill	na	na	Lawal et al. 2013
Montney	British Columbia, Canada	na	Infill	1207	>177	Peterson et al. 2018
Wolfcamp	na	na	Infill	na	na	Lascelles et al. 2017
	Odessa County,Texas, US	2016	Infill	335	73	Rainbolt and Esco 2018
	na	2014 to 2016	Infill	201	58	Liang et al. 2017
	na	na	Sequential	229	na	King et al. 2017
	na	na	Infill	na	na	Sun et al. 2017
	na	na	Infill	322	na	Cao et al. 2017

Table C.2: Summary of formation, drilling, and completion information for the target wells completed in the Horn River Basin.

			Drilling Information				Completion Information						
Pad Name	Well Name	Unique Well Identifier (UWI)	Target Formation	Total Depth, m	True Vertical Depth, m	Spud Date	Completion Start Date	Completion End Date	Number of Stages	Number of Clusters	Average Sand per Stage, tonnes	Average Water per Stage, m^3	Completed Length, m
Pad A	A0	200B096H094O0800	OP	4515	2485	1/28/2010	6/30/2010	8/7/2010	20	20	187.3	2803.8	1904
	AA	200C096H094O0800	MU	4227	2429	12/26/2009	7/16/2010	8/3/2010	16	64	198.7	2617.1	1575
	AB	200B097H094O0800	MU	4380	2450	1/13/2010	7/3/2010	8/9/2010	17	17	198.7	2761.3	1599
	AC	200D096H094O0800	OP	4764	2477	1/25/2010	7/1/2010	8/3/2010	20	80	196.2	2669.3	1975
	AD	200C029I094O0800	OP	4270	2500	1/28/2010	7/3/2010	7/25/2010	15	60	200.3	3751.4	1473.5
	AE	200A021J094O0800	MU	4534	2486	1/4/2010	7/1/2010	8/10/2010	19	19	197.2	3705.3	1804
	AF	200D030I094O0800	MU	4375	2477	1/16/2010	7/14/2010	8/7/2010	17	68	195.9	3801.9	1675.5
	AG	200D021J094O0800	OP	4667	2508	1/24/2010	6/30/2010	8/10/2010	20	20	196.2	3708.2	1900.6
Pad B	B0	200D046H094O0800	MU	4864	2435	7/15/2011	7/1/2012	7/22/2012	18	90	228	2823	2187
	BA	202D046H094O0800	EV	5008	2560	7/23/2011	6/30/2012	7/21/2012	20	70	195	2974	2444
	BB	203D046H094O0800	OP	4886	2462	7/17/2011	7/2/2012	7/21/2012	19	95	116	1529	2310
	BC	202B055H094O0800	MU	4751	2440	7/25/2011	7/2/2012	7/21/2012	18	90	230	2814	2179
	BD	200B055H094O0800	EV	4834	2560	7/20/2011	6/30/2012	7/24/2012	18	54	207	3116	2360
	BE	202A055H094O0800	OP	4792	2491	8/1/2011	7/1/2012	7/28/2012	19	57	223	2699	2293
	BF	200A055H094O0800	MU	4864	2433	7/27/2011	7/4/2012	7/27/2012	18	54	232	2637	2160
	BG	200C054H094O0800	OP	4806	2441	7/31/2011	7/5/2012	7/29/2012	18	54	231	2694	2160
	BH	202C054H094O0800	EV	4963	2563	7/29/2011	7/1/2012	7/28/2012	18	54	212	3066	2269
	BI	202A090H094O0800	EV	4739	2594	7/3/2011	7/28/2012	8/21/2012	20	80	144	2404	2130
	BJ	200B090H094O0800	MU	4613	2467	7/5/2011	8/8/2012	8/21/2012	16	80	232	2653	1928
	BK	203D090H094O0800	OP	4587	2488	7/1/2011	7/3/2012	8/20/2012	19	76	171	2145	1979
	BL	203C089H094O0802	MU	4542	2462	7/7/2011	8/8/2012	8/20/2012	17	85	217	2615	2102
	BM	204C089H094O0800	EV	4559	2592	6/29/2011	7/27/2012	8/18/2012	20	80	163	2409	2102
	BN	200B099H094O0800	OP	4588	2481	7/9/2011	7/29/2012	8/21/2012	17	85	232	2661	2045
	BO	203A099H094O0800	MU	4622	2447	6/27/2011	7/28/2012	8/21/2012	16	80	231	2643	1967
	BP	204A099H094O0800	EV	4818	2580	7/11/2011	7/26/2012	8/15/2012	21	84	150	2307	2178
	BQ	202B098H094O0800	OP	4710	2471	6/23/2011	7/28/2012	8/21/2012	17	85	231	2587	2030
Pad C	C0	200A090H094O0802	MU	4874	2483	11/17/2010	7/1/2011	8/10/2011	16	80	247.55	3532.63	2008
	CA	200D090H094O0800	EV	4822	2615	11/25/2010	7/2/2011	8/2/2011	17	68	155.03	2851	1825
	CB	202D090H094O0800	OP	4635	2505	11/22/2010	7/11/2011	8/12/2011	16	80	245.61	3310.5	1941.5
	CC	202C089H094O0800	MU	4506	2484	11/28/2010	7/10/2011	8/11/2011	15	75	248.65	3343.7	1855
	CD	200C089H094O0800	EV	4605	2598	12/12/2010	7/2/2011	8/4/2011	17	68	157.75	2882.71	1852
	CE	200A099H094O0800	OP	4560	2501	12/1/2010	7/8/2011	8/13/2011	16	80	149.06	3210.94	1930
	D01	202A099H094O0800	MU	4612	2484	12/10/2010	7/11/2011	8/12/2011	15	75	142.56	3171.8	1835
	DA1	200B098H094O0800	EV	4860	2597	12/4/2010	7/2/2011	8/3/2011	18	72	212.59	3482	1809
	DB1	200C098H094O0802	OP	4730	2502	12/7/2010	7/11/2011	8/12/2011	15	75	155.67	3367.13	1929
	CG	200C013J094O0800	OP	4658	2586	5/31/2013	7/12/2014	8/8/2014	18	72	203	2354.9	1786.9
	CH	202C013J094O0800	EV	4870	2640	5/27/2013	7/11/2014	8/8/2014	20	80	170.9	2426.8	1971.1
	CI	200B023J094O0800	MU	4660	2547	6/2/2013	7/7/2014	8/6/2014	20	80	193.2	2408.7	2000.9

	CJ	202C023J094O0800	EV	5050	2640	6/4/2013	7/6/2014	8/8/2014	25	100	169.8	2354	2483.3
	CK	200C023J094O0800	OP	4959	2596	6/4/2013	7/5/2014	8/7/2014	25	100	202.3	2349.6	2411.2
	CL	200D023J094O0800	EV	5279	2630	5/22/2013	7/15/2014	8/8/2014	26	104	162.4	2469.4	2550.9
	CM	200A033J094O0800	MU	5285	2550	5/20/2013	7/4/2014	8/7/2014	26	104	200.4	2415.2	2588.2
	CN	202A033J094O0800	EV	5633	2642	5/20/2013	7/5/2014	8/7/2014	27	108	170.7	2316.5	2713.6
	CO	200B032J094O0800	OP	5488	2580	6/8/2013	7/6/2014	8/7/2014	26	104	203.2	2351.3	2560.4
	CP	202B032J094O0800	EV	5407	2625	5/16/2013	7/8/2014	8/7/2014	25	150	169.1	2394	2466.7
Pad D	D0	200A016H094O0800	MU	5245	2470	5/4/2012	7/6/2013	8/10/2013	25	100	207	2290	2462.1
	DA	202B015H094O0800	EV	5322	2576	5/20/2012	7/10/2013	8/10/2013	25	100	151.2	2532.7	2442.5
	DB	200B015H094O0800	OP	5222	2508	5/7/2012	7/12/2013	8/10/2013	26	104	200.4	2548.7	2528.7
	DC	200C015H094O0800	EV	5204	2579	5/19/2012	7/6/2013	8/8/2013	24	96	158.9	2501.8	2369.2
	DD	202D015H094O0800	MU	5135	2453	5/9/2012	7/6/2013	8/9/2013	24	92	201.5	2305.5	2464
	DE	203D015H094O0802	OP	5162	2493	5/17/2012	7/6/2013	8/10/2013	27	108	199.2	2424.3	2604
	DF	200D015H094O0800	EV	5183	2569	5/22/2012	7/7/2013	8/10/2013	24	96	168.4	2518.2	2418.2
	DG	200C014H094O0800	MU	5160	2443	5/11/2012	7/5/2013	8/9/2013	22	76	201.7	2394.5	2285.8
	DH	200B024H094O0800	EV	5259	2551	5/15/2012	7/7/2013	8/10/2013	25	100	159	2496.5	2461.2
	DI	202B024H094O0800	OP	5220	2490	5/13/2012	7/6/2013	8/10/2013	26	104	208.5	2531.5	2547.2

Table C.3: Summary of microseismic data measured for 21 wells completed in the Horn River Basin. Blank spaces= no reported data. na= no available data.

Pad	Well	Stage	Number of Events (within 500 m)	Total Number of Events	D-value	B-value	Magnitude	Fracture Length			Fracture Width			Fracture height		
								10%	50%	90%	10%	50%	90%	10%	50%	90%
Pad A	A0	11	365	392	1.56	1.8	-1.0300	-316	-71	313	-247	-108	8	8	60	104
		12	411	411	2.68	2.2	-1.0600	-192	21	264	-101	13	113	-7	21	66
		13	364	384	0.14	1.42	-0.9288	-84	41	394	-123	0	119	-20	19	68
		14	771	983	2.62	1.53	-1.1537	-264	198	582	-276	-94	84	2	50	94
		15	634	655	2.27	1.53	-1.1221	-49	68	282	-139	-76	85	-8	93	117
		16	744	816	2.54	1.48	-1.0416	-467	113	288	-73	-13	91	-29	-12	77
		17	797	833	2.29	1.52	-1.1080	-72	26	403	-218	-85	11	-24	12	92
		18	1269	1686	2.46	1.37	-1.3711	15	341	587	-174	-114	5	2	51	109
		19	783	954	2.37	1.32	-1.2310	136	374	514	-112	-86	-10	9	84	120
		20	989	1409	2.37	1.46	-1.5197	186	369	613	-109	-65	-20	-27	30	84
	AA	11	528	580	2.65	1.28	-1.1150	-461	-117	183	-120	16	154	-86	-12	62
		12	911	938	2.87	1.43	-1.1200	-330	112	321	-234	-79	118	-42	14	91
		13	1363	1397	2.71	1.43	-1.0636	-312	-5	246	-138	-39	68	-75	-23	22
		14	1474	1483	2.56	1.45	-0.9800	-208	19	278	-157	-85	5	-49	45	79
		15	1100	1155	2.58	1.35	-1.0166	-315	39	267	-154	-78	19	-44	15	70
		16	599	637	2.84	1.33	-1.0244	-283	14	305	-138	-56	70	-61	-11	41
	AB	14	42	126	1.93	1.4	-1.0886	1	482	763	-111	180	458	-46	-1	62
		15	52	129	2.03	1.64	-1.2596	14	404	904	-1334	-1164	-37	-86	-44	71
		16	255	596	1.83	1.44	-1.4389	154	587	796	-185	-101	-46	-19	14	72
		17	827	1685	2.09	1.11	-1.5268	-215	514	772	-114	-57	53	-12	48	72
	AC	16	302	312	0.63	1.38	-0.9069	-313	-62	142	-73	2	136	-59	48	96
		17	370	379	2.66	1.47	-1.2504	-183	-31	172	-65	9	155	-7	67	99
		18	1242	1340	2.61	1.29	-1.2483	-364	-59	182	-87	-1	184	-12	41	90
		19	717	794	2.85	1.47	-1.4211	-484	-74	54	-68	-11	59	-10	44	113
		20	810	862	2.47	1.36	-0.9937	-437	-248	-15	-32	85	195	-74	-3	51
	AE	14	223	238	2.5	1.17	-1.3549	-71	251	422	-253	-100	75	-129	-19	53
		15	211	286	0.45	1.8	-1.1307	-14	237	629	-366	-35	86	-71	-2	34
		16	159	250	2.03	1.59	-1.3189	-93	266	811	-488	-121	-9	-107	-25	32
		17	266	479	2.45	1.7	-1.4046	152	463	703	-244	-24	33	-20	8	71
		18	923	1179	2.71	1.16	-1.3076	-28	378	610	-55	4	59	-32	-6	30
		19	359	980	2.44	1.16	-1.4936	197	567	723	-73	-36	4	-48	-6	46
	AF	10	501	592	2.8	1.89	-1.1103	-542	-189	234	-159	-25	124	-54	18	68
		11	544	579	2.7	1.86	-1.1336	-409	-95	225	-168	27	142	-52	20	79
		12	924	1082	2.54	1.38	-1.1511	-499	-130	309	-108	29	134	-28	39	72
		13	886	1138	2.59	1.51	-1.1631	-580	-251	318	-42	48	111	-61	-5	71
		14	1130	1202	2.36	1.42	-1.1784	-405	-28	272	-66	58	124	-71	-15	67
		15	1039	1181	2.61	1.45	-1.2221	-519	-148	243	-82	19	111	-83	-27	67

		16	912	984	2.37	1.49	-1.2385	-307	62	288	-70	53	138	-82	-21	56
		17	621	818	2.48	1.73	-1.0974	-69	90	242	-9	66	681	-63	-2	90
		11	343	348	2.75	1.38	-0.8964	-283	20	248	-169	7	128	-58	18	84
		12	632	851	2.23	1.61	-1.1442	-717	-60	306	-144	-43	293	-22	33	101
		13	330	378	2.07	1.54	-0.8178	-524	33	275	-179	-57	97	-14	52	105
		14	333	366	2.6	1.7	-0.9922	-328	41	327	-152	-42	67	-57	32	73
	AG	15	850	875	2.38	1.49	-1.0494	-343	-126	53	-131	-66	35	-68	-14	49
		16	491	502	2.56	1.79	-1.2196	-270	12	349	-84	22	96	-4	29	70
		17	669	681	2.48	1.82	-1.0582	-201	-9	290	-83	22	63	5	23	54
		18	594	601	2.55	1.5	-1.3390	-248	178	399	-28	54	135	-7	19	74
		19	1400	1410	2.36	1.24	-1.3519	-11	174	258	-20	9	99	-132	-86	16
		20	717	789	2.26	1.55	-1.1444	-70	45	472	-67	-4	73	-169	-23	40
	C0	7	25	100	1.56	1.26	-0.6489	35	758	1182	-330	-25	154	-93	-47	36
		8	52	132	1.64	0.56	-1.3350	-18	567	831	-237	-98	51	-92	2	55
		9	519	797	2.55	1.74	-1.2908	-119	262	952	-253	-148	45	-88	-52	-19
		10	714	1097	2.69	1.69	-1.2670	34	377	1049	-362	-92	110	-122	-69	5
		11	176	492	2.1	1.51	-1.0708	208	639	994	-70	120	304	-86	-24	51
		12	99	142	2.13	2.36	-1.2416	51	414	742	-233	-91	41	-102	-28	20
		13	974	1153	2.69	1.66	-1.4780	123	302	526	-192	-106	-28	-69	-35	14
		14	1363	2238	2.5	1.65	-1.5347	197	437	661	-210	-116	-40	-70	-28	24
		15	1107	1729	2.61	1.42	-1.6857	191	399	649	-248	-110	5	-70	-24	44
		16	1553	3068	2.67	1.38	-1.7529	143	472	813	-171	-76	46	-82	-31	28
	CA	13	3594	4004	1.94	1.24	-1.7489	6	212	478	-228	-38	63	-3	73	146
		14	78	181	2.46	1.57	-0.7805	253	525	686	-92	18	128	-17	26	148
		15	520	1261	2.59	1.15	-1.3080	8	773	1110	-86	61	214	-38	25	72
		16	2037	2100	2.76	1.47	-1.8195	-10	102	251	-104	-18	77	-28	15	80
		17	3426	3606	2.72	1.37	-1.8015	56	130	269	-99	-5	87	-20	36	99
Pad C	CB	8	635	775	2.46	1.72	-1.0809	-128	113	580	-218	-33	132	-48	32	73
		9	701	839	2.43	1.72	-0.9726	-156	117	479	-243	-63	147	-65	23	55
		10	935	1093	2.42	1.76	-0.9471	87	281	512	-291	-143	15	-106	-73	-45
		11	755	758	2.75	1.67	-1.0571	-69	154	242	-228	-147	37	-50	-19	49
		12	579	593	2.5	0.79	-0.7669	-28	112	249	-184	-135	-32	-48	-15	23
		13	941	1023	2.48	1.5	-1.3148	-120	140	437	-195	-62	65	-61	-29	30
		14	533	674	2.52	1.58	-1.3456	-4	295	617	-204	-89	61	-46	1	55
		15	1297	2728	2.66	1.46	-1.6856	-98	506	806	-268	-92	40	-38	24	68
		16	3254	5420	2.76	1.06	-1.6776	-60	370	773	-184	-66	45	-82	-20	41
	CC	6	721	1003	2.37	1.38	-1.0006	-339	16	497	-471	-107	39	-123	-13	40
		7	97	284	1.63	1.71	-0.3072	-20	614	999	-393	-139	122	-94	-38	24
		8	330	1049	2.38	1.28	-0.8840	-277	501	686	-380	-225	69	-126	-67	31
		9	1220	1650	2.42	1.53	-1.0045	-303	209	564	-278	-33	194	-132	-65	-7
		10	788	897	2.55	1.33	-1.1136	-193	175	477	-225	-20	166	-124	-65	46
		11	1165	1556	2.69	1.44	-1.1468	-40	281	595	-199	20	180	-135	-51	58

		12	845	2377	2.47	1.43	-1.5519	101	537	643	-195	-90	81	-124	-30	42
		13	969	1443	2.59	1.48	-1.5441	-10	208	619	-159	-79	44	-120	-29	41
		14	1516	1660	2.74	1.51	-1.4132	-118	134	468	-157	-35	81	-62	1	44
		15	1860	2617	2.64	1.19	-1.4210	-147	191	596	-115	-14	361	-212	-24	21
	CD	13	1605	1605	2.55	1.14	-0.8142	152	248	324	-89	-50	24	-28	-7	119
		14	933	1002	2.56	0.95	-0.9773	57	231	450	-133	4	178	-69	-20	50
		15	3471	3874	2.34	1.13	-1.3039	-328	152	446	-45	71	176	-71	6	109
		16	5962	7407	2.53	1.03	-1.2431	-322	357	528	-23	90	147	-78	-10	115
		17	2860	3071	2.61	1.76	-1.4620	-324	-60	350	-86	23	122	-53	-13	120
	CE	8	171	174	1.98	1.29	-1.0223	-158	34	280	-360	-96	28	-102	11	60
		9	1009	1157	2.73	1.64	-1.2015	47	181	312	-671	-114	-29	-320	-125	16
		10	1533	1560	2.38	1.27	-1.0476	-60	129	281	-201	-31	64	-94	-45	59
		11	1554	1603	2.6	1.39	-1.1279	-121	49	270	-199	-57	114	-101	-48	28
		12	1603	1739	2.22	1.37	-1.1289	-199	67	383	-184	-26	124	-65	-22	36
		13	2035	2038	2.76	1.25	-1.1868	-177	100	312	-142	-64	57	-62	-12	59
		14	2877	2890	1.77	1.6	-1.4019	-181	56	321	-124	-28	105	-66	-29	34
		15	4650	5294	2.63	1.55	-1.5213	-62	137	411	-252	-70	33	-126	-40	31
		16	2313	2396	2.41	1.31	-1.6071	-252	45	326	-161	-15	78	-92	-27	22
	CF	6	50	117	2.46	1.49	-0.9672	-573	-361	-52	-489	-136	58	-130	1	33
		7	503	769	2.33	1.1	-0.9510	-251	-86	138	-505	-399	-91	-133	-78	12
		8	132	161	1.97	1.15	-0.7615	-254	-23	267	-463	-327	-116	-153	-120	-9
		9	1143	1154	2.52	1.53	-0.9772	-249	-28	197	-283	-79	113	-113	-69	17
		10	2499	2506	2.45	1.21	-1.0042	-201	-54	92	-397	-176	75	-189	-129	-1
		11	1579	1604	2.27	1.27	-1.0469	-198	-58	74	-279	-246	91	-190	-137	-27
		12	833	972	2.36	1.26	-1.1015	-645	-41	106	-382	7	103	-183	-79	-9
		13	1268	1304	2.23	1.31	-1.1868	-231	13	149	-108	79	164	-350	-85	30
		14	2527	2534	2.55	1.06	-1.2299	-188	-35	146	-128	-48	63	-303	-127	6
		14.1	1026	1048	na	1.36	-1.4989							-119	3	45
		15	3099	3387	2.75	1.24	-1.4054	-180	-2	211	-416	-48	74	-281	-99	-16
Pad D	CG	11	2986	2986	2.68	1.21	-0.6724	-309	-194	22	-126	-91	-48	-57	-8	25
		12	2815	3073	2.48	1.08	-1.2779	-452	-127	51	-114	-14	53	-70	17	131
		13	3302	3316	2.46	0.95	-0.7844	-406	-283	-71	-68	-14	112	-24	17	81
		14	5491	5514	2.57	1.08	-1.0708	-420	-230	-46	-55	15	73	-87	-32	25
		15	1279	1330	2.33	1.29	-1.2484	-443	-237	56	-50	46	209	-38	33	100
		16	4606	4608	2.75	1.17	-0.9892	-266	-167	64	2	56	109	-81	-38	37
		17	2017	2017	1.9	1.28	-1.0175	-386	-81	62	-42	52	155	-41	30	51
		18	1929	1995	1.78	1.23	-1.5091	-343	-171	78	-43	37	129	-70	17	148
	CH	7	152	214	2.12	1.37	-0.6946	-517	-327	-68	-423	-22	190	-88	-36	42
		8	262	319	2.4	2.13	-0.9301	-368	-9	57	-421	-11	113	-89	-13	9
		9	549	593	2.56	1.29	-1.2015	-428	-327	-47	-138	-71	90	-201	-103	6
		10	697	1218	2.63	1.15	-1.0756	-422	-328	-223	-379	-313	56	-198	-143	-68
		11	872	974	2.32	1.19	-1.2449	-458	-108	155	-323	-15	98	-105	10	79

	12	1776	2149	2.64	1.2	-1.3066	-580	-295	-23	-74	65	220	-108	-24	71
	13	623	694	2.6	1.64	-1.2444	-404	-149	412	-161	-12	86	-63	-1	56
	14	2263	2607	2.77	1.35	-1.3455	-425	-223	395	-135	-38	128	-257	-49	56
	15	1575	1684	2.91	1.07	-1.2311	-367	-272	145	-86	136	200	-289	-151	13
D0	14	260	270	2.58	1.82	-1.3515	-120	102	366	-31	30	83	-63	-32	42
	15	261	262	2.47	2.25	-1.3624	-59	158	300	-56	38	90	-42	-20	39
	16	408	420	2.71	1.77	-1.4675	-94	58	281	-81	39	112	-51	-4	28
	17	405	406	2.59	2.12	-1.5489	-43	143	297	-27	58	145	-66	-30	1
	18	404	410	2.92	1.86	-1.6169	-140	43	308	-10	74	148	-70	-23	38
	19	321	347	2.84	1.78	-1.6399	-44	178	472	2	80	164	-50	-2	38
	20	746	763	2.66	1.82	-1.5525	-23	164	420	17	95	192	-90	-33	9
	21	850	852	2.53	1.65	-1.6355	-197	38	208	-45	27	104	-63	-9	41
	22	961	1017	2.71	1.69	-1.7197	-178	60	415	-62	53	147	-64	-17	27
	23	607	665	2.95	1.27	-1.6808	-109	60	299	-40	39	135	-268	-41	27
	24	514	527	2.68	1.6	-1.8550	-49	149	345	-19	91	211	-116	-19	73
DA	14	543	543	2.44	1.11	-1.1527	-173	-76	204	-91	7	43	-364	-92	72
	15	568	570	2.61	1.62	-1.4073	-113	-14	220	-101	-27	77	-349	-104	91
	16	863	863	2.93	1.84	-1.3922	-96	24	206	-68	10	75	-64	17	89
	17	269	269	2.12	1.64	-1.5550	-157	-11	188	-70	41	94	-122	6	106
	18	718	719	2.67	1.67	-1.5439	-130	27	192	-29	62	135	-26	10	78
	19	322	325	2.43	1.96	-1.6671	-100	138	277	-82	-17	71	-46	59	95
	20	943	947	2.88	1.83	-1.7593	-46	7	154	-165	-107	31	-162	-98	69
	21	378	382	2.8	1.95	-1.4479	-268	-32	192	-56	5	103	13	59	102
	22	1233	1235	2.22	1.66	-1.7717	-165	-14	222	-156	-25	45	-18	51	123
	23	327	327	2.3	1.23	-1.7306	-87	90	352	-57	4	109	-145	5	132
	24	451	451	2.83	1.56	-1.8008	-109	25	218	-19	34	100	-3	48	117
DB	14	626	626	2.49	2.23	-1.4350	-25	70	204	-97	-23	57	4	34	69
	15	1122	1122	2.7	1.8	-1.5407	-137	5	151	-107	14	123	3	26	49
	16	1111	1111	2.66	1.94	-1.4505	-140	20	128	-54	-12	46	-5	28	60
	17	1413	1413	2.86	1.73	-1.5937	-93	17	93	-63	7	79	-16	15	52
	18	1007	1017	2.74	2.05	-1.5926	-136	17	152	-63	-14	73	-13	13	52
	19	1337	1358	2.59	1.72	-1.5794	-164	1	139	-81	-29	56	-30	4	34
	20	2516	2516	2.64	1.52	-1.7254	-106	18	123	-47	1	68	-41	10	39
	21	847	873	2.75	2.05	-1.6925	-326	-127	48	-73	-18	60	-63	-2	49
	22	1384	1414	2.72	1.55	-1.7950	-235	-55	100	-82	-7	60	-58	5	60
	23	2624	2624	2.89	1.47	-1.7633	-217	-111	31	-68	18	103	-65	-16	50
DC	14	569	783	2.47	1.41	-1.2860	-563	-64	143	-143	14	145	-441	22	119
	15	305	308	2.49	1.98	-1.3963	-238	37	369	-84	1	76	-70	57	114
	16	795	799	2.65	2.19	-1.5125	-220	-8	214	-74	0	76	-37	37	70
	17	633	633	2.66	1.98	-1.5717	-266	-50	171	-68	-9	43	-60	38	76
	18	1424	1424	2.65	1.64	-1.6427	-162	3	198	-40	8	79	-74	2	54
	19	962	981	2.56	1.64	-1.7035	-214	15	229	-71	-6	67	-28	35	85

	20	1171	1174	2.67	1.63	-1.6816	-283	-87	137	-55	-9	47	-17	60	97
	21	1310	1331	2.83	1.6	-1.7283	-277	-66	95	-53	3	43	1	49	109
	22	1438	1470	2.79	1.5	-1.7381	-304	-44	178	-46	7	88	1	48	116
	23	1157	1224	2.57	1.49	-1.7473	-340	-55	145	-59	35	139	-160	15	124
	24	722	736	2.52	1.29	-1.8407	-402	-148	14	16	77	190	-76	-2	104
DD	14	446	446	2.93	1.85	-1.2762	-142	4	105	46	155	248	-62	3	30
	15	800	811	2.79	1.94	-1.3678	-141	-15	223	-100	-11	57	-39	-2	26
	16	764	779	2.66	1.87	-1.4148	-252	-10	324	-75	12	115	-68	-1	56
	17	1154	1158	2.61	1.98	-1.5334	-248	-100	102	-33	19	105	-109	-33	22
	18	774	786	2.56	1.57	-1.5913	-381	-110	52	-62	-5	62	-65	-10	31
	19	1149	1155	2.77	1.66	-1.6586	-309	-79	92	-43	13	100	-65	-22	12
	20	1087	1100	2.6	1.63	-1.6215	-176	-55	176	-50	35	112	-40	-17	15
	21	1236	1241	2.71	1.73	-1.6426	-269	-119	96	-46	20	110	-42	-16	19
	22	1346	1436	2.64	1.5	-1.7211	-469	-163	97	-48	35	161	-97	-35	16
	23	1617	1775	2.65	1.4	-1.7683	-455	-249	-21	-25	71	169	-256	-81	12
DE	14	258	258	2.44	2.34	-1.5098	-97	-21	26	-66	-3	69	-9	7	55
	15	345	345	2.72	3.13	-1.5088	-127	25	121	-53	9	64	-8	10	76
	16	965	965	2.88	2.2	-1.4823	-86	15	180	-29	13	61	-13	3	22
	17	1005	1025	2.83	2.25	-1.5586	-115	14	104	-83	-27	61	-72	-3	25
	18	449	470	2.63	2.14	-1.5362	-263	34	113	-37	18	103	-25	3	30
	19	1462	1462	2.76	2.03	-1.6204	-74	17	168	-66	1	81	-38	3	33
	20	1155	1161	2.74	1.91	-1.6368	-141	-14	82	-66	-30	25	-73	-13	24
	21	750	908	2.62	1.95	-1.5714	-626	-31	39	-52	-8	88	-32	11	48
	22	587	686	2.65	1.86	-1.6500	-523	-26	61	-34	36	136	-24	13	53
	23	775	813	2.77	1.78	-1.5960	-276	-30	62	-54	22	114	-70	31	87
	24	311	327	2.55	2.07	-1.4937	-91	62	417	-73	-11	98	-89	14	101
DF	12	510	513	2.61	2	-1.2959	-271	-7	155	-70	42	199	14	55	104
	13	324	324	2.65	2.36	-1.3999	-313	-2	138	-118	-5	137	24	68	136
	14	704	704	2.7	2.01	-1.3811	-140	19	188	-116	-14	138	12	56	101
	15	603	603	2.75	2.27	-1.4478	-244	-19	127	-95	-32	33	-21	53	82
	16	1038	1040	2.51	1.82	-1.5528	-259	-40	69	-130	-12	108	-16	53	95
	17	881	890	2.44	1.98	-1.6026	-267	-40	103	-73	2	104	-17	39	86
	18	1612	1654	2.74	1.65	-1.5413	-267	-47	81	-103	-32	52	-17	39	71
	19	1494	1537	2.7	1.76	-1.6536	-281	-77	153	-74	20	121	-18	35	71
	20	1537	1587	2.56	1.92	-1.6104	-335	-114	63	-65	-15	59	1	42	92
	21	1014	1183	2.62	1.66	-1.6725	-618	-179	55	-82	-23	82	9	55	106
	22	919	949	2.92	1.93	-1.6904	-388	-74	286	-158	-21	95	-7	59	126
	23	196	216	2.58	2.06	-1.6455	-482	-135	-19	-35	36	132	-82	31	111
DG	4	40	44	1.76	na	-0.9244	-222	86	225	-75	41	239	-81	-22	52
	6	150	155	2.4	2.47	-0.9380	-123	39	221	-221	-37	167	-51	21	41
	7	199	202	2.8	2.43	-1.0093	-190	86	315	-180	-54	77	-53	26	55
	8	119	119	2.53	na	-1.1218	-92	88	260	-95	-14	70	8	29	50

	9	516	517	2.63	1.95	-0.9883	-203	21	183	-68	61	218	-69	-11	36
	10	672	672	2.48	1.8	-1.0893	-166	1	159	-66	-1	52	-39	-8	43
	11	640	644	2.6	1.92	-1.1710	-310	-45	213	-45	22	87	-31	5	45
	12	1043	1063	2.67	1.99	-1.1618	-168	56	294	-51	9	69	-36	33	57
	13	996	1016	2.81	1.83	-1.1228	-233	17	231	-65	10	70	-48	23	60
	14	519	519	2.63	2.09	-1.1603	-131	19	156	-55	18	109	-21	19	59
	15	352	370	2.83	2.22	-1.3057	-119	47	195	-100	-20	57	-49	11	81
	16	594	597	2.65	1.9	-1.5056	-270	-27	139	-83	4	107	-51	5	61
	17	432	444	2.67	1.83	-1.5006	-231	-56	176	-38	41	153	-56	-7	49
	18	292	306	2.67	1.75	-1.5592	-185	-10	440	-47	9	116	-66	-21	29
	19	304	307	2.89	2.24	-1.5811	-247	-69	75	-56	18	139	-58	-28	26
	20	313	319	2.46	1.83	-1.6267	-267	-47	257	-124	-27	60	-70	-17	42
	21	233	233	2.74	1.95	-1.5257	-259	-100	81	-93	-18	81	-120	-78	-20
	22	178	189	2.99	1.85	-1.6577	-131	3	336	-84	-11	67	-80	-27	14
	23	238	327	2.24	1.46	-1.6772	-852	-39	461	-110	-24	82	-244	-23	18
	24	324	376	2.56	1.77	-1.5922	-378	-71	396	-106	51	128	-178	-69	3
DH	14	123	144	2.32	na	-1.3328	-417	-91	505	-140	7	137	-52	-10	72
	15	139	141	2.17	na	-1.3622	-265	11	343	-138	-40	71	20	97	164
	16	294	297	2.31	2.14	-1.3928	-280	-30	124	-58	52	161	24	58	81
	17	510	514	2.52	2.02	-1.5401	-360	-60	225	-51	9	74	-24	29	93
	18	769	769	2.95	1.79	-1.5578	-206	-62	124	-59	-3	118	4	53	89
	19	469	469	2.95	1.93	-1.5601	-207	37	285	-106	-35	23	-9	56	100
	20	729	745	2.79	1.77	-1.5574	-273	-32	203	-91	-36	17	-25	52	97
	21	651	705	2.95	1.85	-1.5313	-259	36	444	-80	-17	47	-15	56	107
	22	469	487	2.56	1.76	-1.6562	-350	-108	300	-111	-46	27	-54	36	126
	23	262	338	2.52	1.76	-1.5067	-1021	-164	16	-80	14	107	-159	-24	84
	24	213	214	2.56	2.33	-1.6344	-267	-33	101	-103	-9	45	-61	11	66
DI	13	444	444	2.67	2.15	-1.2866	-71	42	113	-78	-21	44	11	34	99
	14	309	309	2.83	2.26	-1.2980	-57	30	148	-47	0	54	16	35	80
	15	533	534	2.76	2.42	-1.3254	-176	24	112	-88	-18	46	3	25	83
	16	585	585	2.71	2.1	-1.3429	-227	6	86	-111	-33	86	3	18	32
	17	832	832	3.09	2.04	-1.3648	-167	23	102	-52	-10	31	5	18	34
	18	561	562	2.31	2.19	-1.4049	-93	24	148	-67	-21	43	-14	15	85
	19	950	951	2.99	2.2	-1.4922	-152	-9	105	-80	-25	36	-48	9	33
	20	996	996	2.82	1.93	-1.5388	-137	-9	131	-89	-46	0	-18	26	56
	21	1207	1207	2.96	1.66	-1.5708	-161	-26	127	-92	-38	10	1	41	74
	22	1168	1175	2.75	1.76	-1.6393	-244	-28	144	-113	-44	27	-35	40	92
	23	338	395	2.3	1.78	-1.3450	-965	-49	82	-36	53	145	-209	-5	33
	24	189	189	2.71	1.82	-1.5988	-108	2	131	-119	-81	-22	-181	-61	56

Table C.4: Summary of well name, well spacing, frequency, average pressure increase, and data source for frac-hits in 4 pads. Blank spaces= no reported data. na= no available data.

	Active Well		Observation Well		Well Spacing		Total number of reported Frac-hits	Average pressure increase, MPa	Data Source
	Well Name	Formation	Well Name	Formation	Lateral	Vertical		*dP*	
Pad A	B0	OP	BB	MU	390	65	1	1.7	
			BC	OP	780	0	1	0.9	
Pad B	B0	Mu	BB	OP	150		na	na	
			BC	MU			na	na	
	BE	OP	BF	MU			1	2.1	
Pad C	C01	Mu	CC1	MU	300	0	1	2.74	BCOGC (Accessed in Sep 2018)
	CA	EV	CD	EV	600	0	2	8.6	
	CB	OP	C-0	MU	500	65	1	2	
			CC1	MU	500	65	3	2.13	
	CC1	MU	C01	MU	300	0	1	0.7	
			CE1	OP	200	-65	3	3.56	
	D01	MU	CC	MU	300	0	2	3.4	
	CG	OP	CI	MU	500	65	4		
			CJ	EV	650	-65	1		
	CH	EV	CJ	EV	400	0	7		
			CI	MU	250	130	3		
			CG	OP	250	65	1		
			CH	EV	250	-130	2		
	CI	MU	CG	OP	500	-65	4		
			CK	OP	400	-65	5		
			CM	MU	800	0	1		
	CJ	EV	CG	OP	650	65	1		
			CH	EV	400	0	6		
			CI	MU	250	130	1		
			CK	OP	200	65	4		
			CL	EV	800	0	7		
			CN	EV	1200	0	1		
	CK	OP	CI	MU	400	65	6		
			CJ	EV	200	-65	1		
			CM	MU	400	65	1		
			CP	EV	1000	-65	1		
	CL	EV	CJ	EV	800	0	7		
			CK	OP	200	65	3		
			CM	MU	150	130	2		
			CN	EV	400	0	8		
			Well-CP	EV	800	0	2		
	CM	MU	CJ	EV	550	-130	1		
			CK	OP	400	-65	5		
			CO	OP	450	-65	4		
	CN	EV	CH	EV	800	0	1		
			CL	EV	400	0	5		
			CM	MU	200	130	1		
			CJ	EV	400	0	1		
			CO	OP	250	65	5		
			CP	EV	800	0	12		
	CO	OP	CM	MU	450	65	2		
			CN	EV	250	-65	1		
			CP	EV	250	-65	3		
	CP	EV	CN	EV	450	0	9		
			CO	OP	250	65	6		
Pad D	D0	MU	DA	EV	150	-130	2	0.29	
			DB	OP	300	-65	18	0.84	

		DD	MU	600	0	13	0.48	
		D0	Mu	150	130	24	1.25	
		DB	OP	150	65	22	2.36	Modified
		DC	EV	400	0	16	2.12	from
		DD	Mu	450	130	6	0.53	Sardinha et
DA	EV	DE	OP	700	65	1	0.15	al. (2014)
		DF	EV	800	0	2	0.13	
		DG	Mu	1050	130	2	2.54	
		DH	EV	1200	0	1	1.15	
		D0	MU	300	65	24	1.63	
		DA	EV	150	-65	24	2.88	
		DC	EV	250	-65	22	2.03	
DB	OP	DD	MU	300	65	24	1.18	
		DE	OP	600	0	14	0.72	
		DG	MU	900	65	5	0.18	
		DI	OP	1200	0	3	2.88	
		D0	MU	550	130	24	0.93	
		DA	EV	400	0	12	2.49	
		DB	OP	250	65	24	1.48	
		DD	MU	60	130	21	1.11	
DC	EV	DE	OP	300	65	20	1.24	
		DF	EV	400	0	20	2.44	
		DG	MU	650	130	17	0.79	
		DH	EV	800	0	6	1.61	
		D 0	MU	600	0	21	1.34	
		DB	OP	300	-65	18	1.3	
		DC	EV	60	-130	10	0.72	
DD	MU	DE	OP	250	-65	18	1.2	
		DF	EV	320	-130	1	0.12	
		DG	MU	600	0	17	0.5	
		D0	MU	860	65	4	0.3	
		DA	EV	700	-65	2	0.43	
		DB	OP	600	0	9	0.49	
		DC	EV	300	-65	12	1.04	
DE	OP	DD	MU	250	65	26	1.05	
		DF	EV	70	-65	20	1.91	
		DG	MU	340	65	18	1.03	
		DH	EV	500	-65	10	0.34	
		DI	OP	600	0	1	0.45	
		DA	EV	800	0	2	0.42	
		DB	OP	780	65	3	0.24	
		DC	EV	400	0	18	1.84	
		DD	MU	320	130	14	0.7	
DF	EV	DE	OP	70	65	23	1.74	
		DG	MU	280	130	19	0.93	
		DH	EV	400	0	20	1.59	
		DI	OP	580	65	13	0.39	
		DB	OP	900	-65	7	1.38	
		DD	MU	600	0	14	0.83	
		DE	OP	340	-65	18	1.23	
DG	MU	DF	EV	280	-130	10	0.24	
		DH	EV	150	-130	5	0.48	
		DI	OP	300	-65	18	0.88	
		DA	EV	1200	0	1	0.27	
		DC	EV	800	0	1	0.12	
		DD	MU	750	130	3	0.18	
DH	EV	DE	OP	500	65	4	0.4	
		DF	EV	400	0	12	2.02	
		DG	MU	150	130	25	0.63	
		DI	OP	150	65	25	2.64	
		DE	OP	600	0	4	0.83	
		DF	EV	580	-65	4	1.03	
DI	OP	DG	MU	300	65	17	0.53	
		DH	EV	150	-65	24	1.6	